DESIGN AND PROCESSING OF LOW ALLOY HIGH CARBON STEELS BY POWDER METALLURGY

Alhadi Amar Salem ABOSBAIA

PhD

UNIVERSITY OF BRADFORD

UNITED KINGDOM

2010

DESIGN AND PROCESSING OF LOW ALLOY HIGH CARBON STEELS BY POWDER METALLURGY

P/M Processing and Liquid Phase Sintering of Newly Designed Low-Alloy High Carbon Steels Based on Fe-0.85Mo-C-Si-Mn with High Toughness and Strength

By: Alhadi Amar Salem ABOSBAIA

Submitted for the degree of

Doctor of Philosophy

School of Engineering, Design and Technology

Mechanical and Materials Engineering Department

University of Bradford

United Kingdom

2010

Statement of Originality

To the best of my knowledge, I declare that this thesis is based on my original work except where otherwise noted within the text. I also declare, that this work has not been submitted in whole or in part for my degree at University of Bradford or any other university.

Mr. Alhadi Amar S. ABOSBAIA,

Bradford, UK

Data:

TITLE: Design and processing of low alloy high carbon steels by powder metallurgy.

NAME: Alhadi Amar Abosbaia

Keywords: PM processing; Ultra-high carbon PM steels, phase diagram modelling; liquid phase sintering; heat treatment; warm forging.

ABSTRACT

The work presented has the ultimate aim to increase dynamic mechanical properties by improvements in density and optimisation of microstructure of ultra high carbon PM steels by careful selection of processes, i.e. mixing, binding, alloying, heating profile and intelligent heat treatment. ThermoCalc modelling was employed to predict liquid phase amounts for two different powder grades, Astaloy 85Mo or Astaloy CrL with additive elements such as (0.4-0.6wt%)Si, (1.2-1.4wt%)C and (1-1.5wt%)Mn, in the sintering temperature range 1285-1300ºC and such powder mixes were pressed and liquid phase sintered. In high-C steels carbide networks form at the prior particle boundaries, leading to brittleness, unless the steel is heat-treated. To assist the breaking up of these continuous carbide networks, 0.4-0.6% silicon, in the form of silicon carbide, was added. The water gas shift reaction ($C + H_2O = CO + H_2$, start from ~500ºC) and Boudouard reaction (from ~500ºC complete ~930ºC) form CO gas in the early part of sintering and can lead to large porosity, which lowers mechanical properties. With the use of careful powder drying, low dew point atmospheres and optimisation of heating profiles, densities in excess of 7.70g/cm^3 were attained. The brittle microstructure, containing carbide networks and free of cracks, is transformed by intelligent heat treatment to a tougher one of ferrite plus sub-micron spheroidised carbides. This gives the potential for production of components, which are both tough and suitable for sizing to improve dimensional tolerance. Yield strengths up to 410 MPa, fracture strengths up to 950 MPa and strains of up to 16 % were attained. Forging experiments were subsequently carried out for spheroidised specimens of Fe-0.85Mo+06Si+1.4C, for different strain rates of 10^{-3}, 10^{-2}, 10^{-1} and 1sec^{-1} and heated in argon to 700ºC, density ~7.8g/cm^3 and 769 MPa yield strength were obtained.

Acknowledgements

I am very grateful to my Lord Almighty ALLAH (God) who helped me and guided me throughout my life and made it possible. I could never have done it by myself.

I would also like to take this opportunity to thank my supervisors, Dr. Stephen Mitchell and Dr. Mansour Youseffi for all their kind help, expert guidance, advice and patience during this work to put me in the right way.

I am particularly grateful to Professor Andrew Wronski his assistance, advice and great valuable comments.

Thanks are due to Professor Stefan Sczepanik for his kind assistance with the warm forging experiments.

I would like to thank Ms. Linda Maude and Andy Watts for their technical assistance. Also I would like to thank all my family and friends for their great support and ask their forgiveness for being absent when they need me.

Finally, I would like to thank my sponsor (Libyan Education Ministry Office) to give me this opportunity to finish my studies.

Dedication

*In loving memory of my **MUM**, who encouraged me to become a Doctor.*

May ALLAH (God) bless her.

*To my **Dad** for his advice and guidance all my life.*

*To my great wife **(Amal)** and my lovely children **(Ahmed, Mohammed and Hoor)** for their unceasing support, encouragement, patience and understanding.*

Publications

- S. C. Mitchell, M. Youseffi, A. A. S. Abosbaia, J. Ernest, 2008, 'Processing and heat treatment of high carbon liquid phase sintered steels', Powder Metallurgy Progress, Vol. 8 (2008), No 2, pp 91-100.

- Alhadi A. S. Abosbaia, Stephen C. Mitchell, Mansour Youseffi and Andrew S. Wronski, 2010, 'Liquid phase sintering, heat treatment and properties of ultra high carbon steels', *submitted to* the Journal of Powder Metallurgy, London' UK, July 2010.

- Stefan Szczepanik, Stephen C. Mitchell, Alhadi A. Abosbaia, Andrew S. Wronski, 2010, 'Warm forging of spheroidised ultrahigh carbon steel', *submitted to* the Journal of Powder Metallurgy Progress, Kosice, Slovakia, July 2010.

Table of Contents

List of Figures

List of Tables

Chapter One

1.1 Introduction

Powder metallurgy (PM) is conventionally a commercial metal-forming technology with the fundamental advantage of near net shape competence [1]. Iron and steel parts made by PM conventional process are an integral part of many tools, and machines used in automotive and aerospace industries etc., on a day-to-day basis [2]. Producing steel parts in complex shape by powder metallurgy production method is cheaper than other manufacturing methods [2]. Sintered steel parts have been produced by conventional sintering process which transforms the green compact into a high strength structure by heating the compact to a temperature below the melting point of the main constituent of the alloy, e.g. iron in this case, during which particles weld to each other, and diffusion alloying occurs leading to better strength and higher densities.

Sintered steels containing molybdenum have been used for many applications due to their medium strength, easy production and non-critical sintering conditions. Alloying elements such as Ni and Cu can also be used in these steels to promote the sintering process by forming liquid phase during sintering leading to higher sintered densities and better mechanical properties. These types of steels do not require high purity gas atmospheres during sintering due to their low affinity for oxygen [3]. Additions of Mn, Si, Cr and V have also been used instead of Ni and Cu, to increase the hardenability and strength of sintered steels. However, these elements can be oxidised during the sintering process due to their high affinity for oxygen, but these are less expensive elements compared with Ni and Cu. Manganese and silicon are known as strengtheners and very

common elements used in low alloy steels made by wrought steel processes [3]. Addition of these elements to the base powder has a beneficial effect on the sintered part properties, e.g. sintered density, hardness, tensile and transverse rupture strength [4]. Interaction between two diffusing powders can lead to the formation of liquid phase during sintering which may be of transient or persistent nature. Liquid phase can also be formed by heating a prealloyed powder between the solidus and liquidus temperatures known as super-solidus liquid phase sintering [5]. Higher hardness and strength can be achieved by post-sintering heat treatment for the proper alloy composition and cooling rate, which determines the amount of martensite produced.

Liquid phase sintering, technically proven for high speed steels [6-8], has not been shown to be applicable to structural steels. For direct sintering to full density of high speed steels, annealed high-carbon powders tend to be used. When the starting powder is low-carbon (alloyed) iron, however, one of the processing problems is the introduction of carbon. If it is added simply as graphite, segregation during handling [9] results in banding of the microstructure. Previously Mitchell et al [10, 11] attempted high-carbon sintering utilising thermally degraded PVC as the major carbon donor bonded to the iron base powder. The use of thermally degraded PVC was in response to problems of banding of the microstructure, which occurred due to segregation of graphite during handling [3]. Degradation of PVC is environmentally damaging due to hydrochloric acid forming as chlorine is driven from the PVC and which acts to catalytically convert the structure to a conjugated polymer containing double bonds. Therefore the subject was subsequently revisited using only graphite as the carbon source, but now bound to the surfaces of the base powder by judicious use of liquid lubricants such as liquid paraffin and polypropylene glycol during the mixing process. It

is the purpose of this work to show that a careful combination of Thermocalc modelling, powder mixing, processing and heat treatments can help minimise the potential problems of high carbon sintering and create a microstructure suitable for the production of components with good dimensional tolerance and which are subjected to high cyclical loadings.

Ultrahigh-carbon steels [12-16], UHCSs, i.e. where C is in the range of 1.0-2.1% by weight, have tended to be neglected by industry due to their brittleness, resulting from the presence of a severe grain boundary carbide network. Traditional heat treatments used for normal steels create coarse microstructures [15] but using a spheroidisation treatment can produce fine spheroidised carbides in fine ferrite. Microcracking of the martensite structure can also occur during traditional heat treatments, this microcracking results from impingement of growing martensite crystals against each other during transformation of austenite to martensite [17]. Previous studies [17-19] to eliminate or reduce these martensite microcracks were published, but all of these reports did not show a completely crack-free microstructure and some of them were quite complex procedures and expensive. This work was carried out by a combination of laboratory based experiments and theoretical analysis using Thermo Calc Tcw3 software as well as HSC Chemistry software to develop a new PM alloy composition based on either Astaloy 85Mo or Astaloy CrL powders. This design process allows improvement of the sintering process for achieving higher sintered densities, better microstructures, and desirable mechanical properties by production of a controlled amount of liquid phase.

1.2 Research Objectives

Researchers have been working on PM alloy steels to improve compaction and sintering processes to achieve good mechanical properties in the sintered and heat-treated conditions for various applications in the most cost-effective ways knowing also that mechanical properties are strongly dependent on the sintered density and microstructure. The major aim of this work is to produce high density PM steels with a modulus approaching that of wrought steels and to ensure that the steels possess a combination of good strength and ductility. This aim was to be achieved by liquid phase sintering of ultra-high carbon steels. Specifically this aim was to be accomplished by the following list of objectives:

- To optimise alloy composition using Mo, Si, Mn, Cr and C, and promote liquid phase sintering at a temperature 1300°C maximum. This optimisation to be achieved by phase diagram modelling using Thermo-Calc for Windows (TCW).
- The compositions demand use of ultra-high carbon content and this necessitates improvements in standard mixing techniques to prevent inhomogeneity of the powder mixes and eventual sintered microstructures.
- In view of the large volume of graphite employed for these ultra-high carbon steels, it is anticipated that moisture pickup will create problems, namely:
    1. Graphite agglomeration.
    2. Steam generation.
    3. Reactions between steam and graphite forming CO_2/CO whose partial pressures can damage the microstructure.
- These reactions involving carbon:

$C+2H_2O \rightarrow CO_2+2H_2$

$C+CO_2 \rightarrow 2CO$

$C+H_2O \rightarrow CO+H_2$

Modelling using HSC thermo chemistry software to determine temperatures at which the above reactions begin.

- The normal sintered microstructure of hyper-eutectoid steels needs to be modified by a heat treatment schedule which removes the continuous cementite network.
- One problem during quenching of ultra-high carbon steels is that of micro-cracking of the martensite laths due to large volume change and internal stresses. This will need to be addressed by intelligent heat treatment modification.
- The ultimate objective will be to correlate modelling results with processing, microstructure and mechanical properties throughout the whole processing cycle.

1.3 Outline of the Thesis

The thesis has been divided into six chapters as follows:

Chapter One, is an introduction to this thesis, introduces the problems to be studied, and presents the objectives and aims of this work. ***Chapter Two*** reviews the Literature of powder metallurgy (PM), manufacturing, characteristics, and advantages of use PM rather than wrought alloys. Sintering conditions also have been presented in this chapter as well as the kinetics of protective and reducing furnace atmosphere. Heat treatment process, mechanical tests, warm forging have also been mentioned in this chapter. ***Chapter Three*** shows the methodology that had been used as well as any programming

software. ***Chapter Four*** provides the results obtained in this work. ***Chapter Five*** covers discussion of the results, summarises and draws together the knowledge from chapter four. Finally, conclusions from the work and proposal for future studies are listed in ***Chapter Six***.

Chapter Two

Literature Review

2 Introduction

Powder Technology is a process whereby a mass of dry particles of a metal or ceramic powder, normally less than 150 microns in maximum diameter, is converted into an engineering component of predetermined shape without passing through the molten state and possessing properties which allow it to be used in most cases without further processing. Powder Metallurgy, commonly abbreviated to PM, may thus be defined as the production of useful artefacts from metal powders. Powder metallurgy has been used for over 60 years to produce a wide range of structural PM components, self-lubricating bearings, cutting tools, etc. One attraction of modern PM is the ability to fabricate parts with high quality, rather complex shapes with fine finishing [20-22]. PM studies therefore relate to the characterisation and processing of metal powders in their conversion into useful engineering components. The processing sequence involves the application of basic laws of heat, work, and deformation to powders. It is a processing technique which changes the shape, properties, and structure of powders into a final product [21]. The three main steps in powder metallurgy are shown in Figure 2.1 below.

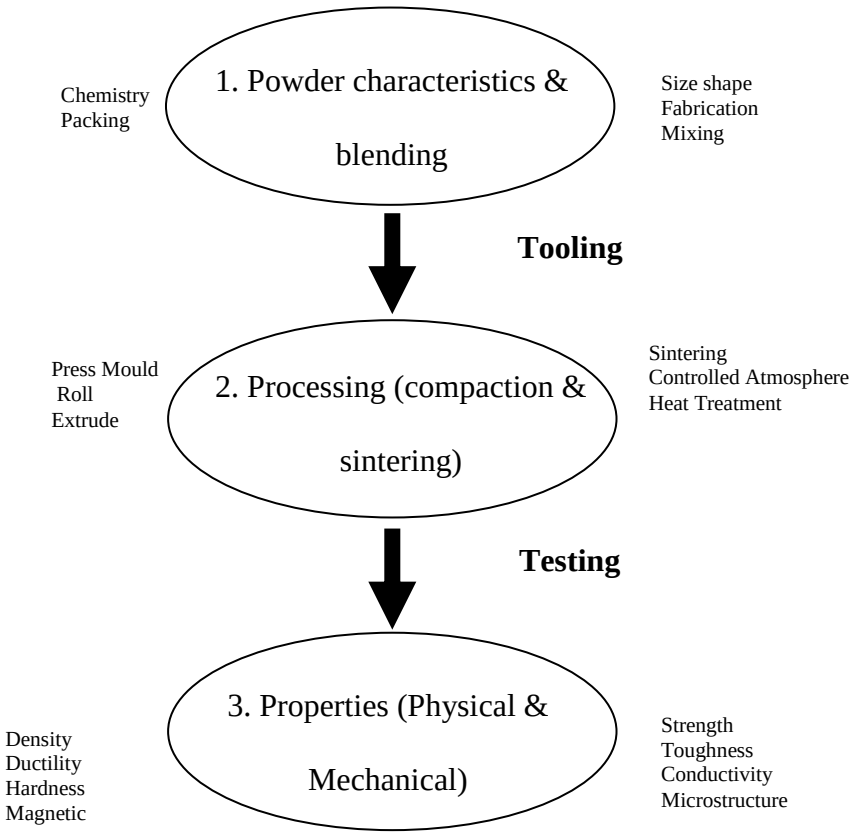

Figure 2.1 The PM PROCESS.

2.1 Powder Characteristics

Processing and the final properties achieved in the sintered part are influenced by the characteristics of the powder. It is therefore important to study and provide quantitative data for the following parameters:

- Particle size, and size distribution
- Particle shape and its variation with particle size
- Surface area
- Inter-particle friction

- Flow and packing
- Internal particle structure
- Composition, homogeneity, and contamination
- Apparent Density (AD) of the powder
- Green density, i.e. density of compact

2.1.1 Particle size

The size of the particle determined depends on the measurement technique, and particle size analysis can be achieved by any of several instruments which usually do not give equivalent determination due to difference in the measured parameters. All the particle size analyzers use one geometric parameter and make the assumption of a spherical particle shape. It is difficult to determine the exact particle size of the powder because only the spherical particles can be defined by their diameter. Irregular particles (see Figure 2.2) are difficult to analyze by conventional methods, thus, some measurable physical properties of the particle such as volume, length, specific density, projection or surface of the particle are used to determine the particle size and form [20, 23, 24]. There are three main groups of methods used to determine the particle size and form:

1. Separation methods (sieve analysis, screening).
2. Sedimentation methods (gravitational field, pipette method, sedimentation balance, photo-sedimentation, centrifugal fields using centrifuges).
3. Counting (direct) methods (microscopic, e.g. electron microscope).

These different measurement methods give different results [20]. Figure 2.2 illustrates various methods of measuring the size of powder particles with some irregular shapes.

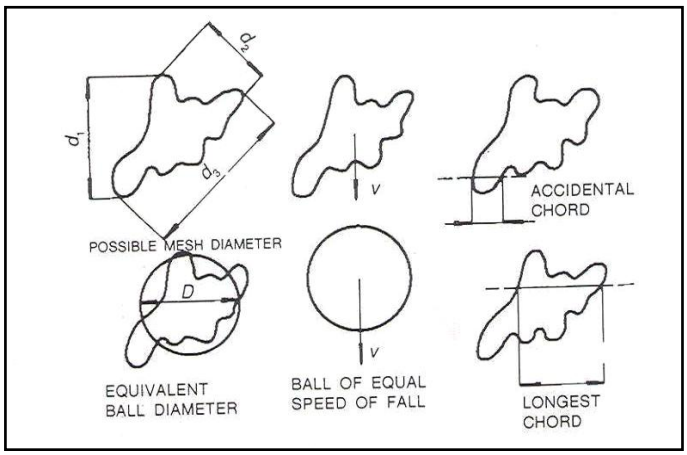

Figure 2.2 Various methods of measuring the size of powder particles [11].

2.1.2 Particle shape

Particle shape influences packing, flow, and compressibility. Powder shape information influences the choice of the powder fabrication route. Particle shape varies with size and manufacturing technique. A particle size analysis which assumes a constant shape could potentially have a large error on apparent and green densities. Typically, most significant powder shapes are flake, spherical, tear drop, cubic, and polygonal which are used in practice. These shapes are shown in Figure 2.3 [11, 20].

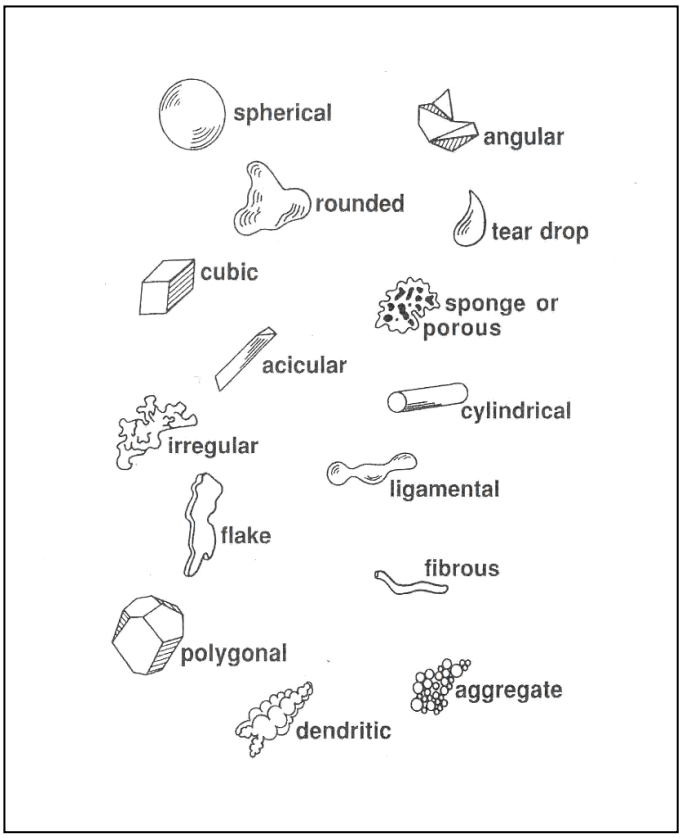

Figure 2.3 Typical metal powder particles [20].

2.1.3 Apparent density

Apparent density of powder is the density of the powder in loose state without any applied external pressure (or agitation). It can also be defined as a ratio of the loose powder mass to the cup volume. Apparent density can be measured using two techniques, Hall or Arnold meter. Hall flowmeter is used mostly, since it is used to measure both the flow time and apparent density. Hall flowmeter uses a funnel and measuring cup and the time taken for 50 g of powder to pass through the funnel is used as a time of flow and the density of the powder is measured as apparent density. The Arnold meter is used for measuring the apparent density only which can be done by

using a die with cavity around 20 cm^3, the loose powder is poured into the die and then the amount of powder mass is measured which can provide the apparent density by the following equation [2].

$$\rho = m/v$$

Where, ρ is the density, m is mass of the powder, and v is volume of the die. Particle shape and size are very important parameters which influence the apparent density. Small particles have a very high surface area, whereas irregular particles have many surface asperities leading to higher surface areas. These characteristics dictate the flow and packing properties of the powder [2, 11].

2.2 Powder Production Techniques

Almost all the metallic materials can be made into a powder form, but the method selected for fabricating a powder depends on the specific material properties. Four main categories of fabrication techniques are based on mechanical comminution, electrolytic deposition, chemical decomposition, and liquid metal atomization [2, 20]. These categories are listed in Table 2.1 with examples for each technique:

Table 2. 1 Fabrication Techniques of Powder.

Technique	**Example**
Mechanical Comminution	Impaction, attrition, shearing, and compression
Electrolytic Deposition	From chemical solution
Chemical Reaction	Solid, liquid, vapour phase reaction
Liquid Metal Atomisation	Water, gas, or centrifugal

2.2.1 Mechanical Comminution

The size reduction of metal powders by mechanical means is performed in the solid state as well as of metals. Grinding and milling are the oldest processes in PM for the production of particulate materials. The general phenomena during size reduction in the solid state are based on fracture mechanics, the nucleation of cracks, followed by crack propagation and fracture, by which new surfaces are formed. The forces acting in these processes cause mainly compression and shear stresses, applied as impact or slow-acting stresses by the milling balls during vessel rotation or vibration, by the rotating arms in an attritor [1, 3, 20, 25].

2.2.2 Electrolytic Deposition

By choosing suitable conditions, composition and strength of the electrolyte, temperature, current density, etc., many metals can be deposited in spongy or powder state. Extensive further processing- washing, drying, reducing, annealing and crushing may be required. Copper is the main metal to be produced in this way. Electrolytic iron was at one time produced on a substantial scale but it has been superseded largely by powders made by less costly processes. Very high purity and high density are two distinguishing features [1-5, 20, 25].

2.2.3 Chemical Decomposition (Reaction)

This has been for long the most widely used method for the production of iron powder. Selected ore is crushed, mixed with carbon, and passed through a continuous furnace where reaction takes place leaving a cake of sponge iron which is then further treated by crushing, separation of non-metallic material, and sieving to produce powder. Since no refining operation is involved, the purity of the powder is dependent on that of the raw materials. The irregular sponge-like particles are soft, and readily compressible, and give compacts of good green strength. Refractory metals are normally made by hydrogen reduction of oxides, and the same process can be used for copper [1, 3, 5].

2.2.4 Liquid Metal Atomisation

In this process molten metal is broken up into small droplets and rapidly frozen before the drops come into contact with each other or with a solid surface. The principal method is to disintegrate a thin stream of liquid metal by subjecting it to the impact of high-energy jets of air or liquid. Air, nitrogen, and argon are commonly used gases, and water is the liquid most widely used [2, 22]. By varying several parameters, design and configurations of the jets, pressure, and volume of the atomising fluid, thickness of the stream of metal, etc., it is possible to control the particles size distribution over a wide range. The particle shape is determined largely by the rate of solidification and varies from spherical, if a low heat capacity gas is employed, to highly irregular, if water is used. Atomisation is particularly useful for the production of alloys in powder form, since the constituent metals are fully alloyed in the molten state. Thus each powder particle has the same chemical composition [2, 11, 25].

2.3 Reasons for Using Powder Metallurgy

Three overlapping categories dominate and provide an introductory concept for the use of PM. Figure 2.4 is a Venn diagram indicating how the applications for PM can be categorized. The first is economic - on which many industries are relying on the economical production of complex parts (e.g. automotive industry). There are also other unique properties or microstructure justifying PM approaches, e.g. for production of porous metals, oxide dispersion strengthened alloys, cermets, and cemented carbides, which are otherwise difficult to process or manufacture by other techniques. Final circle shown on Venn diagram corresponds to captive applications. These are metals which are difficult to produce by other processes, e.g. reactive and refractory metals [2, 20].

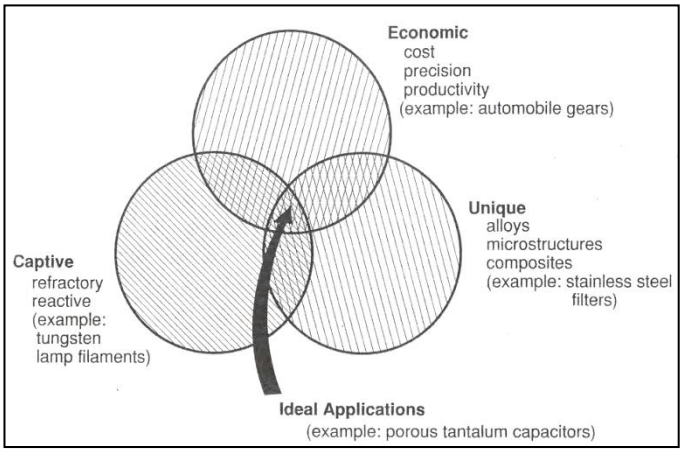

Figure 2.4 Venn diagram [20].

2.4 Conventional P/M Processing

The basic procedure in the manufacture of P/M parts is:

- Blend and mix the metal powder or powders with a suitable lubricant.

- Compaction, load the mixture into a die or mould and apply pressure. This gives what is called a compact, which requires sufficient cohesion to be handled safely and transferred to the next stage. A good green density will be required for some high density products.
- Heat the compact, usually in a protective atmosphere, at a temperature below the melting point of the main constituent, so that the powder particles weld together and confer sufficient strength to the object for the intended use. This heating process is called sintering during which alloying of some metal powders also will take place, usually in the case of steels.

2.4.1 Blending and mixing of the powders

To achieve acceptable compaction and sintering, the main powder must be mixed uniformly with the additive powders (including lubricant or binder). Blending and mixing are necessary to prepare an unique particle size distribution, combine powders together to generate new alloys during sintering, add lubrication for compaction, and to prepare a powder-binder mixture for shaping. Blending is defined as the intermixing of powders of the same nominal composition to remove segregation; this is induced by vibration in transport [1, 20, 21].

Mixing implies intermingling powders of different chemical composition. The mechanisms of powder mixing are diffusion, convection, and shear, as illustrated below in Figure2.5 via diffusional mixing in a rotating drum, convective mixing in a screw mixer, and shear mixing in a blade mixer. For most metal powders mixing and blending is performed using rotating containers such as double-cone, rotating

cylindrical and cubical, and twin shell, shown in Figure 2.6. The most efficient mixing is achieved via a 3-D Turbula mixer.

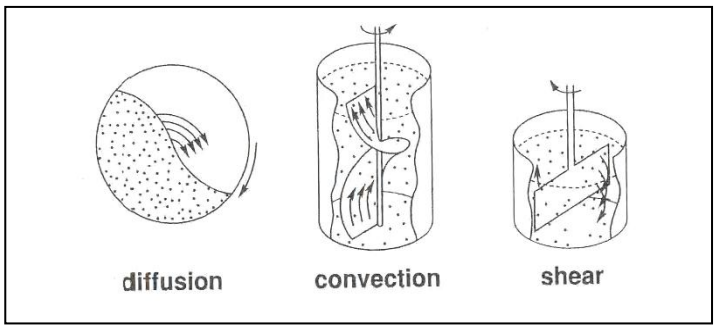

Figure 2.5 Three types of powder mixing are diffusion, convection, and shear [20].

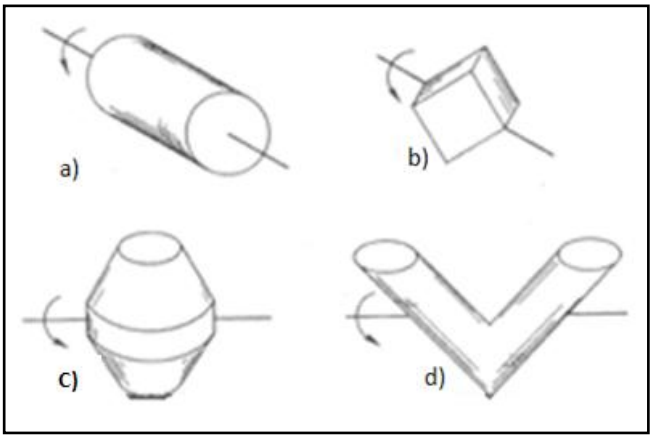

Figure 2.6 Some common equipment geometries for mixing and blending powders: a) rotating cylindrical: b) rotating cube; c) double cone; and d) twin shell mixers [20].

2.4.2 Additives to Powders (binders and lubricants)

Binders and lubricants are usually added to the main powder during blending or mixing processes in small amounts. Suitable range of these additive powders is between 0.5-1.5 percent by weight, to aid compaction uniformity and decrease die-wall friction during

compaction and ejection, thereby reducing die wear. Lubricants can also act as temporary binders to enhance the green strength of a metal part [1-5, 20, 21, 26].

The normal method of lubrication is to coat all particles' surfaces, e.g., by tumbling powder and lubricant in a mixer. Delubrication is commonly achieved in the first zone of a sintering furnace by heating the part to temperatures in the range 400 – 600ºC at a fixed heating rate and under controlled atmospheric conditions. This strategy minimizes defects, carbon contamination, and compact deformation [1, 21, 26]. Table1.2 illustrates some popular lubricants and their melting points.

Table 2.2 Some Popular Lubricants.

No.	Lubricant Name	Melting/Boiling Point (ºC)
1.	Stearic acid	~ 70
2.	Metallic stearates especially zinc stearate	~ 115-125
3.	Liquid Paraffin	~ 200 BP
4.	Paraffin Wax	~ 56 - 61
5.	Linear Polyethylene	~ 95-115
6.	Ethylene Bi-Stearamide	~ 135-145
7.	Acrawax	~ 99
9.	Polypropylene	~140-180
10.	Polyethylene	~140-180

2.4.3 Mixture Homogeneity

Mixing is necessary to homogenise different powder particles into a uniform powder with a certain particle size distribution, or to process different powder components into a powder mixture of statistical distribution. Poor mixing leads to segregation based upon the particle sizes diffusion [1, 21]. The intensity of segregation is measured by the compositional fluctuation from point to point. Figure 2.7 indicates three levels of

homogeneity ranging from stratified mixtures exhibiting large scale segregation, to agglomerated structure that exhibit partial homogenization, to the ideal case of a dispersed homogeneous structure [2]. Maximum homogeneity occurs when the rate of the segregation is equal to rate of the mixing. Homogeneity increases rapidly during mixing, but, when the binder has a low viscosity and the powder has a wide particle size distribution, the homogeneity decreases.

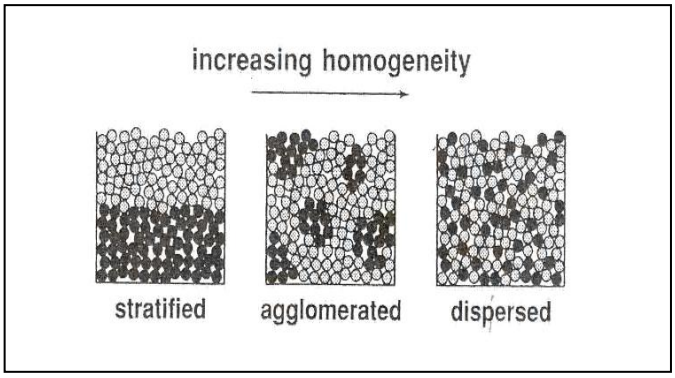

Figure 2.7 Schematic increases in homogeneity [20].

2.4.4 Compaction and shaping

Bulk powders are transformed into preforms of a desired shape and density by compaction or shaping. In most applications, high densities of the compacts are desired. Higher compact densities usually result in better green strength properties and smaller dimensional changes during sintering. A high green density is ~ 80-90 % TD theoretical density for all powder metallurgy products, except products with functional porosity, such as filters and bearings [1, 2, 11, 20, 21].

From the mechanical point of view, the compaction process can be roughly divided into three stages. The first stage is the packing process, referred to as stage 0 compaction.

The next stage is referred to as stage I compaction, and is characterized by the surrounding of the particles by connected pores with a relative density range from around 0.06 up to approximately 0.80-0.90. Stage II compaction is characterized by the sealing off of the pores between the particles, and the material behaving more or less like a porous solid [1, 2, 11, 20, 21, 24]. High green density and uniformity throughout the compact are generally the desired characteristics because they influence the densification of the samples during sintering.

Densification can be achieved through one of three methods: by sintering a low density preform; pressing to a high density followed by sintering, or by simultaneously pressing and sintering using the hot isostatic pressing (HIP) technique. Various powder compaction techniques are listed below:

1. Uniaxial die compaction of simple shapes using hard tooling at room temperature.
2. Uniaxial hot pressing of complex shapes in a rigid die.
3. Hot isostatic pressing (HIPing) in flexible moulds of soft metals.
4. Cold isostatic pressing (CIPing).
5. Powder injection moulding (PIM).
6. High energy rate and triaxial compaction.
7. Roll compaction into sheet or strip.
8. Extrusion of metal powders.

The conventional powder compaction presses used are either mechanical, hydraulic, or a combination of both techniques. The powder mixture is pressed to shape in rigid heat-treated steel or hard tool steel dies under pressure of 150-900 MPa [22]. At this stage, the desired shape of the compacted powder will be generated by virtue of interlocking of the powder grains within the shape. In consequence, the compacts develop significant strength to allow ejection from the die without cracking and readily accept handling before sintering. A schematic diagram of powder compaction is shown in Figure 2.8. It provides a fundamental understanding for defining the stages of the compaction process. The first stage shows the packing and rearrangement of the undeformed particles. As pressure increases, stage two, which consists of two phases elastic and plastic deformations to further increase the density, occurs. This is followed by last stage, which provides bulk compression of the compact. Increasing the pressure provides better packing and leads to decrease of porosity with the formation of new particle-particle contacts.

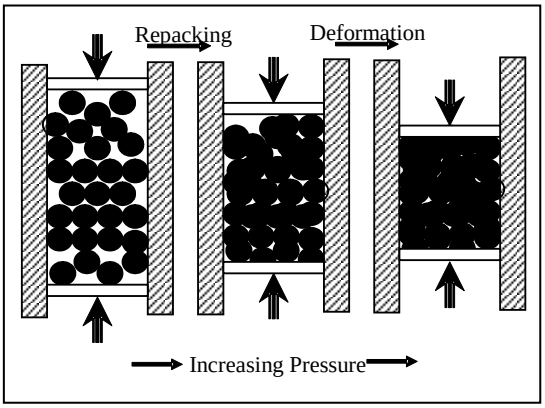

Figure 2.8 The conceptual steps in compaction.

The major functions of powder compaction are:

- To consolidate powder into the desired shape.
- To impart, as high a degree as possible, the desired final dimensions with due consideration to any dimensional changes resulting from sintering.
- To impart the desired level and type of porosity
- To impart adequate strength for subsequent handling

2.4.5 Green Compact Density

One of the most important properties of a PM process is the green density (GD), i.e. density of the as-compacted material. Green density is important since it influences the behaviour of the density of the alloy during sintering [4, 26]. Figure 2.9 below illustrates the green density increase with compaction pressure:

- Increasing compaction pressure, promotes particle movement, deformation, and fracture.
- Decreasing hardness and strength of the particles promotes deformation.
- Increasing particle size and particle softness lead to increases in apparent density; they promote particle movement and a more desirable distribution of stresses within the powder mass, leading to greater deformation.
- Decreasing speed of compaction promotes particle movement and reduces porosity.

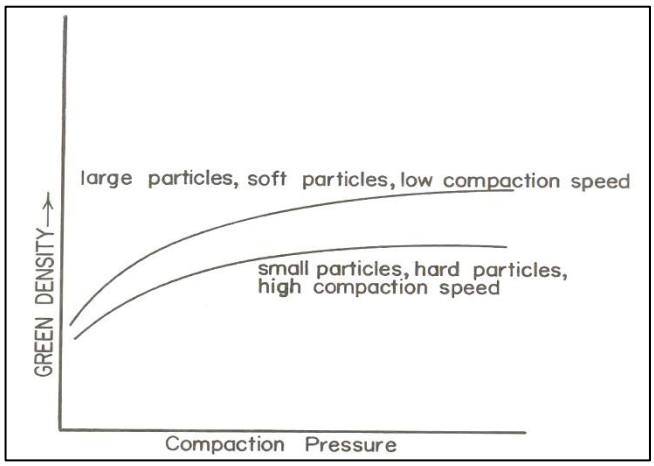

Figure 2.9 Schematic illustrating the dependence of green density on compaction pressure, particle size, particle hardness, and compaction speed [23].

2.4.6 Green Strength

The second major concern in powder compaction is green strength, related to green density, which results chiefly from the mechanical interlocking of irregularities on the surfaces of powder particles [1, 11, 21]. It is enhanced by plastic deformation during the compaction process. Green strength is promoted by:

- Increasing particle surface roughness
- Increasing the powder surface area, i.e. finer particles have higher surface area.
- Decreasing the apparent powder density
- Decreasing particle surface oxidation and contamination
- Increasing green density (or compaction pressure)

2.4.7 Sintering

Sintering is thermal treatment of a powder or compact at a temperature below the melting point of the main constituent, for the purpose of alloying and increasing the strength by bonding together of the particles and reducing porosity of the green state. The operation is almost invariably carried out under a protective atmosphere, because of the large surface areas involved, and at temperatures between 60 and 90% of the melting point of the particular metal or alloys.

For powder mixtures, however, the sintering temperature may be above the melting point of the lower-melting constituent, e.g. copper/tin alloys, iron/copper structural parts; tungsten carbide/cobalt cemented carbides, so that sintering in all these cases takes place in the presence of a liquid phase, hence the term liquid phase sintering [2, 11, 25].

2.4.7.1 Effects of material and process variable on sintering

Some of the material and process variables have a major influence on sintering, as discussed below:

1- **Particle Size:** Decreasing particle size leads to increased sintering.

2- **Particle Shape and Topography:** These can lead to a greater intimate physical contact between particles in the sintered mass and increased internal surface area, which promotes sintering.

3- **Particle Structure:** A fine grain structure within the original particles can promote sintering because of its favourable effect on several material transport mechanisms.

4- **Particle Composition:** Sintering may be affected by alloying additions or impurities in the metal, and diffusion mass transport may also be affected by the presence of alloying or impurity atoms in the lattice.

5- **Green Density:** Green density is a material variable which affects sintering directly.

6- **Temperature:** Increasing the sintering temperature greatly increases the rate and magnitude of any changes occurring, but over-sintering causes defects and reduces sintered mechanical properties.

7- **Time:** Degree of sintering increases with increasing time.

2.4.7.2 Solid-State Sintering

Surface energy is generally a small driving force for sintering. Sintering without formation of a liquid phase is known as solid-state sintering, during which two types of transport mechanisms can be considered, i.e. surface and bulk transports. Surface transport causes neck growth between powder particles without changing the particle spacing and some densification takes place. Surface diffusion and formation of the vapour phase (i.e. evaporation-condensation) are the most important surface transport mechanisms contributing to solid state sintering [20, 25]. These diffusional processes are driven by a variation in chemical potential between the sources, e.g. surfaces and the

sink, neck or contact point of particles, and result in shrinkage by shape change and centre-centre approach of the neighbouring particles.

A well-known example is the accelerated sintering of tungsten and other refractory metals (Mo, Nb and Ta) resulting from the addition of < 0.5 wt. % transition metals, e.g. Ni, Pd, Co, Fe and Pt, which can initiate ~ 60% of the corresponding bulk densification [5, 27-32]. Table 2.3 shows the type of diffusion with their source and location, whereas Figure 2.12 illustrates the bulk transport mechanism - showing the movement of atoms by diffusion process.

Table 2.3 Types of diffusion, their sources and location.

Mechanism Number	Transport Path	Source of Matter	Sink of Matter
1	Surface diffusion	Surface	Neck
2	Lattice Diffusion	Surface	Neck
3	Vapour Transport	Surface	Neck
4	Boundary Diffusion	Grain Boundary	Neck
5	Lattice Diffusion	Grain Boundary	Neck
6	Lattice Diffusion	Dislocation	Neck

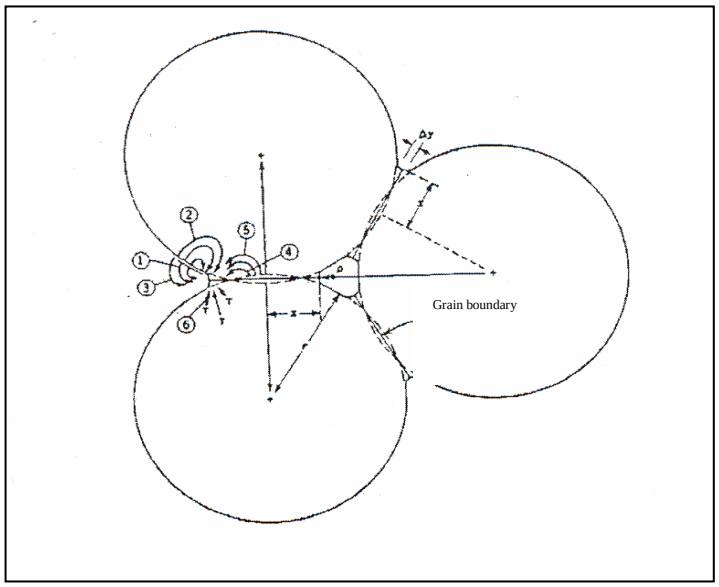

Figure 2.10 Mass transport mechanisms during solid state sintering [33].

2.4.7.3 Pore structure in sintering

The point contact between particles grows into a neck. After the initial stage, grain boundary and pore configuration control the sintering rate. At the intermediate stage the pore geometry is highly convoluted and pores are located at the grain boundary intersections. With continued sintering, the pore geometry approaches a cylindrical shape where densification occurs by decreasing the pore radius as shown in Figure 2.11.

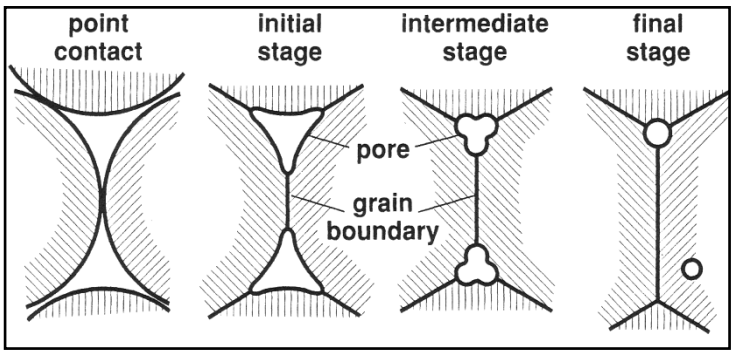

Figure 2.11 Schematic diagram of pore structure changing during sintering [20].

From Figure 2.11, it can be noted that the changes in grain size, number and size of pores, as well as a decline in the total porosity in the latter stage of sintering, interaction between pores and grain boundaries can take three forms:

- Pores can retard grain growth.
- Pores can be dragged by the moving grain boundary during grain growth.
- Grain boundary can break away from the pores, leaving them isolated in the grain interior.

As the temperature increases, the rate of grain boundary motion increases, but at high temperatures the rate of grain growth increases to a point where the boundaries breakaway from the pores. There are two possible pore-boundary configurations and pores can occupy sites on the grain edges, at grain boundaries or inside the grains, i.e. bulk porosity [2, 20]. For the former there is some densification and the latter no densification, as shown in Figure 2.12.

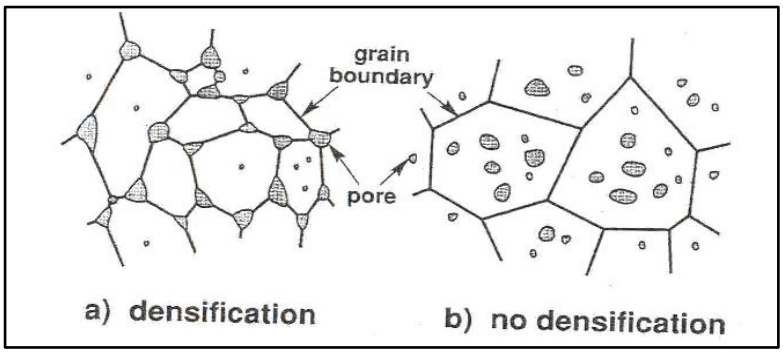

Figure 2.12 Possible pore-grain boundary configuration during sintering [6].

The system energy is lower for pores occupying the grain edges, because the pore reduces the total grain boundary area and energy. If the pore and boundary become separated, the system energy is increases in proportion to the amount of newly created interfacial area [20, 21]. As the densification profits the slower mobility of the pores, coupled with the poorly pinning force, breakaway of the pores from the boundaries is possible, which limits the final densities attainable by sintering.

Consequently, it is important to minimize breakaway pores by careful temperature control. Avoiding the breakaway event is particularly important for PM systems requiring a high sintered density. There are then fewer pores which are small, due to shrinkage and the grains are relatively large. In this situation separation can be avoided if the pores are sufficiently mobile to migrate with the boundaries [20].

2.4.7.4 Activated Sintering

Activated sintering allows for high sintered densities, faster sintering rate, lower sintering temperature, and improved physical and mechanical properties [20, 25, 34]. Among the numerous methods of activated sintering techniques, addition of small amounts of an alloying element to the base powder is of the great practical importance. One of the most common examples via additive sintering is that of the tungsten treated with some transition metals such as nickel, palladium, or platinum and iron. The shrinkage is much higher for activated alloy than that of the base powder without any activator. In activated sintering the amount of activator is important, and usually in the range 0.1 to 10 wt %, but for the optimal quantity is often less than 0.3 wt % [20, 25]. Mixed phase sintering can also be categorized as activated sintering.

Some of the additives are present as solid phases only in solid solution with the base metals or segregate at the interfaces of the base metals. Other additives are present as liquids which spread or penetrate as liquid films between the interparticles and grains of the base metals. The activator should stay segregated to the interparticle interface during sintering. Many investigators have reported [31, 32, 34] that it is possible to obtain PM products with improved mechanical and physical properties by numerous methods of activated sintering. For example, addition of transition metals Pt, Pd, Co, or Ni to refractory metals such as W increases sinterability such that an increase in shrinkage of greater than 10% is obtained. Furthermore, these additives enhance densification by increasing diffusion of the base metal [27]. The best examples of activated sintering occur with the refectory materials, tungsten, molybdenum, chromium, and tantalum. For example, when chromium powder (1μm average size) was sintered at 1400ºC, a sintered density of 78% of the theoretical density was obtained, whereas a sintered density of 96% was achieved for the same powder using the same sintering cycle with an addition of 1.0 wt% Pd, but with 1.0 wt% Fe the sintered density was only about 68% using the same sintering cycle. Figure 2.13 shows that the shrinkage is much higher for tungsten with activator than tungsten without activator [6].

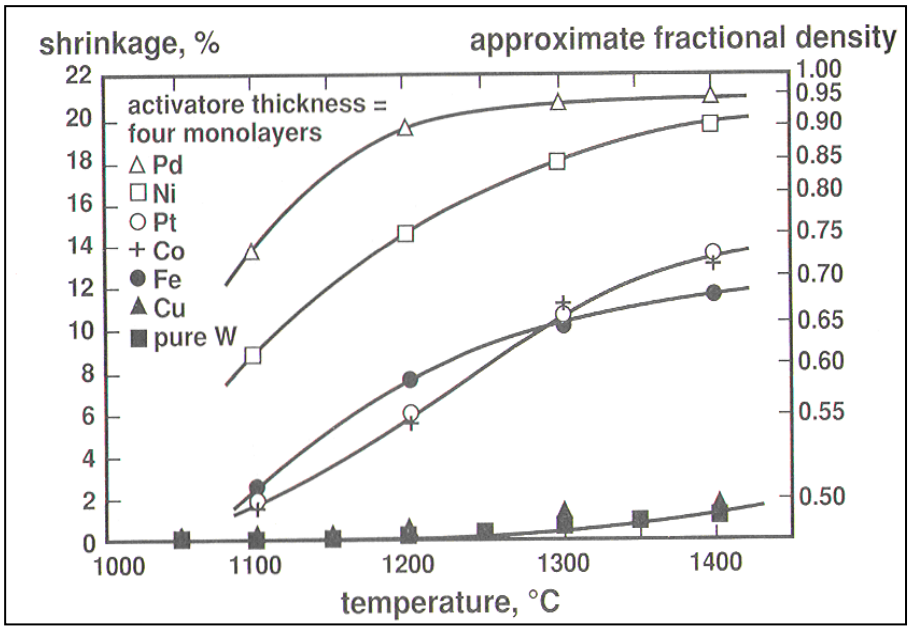

Figure 2.13 Activated sintering behaviour of tungsten treated with transition metal additives [6].

The strength, hardness, mechanical and physical properties increase as the sintered density increase. Figure 2.14 is a plot of the sintering temperature versus strength for the activated sintering of tungsten with some additive elements Ni, Pd, Co, and Fe which shows the effect of these elements on strength. This Figure clearly shows that Ni and Pd have improved the strength at lower temperature, where Co and Fe are more effective at higher temperatures The amount of activator is an important parameter in activated sintering, it is usually quite small, and in some cases it is only a fraction of 1 wt% [6].

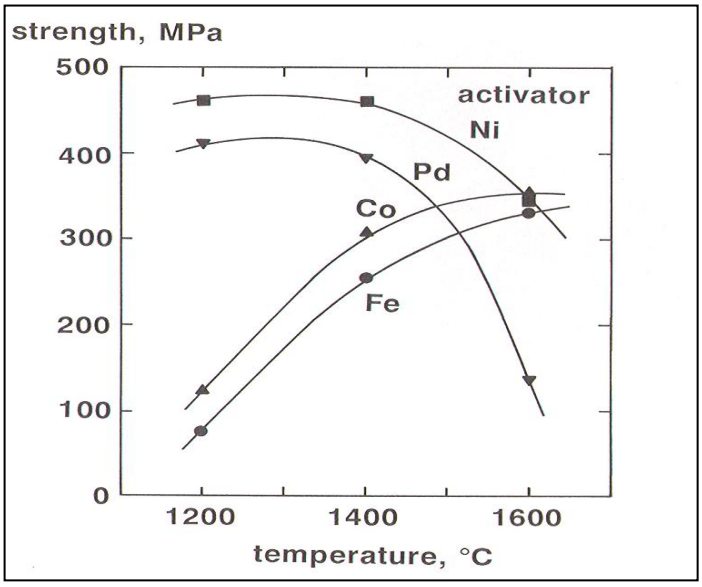

Figure 2.14 Strength versus sintering temperature for tungsten treated with various sintering enhancers such as Ni, Pd, and various more effective elements such as Co and Fe [6].

An additive must meet several criteria to be considered as a successful activator. These criteria are [5, 6, 21, 35]:

- Lower melting point than the base powder.
- Large solubility for the base metal, while the base metal should have low solubility for the activator.
- Activator should stay segregated to the inter-particle interfaces during sintering.

2.4.7.5 Liquid Phase Sintering (LPS)

Liquid phase sintering is used for PM processing of both metallic and ceramic products. It refers to the case in which, during some stage of sintering operation, a liquid phase is present. Of the two techniques to generate a liquid phase, the most common [5, 6, 35-

40], involves mixed powders of different chemistries, as shown in Figure 2.15. Interaction between the two powders during the sintering cycle leads to the formation of a liquid, which may be transient or persistent. Liquid phase can also be formed by heating prealloyed powder between the solidus and liquidus temperatures. This method known as supersolidus liquid phase sintering is illustrated in Figure 2.16. Liquid phase sintering usually enhances the sintering rate, and near full density may be obtained with short sintering times, as long as good wetting by the liquid phase takes place. Tin with copper, copper with iron, and cobalt in cemented carbides, are typical examples of LPS [21, 23, 24, 41].

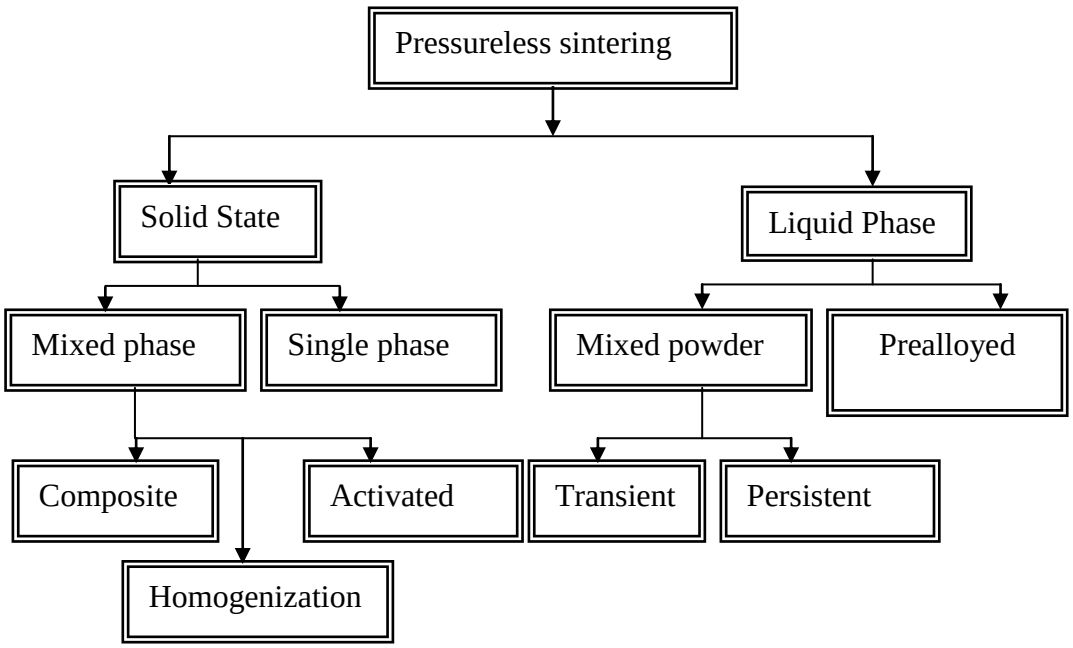

Figure 2.15 Type of Pressureless Sintering [5].

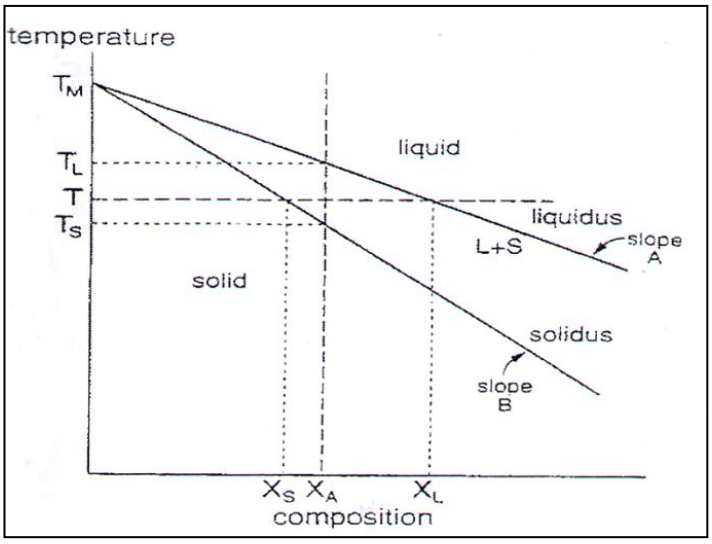

Figure 2.16 Schematic phase diagram of prealloyed powder showing liquid phase forming between the solidus and liquidus temperature [5].

Wetting and Spreading

Wetting is one of the most important characteristics of a liquid phase during sintering. After formation of the liquid during sintering, three phases will be present in the microstructure: solid, liquid, and vapour. Good wetting is obtained when solid-liquid surface energy is low, compared to the liquid-vapour, and solid-vapour surface energies [5, 6]. Wetting is considered to occur effectively by a chemical reaction of the mixed powders at the solid-liquid interface. Wetting generally depends on the solubility of the solid particles in the liquid phase. It can be measured by the contact angle (θ), defined by equation (1) [6, 20].

$$\gamma_{SV} = \gamma_{SL} + \gamma_{LV} COS\theta \qquad 2.1$$

where γ_{sv}, γ_{sl} and γ_{lv} are the interfacial energies between solid and vapour, solid and liquid, and liquid and vapour, respectively. Table 2.4 shows the estimated wettability

regarding the relationship between contact angle and the interfacial energies of a liquid to wet a solid phase. For a better understanding see Figure 2.17.

Table 2.4 Wettability Performance In relation to Contact Angle (θ).

No.	Contact Angle	Wetting Level
1	θ =Zero	Perfect
2	0 < θ < 180	Partial wetting
3	θ =180	No Wetting

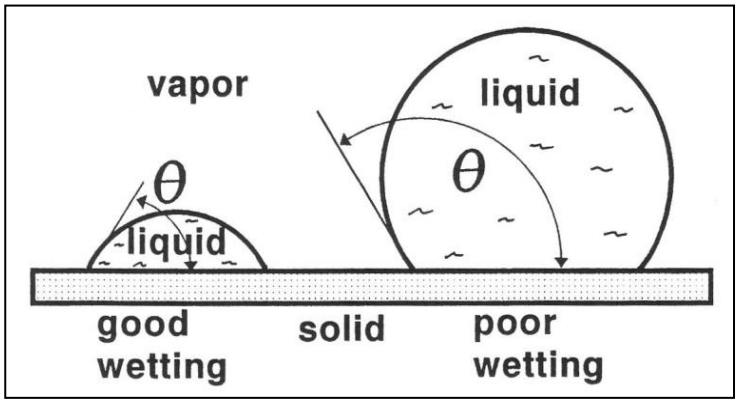

Figure 2.17 Solid-liquid-vapour equilibrium conditions for good and poor wetting situations [5, 6] .

If the liquid phase is insufficient, then it exhibits very poor wetting (flow of the liquid is minimal), which leads to swelling of the compact during heating and possibility of its absorption by the surface pores [5, 6]. Spreading is known as the mobility factor of the liquid, and the kinetic process associated with wetting. The solubility process of the solid into the liquid phase aids spreading, which depends on the free energies, giving an

increase in the solid-liquid and liquid-vapour surface areas, and decrease in vapour-solid surface areas, as estimated from the following equation [2, 5, 6]:

$$\gamma_{sv} \rangle \gamma_{sl} + \gamma_{lv} \qquad 2.2$$

The study of spreading of the solid particles into the liquid is particularly difficult. There are several parameters which effect the behaviour of the liquid, such as, crystallographic orientation, segregation, contamination and mechanical agitation [2, 5].

Dihedral Angle (Φ)

Another important parameter which influences the microstructure during liquid phase is dihedral angle created due to variation in surface energies between the solid-solid grain boundaries which intersect the liquid and can determine the microstructure of the liquid phase [2, 5, 42]. Figure 2.18a indicates the general equilibrium at three phase junctions with associated dihedral angle and interfacial energies. Figure 2.18b shows the three energies and three angles form a triangle.

$$\gamma_{12} / \sin\phi_3 = \gamma_{23} / \sin\phi_1 = \gamma_{13} / \sin\phi_2 \qquad 2.3$$

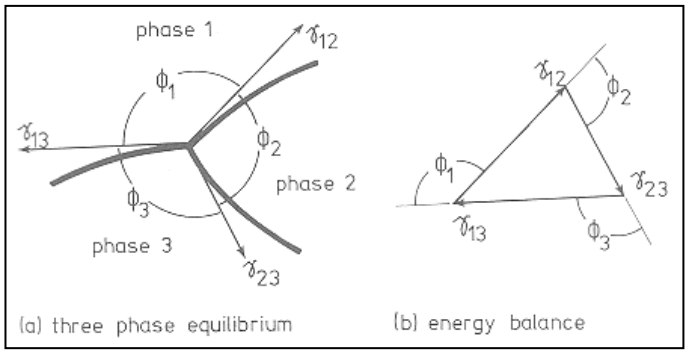

Figure 2.18 The general equilibrium at a three-phase intersection: (a) the interfacial energies and the angle superimposed; (b) equilibrium energy and angles [5].

In the final stage of sintering the vapour will be absent, thus only the solid-solid and liquid-solid phase are present and equilibrium surface energies determine the magnitude of the dihedral angle as shown in Figure 2.19. It can be determined by the following equation:

$$\gamma_{ss} = \gamma_{sl}\, 2\cos\phi \qquad 2.4$$

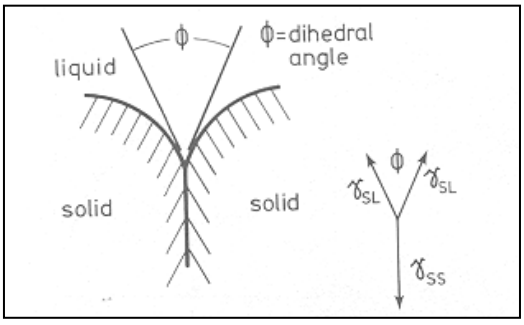

Figure 2.19 Dihedral angle and surface energy between two intersecting grains with a partially penetrating liquid [5].

It can be noted that when the dihedral angle is low, the system has a low solid-liquid interfacial energy, which favours diffusion of solid-solid.

Classic sequence of liquid phase sintering (LPS)

The basic aspects of LPS are usually discussed in terms of three distinct stages that are particularly based on experimental observation [5, 6, 37-39, 41]. These, in the order of their occurrence, are: rearrangement, solution-reprecipitation, solid state bonding. Figure 2.20 shows the schematic sequence of these steps, whereas Figure 2.21 illustrates those three stages in a relationship between the time sintering and densification.

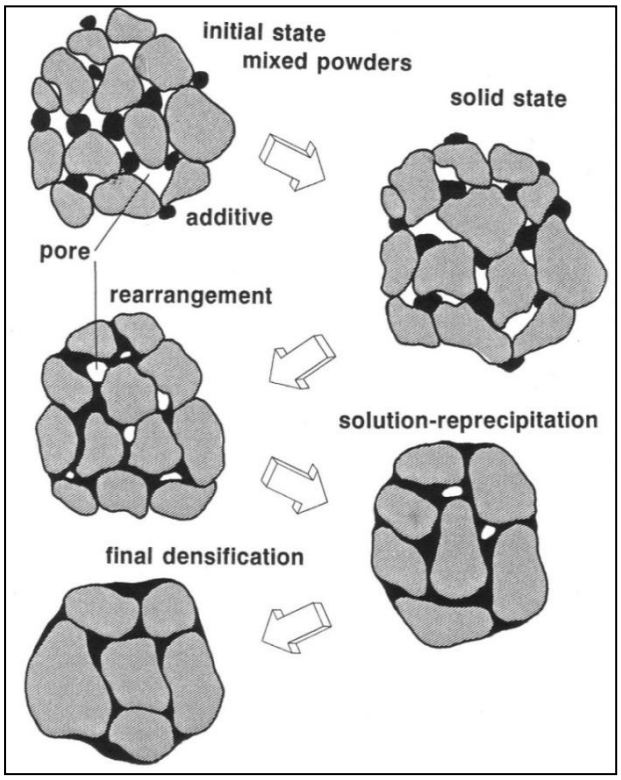

Figure 2.20 Stages of Liquid Phase Sintering [6].

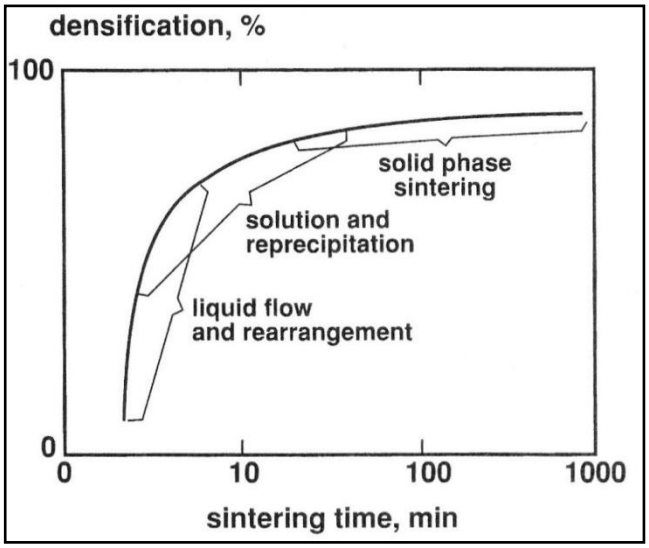

Figure 2.21 Approximate time scale for liquid-phase sintering [6].

Step I- Rearrangement

The **first** stage is **'rearrangement',** during which 'liquid flow' occurs and causes large scale bulk movement of particles within the liquid phase, resulting in particle rearrangement and some densification. Increasing the amount of the liquid phase results in greater densification, that is, particles may move more easily. During rearrangement, the compact responds to the capillary action of the liquid. The amount of densification attained by rearrangement is dependent on the amount of liquid, particle size, and solubility of the solid in the liquid. Greater rearrangement is usually obtained from finer particles and full density (zero porosity) is possible by rearrangement if enough liquid is formed (i.e. in most LPS systems, about 20 volume % liquid) [5, 6, 23, 24, 34, 37-39, 41].

Solution-Reprecipitation

The second stage of liquid phase sintering is termed **'solution and reprecipitation',** and can only take place if there is a limited solubility of the liquid phase. The solubility of a grain in its surrounding liquid varies inversely with grain size. Small grains have a higher solubility than coarse grains. Material is transported from small grains to the large by diffusion. The small grains dissolve and disappear, while the large ones grow and take on a very rounded shape. The process is termed coarsening or Ostwald ripening [24]. Grain shape accommodation leads to porosity elimination. The amount of liquid effects solution-reprecipitation in terms of both diffusion distance and amount of grain shape accommodation [41].

Solid Phase Bonding

The third stage of liquid phase sintering is known as **'solid phase bonding'**. The solid skeleton which was formed during compaction causes slow densification. If the liquid is not wetting the solid completely, then there is still some contact between solid particles rather than complete separation of the particles by the liquid. Solid skeleton rigidity inhibits further rearrangement, and the microstructural coarsening continues by diffusion [5, 23-25]. There are some advantages and disadvantages of liquid phase sintering.

Advantages are:

- Faster sintering.
- Faster atomic diffusion.

- Due to wetting by liquid, rapid compact densification occurs.
- Reduction in interparticle friction.
- Rapid rearrangement of solid particles.

Disadvantages are:

- Compact slumping (shape distortion) which occurs when too much liquid is formed during sintering, which leads to lower tolerances.

2.4.8 Protective Sintering Atmospheres in Powder Metallurgy

The following gases, at present, are used as the sintering atmosphere: nitrogen, hydrogen, hydrogen-nitrogen mixture, hydrocarbon gases, helium, argon, or only vacuum. Sintering atmosphere performs numerous roles: the most important task is to protect the compact from the air attack at higher temperatures, and, especially for sintering ferrous materials, to reduce the surface oxides [43]. Therefore uncontrolled atmosphere furnaces are not acceptable. The atmosphere assists in removal of lubricants or binders as lubricants and binders used in the pressing process may create oxidation and some other contamination that hinders diffusion bonding. Further, a suitable atmosphere can reduce decarburization and adjust the impurity level, such as the nitrogen content. The pure gases of CO and H_2 are appropriate for this purpose, but are often costly and dangerous to use. In practice dry hydrogen, cracked ammonia, and partially combusted hydrocarbons are mainly used, as well as argon and pure nitrogen [2]. Vacuum sintering involves heating in a closed chamber with a pumping mechanism

constantly pulling evolved vapours out of the furnace, keeping the chamber pressure between 10^{-4} and 10^{-7} atm (10 and 0.01Pa) [6]. Vacuum sintering is preferred in cases involving highly reactive materials (beryllium, titanium, and tantalum), high temperature materials (refractories (tungsten, molybdenum), and tool steels), hydriding elements (zirconium or uranium), and corrosion-resistant materials (stainless steels) [6].

Thus sintering atmospheres fulfil several functions, depending on the material to be sintered [2, 4, 6, 23, 25]. These functions are:

- To avoid, undesired evaporation of any component.
- To control chemical reaction-oxidation, reduction, carburisation, decarburisation and decomposition.
- To remove volatile admixtures and their decomposition productions such as lubricants.
- To provide heat transfer by convection in furnace.
- To provide the external hydrostatic pressure required in hot isostatic pressing.

The sintering atmosphere must be compatible with the interior material of the furnace and with the heating elements, in so far as they are in contact with the gas.

2.4.8.1 Reduction Reactions

It is well known [43] that surface oxides of the powder particles obstruct diffusion during sintering and inhibit both neck growth between particles and liquid phase penetration. Therefore, thermochemical reactions are essential in choosing the proper

atmosphere for sintering ferrous PM alloys. Equilibrium between oxygen and an oxide such as FeO_2 can be written in reaction form as follow [44]:

$$Fe\ (s) + O_2\ (g) \Leftrightarrow FeO_2\ (s) \qquad 2.5$$

Solids and gases are indicated by (s) and (g), respectively. In some metals oxide reduction proves more difficult, e.g. chromium oxide. Then the reaction is represented as follows:

$$_x M(s) + O_2(g) \Leftrightarrow M_x O_2(s) \qquad 2.6$$

where M and M_xO_2 represent metals and oxides, respectively.

For this reaction, the equilibrium constant K is defined as follows [27]:

$$K = \frac{aM_xO_2}{a\,M^x P_{O_2}} \qquad 2.7$$

where a designates a thermodynamic quantity known as the activity of the solid phase. Activity is defined as the ratio of the vapour pressure of a material under the considered conditions, and the P_{O2} oxygen partial pressure is the only factor that determines which way the reaction proceeds. Thus, the equilibrium constant for oxidation-reduction reaction depends only on the inverse partial pressure of oxygen, and lower partial pressures favour oxide reduction. Metal oxide and the metal are pure materials and thus eq. 2.7 reduces to:

$$K=1/p_{O2} \qquad 2.8$$

In turn, the equilibrium situation reflects the standard free energy ΔG for the reaction,

$$\Delta G = -RT\ lnK = RTlnp_{O2} \qquad 2.9$$

where R=8.314 J/(mol K) is the universal gas constant and T is the absolute temperature in degrees Kelvin:

$$p(O_2) = exp\left[-\frac{\Delta G^\circ}{RT}\right] \quad 2.10$$

ΔG° is the Gibbs free enthalpy, for a chemical reaction determined from:

$$\Delta G^\circ = \Sigma G^\circ \text{ (products)} - \Sigma G^\circ \text{ (reactions)} \quad 2.11$$

The free energy can be obtained from tables, charts or by using computer software, e.g. HSC Chemistry software [45].

2.4.8.2 Reducing Atmospheres

The sintering atmosphere is very important variable which when optimized can lead to improvement in the sintered steel properties of iron-carbon PM components. Atmospheres of mixed gases N_2 and H_2 in different percentages between 25/75 and 95/5, and eventual additions of CH_4, have commonly been used [36, 46-53] to ensure sufficient oxide reduction (i.e. complete reduction of oxides to achieve strong interparticle bonding), provide further protection against additional oxidation and also to adjust the carbon potential of the sintering atmosphere [51].

The decomposition of relatively unstable oxides is directly connected with decrease in partial pressure of oxygen in the sintering atmosphere (see Figure 2.22). It is well known that vacuum furnace atmosphere minimizes oxidation; however vacuum in a sintering furnace in general is not sufficient to lower the pO_2, to reduce oxides as used in industry and is also quite expensive. The effect of carbon on the degassing and oxides reduction of several compositions of Fe-based alloys mixed with graphite has been

studied during sintering under different sintering atmospheres including vacuum [47, 54]. Hydrogen and carbon monoxide gases are very common, economical and feasible gases used as reducing agents, as illustrated below:

$$\frac{2}{y}M_xO_y + 2H_2 = \frac{2x}{y}M + 2H_2O \quad 2.12$$

$$\frac{2}{y}M_xO_y + 2CO = \frac{2x}{y}M + 2CO_2 \quad 2.13$$

Where M and M_xO_y represent metal and metal oxide, respectively.

From the thermodynamic fundamentals, the equilibrium condition between the metals and their oxides in contact with oxygen at certain temperature indicates that the reduction of metallic oxide will take place when $pO_2^{atm} < pO_2^{oxide}$ 2.14

The Gibbs free energy for reaction 2.12 can be obtained by using equation 2.11 as follows:

$$\Delta G_2^\circ = \frac{2x}{y}G^\circ(M) + 2G^\circ(H_2O) - \frac{2}{y}G^\circ\left(M_xO_y\right) - 2G^\circ(H_2) \quad 2.15$$

Then, equilibrium constant K can be obtained from the following relationship:

$$K = \frac{P^2(H_2O)}{P^2(H_2)} = exp\left[-\frac{\Delta G_2^\circ}{RT}\right] \quad 2.16$$

This can be written as,

$$\frac{p(H_2)}{p(H_2O)} = exp\frac{\Delta G_2^\circ}{2RT} \quad 2.17$$

Similar for CO as the reducing gas as in reaction 2.13:

$$\frac{p(CO)}{p(CO_2)} = exp\frac{\Delta G_3^\circ}{2RT} \quad 2.18$$

The equilibrium between metal, metal oxide and partial pressure ratio is presented in the following Figures 2.22-2.25.

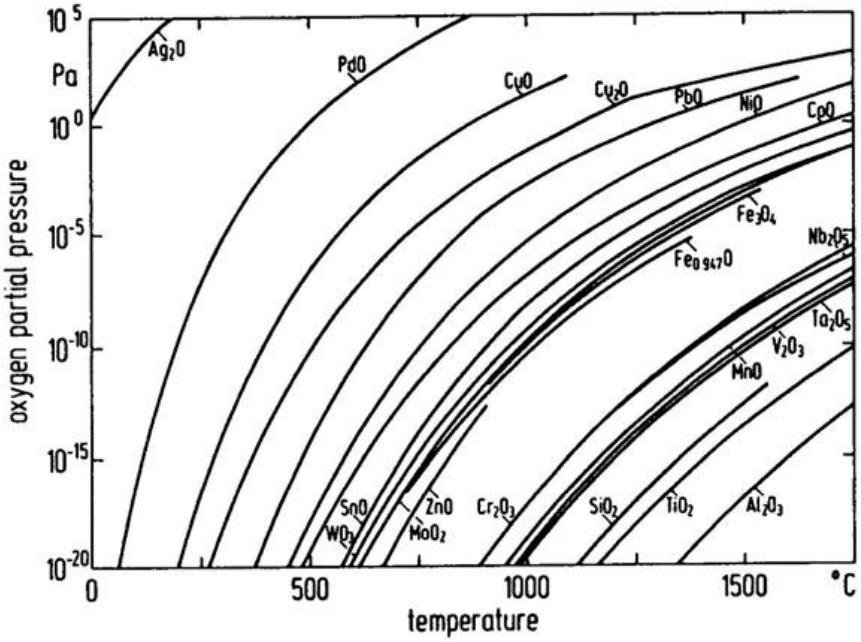

Figure 2.22 Equilibrium oxygen partial pressures of a few metal oxide [55]

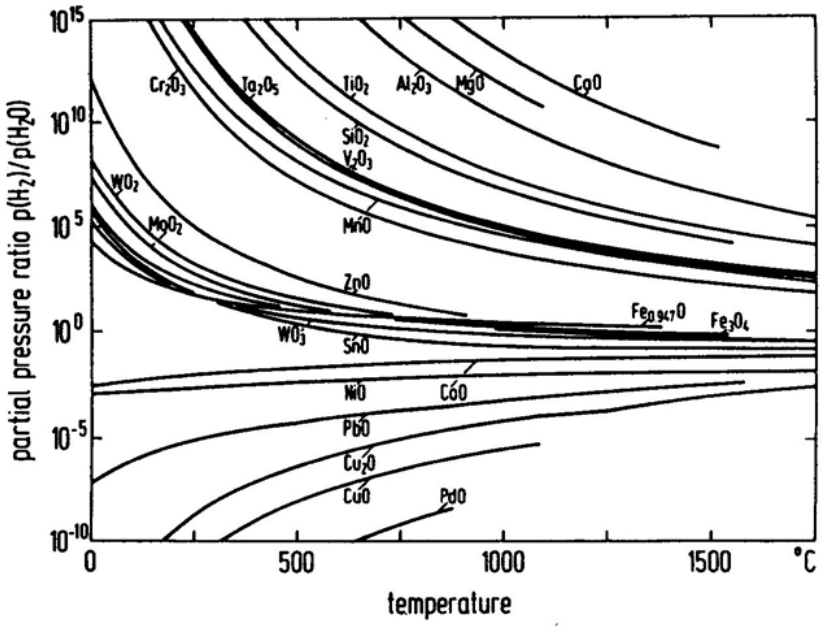

Figure 2.23 Partial pressure of hydrogen and water vapour in equilibrium with metal oxides [55].

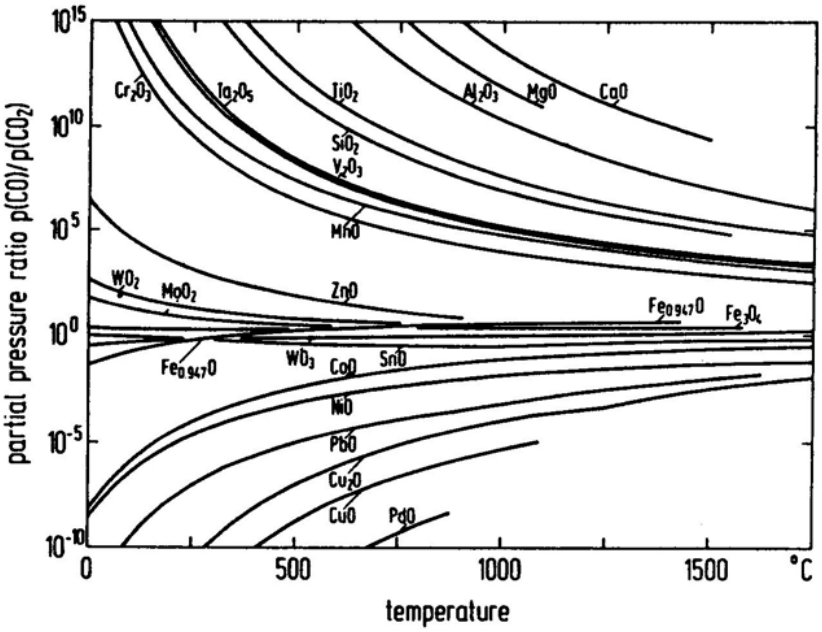

Figure 2.24 Partial pressure of carbon monoxide and carbon dioxide (pCO/ pCO_2) in equilibrium with metal oxides [55].

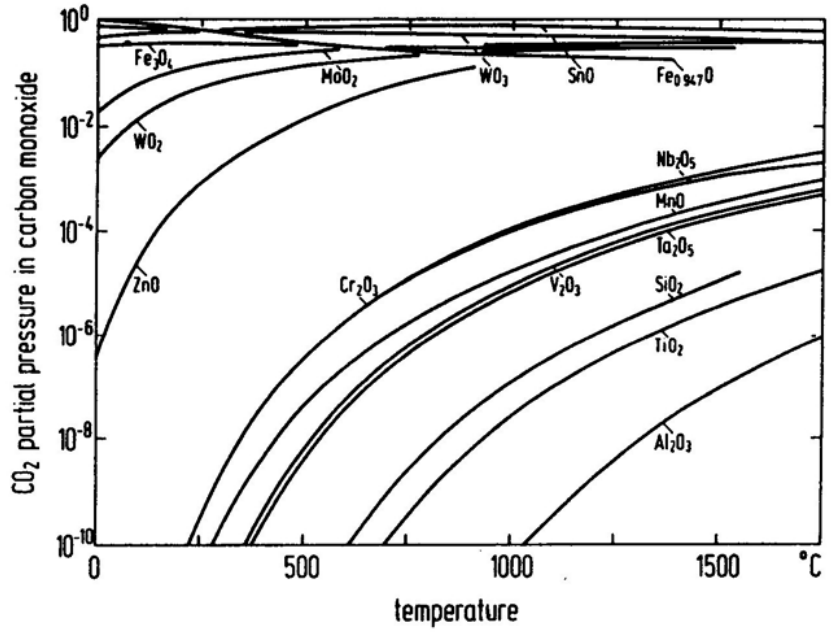

Figure 2.25 Partial pressure in pure carbon monoxide in equilibrium with metal oxides [55].

It's worth remembering that the dewpoint is one of the important parameters that controls the reducing atmosphere. Dewpoint specifies the temperature at which water vapour in the atmosphere becomes saturated, and thus will be generated. Therefore it provides a comparative assessment of the moisture content in an atmosphere[6, 55]. It is used to measure water to hydrogen partial pressures (pH_2/pH_2O ratio). Figure 2.26 presents the oxidation-reduction equilibrium in terms of the atmosphere dewpoint for several metals and oxides [55]. Lower dew points enhance oxide reduction. During the sintering cycle of a metallic powder, the compact will initially be under oxidising conditions caused by trapped oxygen in the pores. At higher temperatures, the atmosphere and temperature can create reducing conditions. On cooling, the compact may again experience oxidising conditions caused by the decrease in temperature [27].

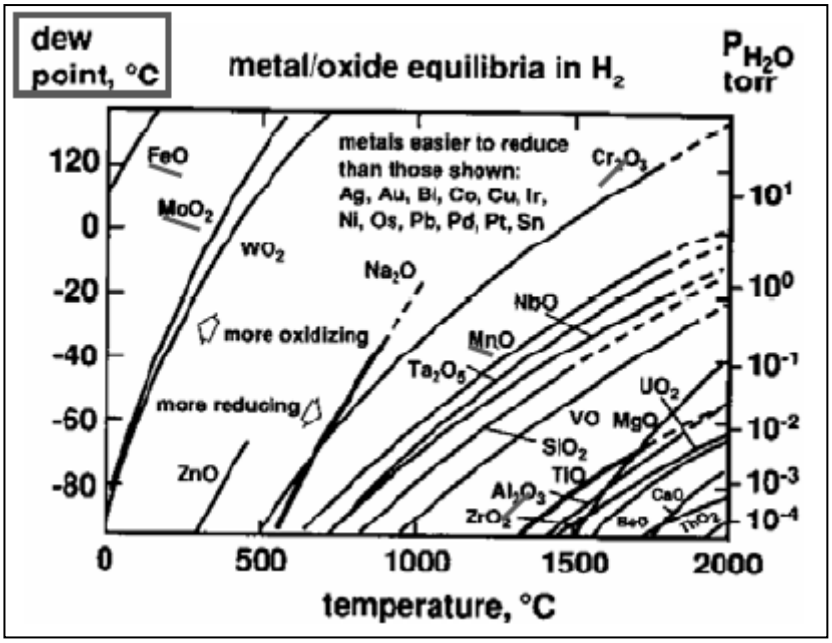

Figure 2.26 Oxidation-Reduction equilibrium in terms of the atmosphere dewpoint for several metals and oxides [55].

2.4.8.3 Carburization-Decarburization

Carbon plays a major role in ferrous powder metallurgy and extremely enhances the mechanical properties of sintered steels. Properties such as tensile strength and hardenability are very perceptive to changes in carbon content. Therefore the choice and control of the sintering atmosphere is essential to obtaining strong mechanical properties [56]. Austenite steels must be in equilibrium with the composition, any imbalances in the process can lead to carburising and decarburising reactions.

A carburising and decarburising reaction is an increase and decrease respectively, in the carbon content (from the surface layer of hot-worked steel products) of steel caused by the interaction with the atmosphere [1, 57]. Steels with low carbon contents at the surface when exposed to the atmosphere concentrated of high carbon content (e.g. CO or CO_2) at high temperatures will try to gain some carbon to establish a balance between the atmosphere and the powder compact, this leads to a carburising process. The opposite reaction of high carbon content steel sintered in a poor carbon atmosphere causes a decarburising reaction where the sintered steel loses carbon to the atmosphere. For equilibrium in the atmosphere the CO, CO_2 will dramatically change with temperature due to the Boudouard reaction as seen in equation 2.19 [56].

Decarburization increases with increase in the rate of carbon diffusion and activity, and α-γ transformation temperature, whereas for the carburization it is vice versa. Based on the equilibrium between, the materials, carbides and sintering atmosphere, carbides can be formed or decomposed during sintering. The general reaction between metals (M)

and their carbides (M_xC) is considered in terms of the carbon monoxide (CO) and methane (CH_4) reactions, as shown in equations 2.20 and 2.21 [6]:

$$CO_2 + C \rightarrow 2CO \quad 2.19$$

$$xM(s) + 2CO(g) \leftrightarrow M_xC(s) + CO_2(g) \quad 2.20$$

$$xM(s) + CH_4(g) \leftrightarrow M_xC(s) + 2H_2(g) \quad 2.21$$

Control of the carbides plays a large role during sintering process for many sintered products such as, cemented carbides, tool steels, and silicon carbide. Decarburization can be controlled by use of copper plating, controlled atmosphere such as vacuum, inert gases (N_2, N_2+ 5-10H_2) or H_2, and salt heating. It's also can be corrected by carbon restoration [57].

2.5 Evolution of Steel Microstructure

2.5.1 Introduction: The Iron-Carbon Phase Diagram.

The amount of carbon in iron plays a significant role in microstructure evolution and properties and it is important to specify the type of structure, either iron, steel or cast iron. Pure iron or in tiny amount, i.e. <0.008wt%C, is referred to as pure iron (α-Fe or ferrite phase); whereas iron alloyed with carbon from 0.008wt%C to 2.1wt%C is classified as steel, and all compositions containing higher carbon contents are termed cast iron. The amount of carbon is largely responsible for the wide range of mechanical and physical properties that can be achieved and which make steel a very essential

commodity in life [58]. Figure 2.27 illustrates equilibrium phase transformations (i.e. ferrite to ferrite + pearlite, then pearlite and finally cementite + pearlite).

Most steels have above 95 % by weight iron and the remaining are other elements such as Cr, Mo, Mn, Si, Ni, V, etc. added to improve the mechanical, chemical and physical properties.

Iron at room temperature is named Ferrite or (α-iron), with Body Centered Cubic (B.C.C) structure, but when heated up to 912 ºC, the crystal structure changes spontaneously to a new crystal structure termed Face Centered Cubic (F.C.C) structure, and the Ferrite changes to Austenite or (γ-ion) [42, 57, 59, 60]. In addition, there is another Fe structure with Body Centered Tetragonal (B.C.T) structure, known as Martensite which forms from the austenite phase via quenching operation (rapidly cooling) in hyper-eutectoid steels >0.83 wt % C. These three crystals structures are the most common structures of iron. As shown in Figure 2.27, there are many different phases within steels which are created by the heat treatment operation with changes of the amount of carbon content.

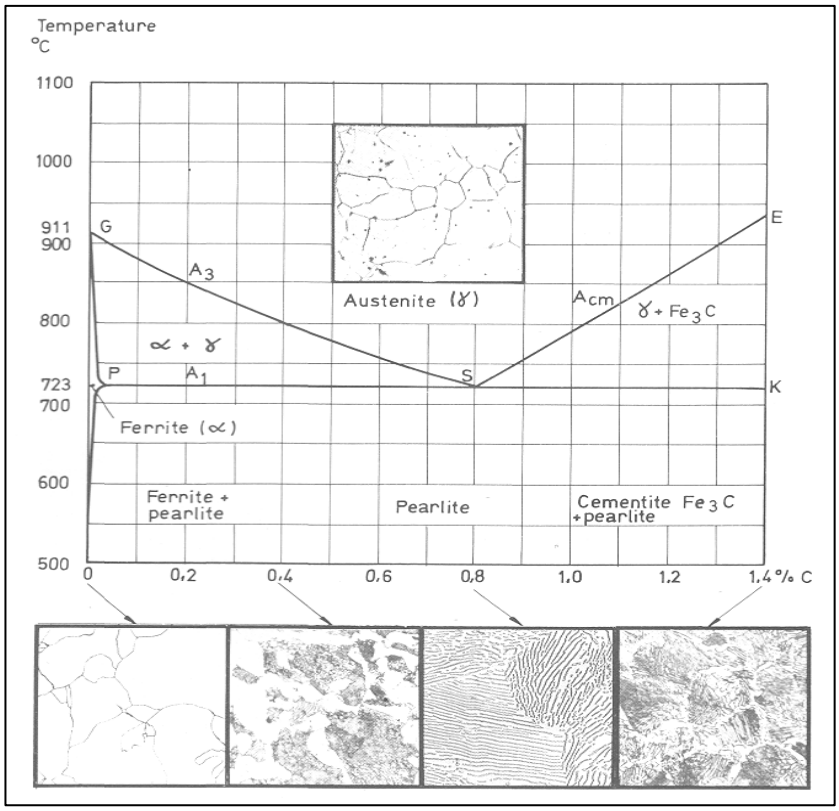

Figure 2.27 Iron-carbon equilibrium diagram [58].

Classification of steels and their carbon content with some applications and characteristics are illustrated in Table 2.5 [58].

Table 2. 5 Steel Classifications.

No.	Type of Steel	C % wt. Range	Application	characteristics
1	Low Carbon Steel	0.022-0.3	Pipes, chain, machine parts	Soft, tough, but low hardness
2	Medium Carbon Steel + other Alloying element (Mo, Ni, Cu,etc.)	0.3-0.8	lead screws, gears, crankshafts, hammers	Toughness, ductility, hardness
3	High Carbon Steel + other alloying element (W,Mo, V, Co, etc.)	0.8-2.1	drills, cutting tools, milling cutters	Good wear resistance, high tensile strength

2.5.1.1 Metallographic Structures

The main constituents of steel, depends on carbon content, heating and cooling temperatures, holding time and gas atmosphere, austenite, ferrite, pearlite, cementite, and non-equilibrium constituents, upper and lower bainite and Martensite. These constituents directly affect mechanical properties, which are dictated by microstructure of the alloy. These microstructures can be modified by employing proper heat treatments to achieve the unique properties suitable for its intended application.

Austenite

This phase has a Face Centered Cubic (FCC) structure, which can hold a maximum of around 2% by weight of carbon in solution at a temperature about 1147 ºC. Austenite has also been referred as (γ), or γ-Fe. Austenite is a soft and ductile phase, and can exist only at elevated temperature in plane carbon steel, but it can be stable at room temperature for some alloy steels such as Hadfield steel [58].

Ferrite

Ferrite is the α-Fe known as α-phase solid solution where the solvent is alpha iron, and the solute is carbon. This phase can hold very little amount of carbon, typically, 0.008% at room temperature and when heated up to 723ºC the maximum amount of carbon will be around 0.02wt%. The ferrite phase has a Body Centered Cubic (BCC) structure, and is designated as either alpha (α) or delta (δ) phase. Ferrite is a very soft form of iron and also shows high level of ductility [58].

Cementite

Cementite is very hard and brittle iron carbide with 6.67 wt % carbon corresponding to the composition Fe_3C, having ~650 Brinell hardness [58]. When Cementite is mixed with soft ferrite layers this leads to reduced hardness [58, 59].

Pearlite

Pearlite is a mixture of alternate thin layers or lamella of iron carbide (Cementite) and ferrite in a single grain called pearlitic structure as seen in Figure 2.28. Spacing between layers is dependent on the cooling rate of the material, and when the cooling rate is fast thin layers will be created, whereas slow cooling rate creates a much coarser structure less strong, 0.8wt% carbon creates as fully pearlitic structure. Further increases in carbon will produce cementite between grain boundaries causing the steel to be weak and brittle [42, 57, 58]. Pearlite has combination of properties which are intermediate between ferrite and cementite. Thus, it is harder and stronger than ferrite but softer and more ductile than Cementite. Because pearlite is consists a mechanical mixture of the two phases. It's well known, that the formation of pearlite is started at the austenite grain boundaries or at some other disarray in the austenite grains itself [58].

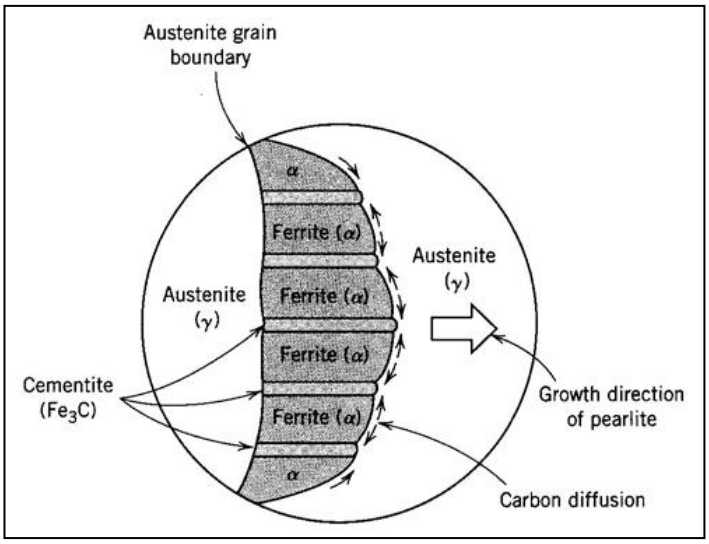

Figure 2.28 Diagram of pearlite growth [42].

Martensite

Martensite is a metastable transitional constituent indicating the first stage in decomposition of austenite. Martensite holds a Body Centered Tetragonal (BCT) form of iron in which carbon is dissolved and trapped during quenching and the (FCC) structure of austenite is distorted into body centered tetragonal (B.C.T) structure without loss of its carbon atoms [42, 57-59].

Martensite is undoubtedly the most important and widely discussed metallographic constituent in steel. The martensite transformation is a diffusionless transformation, which results in effect in a supersaturated solution of carbon in iron, into which hot austenite turns when rapidly freezing. Martensite is the hardest and strongest transformation product of austenite, but unfortunately is also very brittle.

Martensite start temperature (Ms) is the temperature at which martensite begins to form during quenching from the austenite region and continues to form as the temperature is lowered. Ms has a big affect on the martensite structure. The chemical composition of steel plays the main factor affected its Ms, although the austenitisation status (grain size and temperature of austenitisation) and external stresses and stored deformation energy also have an affect [58]. Recently studies have shown that the austenite grain size also may sometimes plays an important role in determining Ms, as the austenite grain size increases, so does the Ms [61]. Martensite start temperate (Ms) is relatively easy to calculate for steels having low alloy content, whereas, for those having high alloy content empirical equations were used [62]. Carbon level plays the big role on the amount of Martensite forming as well as the temperature of respectively the start of austenite-to-martensite transformation (Ms) and the end of this transformation (Mf), as seen in Figure 2.29. It is also known the higher the carbon content, the lower the temperature needs to be to form martensite [63].

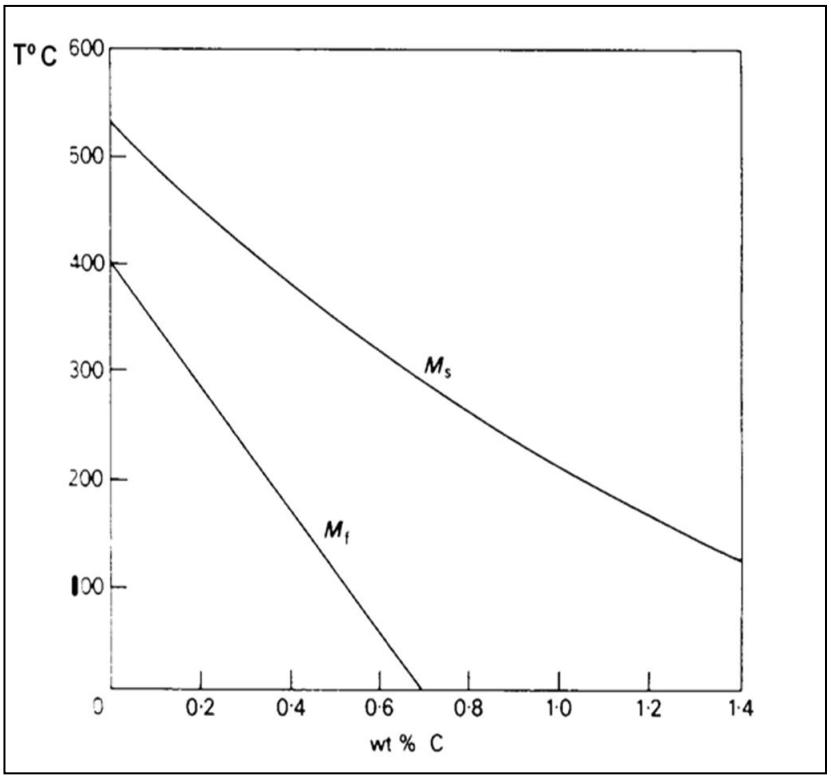

Figure 2.29 Effect of carbon on Ms and Mf [63].

Bainite

When cooling steel, at moderate cooling rates between water quenching and air cooling, a constituent known as the bainite microstructure forms [64]. Bainite microstructure is very fine and consists of ferrite and cementite, in some ways similar to pearlite, but bainite has a different morphology. Generally, bainite appears over a large range of temperatures with different morphologies at different transformation temperatures (temperature range between the high temperature transformation of ferrite and Pearlite and the low temperature transformation of martensite start M_s). The bainite forming at higher temperatures is called upper bainite and consists of laths of ferrite divided by cementite in parallel orientation with the major axis of the laths. Bainite

forming at low transformation temperatures comprises plate-like ferrite and cementite within the ferrite at an angle of 55-65º to the main axis of plates, and this structure is called lower bainite. The lower bainite structure is finer and has a more uniform carbide distribution than the upper, consequently lower bainite has higher mechanical properties than the upper [65].

2.5.1.2 Equilibrium Cooling Transformations

Equilibrium, (slow) cooling always produces structures indicated on the Fe-C diagram, Figure 2.27, which are free from internal stresses. The configuration of phases forming is dependent on the carbon content. Equilibrium cooling will be described for three different steels.

First, alloy steels which consist of 0.02 to 0.76 wt percent carbon are named hypo-eutectoid. On slow cooling from the austenite region to room temperature, when the temperature reaches A_3, austenite starts to transform to ferrite and as cooling continues, more ferrite forms and a mixture of ferrite (α) and austenite (γ) coexists until the eutectoid temperature is reached. The relative amounts of ferrite and austenite are given by the lever rule. Subsequently, below 723 ºC, all the remaining γ-Fe transforms to pearlite [58, 63]. Second example is for the eutectoid steel (0.76 wt % C), which remains austenitic until the eutectoid temperature is reached. Immediately, below the eutectoid temperature, the austenite is completely transformed into pearlite, i.e. alternate layers of ferrite and iron carbide (Fe_3C), [2, 3, 26].

Thirdly hypereutectoid alloys, steels with carbon content between 0.76 and 2.14 wt %, will be considered. On cooling a fully austenitic structure, when the temperature crosses

the A_{cm} line, the austenite begins to precipitate cementite along the austenite grain boundaries, becoming itself less rich in carbon, and the process continues until the eutectoid temperature is reached. The relative amounts of austenite and cementite are given by the lever rule. As the temperature is decreased below the eutectoid temperature, all the remaining austenite is transformed to pearlite, which consists of lamellae of ferrite and cementite [6, 33, 34]. Grain boundary cementite, if continuous, embrittles the steel. Low carbon steels produced by equilibrium cooling have mainly soft ferrite and some hard cementite, thus, the steel is relatively soft and weak. For higher carbon steels, the situation reverses, and steel is hard, strong and less ductile. Figure 2.30 shows the phases for the three types of steel (hypo-eutectoid, eutectoid and hypereutectoid) following slow cooling.

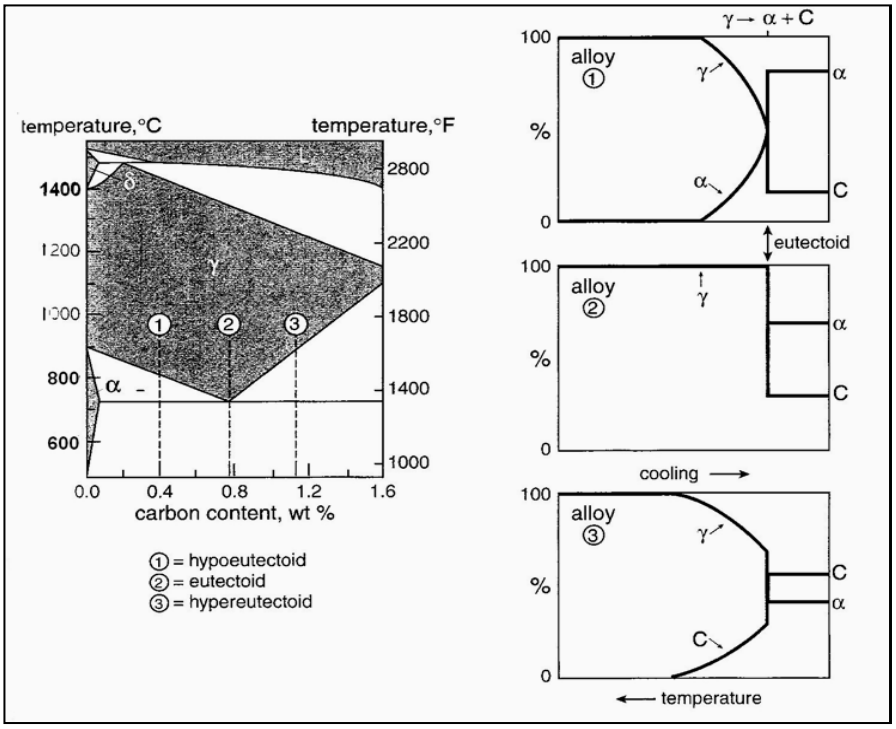

Figure 2.30 Phase changes during slow cooling of three steel compositions [58].

2.5.2 Heat Treatment

Heat treatment is the thermal operation or combination of operations which involves the controlled heating and cooling of a metal alloy in order to enhance and improve its mechanical properties without any change in the part shape. Furthermore, it is also done to remove residual stresses from machined or deformed components and to provide a good microstructure. Heat treatment is generally performed to markedly increase the strength and hardness, as well as retaining toughness or ductility of the metals [58, 59]. However, it can be used for soften the metal in order to improve the machinability and for easier forming [42, 57, 58].

Heat treatment operations are necessary for those sintered parts for these reasons:

- To soften, i.e. to reduce hardness, reduce strength, remove residual stresses, improve toughness, and restore ductility.
- To increase hardness, strength and wear resistance,.
- To modify the properties in order to improve machinability and enable easier forming.

The processes of heat treatments which are very important include austenitisation quenching, tempering and spheroidisation (for high carbon steel only).

2.5.2.1 Austenitisation

Austenitisation produces the austenite phase and dissolves uniformly carbon and any alloying element present in γ-Fe. This process is done by heating the steel above the A_3

or A_{cm} temperature, for sufficient time to ensure that the alloy is fully transformed into the austenite phase. Austenitisation temperature has a big affect on the properties of the component [42, 66].

2.5.2.2 Quenching

Quenching is a simple definition of rapid cooling of the hot steel from austenite phase field to room temperature to get higher hardness by formation of Martensite. Quenching can be done by immersing the hot steel in a quenching media such as water, oil or air [42, 66].

2.5.2.3 Tempering

Quenching of austenite to room temperature results in the formation of martensite, which is a very hard but also very brittle phase. Tempering is a heat treatment used for removing the quenching stresses and reducing the brittleness, so as to modify the mechanical properties, by heating the steel in the range 150 – 700 ºC. Tempering is a diffusion operation which depends on time and temperature [42, 66].

2.5.2.4 Spheroidisation

Spheroidisation involves heating the material to a temperature just below the eutectoid point for a sufficient time to ensure that all the cementite (or alloy carbide, when some alloying elements were added such as Cr, V, Mo, etc.) laths or plates transform to produce fine spheroidised cementite (or carbide) particles within the ferrite [58]. This treatment is usually selected in order to improve the cold formability due to the lower flow stress of the spheroidised structure. Therefore, spheroidisation is a suitable heat

treatment to produce a ductile microstructure which enables plastic or even superplastic deforming. Influence of spheroidised macrostructure which consists of fine spheroidised carbide particles size (0.2-1.5-µm) within fine-grained ferrite matrix (0.3 to 5-µm) on tensile properties of ultrahigh carbon steel (1.8%C), has been studied by [67], the found that the yield strength of the UHCS (1.8%C) material, was shown to follow a Hall-Petch relationship. Recently, high mechanical properties have obtained using a new optimization spheroidising process of UHCS containing 1.5%Al [12].

2.5.2.5 Non- Equilibrium Cooling Transformations

Phase Transformations

The iron-carbon diagram is of fundamental significance to heat treatment, but it can only predict the equilibrium transformation phase at any temperature and carbon content. Non-equilibrium cooling, for the same carbon content, can produce a sequence of transformations, which can be manipulated to attain different microstructures and resultant physical and mechanical properties of the steel [66].

In heat treatment, the time parameter, absent from phase diagrams, plays the additional important role in phase transformations. Davenport and Bain were the first to establish the isothermal transformation approach by studying reactions isothermally at a sequence of temperatures under the A1 line, and presented their data in terms of an isothermal transformation or time-temperature-transformation (TTT) diagram. Such a diagram can be obtained for each particular steel [68, 69].

Time-Temperature transformation TTT Diagram

Steel is first heated to ensure the phase is fully austenitic, then rapidly cooled to a specific lower **T**emperature and held for a specific **T**ime, undergoing **T**ransformation to the determined products, depending upon the period of the time held at the temperature. Various types of structure produced from this transformation are indicated on the diagram with the holding times needed for start and complete a transformation. The result is a collection of curves representing the various stages of transformation at time versus temperature [69].

Isothermal transformation or time-temperature-transformation (TTT) diagrams as shown in Figure 2.31 for the transformation of austenite-to-pearlite for a Fe-0.79%C+0.76%Mn austenitized at 900°C. The upper portion of Figure 2.31 shows the S-shaped curve of percentage transformation versus time at a constant temperature (675 ^{o}C). [42, 66].

Repeating this process of measurements i.e. transformation process for various temperatures and then collecting these curves together, the compound diagram can be created and plotted on temperature versus the time axes, as shown in the lower section of the Figure 2.31, the TTT diagram [42].

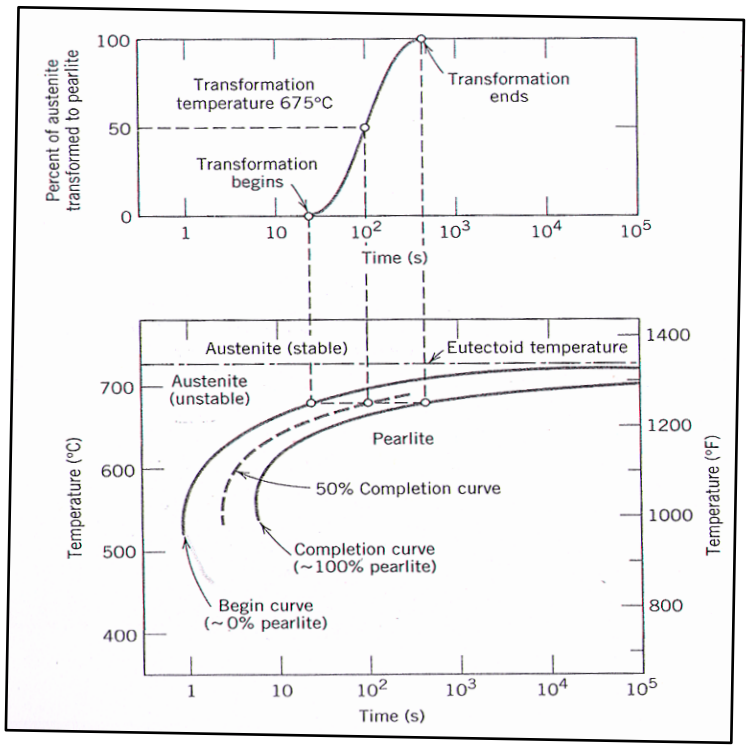

Figure 2.31 Comparison of an Isothermal Volume Fraction Transformation curve to TTT Diagram at the Corresponding Temperature [42].

An example of isothermal transformation of eutectoid alloy is illustrated in Figure 2.32: very fast cooling of austenite from A to a temperature below the eutectoid temperature, B, ~ 620 ºC, and then isothermally holding, BCD line. It can be seen that transformation of austenite-pearlite, begins at the intersection point C (after about 3.5 s), and is completed at point D, after ~ 15s [42]. Various schematic microstructures at different times during the transformation process are also represented in Figure 2.33.

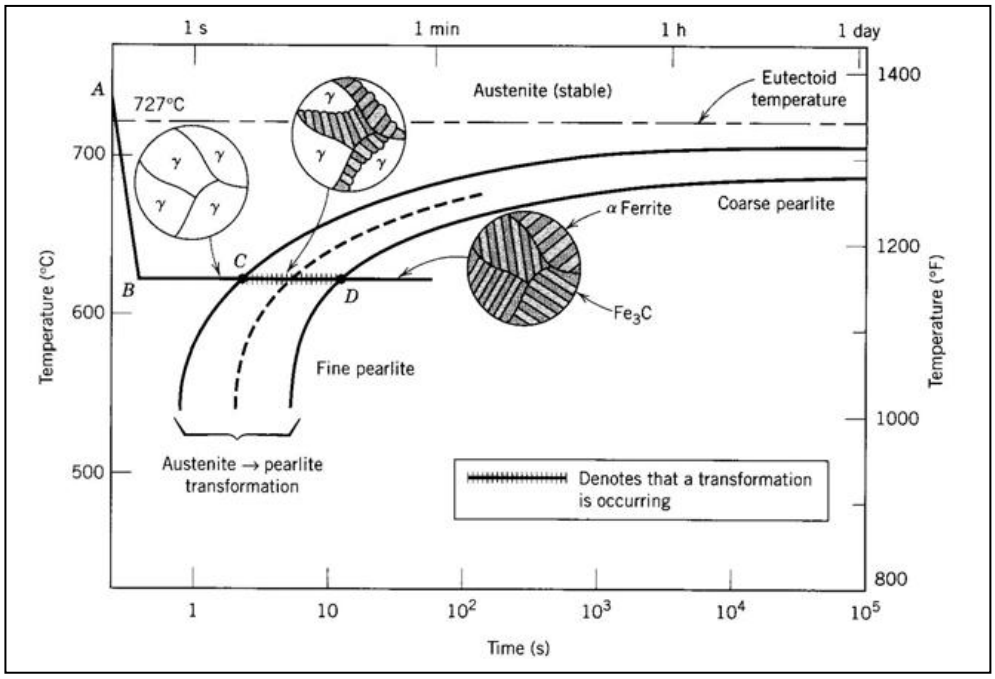

Figure 2.32 Isothermal Transformations or TTT Diagram of Eutectoid Alloy [42].

If the above procedure is repeated at different temperatures, a complete TTT diagram achieved, as illustrated in Figure 2.33. It is seen that at 727ºC and above, the phase is completely stable austenite, whereas below this temperature the austenite is unstable and, given enough time, undergoes a transformation. From below 723ºC to ~ 566ºC, particularly at the critical temperature transformation point (at nose), the lower temperature the shorter time taken for austenite to begin forming pearlite. As temperature decreases, diffusion rate decreases, and, at temperatures of 566ºC to 215ºC.after a sufficient time, unstable austenite transforms to bainite. Martensite transformation of unstable austenite occurs at temperatures 215ºC to -20ºC [66].

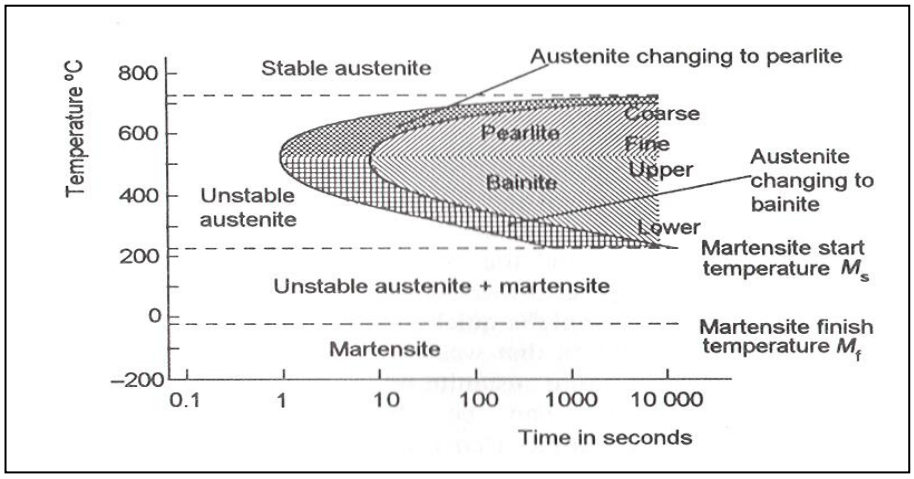

Figure 2.33 TTT Diagrams for a 0.8 % Carbon Steel [66].

Carbon and any alloying elements such as chromium, nickel, and molybdenum highly affect the TTT diagram. Figure 2.34 shows the TTT diagram for alloy steel with 0.4 % C and 0.8 % Cr. It can be seen the 'nose' of the TTT diagram shifts to the right (time required at any particular temperature for any transformation) due to the effect of the chromium addition [66, 70].

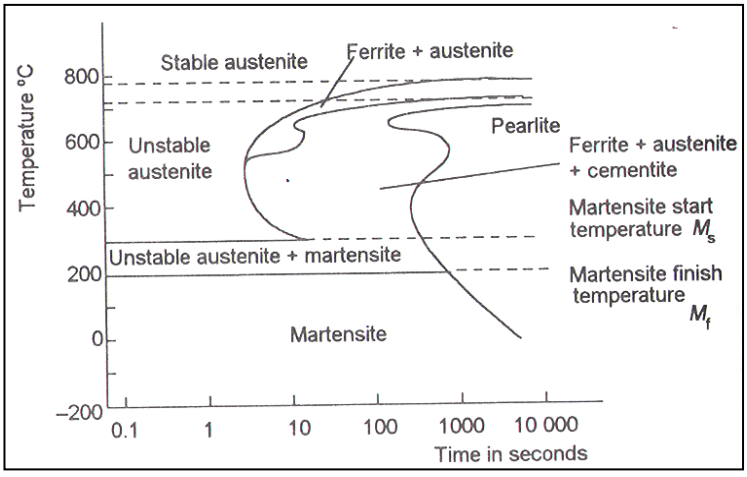

Figure 2.34 TTT diagram for a 0.4 % Carbon, 0.8% Chromium Steel [66].

Continuous Cooling Transformation

Most heat treatment processes of steel involve the continuous cooling to room temperature, and therefore Continuous Cooling Transformation, (CCT) diagrams are also used. The microstructure indicated on these diagrams result from the continuous cooling of the specimen from a temperature above the eutectoid temperature to room temperature, at different, specified cooling rates. Thus CCT diagrams are completely different from TTT diagrams.

To generate CCT diagrams, the steel is heated until completely austenitic, and then put immediately into a suitable cooling medium to obtain the required cooling rate and to measure the start and finish transformations. Cooling can be air-cooling, oil quenching, or water quenching. CCT diagram for an alloy steel with different cooling rates with Data Points of Transformation Temperature, i.e. start (Ps) and finish (Pf) transformation points are shown in Figure 2.35 [66, 68].

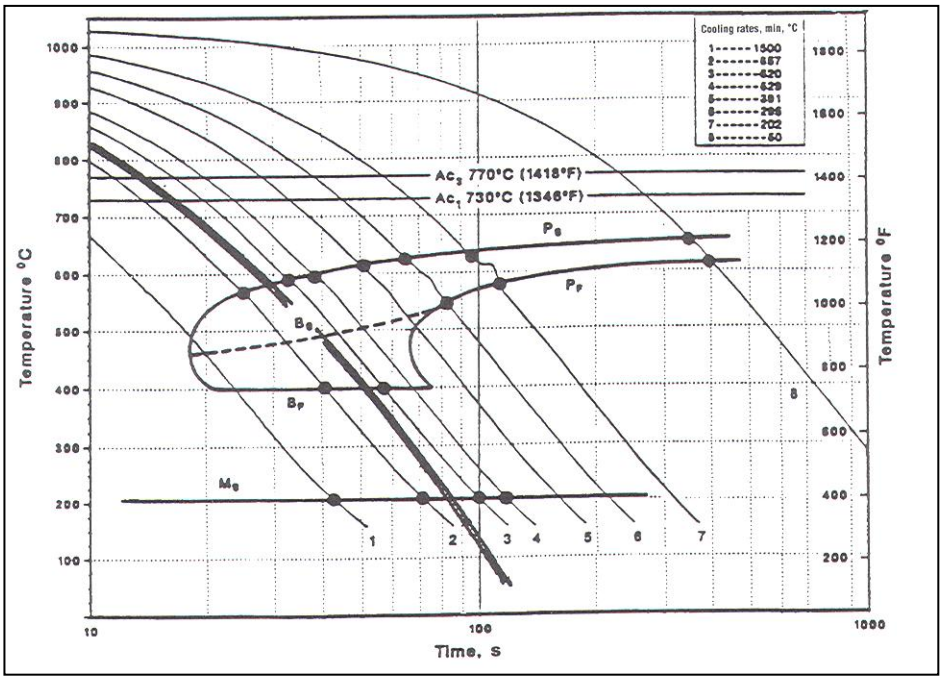

Figure 2.35 CCT diagram, superimposed eight cooling rates with data points of transformation temperature [68].

2.5.2.5.1 Effect of Cooling Rate

Cooling rate is an important parameter in heat treatment as it can control the microstructure produced, consequently improving the hardenability, and mechanical properties. Cooling rate is dependent on the cooling medium applied, i.e. water quenching, oil quenching, or air-cooling. Water cools faster than oil, and oil quicker than air, consequently the hardness is higher, respectively. Rapid cooling rates produce martensite below 200°C in Figure 2.35 and more martensite is formed as the temperature decreases. This influences hardenability i.e. hard Martensite greatly influences hardness of the alloy. Ferrite plus pearlite can be obtained by slow cooling, whereas bainite is the structure produced by moderate cooling rates. Figure 2.36 indicates the effect of cooling rate on forming different structures [58, 71].

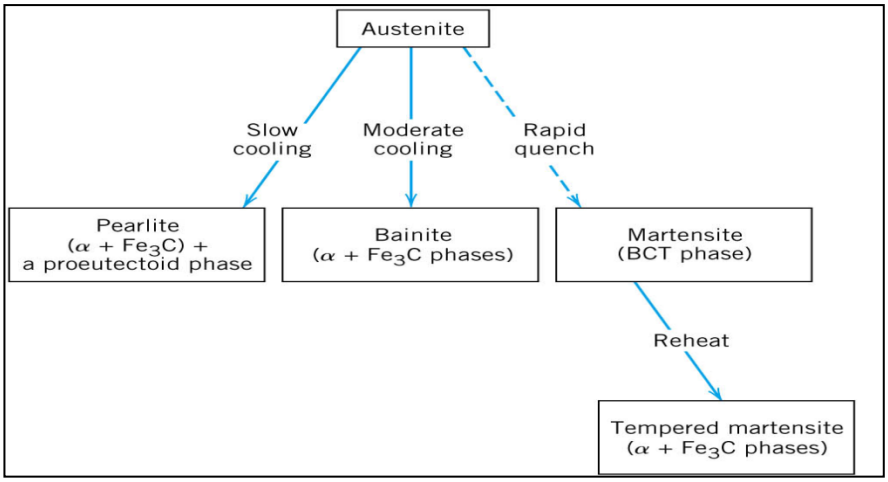

Figure 2.36 Flowchart of Cooling Rate [42].

2.5.2.6 Hardenability

Hardenability is to be differentiated from hardness, which is defined by the degree of resistance to indentation in a hardness test, e.g. Brinell, Vickers, Knoop test, or Rockwell. The ability of steel to be hardened (to produce martensite) by quenching is referred to as hardenability [70]. The measuring parameter is the depth of the martensite layer. During quenching of rod steel, the surface exhibits different cooling rate to that of the inner core. The surface has rapid cooling rate and the result of the microstructure is fully Martensite, whereas the inner core of the rod with moderate cooling rate had pearlite plus Martensite as shown in Figure 2.37 [72].

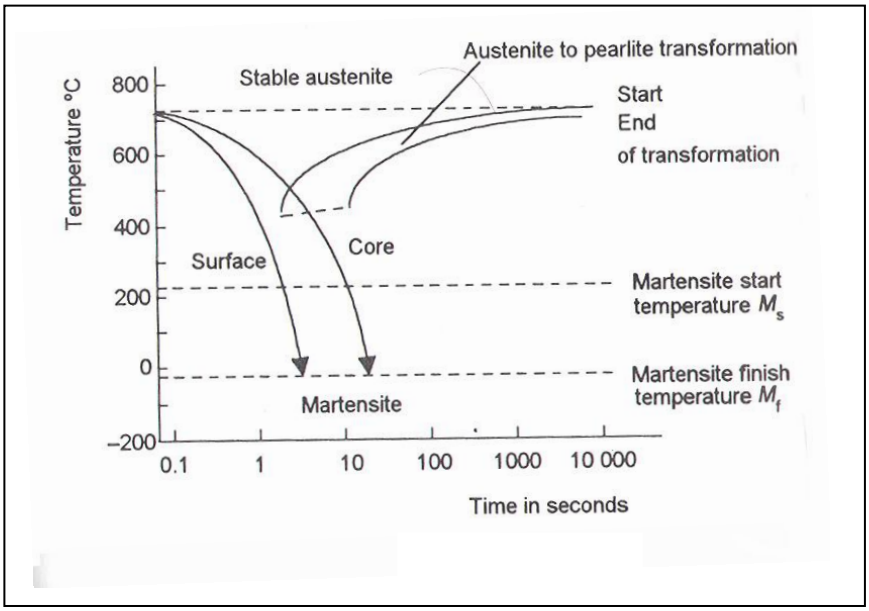

Figure 2.37 Quenching a bar and production of different phases [66].

Continuous cooling diagram can be constructed and plotted for temperature versus bar diameter. Figure 2.38 illustrates the continuous cooling transformation that occurs as a function of the bar diameter for different cooling media. From the Figure, it can be noted that the microstructure produced for10 mm bar diameter cooled in comprises ferrite, pearlite, and a small amount of bainite. For oil quenching, the microstructure is bainite plus Martensite at the same diameter. For water quenching, the microstructure generated is fully martensitic, so only water quenching is suitable if a fully martensitic structure is required [66, 69].

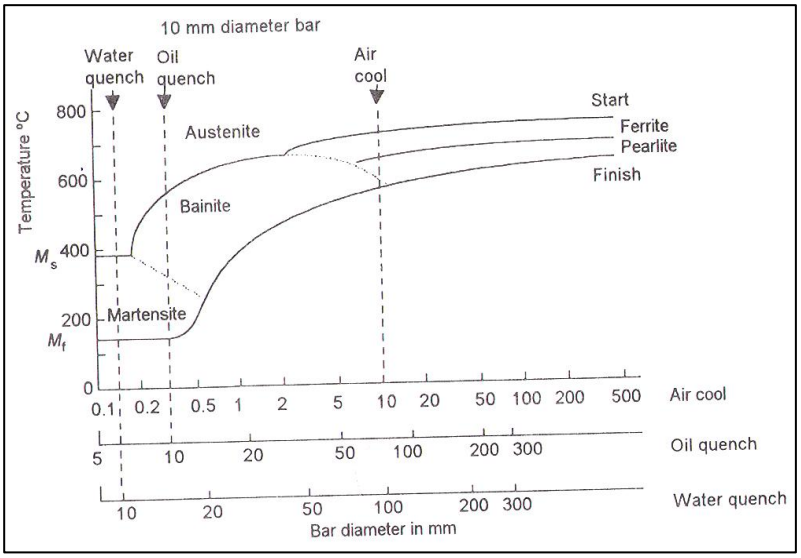

Figure 2.38 Shows the CCT with different cooling rates as a Function of Bar Diameter of 0.38 % Carbon Steel [66].

The most common method of assessing hardenability is the Jominy end-quench test. The procedure is austenitizing a standard-size steel bar, 100 mm long and 25 mm in diameter, and then placing it vertically in a fixture and quenching the lower end directly by a stream of water at 25 ºC. The cooling rate is completely different throughout the length of the bar, at the lower end, the cooling rate is the highest, due to direct contact with the water, and vice versa [42, 66]. Once cooled the bar is cleaned and ground flat along its length for hardness testing. Jominy test results present hardness as a function of distance from the quenched end, i.e at various cooling rates. Figure 2.39 shows the results of a Jominy test of a steel bar with 0.4 % carbon [42, 66].

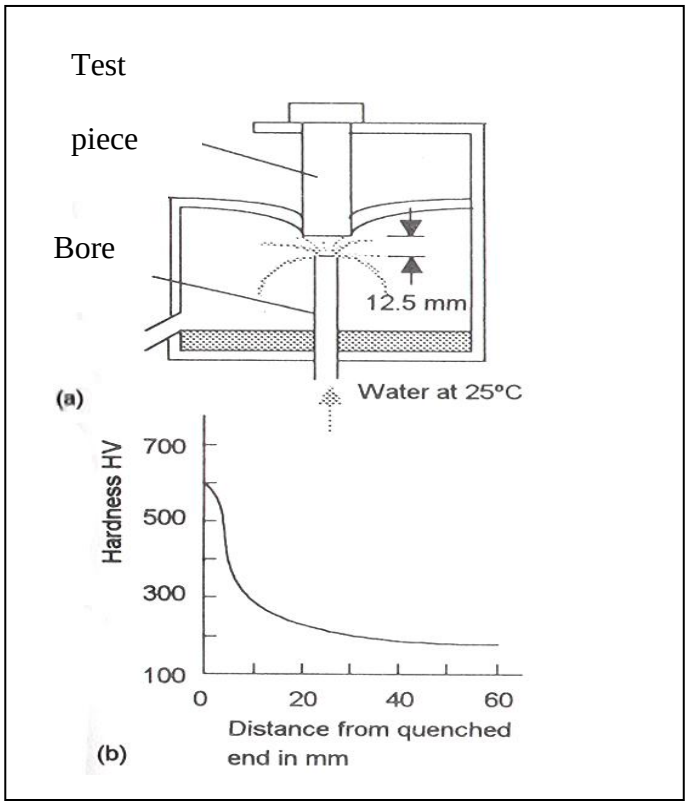

Figure 2.39 Effect of cooling rate on the hardness of a 0.4%C-steel bar [66].

2.5.3 Influence of Alloying Elements

By adding other alloying elements, e.g. Mo, Ni, Cr, Si, Mn, remarkable changes are made to the mechanical and physical properties, as well as the Fe-C phase diagram. The changes in positions of phase boundaries and shapes of phase regions depend on the amount of the alloying element, response to coexisting other elements and their concentrations as well as the ability to dissolve into the matrix. The most important change is the transfer in location of the eutectoid with reference to temperature and carbon concentration. Alloying elements change the temperature of the eutectoid and the relative fraction of Pearlite and proeutectoid phases [42]. Heat treatments subsequent to the addition of other alloying elements are well documented [42, 58]. Most metal additions stabilize either ferrite or austenite, but some form carbides. The

alloying additions change the transformation temperature, which can increase or impede the formation of desirable phases by heat treatment. Some alloying additions allow slower cooling of austenite to martensite thereby leading to slower transformation, making it easier to form high-strength sintered components. It is very important to understand the function of each elements and how it reacts with iron and carbon, the two key constituents of steel [73]. Figures 2.40 and 2.41 show the effect of different alloying elements on solid solution strengthening of the ferrite phase. In solid solution hardening the elements P, Si and Mn have the highest effect; for example to reach a ferrite hardness of ~ 160 HB only 2 wt % Si or ~ 4 wt % Mn are needed as compared with > 14 wt % V or ~ 13 wt % Mo. For ultimate tensile strength (UTS) of ~ 310 MPa only 0.5 wt % Si is needed as compared with ~ 2.25 wt % Mo. This implies that to attain comparable strength and hardness much higher quantities of V or Mo are required than those of Si or Mn. For sintering at >1200 ºC with iron alloying elements such as P, Si, Mn, and Cr, protective atmospheres with a low dewpoint (~ -60 ºC)are needed [73]. The above is only associated with solid solution hardening.

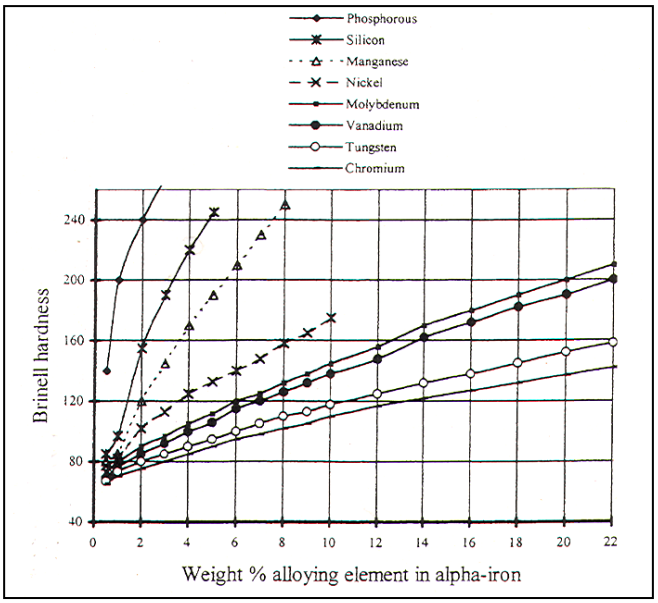

Figure 2.40 Solid Solution Hardening Effect of Various Alloying Elements [73].

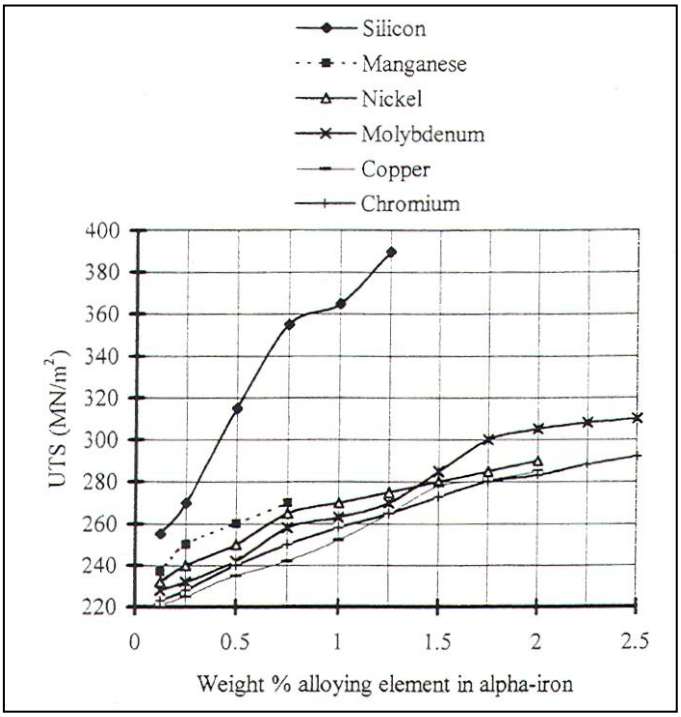

Figure 2.41 Solid solution strengthening of various alloying elements[73].

Youseffi et al [74] have examined additions of Si to 316L stainless steel. They found a correlation between sintering temperature and Si content. Sinterablility, rate of densification, and shrinkage increased, whereas porosity decreased by increasing the content of Si and sintering temperature. They also found that both hardness and tensile strength had improved by Si addition.

There are three categories of alloying element for P/M steels: ferrite strengtheners, austenite stabilisers, and carbide forming elements.

2.5.3.1 Ferrite-forming elements

Alloying elements such as Cr, Si, Mo, W, and Al are the most important elements in this category. Fe-Cr alloys containing more than 13 % Cr are ferritic at all temperatures

until the initial melting. Figure 2.42 shows the range of stability of ferrite in iron-chromium [58].

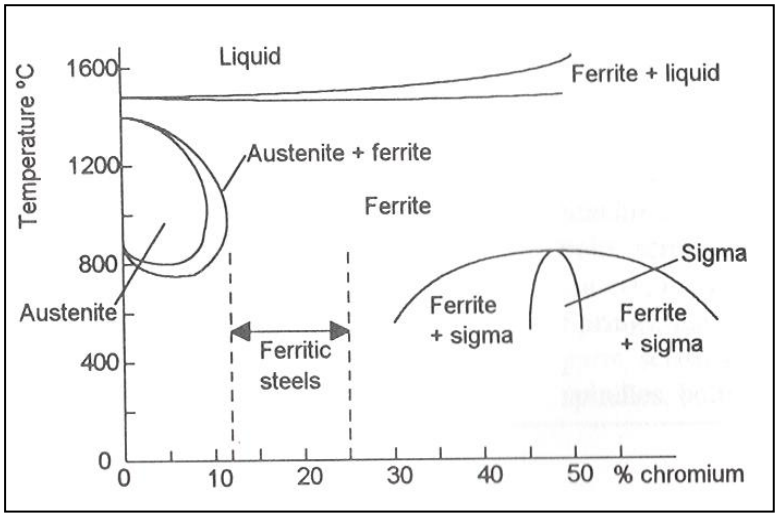

Figure 2.42 Cr-Fe Equilibrium Diagram [66].

2.5.3.2 Austenite forming elements

The most important austenite forming elements are C, Ni, and Mn. Sufficiently large quantities of Mn or Ni render steel austenitic even at room temperature. The equilibrium iron-nickel diagram Figure 2.43 shows that the stability of austenite increases with increasing Ni content. For example, with 10 % Ni, the steel becomes completely austenitic at 700 ºC [58]. Another example is Hadfield steel containing 13 % Mn, 1.2 % Cr, and 1 % C; these elements surely take part in stabilizing the austenite.

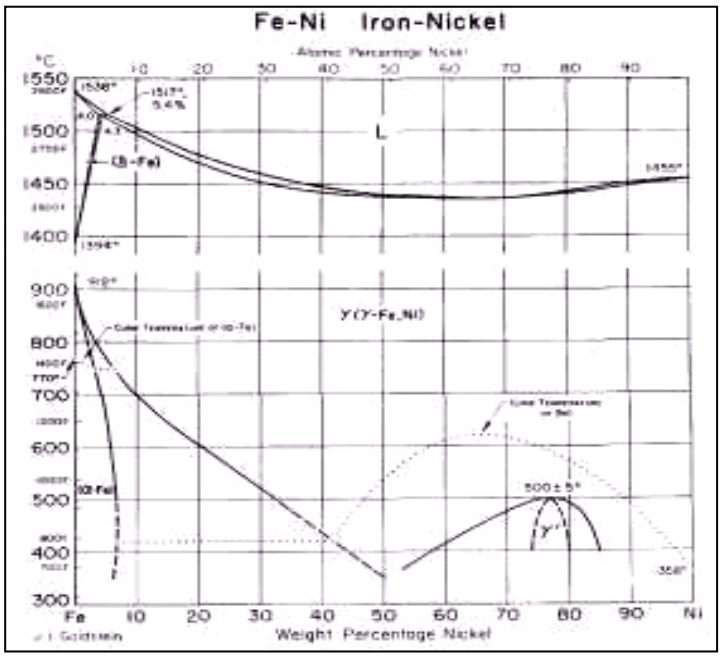

Figure 2.43 Fe-Ni Equilibrium Diagram [58].

2.5.3.3 Carbide Forming Elements

Alloying elements such as Cr, W, Mo, V, Ti, Nb, Ta, Zr have a great affinity for carbon. High-speed and hot work tool steels typically include three categories of carbides, which are usually designated M6C, M23C, and MC. The letter M represents collectively all the metal atoms. Thus M6C represents Fe_4W_2C or Fe_4Mo_2C, M23C represents $Cr_{23}C_6$ and MC represents VC or V_4C_3 [58].

2.5.3.4 Effect of Alloying Elements on Fe-C Phase Diagram

Carbon changes iron to steel and consequently increases hardness and strength. When further alloying elements are added to Fe-C, changes take place in the three important lines on the phase diagram, i.e. A1, A3, and Acm will move somewhat up or down.

When there is only one further addition, Fe-C-X (X is any element e.g. Cr, Mo, Mn, Ni, etc.) a ternary phase diagram is generated [42, 58, 70].

Molybdenum, chromium and silicon have the bcc crystal structure, thus favour the bcc structure of ferrite; therefore these elements are known as ferrite stabilizers. Chromium steel of eutectoid composition, 12% Cr and 0.4 % C, will require a higher austenitizing temperature ~ 880 ºC than carbon steel, 727 ºC, In contrast for a 3 % nickel steel, the austenitization will be at a lower temperature, ~ 700 ºC. Elements such as nickel and manganese have the FCC structure and are known as austenite formers. With these elements the austenitizing temperature will decrease to below 727 ºC, as illustrated on Figure 2.44 [75].

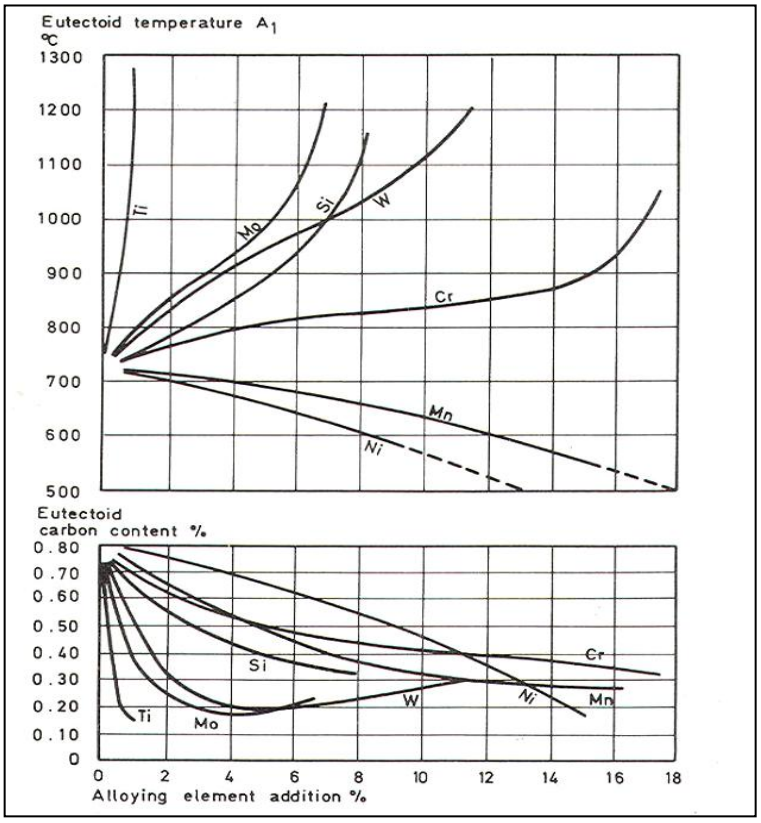

Figure 2.44 Shows the Effect of Alloying Elements on Fe-C Phase Diagram [58].

2.5.3.5 Effect of Some Element on Alloy Steel

Effect of Carbon

Carbon, a cheap alloying element present in all structural steels, classifies the type of steel: i.e. low, medium, or high carbon steel, even a small amount of carbon plays an important role in determining the mechanical properties of steel. However as the carbon content increases to between 0.8 and 0.9 % C, although hardness and tensile strength increase, ductility and weldability decrease. Effect of the carbon content on prealloyed Fe-1.5 Mo powder was studied by Youseffi et al [54]. They found the increasing carbon content had a marked effect on the both physical and mechanical properties: UTS, TRS, and hardness increased with increasing carbon content up to 0.8wt. %. During sintering, carbon is very rapidly dissolved in iron; the increasing carbon content reduced the sintering temperature, by lowering the solidus temperature. Insufficient carbon content results in incomplete sintering, whereas excessive carbon content gives oversintering. Carbon additions up to 0.2 - 0.3 % are useful in terms of eliminating porosity and extending the range of sintering temperatures [41].

Figure 2.45a depicts the Fe-0.47%C binary alloy and Figure 2.45b the same material with slightly increasing the carbon to 0.68 wt%. Penetration of the carbon atoms in the austenite phase lattice increases its dimensions during sintering, being greater, the bigger the carbon content [41, 76]. Figure 2.46 shows the effect of carbon content on the mechanical properties (upper graph) and also indicates the transformation phase forming i.e. from ferrite to pearlite and then where the cementite start forming (lower graph).

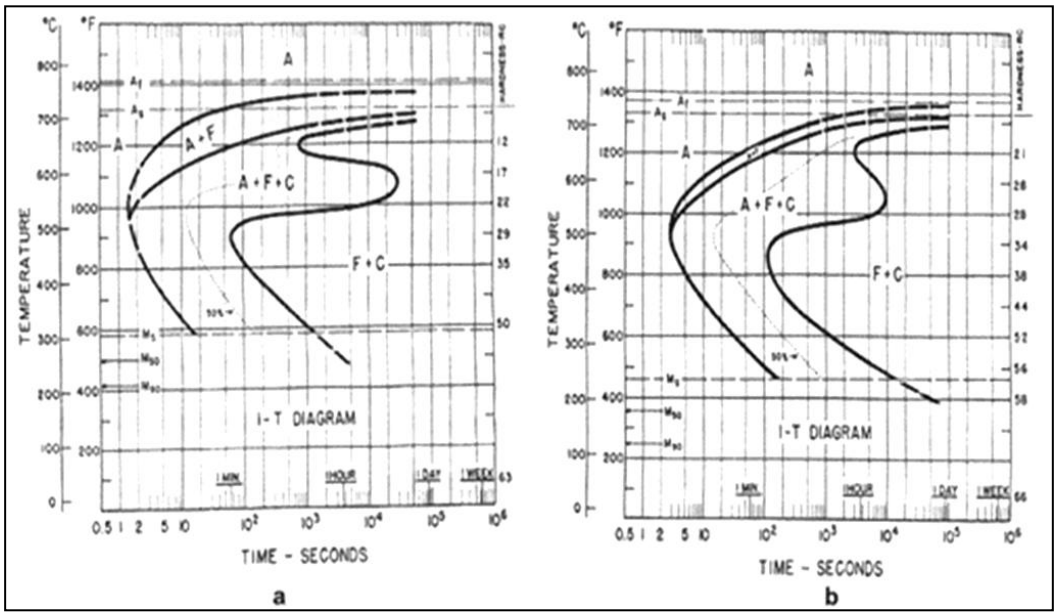

Figure 2.45 Effect of Carbon Content on the Phase Diagram [58].

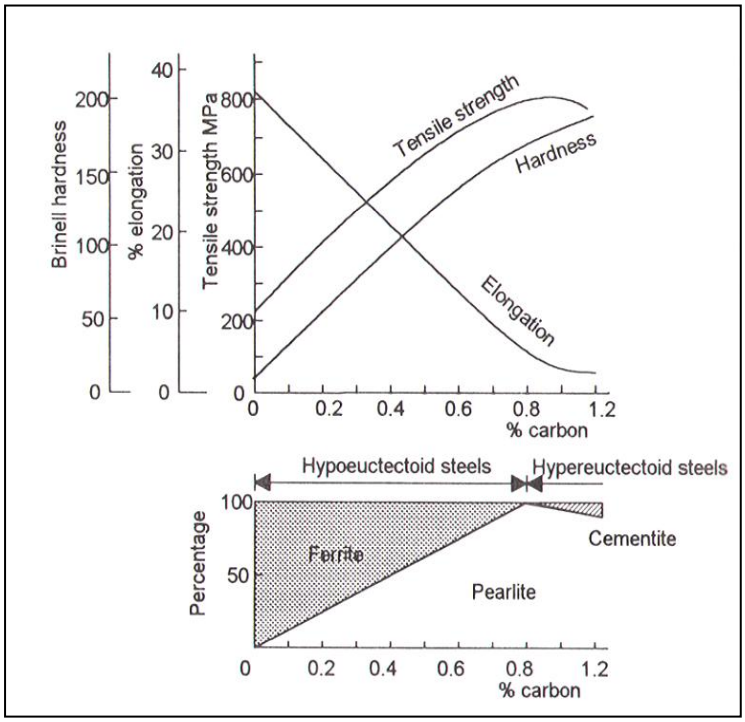

Figure 2.46 Effect of Carbon Content on the Mechanical Properties [66].

Effect of Manganese (Mn)

An important alloying element is manganese; one of the cheapest alloying elements as well as more effective for many iron-based alloys. Manganese is added to steels as a deoxidizer. A number of investigations [77-80] reported the effect of manganese on the mechanical properties, hardenability and magnetic properties of steel. Manganese contributes to promoting hardness and strength of all steels, but is not as potent as carbon. Increasing the manganese content leads to decrease in the ductility and weldability of steel. Of particular economic interest for PM steels is replacement of nickel by manganese because of its low cost. Manganese is usually presents in small quantities in steels, from 0.5 to 2 % wt, but sometimes in the range of 10 % to 15 % for special steels, e.g. Hadfield steel with 13 % Mn, with its unique combination of properties of high toughness, strength, and wears resistance [76].

Effect of Molybdenum (Mo)

Additions of alloying elements such as molybdenum, nickel, chromium to sintered steel have been practiced for many years to improve the mechanical properties and hardenability. Molybdenum increases hardness and toughness significantly [81], and it has a very good resistance to oxidation, hence sintering atmosphere and conditions are non critical. Molybdenum is a refractory metal, which is characterised by a high melting point and inter atomic bond strength [82], therefore, it was selected in the base powder, to improve hardenability by enhancing the martensite formation as well as enhancing both toughness and grain refinement during melting. Molybdenum is usually added in relatively small quantities ranging from 0.1 to 0.4 % wt [81]. Alloying combination of molybdenum and nickel has been investigated by Bepari et al [83] regarding the effect

on the structure and properties of carburized and hardened low carbon steel. They found that molybdenum produces fine Martensite, but, when combined with nickel, refines the size of Martensite more than the molybdenum without nickel. Both enhance austenite retention in the cases of carburized and hardened steel, but nickel is more effective. Mn and Ni increase the core hardness of low carbon steel, molybdenum is more effective and molybdenum and nickel together even more so. They reduce the toughness, nickel more, with the combined effect being greater than of either alone.

Effect of Silicon (Si)

Silicon is one of the most familiar deoxidizers used in steel manufacturing, since it has a high affinity for oxygen. In the case of liquid phase sintering, using silicon, selection of the sintering temperature and atmosphere are very important parameters [73]. Silicon is present in varying quantities up to 1wt.% in the finished steel and has useful effect on certain mechanical properties such as tensile strength. It is present in quantities in the range of 0.4 to 1.2wt.% to enhance hardenability [84, 85]. In alloys with certain electrical characteristics, silicon is present in higher quantities. The effect of silicon addition on prealloyed Fe-1.5Mo under various process conditions have been studied by Youseffi, et al [54, 74]. They found that the sintering process is enhanced by addition of Si, consequently increasing the tensile strength from 174 to 445 MPa. Silicon particles are harder to compress compared with the pre-alloyed Fe-Mo particles, and this has a negative effect on the compact density [74, 85]. Silicon is a well known element for liquid phase sintering and strengthening of ferrite [74, 85].

Effect of Chromium (Cr)

Chromium, in combination with carbon, has the ability to increase strength, depth of hardness penetration and achieve higher hardenability [86, 87]. Chromium is widely used in bearing alloys containing 0.5 to 1.5 wt%. Usually chromium combines with toughening alloying elements such as nickel and molybdenum to produce unique mechanical properties. Cr-Mo low carbon steels are extensively used in the petrochemical manufacturing [42]. In high speed steels chromium is found in approximately 4 wt%, whereas in stainless steels at 12 to 25 wt% [11, 21]. Chen et al [88], investigating the influence of Cr on microstructure and sintering properties of FeNiMoCu, found homogenous diffusion of chromium, which improved the microstructure and hardness.

2.6 Ultrahigh Carbon Steels

The carbon content of ultrahigh-carbon steels (UHCSs) is in the range of 1.0-2.1% [13-16, 78, 89, 90]. Traditionally, steels of such high-carbon contents have been neglected by industry due to their brittleness, resulting from the presence of a severe carbide network [12], consequently ductility of steel dramatically decreases. Figure 2.47 shows the relationship between the carbon contents versus elongation (ductility) of steel. In contrast, reducing the carbon content leads to reducing the tensile strength of steel as presented in Figure 2.46. Traditional heat treatments used for normal steels create coarse microstructures and do not produce optimal properties for the UHCSs [15, 90]. However, following the proper and controlled heat treatment, a unique microstructure and good mechanical properties can be obtained. Processing, not only to obtain fine spheroidised carbides, but concurrently fine ferrite, can result in superplastic properties

[14-16, 67, 89, 91-93]. Studied were: heat treatment, microstructure and mechanical properties, including of extruded ultrahigh carbon steels [16, 91], the influence of processing and microstructure on the mechanical behaviour of UHCS (1-1.8%wt.C), pearlite in ultrahigh carbon steels (1.5 and 1.8C). Decreasing the pearlite interlamellar spacing increases the yield strength and ultimate strength and decreases the tensile ductility [16]. Yield strengths reaching 1.5 GPa [12, 90] and superplastic properties of UHCs have been reported [12, 16, 67].

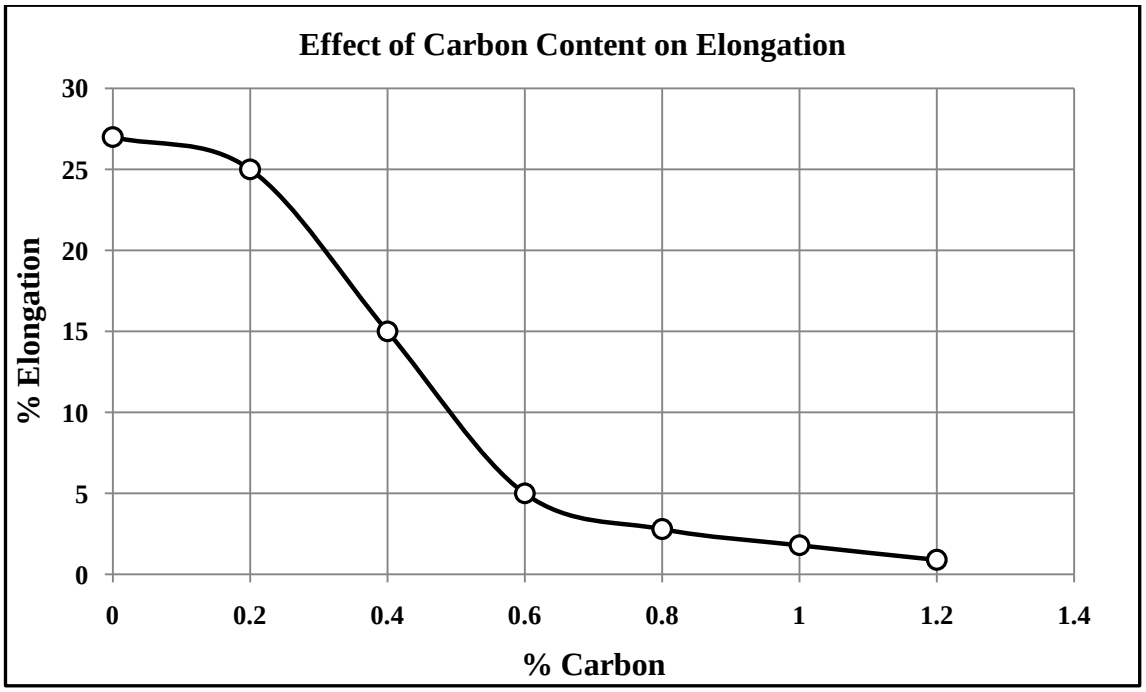

Figure 2.47 Relationship between the carbon content versus elongation of carbon steel. Diagram refers to steel pearlatical microstructure [67].

2.7 Warm-Forging

Warm Forging of PM materials is a technique which involves hot re-pressing of a metal blank in a closed die, where the shape geometry of the blank transforms significantly, thus improving density and dimensional accuracy. Warm forging process can achieve full density and produce complex geometries to a very high level of precision [75]. In ultra high carbon steel microstructures can be created consisting of very fine spheroidised carbide particles within a fine grain ferrite matrix [94]. Such microstructure has been shown subsequently to exhibit superplasticity [95], which is the capability of the material to deform to very large tensile elongations in a specific temperature and strain rate regime. Other studies of the deformation behaviour and superplasticity of UHCSs have been reported in Sherby, et al [92] whom published an overview of the subject in 1994.

2.8 Summary

Powder characteristic and processing plays a major role in improving the mechanical properties of PM products. It is well established that better sintering results in improved physical and mechanical properties. Modification of the sintering cycle leads to achievement of rapid sintering, higher sintered densities and mechanical properties and also to lower sintering temperature, which is more acceptable in industry. High density and uniform microstructure both are linked with high mechanical properties of PM sintered steel. High density can be obtained in different ways; such as double press double sintering operations, hot powder forging, infiltration, or by liquid phase sintering. In the liquid phase sintering process, considerable quantities of additives are

required such as C, Si, Cu, B, etc. For the ultrahigh-carbon steels, C content is in the range of 1.0-2.1wt%, and UHCSs have tended to be neglected by industry due to their brittleness, resulting from the presence of a severe grain boundary carbide network. Traditional heat treatments used for normal steels create coarse microstructures and thus a spheroidisation treatment can produce fine spheroidised carbides in fine ferrite. Microcracking of the martensitic structure can occur during traditional heat treatments, and this microcracking is the result of impingement of growing martensite crystals against each other during transformation of austenite to martensite.

This work attempts to offer solutions to some of the problems of processing high carbon, high-density steels. Thermocalc modelling was used to predict the amount of densifying liquid phase for a range of alloys versus sintering temperature, in the range 1285 to 1300°C and 1.2 to 1.4 wt. %C. The water gas reaction forms CO gas in the early part of sintering and can lead to large porosity, which lowers mechanical properties. With the use of careful powder drying, low dew point atmospheres and optimisation of heating profiles, densities in excess of 7.5 g/cm^3 can readily be achieved. The brittle microstructure, containing carbide networks, is transformed by intelligent heat treatment to a tougher one of ferrite plus sub-micron spheroidised carbides. This gives the potential for production of components, which are both tough and suitable for sizing to improve dimensional tolerance.

Chapter Three

3 Experimental Procedure

3.1 Materials and Methods

3.1.1 Base-Powder

The base-powders used in this work were prealloyed Fe-0.85Mo (Hogänas Astaloy 85Mo-) and Fe-1.5Cr-0.2Mo (Hogänas Astaloy CrL). Table 3.1 below gives the specifications of these powders used in this work.

Table 3.1: Specifications of the base-powders (Astaloy 85Mo and Astaloy CrL) used in this work.

Name of Powder	Astaloy 85Mo	Astaloy CrL
Source	Höganäs	Höganäs
Apparent Density (g/cc)	2.9 - 3.10	~2.85
Green Density (g/cc), 600 MPa	7.05 - 7.18	7.15
Chemical Analysis (%by wt)	0.85% Mo, 0.03% O-total, and Fe balance	Fe-1.5%Cr+0.2Mo
Flow (Hall) s/50 g	24-30	~26
Particle shape	Irregular	Irregular
Sieve Analysis (microns µm)	150-250→12.3% 106-150→22.0% 75-106→25.1% 45-75→24.5% -45→16.1%	>145

Different particle shapes of the above powders are shown in Figure 3.1.

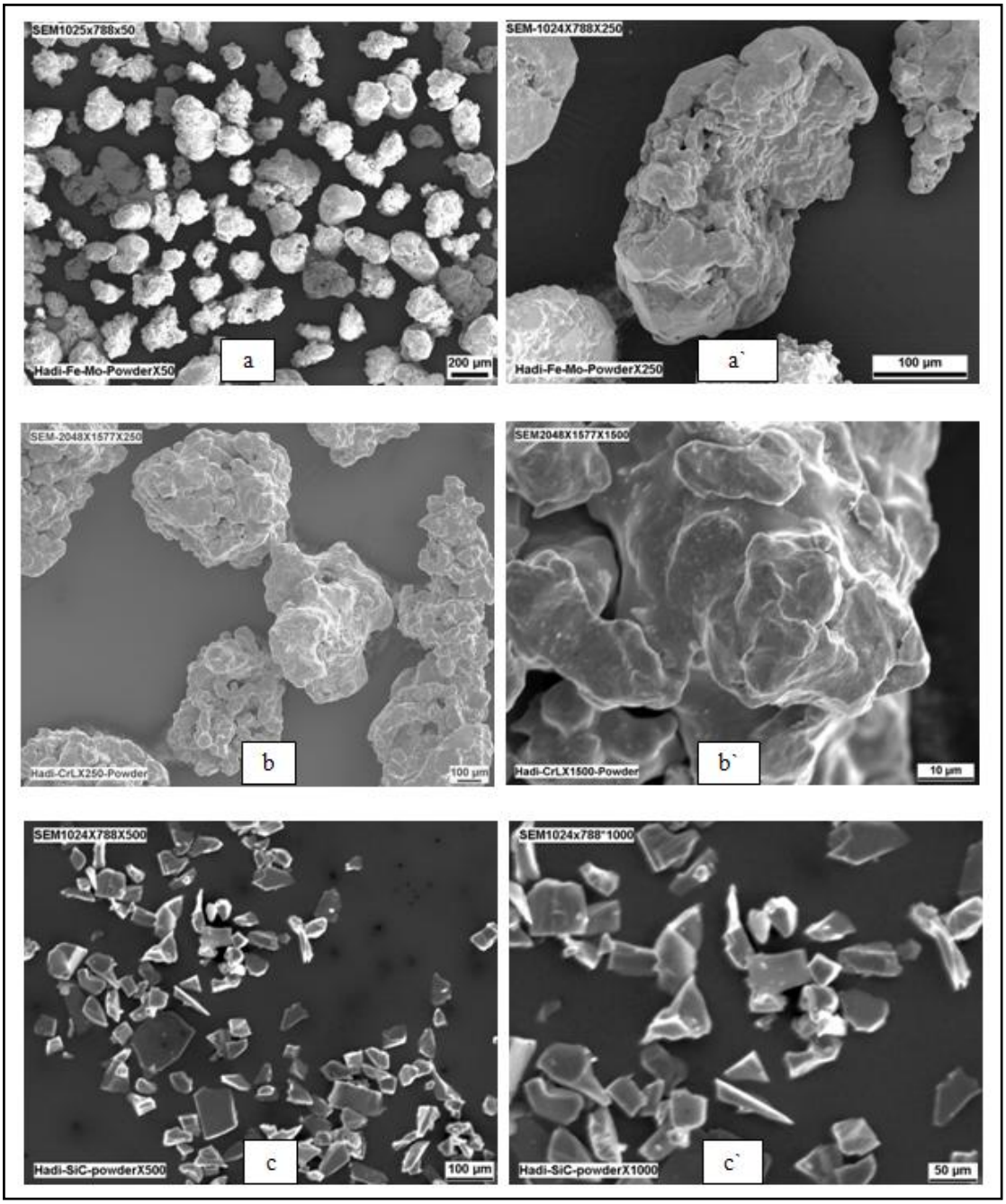
SEM1025x788x50
Hadi-Fe-Mo-PowderX50
a
200 µm
SEM-1024X788X250
Hadi-Fe-Mo-PowderX250
a`
100 µm
SEM-2048X1577X250
Hadi-CrLX250-Powder
b
100 µm
SEM2048X1577X1500
Hadi-CrLX1500-Powder
b`
10 µm
SEM1024X788X500
Hadi-SiC-powderX500
c
100 µm
SEM1024x788"1000
Hadi-SiC-powderX1000
c`
50 µm

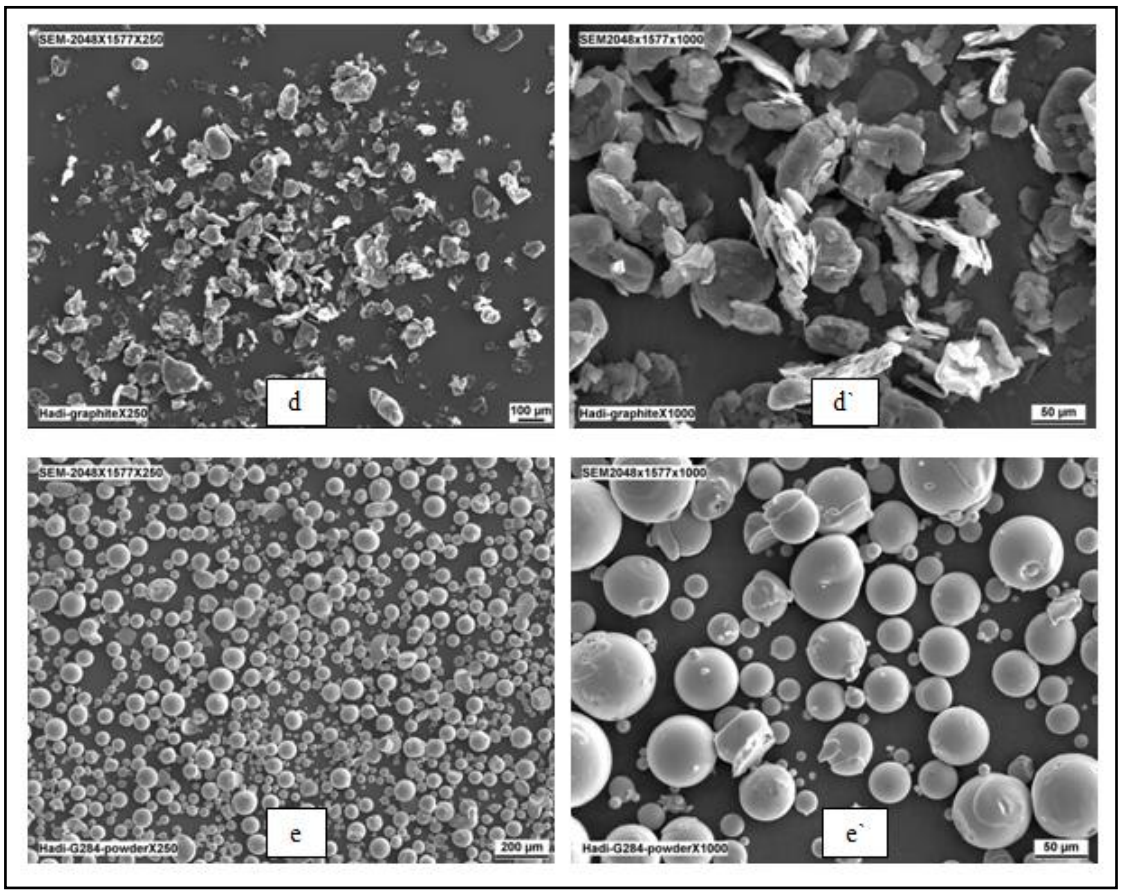

Figure 3.1: SEM micrographs of the starting powders used in the present work: (a) Astaloy 85Mo; (b) Astaloy CrL; (c), Silicon Carbide; (d) Graphite and (e) Master Alloy of G284 (Fe-35Mn-4.4C) powders.

3.1.2 Additive Powders

Three different types of powder additions were employed in this work. 1) Pure UF4 graphite of 99.8% purity, 2) Silicon carbide: Silicon has a high affinity for oxygen, therefore to minimise oxidation, it was introduced in the form of <9µm silicon carbide powder having a lower oxygen activity [96]. The selection of sintering atmosphere and temperature is very important for a silicon-containing alloy. To prevent oxidation, a low dewpoint atmosphere is essential and sintering should be carried out at temperature greater than 1200°C to relax redox conditions [73]. This alternative technique improves

the strength and ductility, prevents formation of oxide networks compared with use of pure, elemental silicon and also helps to limit the thickness of cementite networks [20, 42]. 3) The third addition used was manganese in the form of a gas atomised master alloy, G284, of composition Fe-35%Mn+4.4%C and <20μm particle size. Table 3.2 gives the specification of these powders.

Table 3.2: Specifications of the Additive Powders used in this work.

Powder	Graphite	Silicon Carbide	Ferro-Manganese
Manufacturer	Grafitwerk Kropfmuhl	Carborundum Company Ltd.	Atomising Systems Ltd. Sheffield, UK.
Particle size (μm)	3 μm (±1.5 μm)	~9 μm	Classified to <20μm
Apparent density (g/cc)	2.25	NA	NA
Chemical Composition (wt%)	99.8% pure	70%Si+30%C	Fe-35Mn-4.4C
Particle shape	Flake, Acicular	Angular	Spherical

3.1.3 Lubricants

Different types of lubricant were used in this work. Liquid Paraffin with density of 0.88 g/cc at concentration of 0.5cc/100g of powder was admixed into the base-powder using 20 min mixing time and a 3D Turbula mixer. Liquid paraffin is easily available and very common lubricant used at UOB. However, liquid paraffin is quite viscous and often more has to be added, to ensure coverage of the iron powder, than is optimum. Too much coverage can lead to distribution of the graphite into high concentration pools during pressing, which can lead to localized melting, porosity and severe distortion of sintered compacts. Polypropylene Glycol diluted with 0-75% of methanol was also used as a lubricant in order to decrease segregation, i.e. to guarantee that all the additive powders were ‘glued’ to the iron base powder. This mixture was then heated to 80ºC in a vacuum oven to boil off the methanol, leaving the powder with optimum coverage thus eliminating the segregation of graphite and ensuring that best densification would

be attained. Dry PTFE spray was used in this work to lubricate the die wall cavity and the faces of upper and lower punches in order to reduce the friction between powder particles and die walls and punch surfaces. It also lowers the ejection force, which eases removal of the green compact after pressing, prevents cracking, reduces die wear and prolongs die life. Acrawax was also used in different amounts as a dry powder lubricant but gave disappointing results (very poor densification), as reported by others [97].

3.2 Mixing Procedure

Homogenisation of the mixture was achieved by using the laboratory turbula powder mixer shown in Figure 3.2. Mixing time for each step was about 20 minutes and the mixing procedure, illustrated in Figure 3.3, was as follows:

- Mix the base-powder with silicon carbide for 20 min.
- Add Mn master alloy powder to the mixture and mix for 20 min.
- Add liquid paraffin to the mixture and mix for 20 min.
- Graphite is then added last to the mixture and mixed for 20 min.

Different powder mixtures were prepared for compaction, sintering and microstructural studies. These mixture compositions are given in Table 3.3.

Figure 3.3 shows the processing route of the mixing procedure of the base powder with the additives and different lubricants used in this work.

Figure 3.2: Laboratory 3-D Turbula Powder Mixer used in this work.

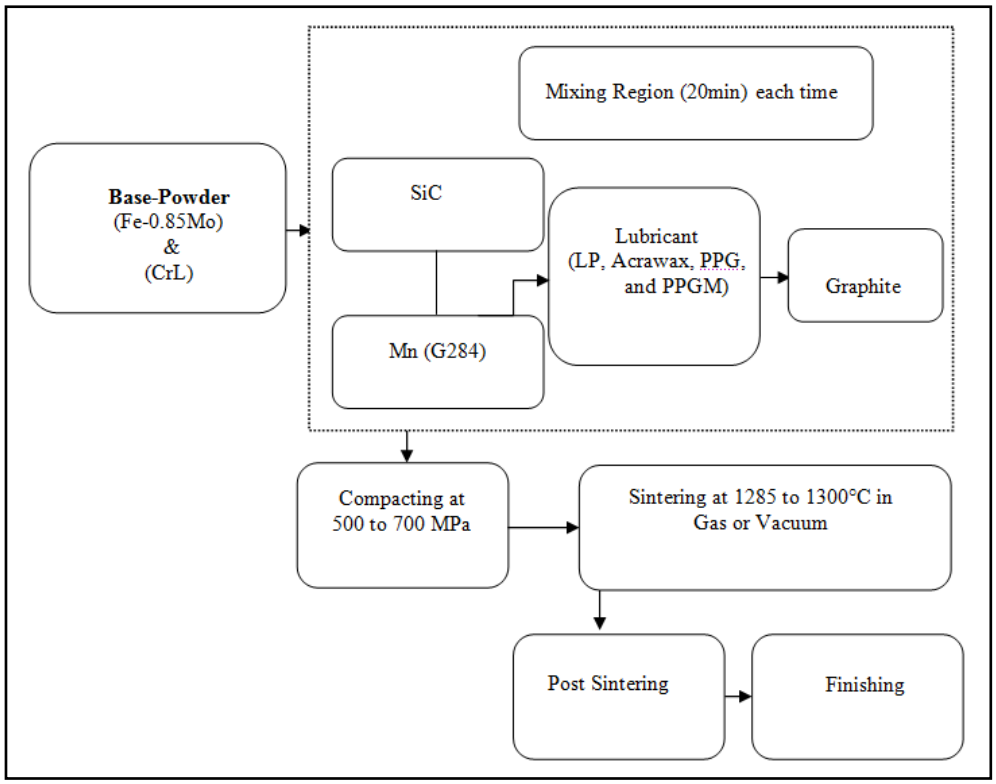

Figure 3.3 The mixing and processing procedure of the base powder with the additive elements and different lubricants used in this work.

Table 3.3 Chemical compositions (% by wt.) of powder mixtures used in this work.

No.	Composition
1	Fe-0.85Mo+1.2% C+0.4 -0.6% Si
2	Fe-0.85Mo+1.2% C+0.4 -0.6% Si+ LP or PPGM
3	Fe-0.85Mo+1.3% C+0.4 -0.6% Si
4	Fe-0.85Mo+1.3% C+0.4-0.6 % Si+ LP or PPGM
5	Fe-0.85Mo+1.4% C+0.4 -0.6% Si
6	Fe-0.85Mo+1.4% C+0.4 -0.6% Si+ LP or PPGM
7	Fe-0.85Mo+1.27% C+0.6 % Si +1.5% Mn+LP or PPGM
8	Fe-0.85Mo+1.3% C+0.65 % Si+1% Mn+LP or PPGM
9	Fe-0.85Mo+1.4% C+0.6 % Si+1.5%Mn+LP or PPGM
10	Fe-CrL+1.5%C+(0.5-0.65wt%)Si+PPGM
11	Fe-CrL+1.4%C+(0.65wt%)Si+PPGM

Where, LP ≡ liquid paraffin, and PPGM≡ Polypropylene Glycol diluted with methanol, in amount about 0.5 cc per 100g of powder mix.

3.3 Theoretical Alloy Design using ThermoCalc.

ThermoCalc TCW3 software was used to design and predict the proper alloy composition(s) and temperature(s) to create liquid phase during sintering, and thus improve sintered density as well as microstructure. Sintering temperature and carbon content are both critical parameters that affect the phase diagram applicable to furnace sintering. ThermoCalc software can be used in this manner to predict the solidus and liquidus windows, which can set the proper temperature for the chosen alloy and to have the correct amount of liquid phase during sintering, and hence obtain full sintered densities (i.e. Liquid phase > 20%) [6,22]. As an example, Figure 3.4 shows the typical equilibrium diagram calculated using ThermoCalc to predict the amount of liquid versus composition and temperature. The elliptical red area shows the region where the temperatures match the highest temperature used in normal industrial processing versus

carbon concentration with a fixed Si level. Many of these diagrams and calculations were made to produce data similar to those given in Table 3.4.

Table 3.4: Percentage liquid phase calculated using Thermo Calc TCW3 for various alloy compositions, with prealloyed Fe-0.85Mo, or Fe-CrL, as the base powders.

Base-Powder	Carbon wt. %	Silicon wt. %	Manganese wt. %	Temperature (ºC)	Liquid Phase %
Fe-0.85Mo	1.2	0.4	0.0	1285	3.16
	1.2	0.6	0.0	1285	5.78
	1.3	0.6	0.0	1285	10.80
	1.3	0.6	0.0	1295	15.27
	1.4	0.6	0.0	1285	18.10
	1.4	0.6	0.0	1295	20.80
	1.27	0.6	1.5	1300	18.80
	1.3	0.65	1.00	1300	20.00
	1.4	0.6	00	1300	22.00
	1.4	0.6	1.00	1300	25.20
Fe-1.5Cr+0.2Mo	1.4	0.65	00	1290	13.26
	1.4	0.65	00	1295	15.30
	1.4	0.65	00	1300	17.35
	1.5	0.65	00	1290	19.50
	1.5	0.65	00	1295	21.60
	1.5	0.5	00	1300	21.51
	1.5	0.55	00	1300	22.30
	1.5	0.6	00	1300	23.00
	1.5	0.65	00	1300	23.76

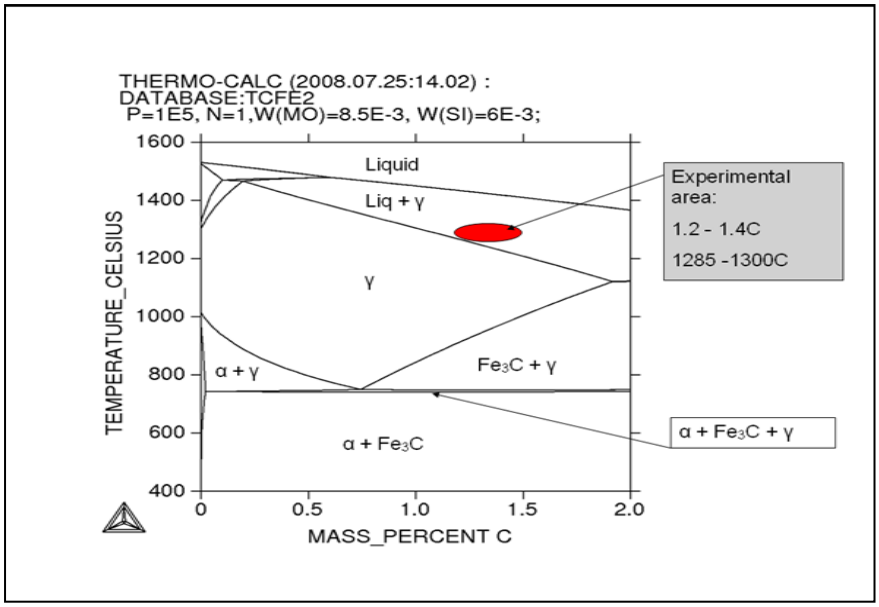

Figure 3.4: Predicted Phase Diagram via ThermoCalc obtained in this work for Fe-0.85Mo+1.2-1.4C+0.4Si.

The percentage liquid phases that can be obtained for each composition at various temperatures are given in Table 3.4 and therefore enabled the selection of the optimum sintering temperature for each alloy composition.

3.4 Compaction

A Churchill hydraulic press with 20 Ton capacity was used for compaction processes. Mixed powders were weighed precisely (7.00 g) for each compact and pressed in a die of dimension ~15.3mm square to produce ~4mm thick specimen. Die wall lubricant (Dry PTFE aerosol spray) was applied via a thin layer over the die wall cavity and the top of upper and lower punches in order to reduce the friction effects. Compaction pressure was applied by a manual hydraulic press in the range 500 to 700 MPa, followed by measurement of green density. Rectangular 3-point bend test specimens of dimension 33.5 mm × 4.5 mm × 5.5 mm, pressed at 600 MPa were also pressed. Dog-bone tensile test specimens of dimensions specified in ISO 2740, using spring floating die were produced by Denison pressing machine with capacity 100 Tons at 600MPa.

3.5 Sintering Furnace

Two different types of furnace were used to accomplish this work, gas and vacuum furnace. A standard Carbolite laboratory mullite-tube furnace, as seen in Figure 3.5 was modified to allow precise mixing of gases, using mass flow controllers, to maintain specific sintering atmospheres. The mixed gases are then passed through a drying column to maintain dewpoint <-60°C in order to minimise oxidation and reduce decarburisation. Temperature can exceed 1300°C in this furnace. Additionally, a ceramic-tube vacuum furnace (Figure 3.6), evacuated by an Edwards oil diffusion in

combination with a 2-stage rotary pump was used in this work. Heating, cooling and pressure curves can be obtained throughout the sintering cycle via a chart recorder attached to a Penning vacuum gauge and Pt-Rh thermocouple during the sintering process.

Figure 3.5: Laboratory gas sintering furnace.

Figure.3.6: Laboratory vacuum sintering furnace.

3.6 Sintering Operation

Green specimens (compacts pressed at 500 to 700MPa) of size ~15.3×15.3×4 mm^3 were sintered under both vacuum (~10^{-6} mbar) and dried Nitrogen/Hydrogen gas (< -60ºC dewpoint to meet the required specification without any oxidation). Sintering temperatures employed in this work were 1285, 1295 and 1300ºC, with sintering time of 30 or 60 minutes. Initially, heating rates (Figure 3.7) were 10ºC min^{-1} to 600ºC with a hold of 30 minutes for removal of liquid paraffin and adsorbed water and hydroxides, then 10ºC min^{-1} to 900ºC with a hold of 2 hours, to allow distribution of the carbon and silicon, followed by heating to the sintering temperature at 5ºC/min with sintering hold time of 30-60 minutes at temperatures varying from 1285 to 1300°C. After sintering, the specimens were allowed to cool slowly to room temperature.

Microstructural observations of initially sintered specimens showed excessive porosity. Figure 3.8 shows an alternative heating cycle which was performed in this work, replacing the previous one. Gas escape was hindered for the former process by very low carbon diffusion rates below 700ºC, so initial heating stage was changed to 900ºC, when the graphite would diffuse into the austenitic Fe-Mo, thus leading to creation of linked porosity to facilitate gas escape. This heating profile also reduced the time spent in the alpha phase where Fe-Fe self-diffusion is very high, then followed heating to 1100ºC with a hold of 2 hours to homogenise the added elements with the iron base powder. Heating profile sintering cycles are listed in Table 3.5. Furthermore, all samples sintered in the gas atmosphere furnace were sintered in a container steel box for all sintering temperatures in order to reduce decarburisation and improve deoxidation of the difficult elements, Mn and Si. This new procedure was originally introduced by Mitchell et al [50].

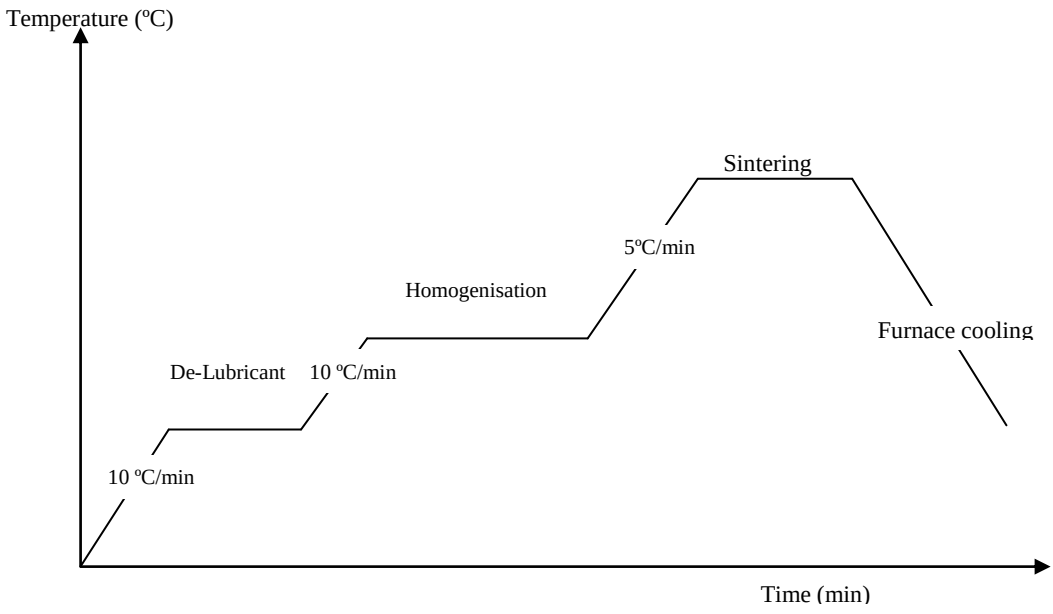

Figure 3.7: First heating cycle profile.

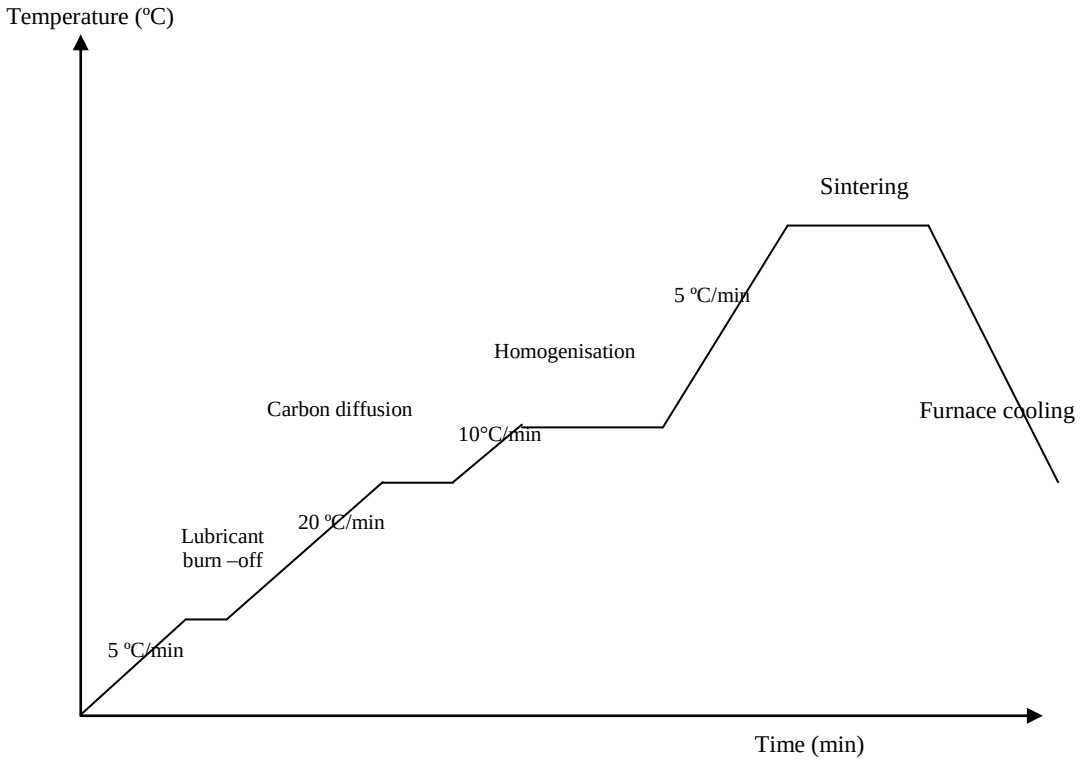

Figure 3.8: Second heating cycle Profile.

Table 3.5: Shows the types of heating sintering profile used in this work.

Sintering Cycles	R_{m1}	Lubricant Burn-off		R_{m2}	Carbon Diffusion		R_{m3}	Homogenization		R_{m4}	Sintering	
		T	t		T	t		T	t		T	t
Cycle 1	--	--	--	10	600	30	10	900	120	5	1285-1300	30-60
Cycle 2	--	--	--	10	730	30	10	900	120	5	1285-1300	30-60
Cycle 3	--	--	--	10	730	30	10	900	120	5	1285-1300	30-60
Cycle 4	5	450	15	20	900	15	10	1100	120	5	1285-1300	30-60
Gas-Atmospher	Pure N_2			($90N_2/H_2$)								
R_m-Ramp (°C/min) T-Temperature (ºC) t-Time (min)												

3.7 Calculation of Reduction of Metal Oxide

3.7.1 Gaseous Reduction

Alloying elements such as those used in this presented work e.g. Mn, Cr and Si are elements which have high oxygen affinity and tend to produce thermodynamically stable oxides. Oxides, present on powder particles as a very thin layer, obstruct diffusion during sintering and may inhibit the metallic bonding (neck growth) between particles and reduce liquid phase penetration. Consequently, the physical and mechanical properties of the final sintered products can be affected. Therefore, a protective atmosphere with low oxygen partial pressure is required to reduce these oxides [98]. Accordingly, consideration of the appropriate thermochemical reactions (combined action of admixed carbon and oxygen potential of sintering atmosphere) is essential to determine the correct choice of atmosphere for sintering of these ferrous PM alloys [50, 51].

3.7.2 Reactions occurring during sintering

During the sintering process, there were some processes that strongly affect the final properties of the final component, such as lubricant burn off, changing of particles' surface chemistry (oxides formation) and metallic bonding. All these processes may be enhanced or completed by reactions that take place during the sintering process; these reactions can be listed as follows:

- Reduction of oxides: involving H_2 and CO sintering atmosphere.
- Oxidation of metals: involving O_2, H_2O and CO_2 during sintering.
- Decarburising of steels: involving O_2, H_2O and CO_2.

- Carburising of steel: involving CO, CH_4, C_3H_8, C_4H_{10}.

Ellingham-Richardson diagrams illustrate graphically the relative stability of different oxides (e.g. FeO_2, Cr_2O_3, MnO and SiO_2) in contact with metals and the sintering atmosphere. From these graphs, the equilibrium dissociation temperature for metal and metal oxide can be easily determined, as shown in Figures 3.9-3.10, reducing by hydrogen atmosphere and solid carbon, respectively. Metals found towards the top of the Ellingham diagram have oxides which are unstable and easily reduced, whereas, moving down the diagram the oxides are more stable and harder to reduce. Also, it should be realised that metals can directly reduce the oxides of those metal oxides whose lines lie above it. Therefore, in this present work, SiO_2 is the hardest oxide to reduce but Si can act as a reducing agent for the other metal oxides lying above it in the Ellingham diagram. The reduction of metallic oxide will take place just when the partial pressure of oxygen in atmosphere is less than the partial pressure of oxygen of the oxide, i.e. oxygen dissociation:

$$p\,(O_2)^{\text{atmosphere}} < p\,(O_2)^{\text{oxide}} \quad (1)$$

Iron Oxide can be easily reduced by hydrogen atmosphere at temperature above ~500°C according to reaction (6) [99], when the $pH_2O/pH_2 \sim 10^{-1}$ and dewpoint +45°C, as seen in Figure 3.9, whereas, for Mn oxide it is very difficult to reduce by hydrogen atmosphere, as it requires temperature >1100°C, where the $pH_2O/pH_2 \sim 10^{-5}$ and dewpoint ~ -63°C which is very hard to achieve.

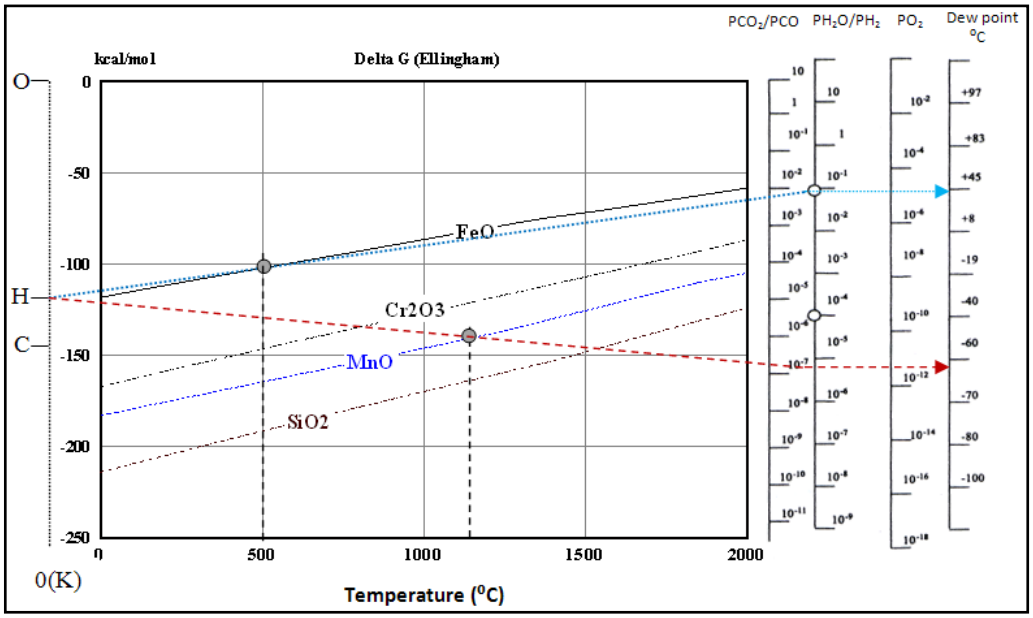

Figure 3.9: Ellingham diagrams of metal-metal oxides showing their equilibrium temperatures of 500 and 1140°C for reduction by H_2 atmosphere: refer to FeO and MnO respectively.

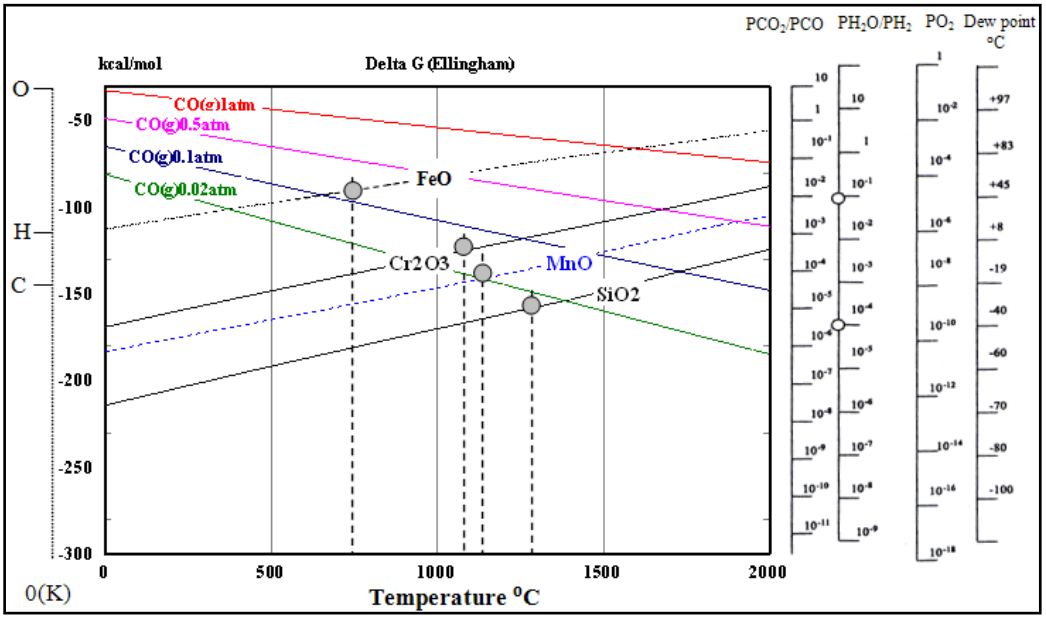

Figure 3.10: Ellingham diagrams of metal-metal oxides showing their equilibrium temperatures of 700, 1100, 1140 and 1300°C in CO atmosphere of differing partial pressures; refer to FeO, Cr_2O_3, MnO and SiO_2 respectively.

3.7.3 Reduction of oxides by solid carbon

There are some assumptions that should be taken into account such as:

Total pressure is ~1 atmosphere

Nitrogen is considered inert at the sintering temperature

If metal oxides such as FeO_2, MnO, Cr_2O_3, and SiO_2 are to be reduced by solid carbon, then the maximum pressure of active gases, that may be tolerated in the system can be calculated by consideration of free enthalpy changes, ΔG° , at absolute temperature 700°C (973.15K), 1250°C (1523.15K), 1400°C (1673.15K) and 1300C (1573.15K) for those metal oxides respectively, as shown in Figure 3.10,

Since:

$$\Delta G_T^\circ = \Delta H - T\Delta S \quad (2)$$

and

$$\Delta G_T^\circ = -RT\ln K_P, \quad (3)$$

Where, ΔH, ΔS, R and K_P are the enthalpy, entropy, gas constant and equilibrium constant, respectively.

For the reduction of those oxides by solid carbon (graphite) at chosen equilibrium temperature, the following reactions have to be considered:

$FeO = Fe + 0.5O_{2\,(g)}$ (4)
$FeO + C = Fe + CO_{(g)}$ (5)
$FeO + H_{2(g)} = Fe + H_2O_{\,(g)}$ (6)
$MnO = Mn + 0.5O_{2(g)}$ (7)
$MnO + C = Mn + CO_{(g)}$ (8)
$MnO + H_{2(g)} = Mn + H_2O_{\,(g)}$ (9)
$1/3Cr2O_3 = 2/3Cr + 0.5O_2$ (10)
$1/3Cr_2O_3 + C = 2/3Cr + CO_{\,(g)}$ (11)
$1/3Cr_2O_3 + H_{2(g)} = 2/3Cr + H_2O_{(g)}$ (12)
$SiC + 4MnO = MnSiO_3 + 3Mn + CO_{\,(g)}$ (13)

$SiO_2 + C = Si + CO_{2\,(g)}$ (14)
and
$C + O_{2(g)} = CO_{2\,(g)}$ (15)
$2C + O_{2\,(g)} = 2CO_{\,(g)}$ (16)
$2CO_{\,(g} + O_{2\,(g} = 2CO_{2\,(g)}$ (17)
$C + CO_{2\,(g)} = 2CO_{\,(g)}$ from ~700C° Boudouard reaction (18)
$C + H_2O_{\,(g)} = CO_{\,(g)} + H_{2\,(g)}$ at ~500°C water gas shift reaction (19)

Iron Oxide is very ease to reduce, and by considering reduction temperature of ~740°C. The HSC Chemistry 5.11, computer software, was used to calculate the partial pressure of O_2, CO, CO_2, CO/CO_2, H_2O, H_2 and H_2/H_2O, as follows:

If the reaction is considered to be as in equation 4, combined with equation 3, where $\Delta G_T^{o} = -R.T\ln K_P$ = 47376 calories, thus:

$K_p = p(O_2)^{1/2} \rightarrow pO_2 = (K_P)^2 = 3.63E^{-21}$atm

Then the partial pressure of CO can be calculated from equation 5, since ΔG_T^{o} = -772.0 calories, then:

$K_{P(eq.5)} = pCO \quad \rightarrow \quad pCO = (K_P) = 1.47$atm

CO is in equilibrium with C and CO_2, the partial pressure of CO_2 can be obtained from equation 18, (Boudouard reaction), ΔG_T^{o} = -1680.0 calories, then:

$K_{P(eq.18)} = \frac{p(CO)^2}{p(CO_2)} \quad \rightarrow \quad p(CO_2) = \frac{p(CO)^2}{K_P} = 1.275$atm,

These results show that Fe-C-O system, at 740°C to be in equilibrium with gases atmosphere, then the composition of atmosphere must be:

$pCO = 1.47$atm

$pCO_2 = 1.275$atm, thus $p(CO_2)/p(CO) = 0.867$

$pO_2 = 3.63E^{-21}$atm, or even less.

The reduction would proceed providing the total pressure of the reactive gases is less than 1.47+1.275=2.745atm,

Water-gas reaction needs to be taken in consideration as well:

From equations 6 and 19, since where ΔG_T^o=-2257calories: $p(H_2)$=1atm,

since: $K_P = \frac{p(H_2).P(CO)}{p(H_2O)} \rightarrow p(H_2O) = \frac{p(H_2).p(CO)}{K_P}$ = 0.478atm,

and, $\frac{p(H_2O)}{p(H_2)} = 0.478$, (Dewpoint~+62°C)

since: gas atmosphere is $90N_2/10H_2$, then, $\frac{P(H_2O)}{P(H_2)} = 4.97$ (Dewpoint~+90°C)

Both, water-gas and Boudouard reactions, are improving the dewpoint, thus metal oxide dissociation would occur at the chosen temperature.

Reduction of Cr_2O_3, MnO and SiO_2, data are calculated in a similar manner to FeO method performed previously. Table 3.6 presents atmosphere composition partial pressures of metal-metal oxide at different chosen temperature, in $90N_2/10H_2$ gas atmosphere.

Table 3.6: Required composition of sintering atmosphere to reduce the metal oxide of Cr_2O_3, MnO and SiO_2, at 1100, 1140 and 1300C, respectively, in $90N_2/10H_2$ sintering atmosphere.

M-Oxide	T(°C)	pO_2	pCO	pCO_2	pCO_2/pCO	pH_2O	pH_2O/pH_2	Dewpoint °C
Cr_2O_3	1100	$1.84E^{-20}$	0.0979	$2.17E^{-5}$	$2.22E^{-4}$	$4.68E^{-4}$	$4.68E^{-3}$	-32
MnO	1140	$1.85E^{-21}$	0.0234	$8.213E^{-7}$	$3.51E^{-5}$	$8.0E^{-5}$	$8.00E^{-4}$	-65
SiO_2	1300	$1.021E^{-21}$	0.00639	$2.93E^{-8}$	$4.59\ E^{-6}$	$6.79E^{-6}$	$6.79E^{-5}$	-77

From the Ellingham diagram Figure 3.10, it can be seen that the SiO_2 line lies at the bottom showing that SiO_2 is very difficult to reduce. Another thing to note is that Mn vapour will start to evolve at 740ºC [50], and react with O_2 and any water vapour to form MnO. This will then be followed by reaction of any undiffused SiC to reduce MnO formed during the heating part of the sintering cycle beginning at ~1175ºC, i.e. the point at which ΔG becomes negative for the reaction $SiC+3MnO=SiO_2+3Mn+CO(g)$. This explains why SiO_2 or perhaps more complex $MnSiO_3$ [according to $SiC+4MnO=MnSiO_3+3Mn+CO(g)$] particles have been seen in some sintered specimens. These oxides are stable as they cannot be reduced during sintering under normal atmosphere conditions even at high sintering temperature ~1300ºC. However, there is no doubt that some of Si has gone into solution in the Fe matrix as seen during sinter quench experiments where SiC is beginning to dissociate at ~900-1000ºC.

3.8 Density and Volume Change Measurements

Green densities were calculated physically from weight and dimensional measurements of the specimen. The dimensions, i.e. height, width and length were measured using a micrometer with ±0.005mm accuracy, whereas, a Sartorius balance with ±0.0005g accuracy was used to measure the weight.

Archimedes' method (water displacement technique) was used to determine the sintered densities of the specimens, which were coated with a cellulose lacquer to prevent water penetration to the pores, and then calculated as follows:

$$Sintered\ density = \frac{W_a}{(W_{la} - W_{lw}) - (\frac{W_{la} - W_a}{\rho_l})} \quad \ldots\ldots\ldots\ldots\ldots\ldots\ldots\ldots\ldots\ldots\ldots\ldots \quad 3.1$$

Where W_a is the weight of the specimen in air, W_{la} is the weight of the specimen coated with lacquer and weighed in air, W_{lw} is the weight of the lacquered specimen whilst suspended in water, and ρ_l is the density of the lacquer.

Furthermore, theoretical density, ρ_{th}, for the elements of the alloy composition without any sintering aids, was calculated as follows:

$$\rho_{th} = \frac{1(g)}{\sum_{i=1}^{n} \frac{wt_i}{\rho_{thi}}} \quad \text{.....3.2}$$

ρ_{thi}, $w_{thi,}$ are theoretical density and weight in gram of element, respectively, n is the number of the elements in the alloy.

In addition, volume changes for the sintered specimens were also calculated from the volumetric changes between the green and sintered specimens as follows:

$$\text{Volume change}\% = \frac{(\text{Green volume} - \text{As sintered volume})}{\text{Green volume}} \quad \text{.....3.3}$$

Positive value indicates shrinkage, and vice-versa indicates expansion. Volume change also leads to determine the densification (ψ), which refers to the degree of shrinkage or expansion using the following formula:

$$\psi = \frac{\rho_s - \rho_g}{\rho_{th} - \rho_g} \quad \text{..... 3.4}$$

where, ρ_s, ρ_g and ρ_{th} are the sintered, green, and theoretical densities, respectively. Positive results of ψ refer to shrinkage.

3.9 Heat Treatment

A muffle furnace was used for heat treatment of all the sintered samples. Samples were austenitised at temperature 970 ºC for 2 hrs (under flowing argon atmosphere) to ensure all carbides were in solution and oxidation was minimised. This was followed by oil quenching or air cooling which resulted in some microcracking. To avoid this micro-cracking an isothermal quench to MS-10% temperature, ~125-130ºC, into a preheated fan assisted oven proved necessary, for ~20-40 minutes, note that compositions containing Mn, the MS-10% temperature, ~180-185ºC. The crack-free hardened specimens were then given a standard spheroidising treatment by heating to 750 ºC and holding for 3 hrs under argon atmosphere, and then cooled slowly to room temperature to produce a ferrite plus sub-micron carbide structure, soft enough to allow a modest amount of resizing for dimensional control purposes.

3.10 Characterisation of Microstructures

3.10.1 Metallography

Sintering and heat treated samples were mounted in electrically conducting Bakelite (polymeric thermo-plastic resin) using a Struers Cito Press-1 mounting machine, followed by grinding on silicon carbide papers under flowing water, moving gradually from coarse paper of 120 grit to the finest of 1200 grit, followed by polishing on rotating selvyt-cloths using 6µm and 1µm diamond paste. All the samples were etched in 2 or 5% of Nital (nitric acid in alcohol) or Nital/Picral (nitric plus picric acid in alcohol) solutions, in order to reveal grain boundaries and microstructure, followed by

microstructural examinations of the alloys carried out by both Optical and Scanning Electron Microscopy (SEM).

Optical Microscopical analysis of the alloys was done on a MeF3 optical light microscope and images were taken on a Leica DC300 digital camera connected to Leica IM 1000 database and image analysis software. Recorded were general observations of the microstructure and common defects such as porosity content, pore shape, size and distribution, as well as the phases. Scanning electron microscopy (SEM) was performed, using a JEOL-JSM 6400 instrument equipped with a Kevex Sigma-3 Energy Dispersive X-ray (EDX) microanalyser, on selected areas of particular microstructural and microanalytical interest. This enabled the acquisition of more detailed information such as chemical micro-analysis of phases within the specimen and important dimensional measurements such as grain size, carbide particle diameter or length, etc.

3.10.2 Quantitative Image Analysis

Quantitative image analysis was performed using University of Texas Image Tool based Software to determine the metallurgical quality and repeatability by evaluation of grain size, pore shape and measurement of the area fraction of any phase. Evaluation of fracture surfaces was performed to determine the fracture type, i.e. brittle fracture or ductile fracture, and the starting of the fracture point, as well as the cause of fracture. This analysis can be performed by thresholding, based on grey level, of an image to produce binary (2-bit) images where the features of interest are black and the rest of the image becomes white. The images were taken from either optical microscope (OM) or scanning electron microscope (SEM).

3.10.3 Hardness and Microhardness

One of the microstructural properties which can be categorised is microhardness. It is well known that the hardness in general is defined as material resistance to plastic deformation such as scratching, cutting, bending, abrasion and penetration. Macrohardness (apparent hardness) and microhardness both were measured in this work by Vickers hardness in different loads ranging from 5 to 30kg (macrohardness) and 1 to 100g (microhardness). Vickers hardness value can be obtained when dividing the applied load (kgf) by surface area of the indentation (mm^2). If the indentation is large enough to contain all microstructural features to give general apparent hardness, the hardness number should be the same when the applied load is higher than 10kgf. This means that the apparent hardness is independent of the applied load and constant of the bulk material. Diagonal of the indentation (d) is proportional to the applied load P as follows:

$$d = \left(P/a\right)^{1/2} \quad \text{.....3.5}$$

where 'a' is the materials constant value under test (Kick's law) [113].

In contrast, microhardness is dependent on the applied load because the indentation is very tiny in comparison with individual microstructural phases and porosity; in this case Kick's law is replaced by Meyer's law, as follows [114]:

$$d = \left(P/a\right)^{1/n} \quad \text{.....3.6}$$

'n' represents Meyer's exponent, and is a constant for the material under test.

The surface area of the indentation can be obtained as follows:

$$A = \frac{\frac{1}{2}d^2}{\sin(136^\circ/2)} \quad \text{.....3.7}$$

Then Vickers Hardness Number (HV) is obtained as follows:

$HV=1854.4P/d^2$, kgf/mm^2 .....3.8

HV for microhardness can be calculated using equation 3.8 by knowing the load (*P*) in grams and diagonal of the indentation (*d*) in μm.

Apparent hardness and microhardness were determined on samples which were mounted, polished and etched. Used were, with three measurements taken for each specimen: for macrohardness - a standard Vickers machine with a 10kgf load, and for microhardness - a Reichert microhardness tester (attached to a Reichert optical microscope type MeF) using various loads up to 100 gf.

3.11 Mechanical Testing

Mechanical properties were evaluated by measuring the yield and (ultimate) tensile strengths, bend strength, and % elongation to failure. ISO 2740 tensile specimens were uniaxially tested on an Instron 1195 SM219 machine at a crosshead speed of 0.5mm/min. Three-point bend test was performed to evaluate the transverse rupture strength (TRS) using specimens of rectangular beam cross section according to ASTM standard B528-76 [100, 101]. The jig for this test was designed and made at the University of Bradford and fitted to a J.J. Lloyd tensile testing machine, which has a maximum load 50kN. If force is applied uniformly transversely at halfway between the supports of the test piece (Figure 3.11) and elastic (brittle) [42] behaviour is assumed, TRS evaluates to:

$$TRS = \frac{3PL}{2bh^2} \quad \text{3.5}$$

where P = [failure] load, L = span (25.4mm), b= specimen width, and h= specimen depth. The crosshead speed was 0.5mm/min. For ductile specimens the same formula can be used to evaluate the yield stress in bending with the load now relating to the end of elastic behaviour.

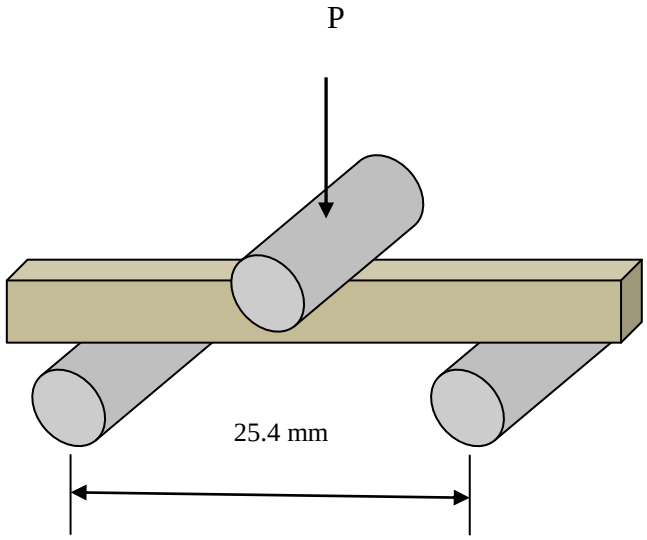

Figure 3.11: Schematic View of Three-Point Bending Test.

3.12 Warm Forging

Rings with outside and inside diameter 30 and 10 mm, respectively, and height 26.5 mm were pressed at 550 MPa to give green densities of ~ 6.8 g/cc. Sintering of Fe-1.4C-0.6Si-0.85Mo at 1300°C was carried out for 1 hr in nearly full semi-closed steel containers pushed into a mullite tube furnace in nitrogen plus 10% hydrogen, with a gas flow of ~500 cm^3 min^{-1} and an inlet dew point no worse than -60°C. The rings were cooled slowly from the sintering temperature, austenitised at 950°C for 1 hour, then

quenched into a warm fan assisted oven at ~130°C, followed by air cooling and refrigeration. They were then spheroidised at 750°C for 3 hours, slow cooled to room temperature, to give densities of ~7.2 g/cc and grain sizes of ~ 30 μm.

Two types of forging experiments were subsequently carried out for spheroidised specimens of dried Höganäs Astaloy Mo85 which was used as the base iron-molybdenum powder, 0.6% silicon was introduced as fine <9μm silicon carbide, and 1.4% carbon as fine graphite (of 99.5% purity), sintered densities were in range the 7.1-7.15g/cm^3 . In the first set of experiments, a specimen was heated up to 700°C then hit with one forging strike while a second specimen was heated to 700°C then struck once followed by re-heating to 750°C and struck once again. These warm forging experiments were conducted in Poland at The University of Mining & Metallurgy, Krakow, (courtesy of Prof. Stefan Sczepanik).

The second set of experiments was carried out on cylinders of 8 mm diameter and 12 mm in height (cut from the original rings) using a Gleeble HDV-40 machine at TUBA, Freiburg. The specimens were heated in argon to 700°C and then forged at strain rates of 10^{-3}, 10^{-2}, 10^{-1} and 1 sec^{-1} to (recorded) ~ 1.15 natural (logarithmic) strains. The deformation possible at quite modest pressure (150MPa) and temperature (700°C) is enormous without any cracking. The original 12mm height samples were squeezed to ~3mm with the lowest strain rate 0.001 samples compressing the most. A laboratory test jig has been fabricated at UOB in order for diametral compression tests to be carried out to determine the yield strength of the forged material, as seen In Figure 3.12.

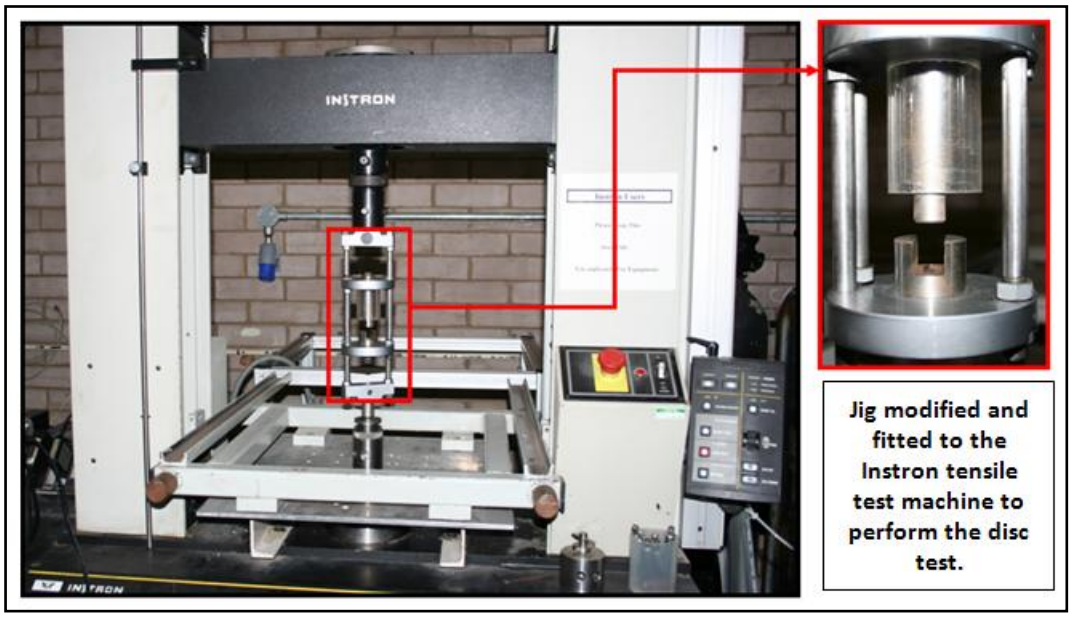

Figure 3.12: Jig for diametral compression tests.

Chapter Four

4 Results and brief discussion

4.1 Green Densities

Green densities for different compositions of Fe-0.85Mo + (1.2, 1.3 and 1.4 wt %) C + (0.4 and 0.6 wt %) Si+ (1 or 1.5 wt %) Mn and pre-alloy composition of CrL plus (1.4-1.5 wt%)C and (0.5-0.65wt%)Si, mixed either with or without lubricant (liquid paraffin, polypropylene glycol diluted with 0-75% methanol, dry PTFE spray, and Acrawax) depended on parameters such as alloy composition (Table 3.3) and compaction pressure (from 500 to 700 MPa). Table 4.1 gives the green densities for different compositions based on powder Fe-0.85Mo (Hogänas Astaloy 85Mo) pressed at 600 MPa. Green densities decreased with an increase in silicon and carbon contents, but increased with increase in compaction pressure, as seen in Figures 4.1 and 4.2, respectively, in agreement with [74, 102]. Manganese appears to have an opposite effect on green densities to that of Si and C. This is perhaps because the Mn particles are from master alloy which is spherical powder and does not perfectly fill the small pores between base powder particles, thus green density decreases. Figure 4.1 clearly reveals that dry lubricant produces higher green density than liquid lubricant, but powder lubricant Acrawax always gave low green densities.

Table 4.2 shows the green densities for different compositions based on powder CrL, pressed at 600 MPa. It clearly reveals that the green densities decrease with increasing carbon and silicon contents. These results are comparable to Fe-0.85Mo compositions.

No	Composition		Green Density (g/cm^3) ±0.05					
			Type of Lubricant					
		Dry	LP	PPG 0%M	PPG 25%M	PPG 50%M	PPG 75%M	Acrawax
1	Fe-0.85Mo+1.2 C+0.4 Si	6.99	6.96	--	--	--	--	--
2	Fe-0.85Mo+1.2C+0.6Si	6.95	6.93	--	--	--	--	--
3	Fe-0.85Mo+1.3C+0.4 Si	6.96	6.91	--	--	--	--	--
4	Fe-0.85Mo+1.3C+0.6Si	6.92	6.89	--	--	--	--	--
5	Fe-0.85Mo+1.35C+0.4Si	6.93	6.88				--	
6	Fe-0.85Mo+1.35C+0.6Si	6.89	6.86	6.91	6.93	6.94	6.92	6.87
7	Fe-0.85Mo+1.4 C+0.4Si	6.88	6.83	6.89	6.91	6.93	6.90	6.84
8	Fe-0.85Mo+1.4C+0.6Si	6.86	6.82	6.88	6.90	6.92	6.89	6.82
9	Fe-0.85Mo+1.27C+0.6Si +1.5Mn	6.83	6.80	--	--	--	--	--
10	Fe-0.85Mo+1.3C+0.65 Si +1 Mn	6.78	6.76	--	--	6.81	--	--
11	Fe-0.85Mo+1.35 C+0.6 Si+1Mn	6.74	6.71	--	--	--	--	--

Table 4. 1 Green densities of different alloy compositions based on Hogänas Astaloy 85Mo, pressed at 600 MPa.

LP = liquid paraffin, PPG = polypropylene glycol, M = methanol.

Table 4. 2 Green densities of different alloy compositions based on Hogänas Astaloy CrL, mixed with polypropylene glycol diluted with 50% methanol, and pressed at 600 MPa.

No	Composition	Green Density (g/cm^3) ±0.02
1	Fe-1.5Cr+1.4 C+0.65 Si	6.89
2	Fe-1.5Cr+1.5C+0.50 Si	6.86
3	Fe-1.5Cr+1.5 C+0.55 Si	6.84
4	Fe-1.5Cr+1.5 C+0.60 Si	6.82
5	Fe-1.5Cr+1.5 C+0.65 Si	6.80

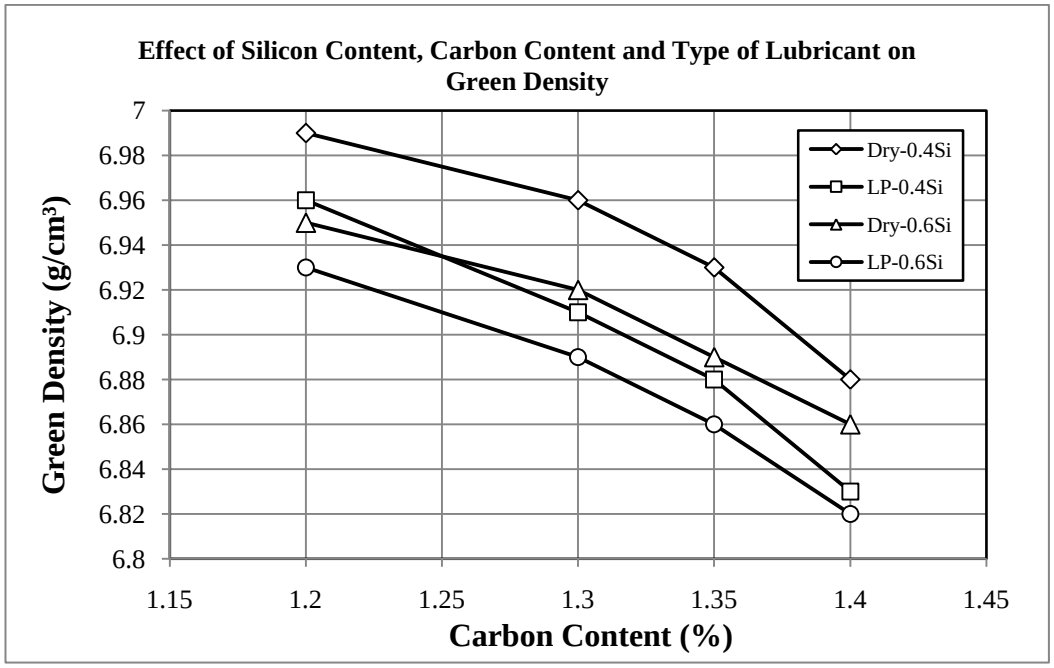

Figure 4.1:Effect of silicon content, carbon content and lubricant type on Fe-0.85Mo+ (1.2-1.4)C+0.6Si.

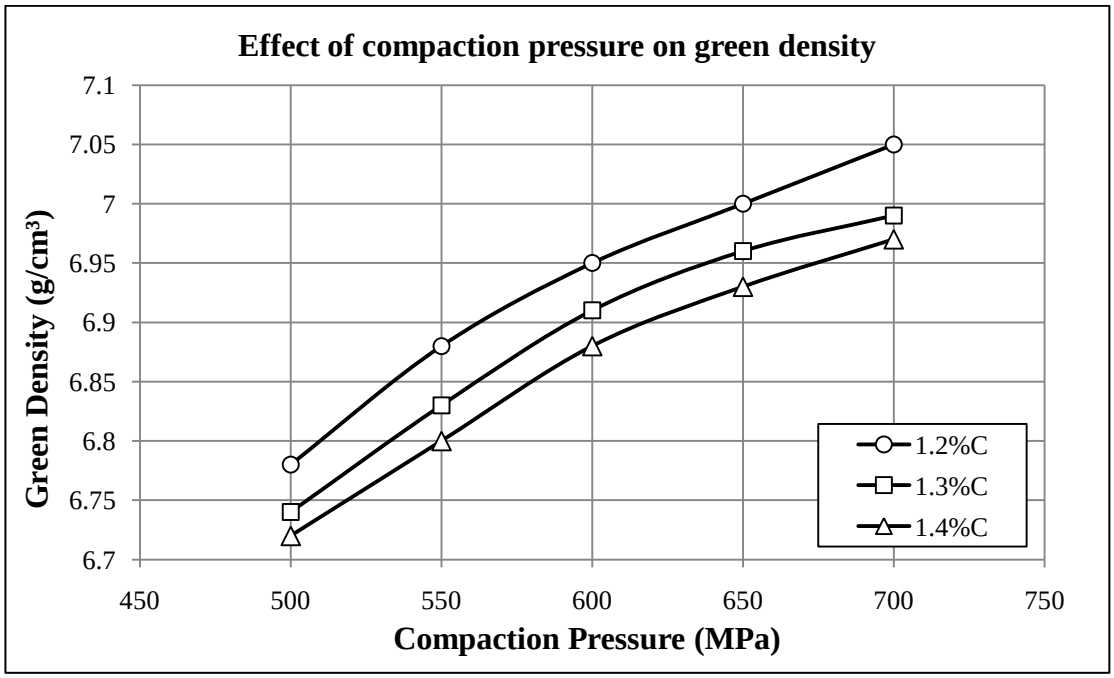

Figure 4.2: Effect of compaction pressure on green density of Fe-0.85Mo+0.6Si+ (1.2-1.3-1.4)C.

4.2 Sintered Densities

Densities for specimens based on powder Fe-0.85Mo and sintered at different temperatures and times using vacuum and gas atmosphere are listed in Table 4.3. For the initial heating cycle, specimens sintered under vacuum produced higher densities, with smaller pores and finer microstructures, than those sintered in gas atmosphere. Table 4.3 shows the sintered densities for different heating sintering cycles for alloy compositions based on powder Fe-0.85Mo (Hogänas Astaloy 85Mo). Sintering temperature played an important role, e.g. for Fe-0.85Mo+1.4C+0.6Si (0.5cc liquid paraffin) sintered in vacuo for 30 min at 1285 and 1295°C the sintered densities were7.26 and 7.43g/cm^3 respectively. Table 4.3 also shows the effect of sintering time improving the sintered density, e.g. for Fe-0.85Mo+0.65Si+1.3C+1.0Mn+(0.5cc liquid paraffin) pressed at 600 MPa, sintered in vacuo at 1300ºC it was ~ 7.32 g/cm^3 for a sintering time of 30 min, and ~ 7.44 g/ cm^3 for 60 min. Carbon and silicon contents are positive parameters for increasing the sintered densities, as seen in Figures 4.3-4.5. In contrast, sintered densities decrease with adding manganese, e.g. sintered density of Fe-0.85Mo+1.35C+0.6 Si (+0.5cc polypropylene glycol/methanol) alloy gas sintered at 1300°C for 1 hour is ~ 7.64 g/cc, and 7.56 g/cc when adding just 1wt%Mn. Acrawax lubricant resulted in very poor densification, nonuniform microstructure and interconnected pores, in agreement with [97].

Table 4.3: Sintered densities of alloys based on Fe-0.85Mo pressed at 600MPa.

No.	Composition	ST °C	St min	Sintered Density (g/ cm^3)						
				1st heating cycle				2nd heating cycle		
				Dry Wall Lub.		0.5 cc Liquid Paraffin		Dry Lub	LP	PPGM 50%
				Vac	Gas	Vac	Gas			
1	Fe-0.85Mo+1.2C+0.4Si	1285	30	7.07	6.97	7.04	6.95	--	--	--
		1295	30	7.08	7.07	7.05	7.03	--	--	--
		1300	30	--	--	--	--	--	7.2	7.25
2	Fe-0.85Mo+1.2C+0.6Si	1285	30	6.99	6.96	7.04	7.04	--	---	--
		1295	30	7.03	7.05	7.02	7.03	--	--	--
		1300	30	--	--	--	--	--	7.25	7.31
3	Fe-0.85Mo+1.3C+0.4Si	1285	30	7.17	7.13	7.2	7.04	--	--	--
		1295	30	7.12	7.11	7.2	7.11	--	--	--
		1300	30	--	--	--	--	--	7.35	7.4
4	Fe-0.85Mo+1.3C+0.6 Si	1285	30	7.03	7.08	7.14	7.07	--	--	--
		1295	30	7.22	7.10	7.16	7.15	--	--	--
		1300	60	--	--	--	--	7.30	7.5	7.54
5	Fe-0.85Mo+1.4C+0.4Si	1285	30	7.1	7.1	7.2	7.14	--	--	--
		1295	30	7.35	7.1	7.42	7.16	--	--	--
		1300	30	--	--	--	--	--	7.55	7.58
6	Fe-0.85Mo+1.4C+0.6Si	1285	30	7.27	7.3	7.26	7.18	--	--	--
		1295	30	7.44	7.3	7.43	7.4	--	--	--
		1300	30	7.46	7.36	7.50	7.42			
		1300	60	7.45	7.4	7.55	7.5	7.65	7.71	7.75
7	Fe-0.85Mo+1.35C+0.6Si	1300	60	7.4	7.3	7.43	7.4	7.52	7.62	7.64
8	Fe-0.85Mo+1.375C+0.6Si	1300	60	--	--	7.43	7.46	--	7.66	7.69
9	Fe-0.85Mo+1.27C+0.6Si+1.5Mn	1300	30	--	--	7.28	7.25	--		
		1300	60	--	--	7.35	7.3		7.4	7.42
10	Fe-0.85Mo+1.3C+0.65Si+ 1Mn	1300	30	--	--	7.32	7.33	--	--	--
		1300	60	--	--	7.44	7.4	--	7.42	7.47
11	Fe-0.85Mo+1.35C+0.6Si+ 1Mn	1300	60	7.42	7.4	7.47	7.44	--	7.5	7.56

ST ≡ Sintering Temperature, St ≡ Sintering time, LP ≡ Liquid Paraffin
PPGM ≡ Polypropylene glycol diluted with methanol, 1st Cycle ≡ Sintering in vacuum and $90N_2/10H_2$ gas atmosphere, 2nd Cycle ≡ Sintering in $90N_2/10H_2$ gas atmosphere

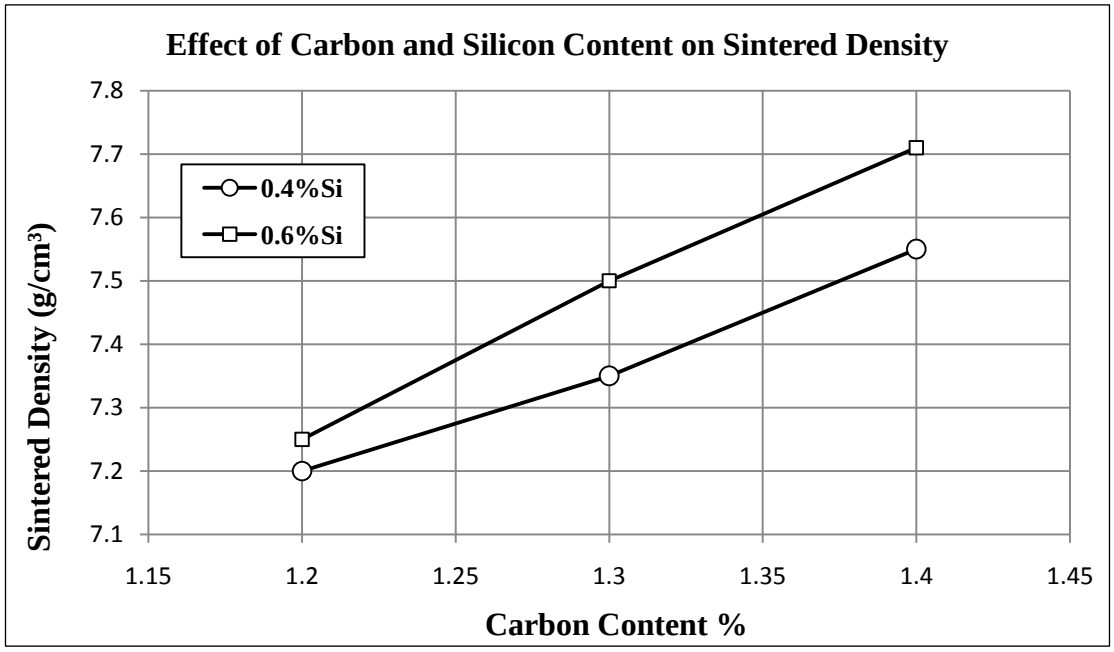

Figure 4.3: Variation in sintered density with carbon and silicon content for various carbon content of Fe-0.85Mo+(0.4-0.6 wt%) Si alloy composition with and without liquid paraffin sintered at 1300ºC for 60 min.

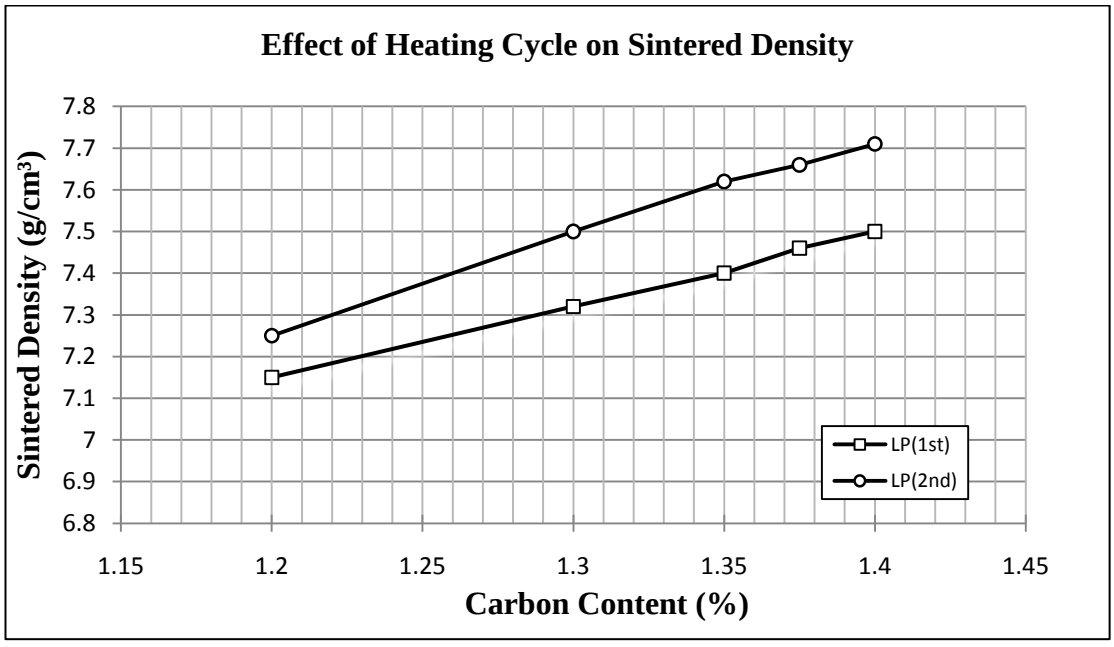

Figure 4.4: Variation in sintered density with heating cycle for Fe-0.85Mo+0.6Si+(1.2-1.4)C, sintered in 90N2/10H2 at 1300°C for 60 min.

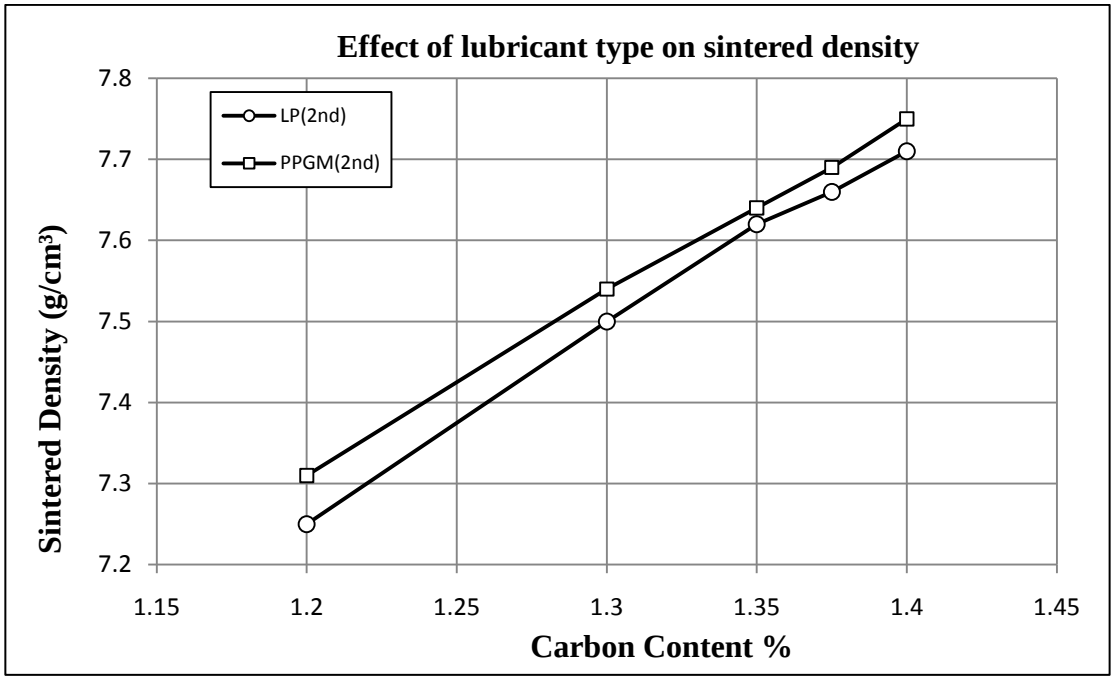

Figure 4.5: Variation in sintered density with lubricant for Fe-0.85Mo+0.6Si+ (1.2-1.4)C mixed either with LP or PPGM , sintered in 90N2/10H2 at 1300°C for 60 min. LP = liquid paraffin, PPG = polypropylene glycol, M = methanol.

Table 4.4 shows the sintered densities for compositions based on powder CrL (Hogänas Astaloy CrL) sintered at 1295 and 1300°C for one hour using the second cycle under $90N_2/10H_2$ gas atmosphere.

Table 4. 4 Sintered densities of different alloy compositions of CrL, mixed with polypropylene glycol mixed with 50% methanol, SD= sintered density.

No	Composition	Sint. Time (min)	SD(g/cm^3), Pure N_2,	SD (g/cm^3), $90N_2/10H_2$ at different Sintd. Temp.		SD (g/cm^3), $25N_2/75H_2$,
			1300°C	1295°C	1300°C	1300°C
1	Fe-1.5Cr+1.4 C+0.65 Si	60	6.84	7.3	7.45	6.98
2	Fe-1.5Cr+1.5C+0.5 Si	60	6.85	7.41	7.51	7.10
3	Fe-1.5Cr+1.5 C+0.55 Si	60	6.89	7.43	7.54	7.15
4	Fe-1.5Cr+1.5 C+0.6 Si	60	6.89	7.47	7.56	7.20
5	Fe-1.5Cr+1.5 C+0.65 Si	60	7.10	7.5	7.57	7.22

4.3 Metallographic Preparation

Sintered samples were sectioned, ground and polished conventionally with a 1 µm final surface finish. The polished specimens were then etched in 2 % Nital. Both optical and scanning electron microscopes were used to study the sintered and heat-treated microstructures. The sintered microstructures consisted of ferrite, fine and coarse pearlite plus cementite networks at the grain boundaries and bainite as seen in Figure 4.6.

Figure 4.6: Microstructure of as-sintered composition specimen of Fe-0.85Mo+1.4C+0.6Si, processed with polypropylene glycol diluted with 50%methanol.

4.3.1 Heating Cycle Profile Modification

Initially heating rates were 10°C-min^{-1} to 600ºC with a hold of 30 minutes for the removal of lubricant and adsorbed water and hydroxides, then 10ºC min^{-1} to 900ºC, with a hold of 2 hours, to allow distribution of carbon and silicon, followed by heating to the sintering temperature at 5ºC/min, with sintering time of 30-60 minutes at temperatures varying from 1285 to 1300°C. After sintering, the specimens were allowed to cool slowly to room temperature. This heating cycle produced a non-uniform microstructure with large connected pores. It was obvious that the large porosity observed was the result of evolved gas pressure, therefore different heating profiles were studied to try to minimise CO/CO_2 evolution and concurrently take graphite into solution as quickly as possible to create sufficient interconnected porosity to relieve any build up of gas pressure.

Figure 4.7 shows different microstructures produced by processing in different heating cycle profiles for the same composition. The **first** heating cycle was heating to 600°C for 15 min with heating rate 10°C-min^{-1}, followed by heating to 1100°C for 20 min, then furnace cooling. **Second** heating cycle was to heat the samples to 730°C for 15min, with heating rate 10°C-min^{-1} followed by heating to 1100°C for 20 min, then furnace cooling. **Third** heating cycle was by heating straightaway to 750°C for 15 min with heating rate 10°C-min^{-1}, followed by heating to 1100°C for 20 min, then furnace cooling. **Fourth** heating cycle was by heating straightaway to 900°C for 15 min with heating rate 10°C-min^{-1}, followed by heating to 1100°C for 20 min, then furnace cooling. Figure 4.7 reveals that the fourth heating cycle profile shows least gas porosity and better uniform microstructure with very tiny pores. Different lubricants were also

tried in conjunction with these heating profiles in order to establish the best heating profile coupled with the best lubricant. Liquid paraffin and polypropylene glycol diluted with 0-75% methanol were employed as lubricant/binder with best results obtained using the fourth heating cycle profile when the composition was processed with polypropylene glycol diluted with 50%methanol.

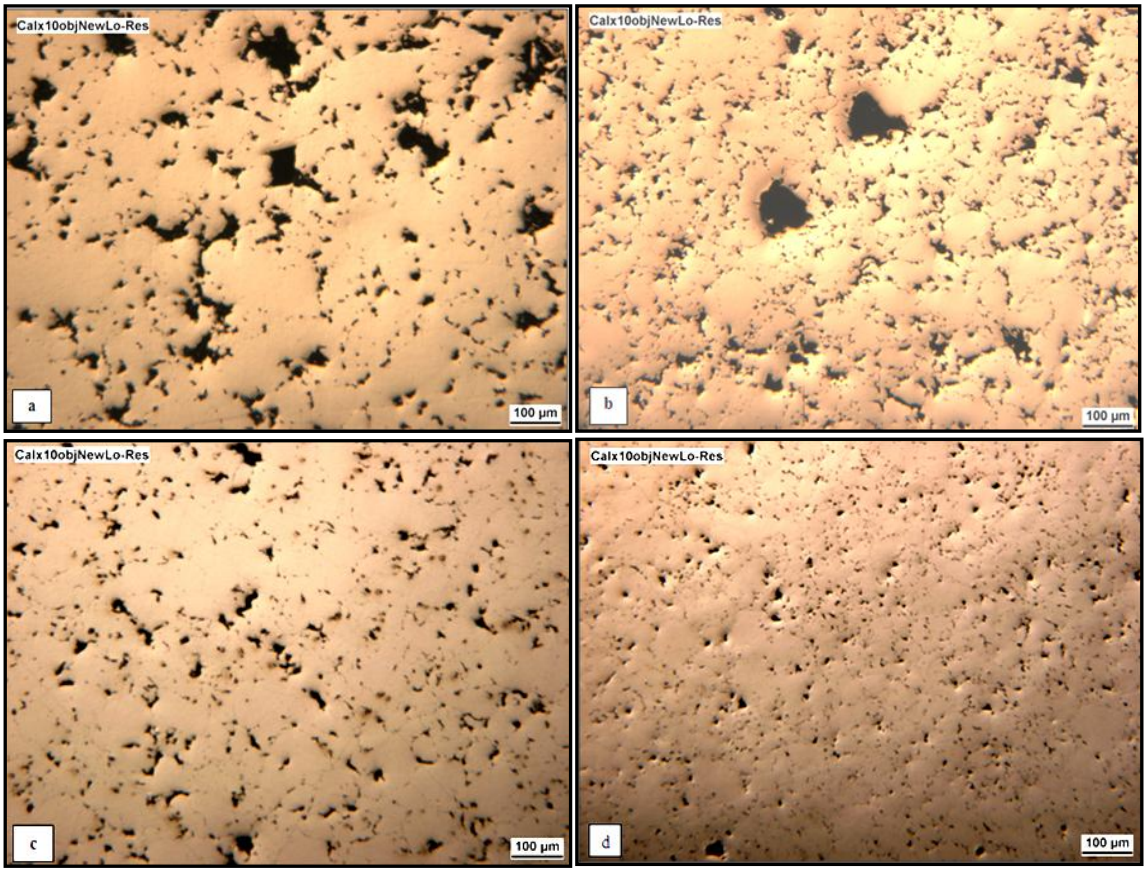

Figure 4.7: Different microstructures for the same alloy composition Fe-0.85Mo+0.6Si+1.4C processed by different heating cycle profiles, a) First heating cycle, b) second heating cycle, c) third heating cycle and d) fourth heating cycle.

4.3.2 Microstructural Studies

Sintering temperature increase promoted liquid phase sintering [5, 6, 35]; to prevent distortion of the samples over-sintering at high temperatures was avoided. Sintering furnace also has the ability to influence the obtained microstructure. Microstructural observations of initially sintered specimens showed excessive porosity. Examination of microstructures such as those of Figures 4.8a and 4.8b led to the belief that the additional porosity and its size must be linked to gas evolution during the heating cycle. As the evolving gas was formed either from reduction of oxides or from adsorbed water vapour, via the water-gas reaction: $C + H_2O \rightarrow CO + H_2$ from ~500ºC, it was decided to dry the graphite by heating to 120ºC overnight in a vacuum oven and then reproduce the same composition mixes, but with reduced water content. Figures 4.9a and 4.9b show gas sintered microstructure after graphite drying, sintered at 1300ºC for 60min, in vacuum and $90N_2/10H_2$ gas atmosphere, respectively. It was further noted that, on comparing samples from gas and vacuum sintering, that porosity was less for vacuum, because more gas could escape from the internal part of the compact during the early stage of heating in vacuo while porosity was still interconnected. Even after drying the best density obtained for Fe-0.85Mo+0.6Si+1.4C(+0.5cc liquid paraffin) alloy sintered at 1300ºC for 60 min, in gas atmosphere was ~7.50 g/cm^3 compared with 7.55 g/cm^3 in vacuum.

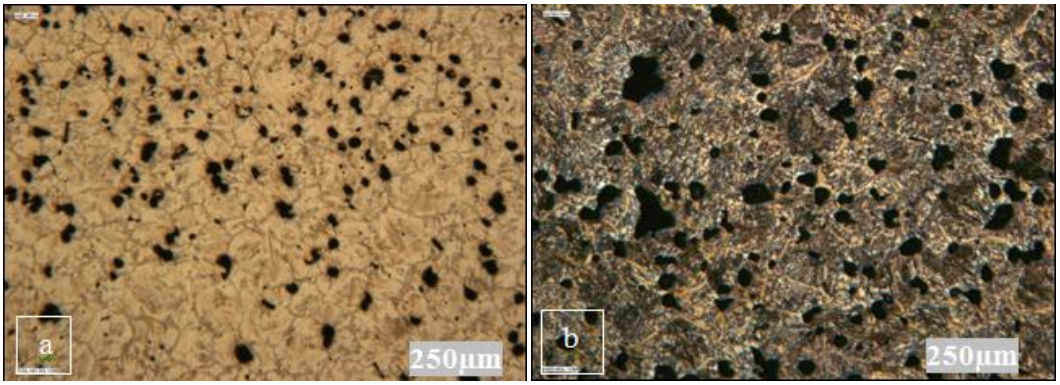

Figure 4.8: Microstructures of Fe-0.85Mo+0.6Si+1.4C(+0.5cc liquid paraffin), sintered at 1295°C for one hour in: a) vacuum, and b): 90N2/10H2 gas using initial cycle.

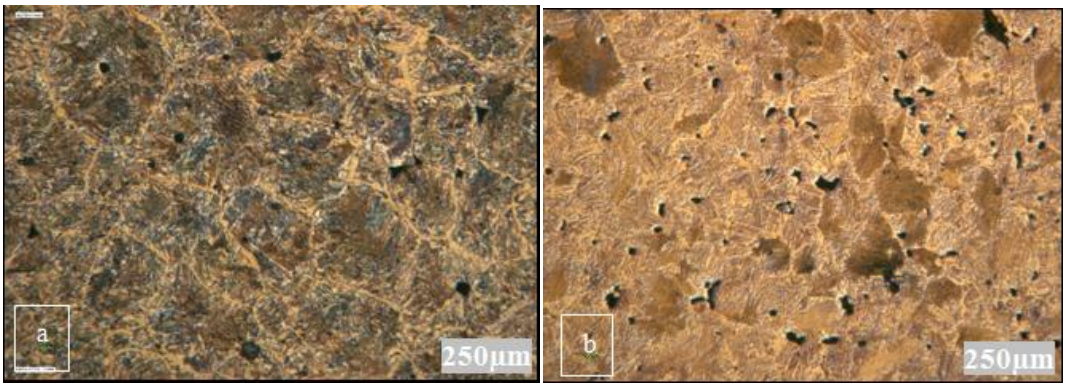

Figure 4.9: Microstructures Fe-0.85Mo+0.6Si+1.4C (+0.5cc liquid paraffin), sintered at 1300°C for one hour sintered in a) vacuum and b) 90N2/10H2, after drying the graphite overnight using initial cycle.

Again, on comparing vacuum and gas sintered microstructures, it was obvious that some gas 'bubbles' were still preventing maximum densification during sintering. It was therefore decided to adjust the conventional sintering heating profile to minimise the amount of alpha sintering due to the Fe in Fe self diffusion by speeding up the heating rate and also increasing the temperature for the first hold to above the alpha-

gamma transition temperature. The results showed significant improvements in sintered densities, which can be seen in Figure 4.10.

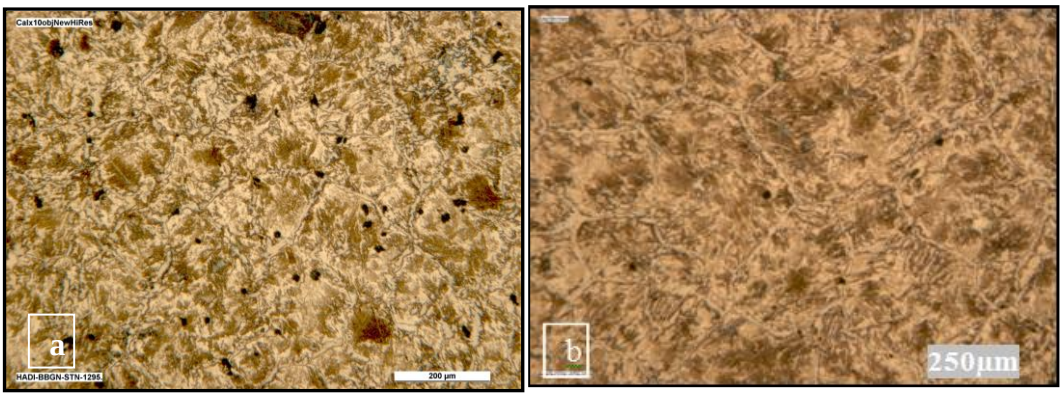

Figure 4.10: Microstructures of Fe-0.85Mo+0.6Si+1.4C(+0.5cc liquid paraffin), sintered at 1300°C for one hour in a) vacuum, and b) 90N2/10H2, using fourth heating cycle.

An alternative mixing procedure was then employed in which polypropylene glycol, diluted to 50% by methanol, was substituted for the liquid paraffin. This procedure gave high densification and better uniform microstructure, as seen by comparing Figure 4.10b with Figure 4.11, when density increased to 7.75g/cm^3.

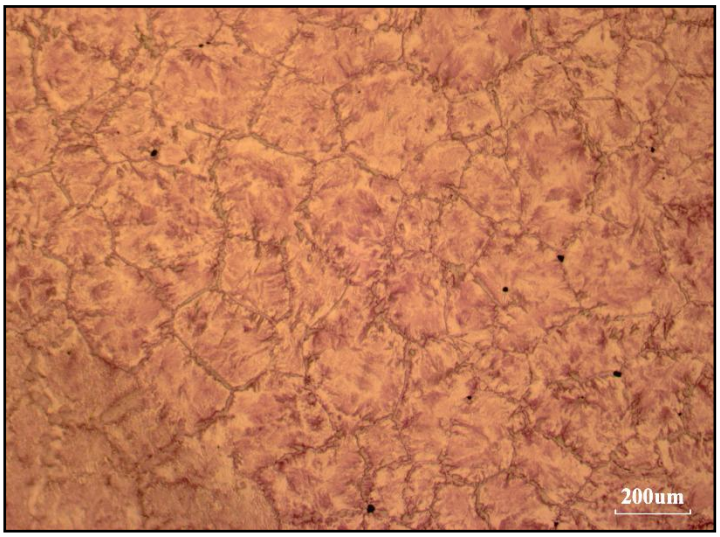

Figure 4.11: Microstructure of Fe-0.85Mo+0.6Si+1.4C alloy, processed with 0.5cc of polypropylene glycol mixed with 50% methanol, sintered at 1300°C for 60 min in 90N2/10H2, using fourth heating cycle.

Manganese was added in the form of a master alloy powder (G284) in an attempt to reduce either the amount of graphite or the sintering temperature necessary to produce sufficient liquid phase to promote densification. Unfortunately, this investigation gives low densification, non-uniform microstructure, and significant connected porosity. Figure 4.12 shows the microstructure of Fe-0.85Mo+0.65Si+1.3C+1Mn (+0.5cc liquid paraffin), sintered at 1300°C for one hour using both first and fourth heating cycles.

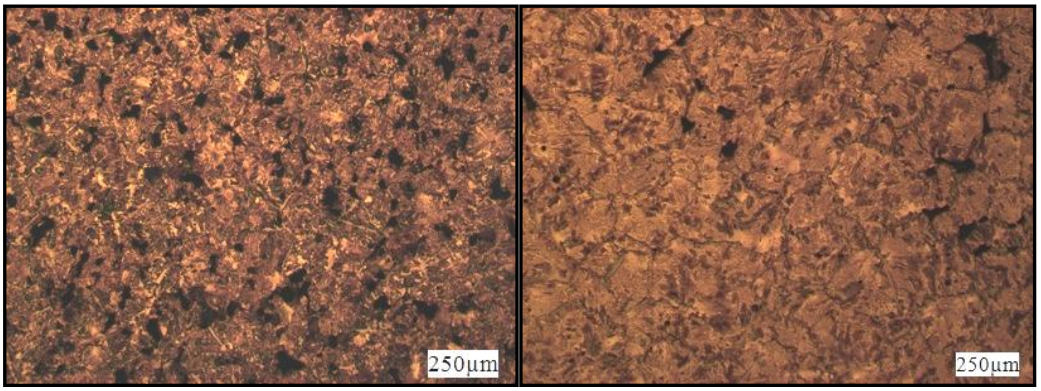

Figure 4.12: Microstructures of Fe-0.85Mo+0.65Si+1.3C+1Mn (+0.5cc liquid paraffin) , sintered at 1300°C for one hour in 90N2/10H2, using first heating cycle (left) and fourth heating cycle (right).

Slightly better densification was obtained when using polypropylene glycol instead of liquid paraffin, when the density increased to 7.47g/cm^3. For Fe-0.85Mo+0.65Si+1.3C+1Mn (+0.5 cc polypropylene glycol/methanol), densities of 7.47, 7.30 and 7.10 g/cm^3 were obtained when using atmospheres of $90N_2/10H_2$, pure N_2 and $25N_2/75H_2$ respectively.

Microstructures for alloy compositions of CrL were particularly dependent on the gas atmosphere, as seen in Figure 4.13. Specimens sintered under $90N_2/10H_2$ show better densification and more uniform microstructure than those sintered under $25N_2/75H_2$ and

pure N_2. In general, these microstructures exhibited low densification, large interconnected porosity and non-uniform microstructures. Burst pores were seen in specimens sintered under pure N_2 atmosphere, due to the reaction between nitrogen and the forming liquid, as seen clearly in Figure 4.13c.

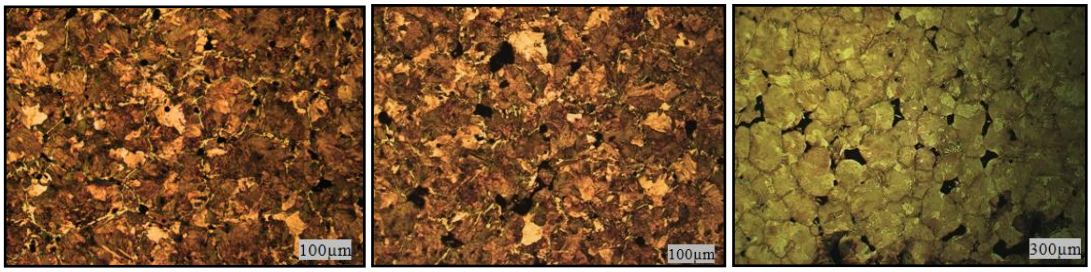

Figure 4.13: Three microstructures of CrL+1.5C+0.65Si processed with 0.5cc of polypropylene glycol mixed with 50% methanol, sintered at 1300°C for 1 hour under three different gas atmosphere, a $90N_2/10H_2$, b-$25N_2/75H_2$ and c-Pure N_2.

4.4 Heat Treatments

Initially a simple quenching heat treatment to produce Martensite plus retained austenite structure was performed. This involved loading the specimens into a small container, through which argon was flowing, placing it into a muffle furnace pre-heated to 950ºC and holding for 60 minutes after reaching this temperature - to ensure that all carbides were taken into solution. The samples were then quenched into oil, which resulted in some microcracking, as seen in Figure 4.14, where large volume change and hence build up of internal stress had occurred. Air cooling to room temperature did not solve the problem due to the high hardenability of the material and an isothermal quench into a preheated fan assisted oven proved necessary.

Calculations were attempted using e.g. Andrew's formula [69] to predict Martensite start temperature. These calculations were obviously in error, as they suggested that M_s would be less than room temperature and from experience this was incorrect. Predictive software using Bayesian networks [103] was employed to predict Martensite start and Martensite 10% of completion temperatures. The Martensite start temperatures for various compositions are summarized in Table 4.5 and Figure 4.15 shows the data graphically. For composition Fe-0.85Mo-0.6Si-1.4C calculations suggested that the $M_{10\%}$ temperature was ~130°C, since the M_s-temperature was calculated to be 144°C. Therefore samples were now quenched into a fan-assisted oven running at 130°C and held for 20min to promote auto-tempering of the Martensite as it formed and hence to reduce the amount of internal stress. The samples were then allowed to cool to room temperature so that more Martensite could form, followed by refrigeration to transform as much retained austenite as possible to martensite. No cracking was then seen in the hardened microstructure, as seen in Figure 4.16. For safety a stress relief was also performed by heating to 200°C for 1 hour, this removed any tendency to crack during metallographic sectioning, but should not be necessary for industrial processing.

The crack-free hardened specimens, with microstructure presented in Figure 4.16, were then given a standard spheroidising treatment to produce a ferrite plus sub-micron carbide structure, soft enough to allow a modest amount of resizing for dimensional control purposes. This process was carried out by reheating these brittle hardened specimens to 750ºC in argon with a holding time of 3 hours. Figure 4.17 shows the typical spheroidised microstructure. It should be noted that the austenitisation, isothermal quenching and spheroidisation temperatures for Crl+0.65Si+1.5C alloy were 1080, 125 and 755 ºC, respectively.

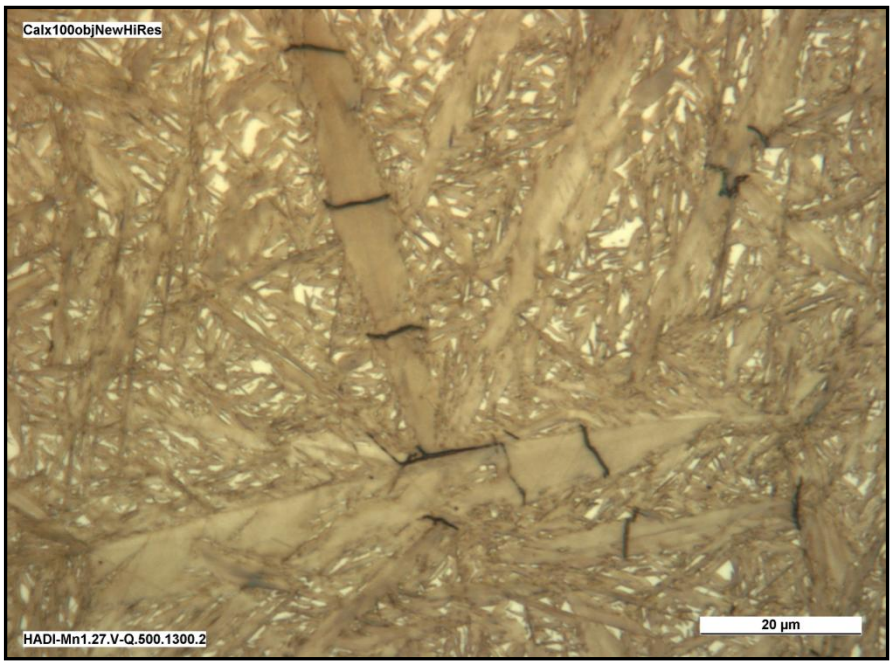

Figure 4.14: Microcracking in Fe-0.85%Mo.0.6%Si.1.4%C, resulting from severe quench-induced large volume change due to Martensite formation.

Table 4. 5 Predicted martensite start temperatures for different compositions.

C%	M_s-Temperature (°C)	
	Fe-Mo+0.6Si	CrL+0.65Si
1.2	160	158
1.25	155	153
1.3	151	149
1.35	147	146
1.4	144	143
1.45	141	141
1.5	140	140

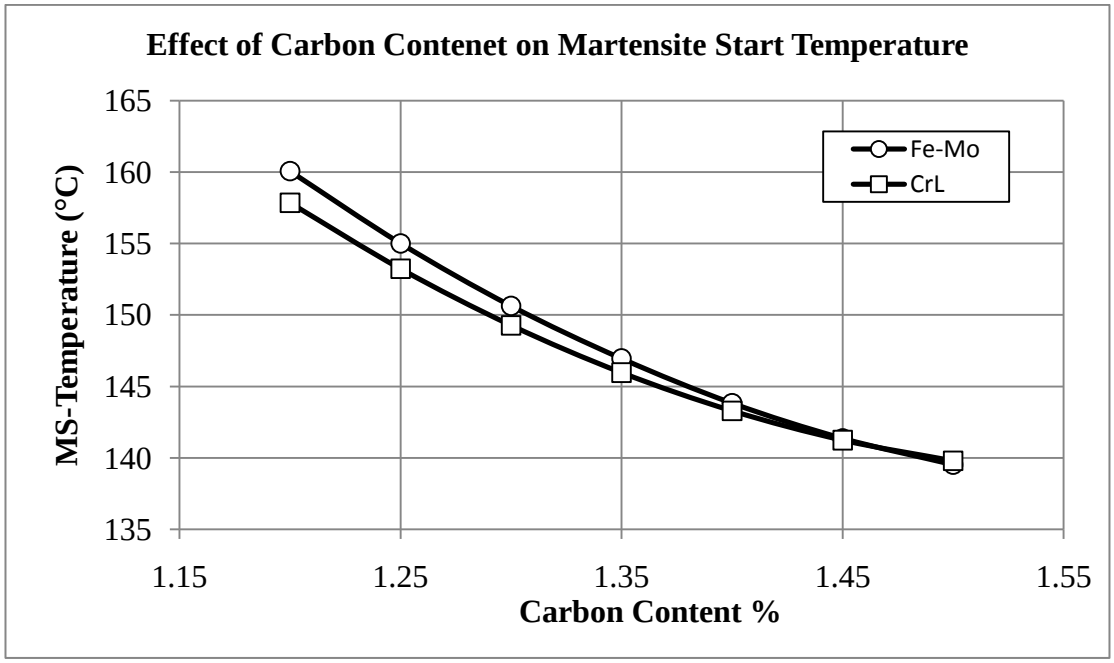

Figure 4.15: The effect of carbon content on the martensite start temperature.

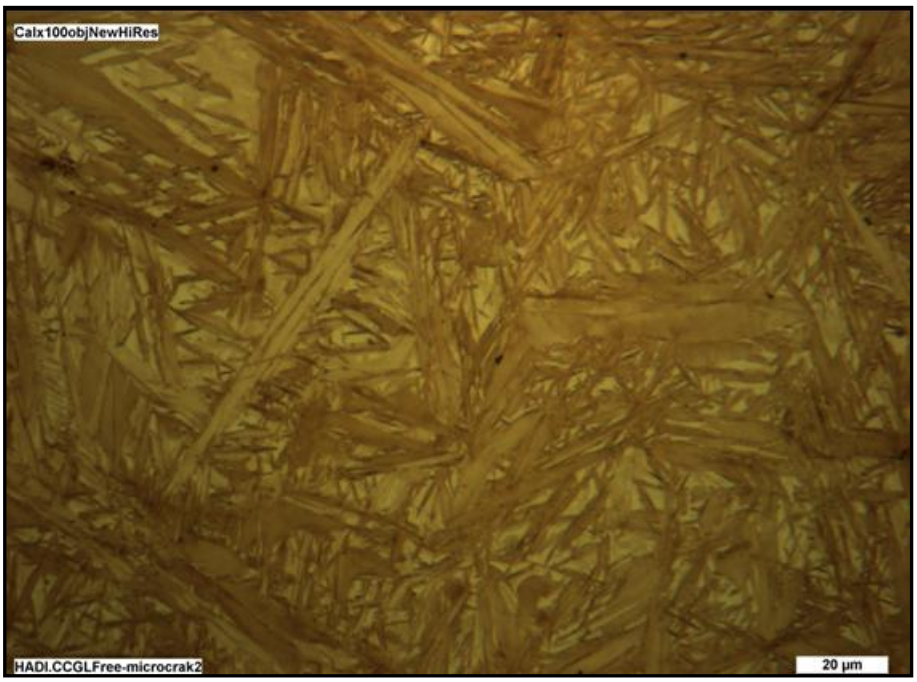

Figure 4.16: Crack-free microstructure of Fe-0.85%Mo.0.6%Si.1.4%C, resulting from PPGM processing and optimised heat treatment, PPGM = polypropylene glycol mixed with 50% methanol.

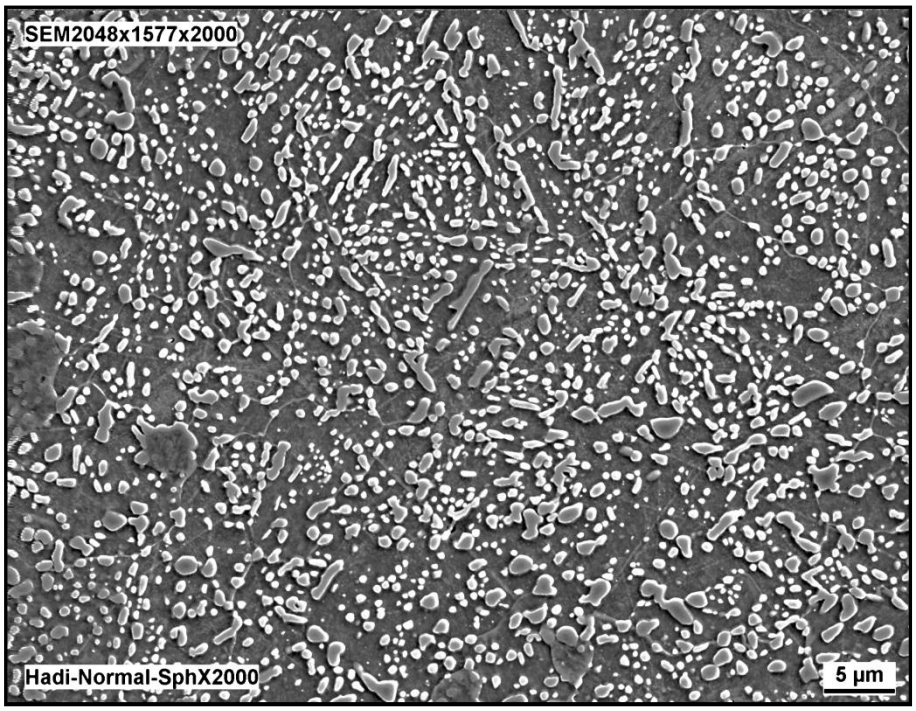

Figure 4.17: Scanning electron microcopy showing spheroidised specimens of Fe0.85%Mo.0.6%Si.1.45%C resulting from the spheroidising treatment at 750°C for 3 hours: ferrite matrix plus fine spheroidal carbides.

4.5 Hardness Test

Hardness tests, on as-sintered and heat-treated specimens, were carried out on a Vickers machine with a 10 kg load (HV_{10}). Table 4.6 lists the apparent hardness values of Fe-Mo-C-Si-Mn alloys processed with, different lubricants, e.g. dry lubricant (dry), and liquid paraffin: (A+0.05C). Table 4.6 clearly reveals that hardness increases with an increase in silicon and carbon contents. Alloy compositions containing manganese provided higher steel hardness, as expected. Manganese is well known for improving the hardenability of steels as evidenced by TTT diagrams which show delayed transformations, i.e. phase transformations are pushed to the right, thus allowing martensite to form at lower cooling rates.

Table 4. 6 Vickers hardness, HV_{10}, for as-sintered, quenched/air cooled and spheroidised Fe-Mo-C-Si alloys, dry processed, and using A: liquid paraffin, 0.5cc lubricant per 100g of mixture.

No	Composition and Processing route		Vickers hardness, HV_{10}							
			Sintered at 1300ºC		Held in argon at 970ºC for 2h				Spherodised : 750ºC for 3h, ±10 HV_{10}	
			Vac ±10	Gas ±10	Oil Quenched, ±30 HV_{10}		Air Cooled, ±30 HV_{10},			
					Vac	Gas	Vac	Gas	Vac	Gas
1	Fe.0.85Mo.1.2C.0.4Si	dry	188	196	613	620	540	546	148	151
		A(+0.05C)	205	210	621	633	560	573	157	163
2	Fe.0.85Mo.1.2C.0.6Si	dry	208	213	620	639	577	589	155	162
		A(+0.05C)	223	227	636	647	610	626	168	160
3	Fe.0.85Mo.1.3C.0.4Si	dry	215	219	634	646	614	620	161	171
		A(+0.05C)	239	242	660	669	637	651	176	168
4	Fe.0.85Mo.1.3C.0.6Si	dry	236	233	659	667	634	643	175	183
		A(+0.05C)	271	278	693	705	669	677	193	197
5	Fe-.0.85Mo.14C.0.4Si	dry	250	256	681	688	662	669	186	194
		A(+0.05C)	291	297	767	778	679	683	214	215
6	Fe.0.85Mo.14C.0.6Si	dry	287	293	748	765	670	672	211	217
		A(+0.05C)	305	315	795	805	710	715	221	225
7	Fe-0.85Mo+1.27C+0.6Si +1.5Mn	A(+.05C)	355	360	830	845	525	545	285	290
8	Fe-0.85Mo+1.3C+0.65 Si +1 Mn	A(+.05C)	330	335	760	790	505	515	275	282
9	Fe-0.85Mo+1.35C+0.6 Si+1Mn	A(+.05C)	370	375	835	850	670	695	295	308

By using polypropylene glycol diluted with 50% methanol instead of liquid paraffin improved powder wettability was achieved, thus better hardness, as seen in Table 4.7.

Table 4. 7 Vickers hardness, HV_{10}, for as-sintered, quenched and spheroidised Fe-Mo-C-Si alloys, processed with polypropylene glycol diluted with methanol (50% methanol), 0.5cc lubricant per 100g of mixture.

Composition	Vickers hardness, HV_{10}		
	Sintered at 1300ºC in ($90N_2/10H_2$ Gas) ±10 HV_{10}	warm-Quenching, held in argon at 970ºC for 2h, ±30 HV_{10}	Spherodising 750ºC for 3h, ±10 HV_{10}
Fe-0.85Mo+1.35C+0.6Si	300	795	215
Fe-0.85Mo+1.4C+0.6Si	325	810	230
Fe-0.85Mo+1.35C+0.6Si +1Mn	345	818	260

As expected, alloy compositions emanating from Astaloy CrL offered high hardness, especially for those samples sintered in high sintering temperature ~1300°C; In contrast silicon contents did not change the hardness, as represented in Table 4.8.

Table 4. 8 Vickers hardness, VH10, for as-sintered, quenched and spheroidised CrL-C-Si alloys, processed with polypropylene glycol diluted with methanol (50% methanol), 0.5cc lubricant per 100g of mixture.

No.	Composition	As-Sintered		Warm-Quenched		Spheroidised	
		1295°C	1300°C	1295°C	1300°C	1295°C	1300°C
1	CrL+1.5C+0.5Si	320	330	687	705	220	228
2	CrL+1.5C+0.55Si	325	338	710	720	235	237
3	CrL+1.5C+0.55Si	331	345	730	770	240	245
4	CrL+1.5C+0.65Si	340	348	752	810	243	248

Table 4.9 gives the microhardness for different samples of different phases. It was very time consuming to measure the microhardness for each phase because of difficulties recognizing phases from each other; additionally the thickness of some of these phases was very small such as cementite. It was also difficult to find individual phase regions large enough to obtain valid measurements, e.g. pure ferrite in the spheroidised samples. Table 4.9 shows that these samples containing Mn and Cr are higher in microhardness, than those without. It can be seen that increase in silicon content also gives slight increase in microhardness.

Table 4. 9 Microhardness for as-sintered, quenched and spheroidised specimens of alloys based on Astaloy 85Mo and Astaloy CrL, mixed with alloying additives such as C, Si, and Mn, processed with polypropylene glycol diluted with methanol (50% methanol), 0.5cc lubricant.

No	Sample	Microhardness					
		As-sintered (1300ºC)				W-Q ±50	F-Mat
		F±30	P±30	B±50	Ce		
1	Fe-0.85Mo+1.35C+0.6Si	210	390	485	1070-1210	992	140-165
2	Fe-0.85Mo+1.4C+0.6Si	215	400	500	1090-1260	995	140-170
3	Fe-0.85Mo+1.35C+0.6Si+1Mn	310	470	560	1100-1310	1060	185-205
4	CrL+1.5C+0.5Si	295	380	520	1090-1290	1010	165-180
5	CrL+1.5C+0.65Si	305	450	525	1095-1300	1030	172-195
F-Ferrite Phase , P-Pearlite Phase, Ce-Cementite Phase , B-Bainite Phase MR-Martensite Phase, RA-Retained Austenite Phase, CR-Carbide Phase W-Q – Warm Quenching, F-Mat- Ferrite Matrix of Spherodised Sample							

4.6 Mechanical Properties

Several dog bone and three-point bend specimens were prepared and tested to measure the tensile strength and transverse rupture strength, respectively. Tables 4.10 and 4.11 give the result of those mechanical properties for Astaloy 85Mo and CrL, mixed with alloying additives such as C, Si, Mn and Cr, in different gas atmospheres (0-10%H_2/N_2). Table 4.10 gives the mechanical properties of Astaloy 85Mo, mixed with (1.4-1.45wt%) C and 0.6wt% Si, processed with liquid paraffin and sintered at 1295ºC for one hour under $90N_2/10H_2$ gas atmosphere. Mechanical properties sintered under $90N_2$/10H2, yield strength 410MPa and fracture strength 907MPa with plastic strain ~12% are slightly higher than those sintered in pure N_2, yield strength 395MPa and fracture strength 880MPa with plastic strain ~10%, for the same composition Fe-0.85Mo+1.4C+0.6Si, whereas those specimens sintered in $95N_2/5H_2$ gas atmosphere gave quite low results yield strength ~370MPa and fracture strength 857MPa, however, it gave good plastic strain ~12%.

Table 4. 10 Mechanical Properties of Astaloy 85Mo mixed with liquid paraffin, processed 1.4 and 1.45C steels sintered at 1295ºC in different gas atmospheres of 0-10H2/N2.

Sintering atmosphere :90N_2/10H_2			
As-Sintered			
Composition	**YS MPa**	**FS MPa**	**P-St %**
Fe.0.85Mo.1.40C.0.6Si		590	0.0
Fe.0.85Mo.1.45C.0.6Si		610	0.0
Quenched			
Fe.0.85Mo.1.40C.0.6Si		530	0.0
Fe.0.85Mo.1.45C.0.6Si		592	0.0
Spheroidised			
Fe.0.85Mo.1.40C.0.6Si	400	906	14
Fe.0.85Mo.1.45C.0.6Si	410	907	12
Sintering atmosphere :95N_2/5H_2			
As-Sintered			
Fe.0.85Mo.1.40C.0.6Si		610	0.0
Fe.0.85Mo.1.45C.0.6Si		600	0.0
Quenched			
Fe.0.85Mo.1.40C.0.6Si		615	0.0
Fe.0.85Mo.1.45C.0.6Si		490	0.0
Spheroidised			
Fe.0.85Mo.1.40C.0.6Si	350	748	10
Fe.0.85Mo.1.45C.0.6Si	370	857	12
Sintering atmosphere : N_2			
As-Sintered			
Fe.0.85Mo.1.40C.0.6Si		680	0.0
Fe.0.85Mo.1.45C.0.6Si		669	0.0
Quenched			
Fe.0.85Mo.1.40C.0.6Si		690	0.0
Fe.0.85Mo.1.45C.0.6Si		586	0.0
Spheroidised			
Fe.0.85Mo.1.40C.0.6Si	380	893	13
Fe.0.85Mo.1.45C.0.6Si	395	880	10
YS: Yield Strength FS: Fracture Strength P-St: Tensile Strain			

After modifying the heating cycle profile and using polypropylene glycol diluted with methanol (50% methanol) as a lubricant instead of liquid paraffin, mechanical properties were improved for all those alloy compositions, as recorded in Table 4.11.

Table 4. 11 Mechanical properties for as-sintered, warm-quenched and spheroidised of different alloy of Astaloy 85Mo and Astaloy CrL, mixed with alloying additive such as C, Si, and Mn, processed with polypropylene glycol diluted with methanol (50% methanol), 0. 5cc lubricant per 100g of mixture, sintered at 1300C for one hour, in $90N_2/10H_2$ gas atmosphere.

Sintering Temperature 1300°C for 1 hour Sintering atmosphere :$90N_2/10H_2$,				
As-Sintered				
No.	**Composition**	**YS MPa**	**FS MPa**	**P-St %**
1	Fe-0.85Mo+1.35C+0.6Si		600	0.0
2	Fe-0.85Mo+1.4C+0.6Si		630	0.0
3	Fe-0.85Mo+1.35C+0.6Si+1Mn		720	0.0
4	CrL+1.5C+0.65Si		650	0.0
Warm-Quenched				
1	Fe-0.85Mo+1.35C+0.6Si		680	0.0
2	Fe-0.85Mo+1.4C+0.6Si		700	0.0
3	Fe-0.85Mo+1.35C+0.6Si+1Mn		995	0.0
4	CrL+1.5C+0.65Si		690	0.0
Spheroidised				
1	Fe-0.85Mo+1.35C+0.6Si	400	951	18.0
2	Fe-0.85Mo+1.4C+0.6Si	410	945	16.0
3	Fe-0.85Mo+1.35C+0.6Si+1Mn	525	980	10.0
4	CrL+1.5C+0.65Si	470	960	13.0
YS: Yield Strength FS: Fracture Strength, P-St: Plastic Strain 3PBS: 3-Point Bend Strength				

To be noted is macroscopic brittleness of all specimens except those spheroidised, which exhibited strains up to 10-18%. Fractographs of as-sintered and spheroidised tensile specimens are presented in Figure 4.18-419; the first showing extensive plasticity and (micro) dimple rupture.

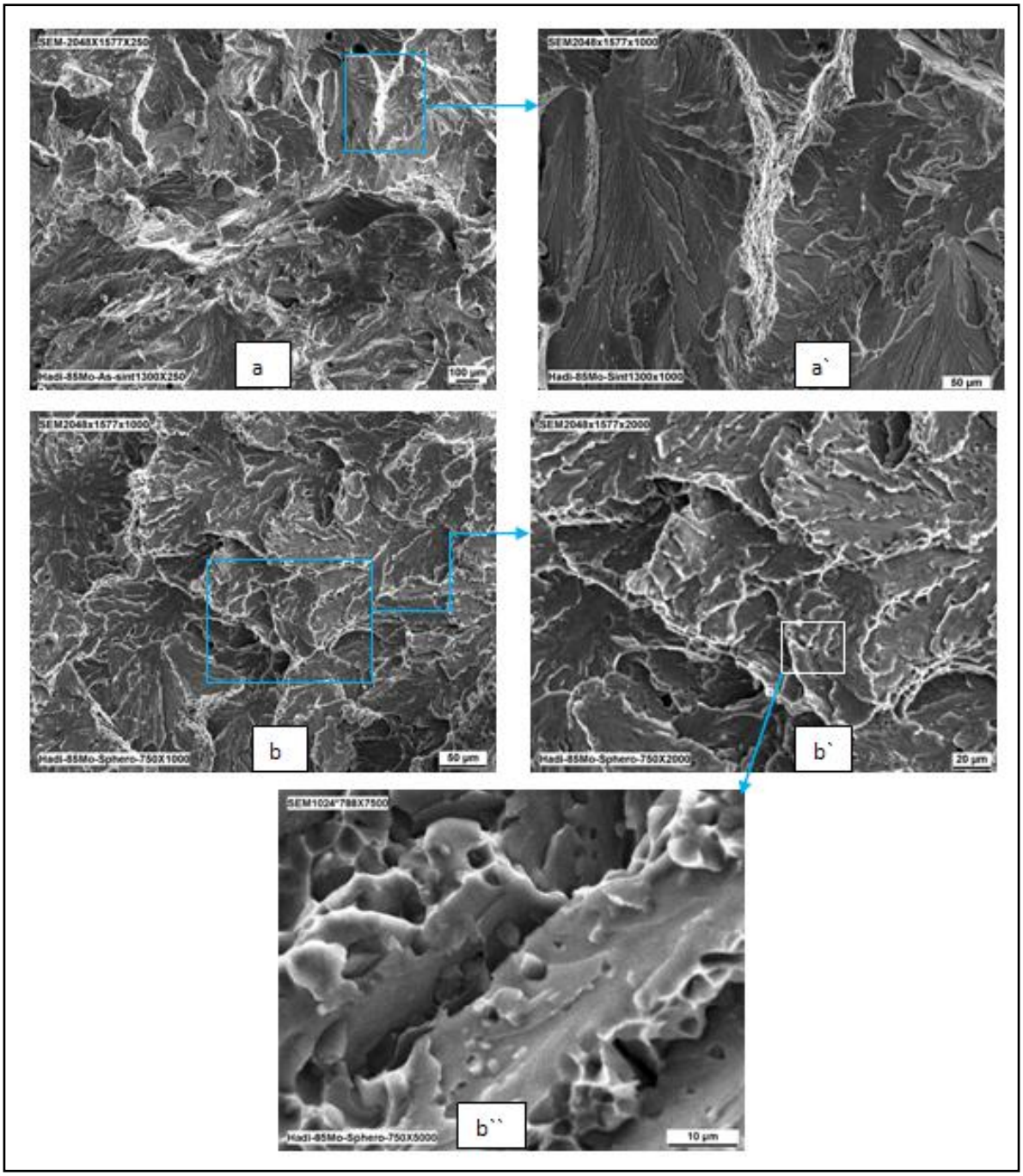

Figure 4.18: Fractographs of tensile specimens of Fe.0.85Mo.0.6Si.1.4C: (a) as-sintered, macroscopically brittle: and (b) spheroidised, exhibiting 16% plastic strain. Please note in (a`) cracking following cementite networks with a tiny amount of ductility in the ferrite, and in (b`&b``) extensive (micro) dimple rupture as well as cleavage and intergranular rupture.

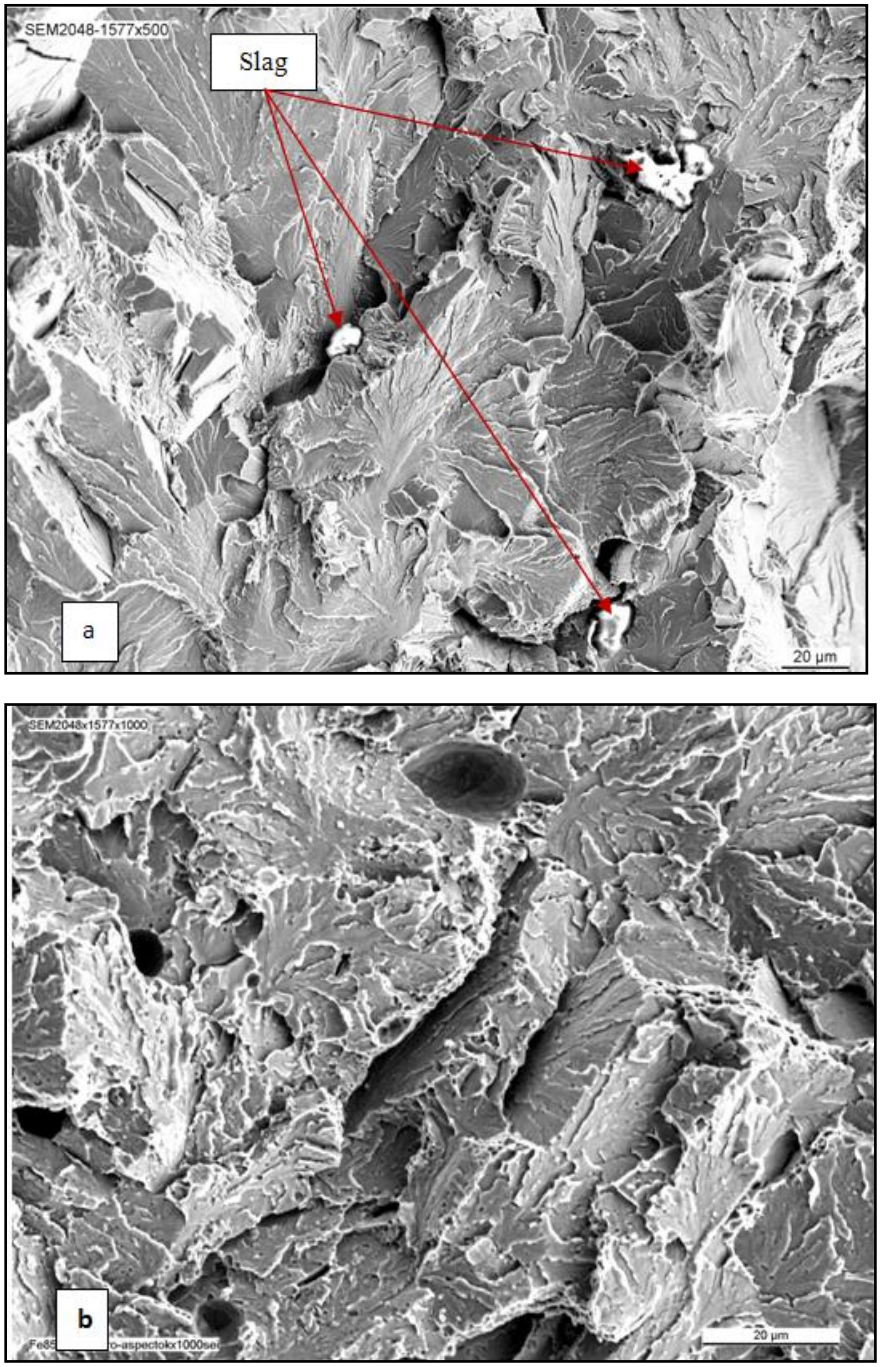

Figure 4.19: Fractographs of tensile specimens of Fe-1.5Cr+0.2Mo+0.6Si+1.4C: (a) as-sintered, macroscopically brittle: and (b) spheroidised, exhibiting 13% plastic strain. Please note in (a) slag precipitated at grain boundary, and in (b) extensive (micro) dimple rupture as well as cleavage and intergranular rupture.

Three-point bend spheroidised specimens were prepared and tested in order to evaluate the transverse rupture strength (TRS) using specimens of rectangular beam cross section. The results are summarized in Table 4.12 for both Astaloy 85Mo and Astaloy CrL based alloys, mixed with C, Si, and Mn, processed with polypropylene glycol diluted with 50% methanol. It appears that increasing Cr and Mn leads to increase in transverse rupture strength, as expected. Figure 4.20 illustrates the materials' ductility.

Table 4. 12 Three-point bend strengths for spheroidised alloys based on Astaloy 85Mo and Astaloy CrL, mixed with as C, Si, and Mn, processed with polypropylene glycol diluted with 50% methanol, 0.5cc lubricant per 100g of mixture.

No.	Composition	Three-Point Bend Strength [MPa]
1	Fe-0.85Mo+1.35C+0.6Si	1644
2	Fe-0.85Mo+1.4C+0.6Si	1650
3	Fe-0.85Mo+1.35C+0.6Si+1Mn	1960
4	CrL+1.5C+0.65Si	2050

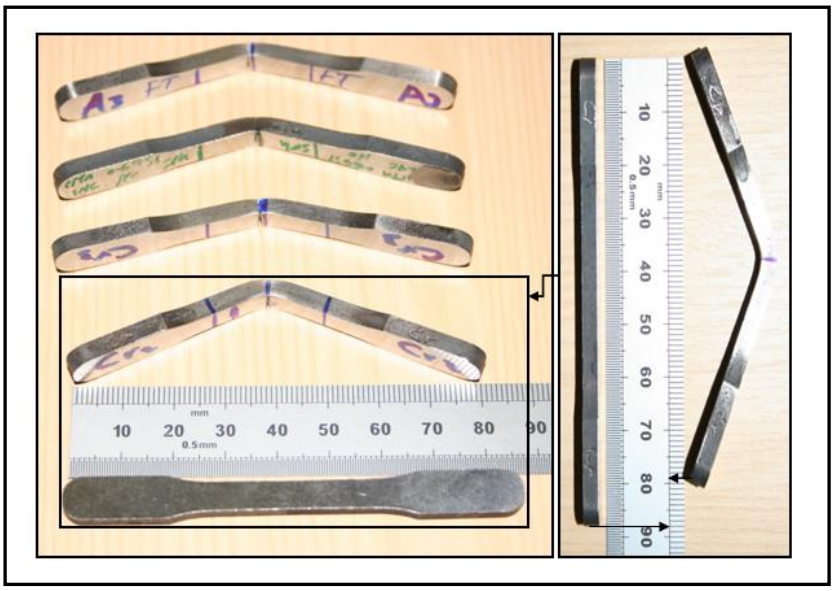

Figure 4.20: Three point bend samples after testing.

4.7 Warm Forging

Several spheroidised specimens with density ~7.2g/cm^3, were warm forged on a screw press between flat plates heated to 200°C at AGH, Krakow [courtesy of Prof. S. Szczepanik]. The first specimen was heated up to 700°C and forged once, whilst the second specimen was additionally re-heated to 750°C and forged. Table 4.13 gives the details and results for those specimens. The one forging strike at 700°C exhibited a crack-free microstructure, but did not weld up the pores completely. Already evident were more smaller carbides, Figure 4.21. The second, at 750C, strike started to break up ferrite grain size and gave an even better carbide distribution, Figure 4.22.

Table 4. 13 Warm forging of spheroidised specimens, with sintered density of ~7.2g/cm3, carried out at AGH, Krakow, Poland.

No.	FD(g/cm^3)	NS	FT (°C)	Hardness VH_{10} (±10)	Height. Red.%
S1	7.65	1	700	195	30.6
S2	7.72	2	700 then 750	205	40.8
FD= forged Density, NS=Number of Strike, FT=Forging Temp.					

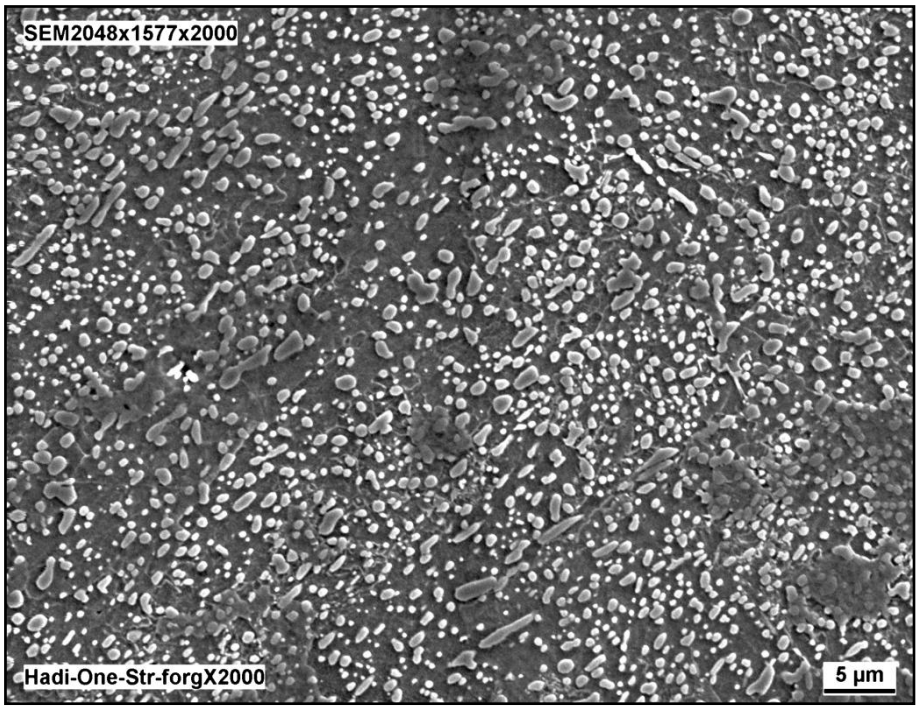

Figure 4.21: Scanning electron micrograph of a spheroidised specimen subsequently forged on a screw press at 700^{o}C.

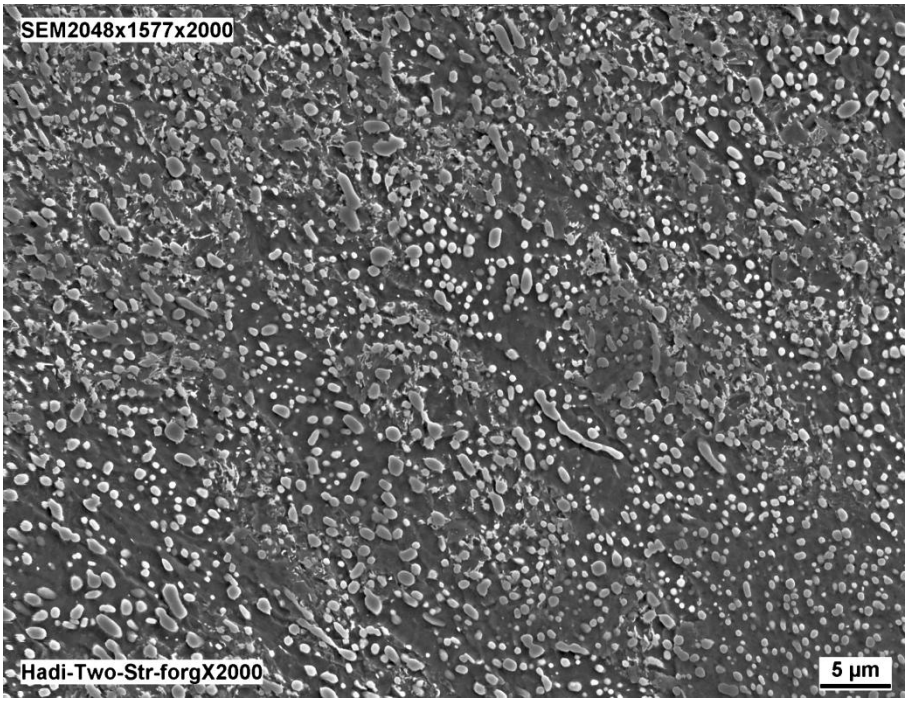

Figure 4.22: Scanning electron micrograph of a spheroidised specimen forged at 700^{o}C, then re-heated to 750^{o}C and given a second strike.

These encouraging results led to testing of further specimens, discs of 8 mm diameter and 12 mm in height (cut from the rings) on a Gleeble HDV-40 machine at the Institut for Metallformung, TUBA Freiburg, Germany [courtesy of Prof. R. Kaualla]. The discs were warm forged at 700°C using a fully instrumented test rig. The specimens were heated in argon to 700°C and then forged at strain rates of 10^{-3}, 10^{-2}, 10^{-1} and 1 sec^{-1} to (recorded) ~ 1.15 natural (logarithmic) strain, Figure 4.23, Table 4.14 presents the details and results of those warm forging experiments. Figures 4.24-4.25 show two Freiburg processed spheroidised samples at strain rates of 0.01 and 0.001sec^{-1}. These resultant discs had unsuitable geometry for conventional mechanical testing.

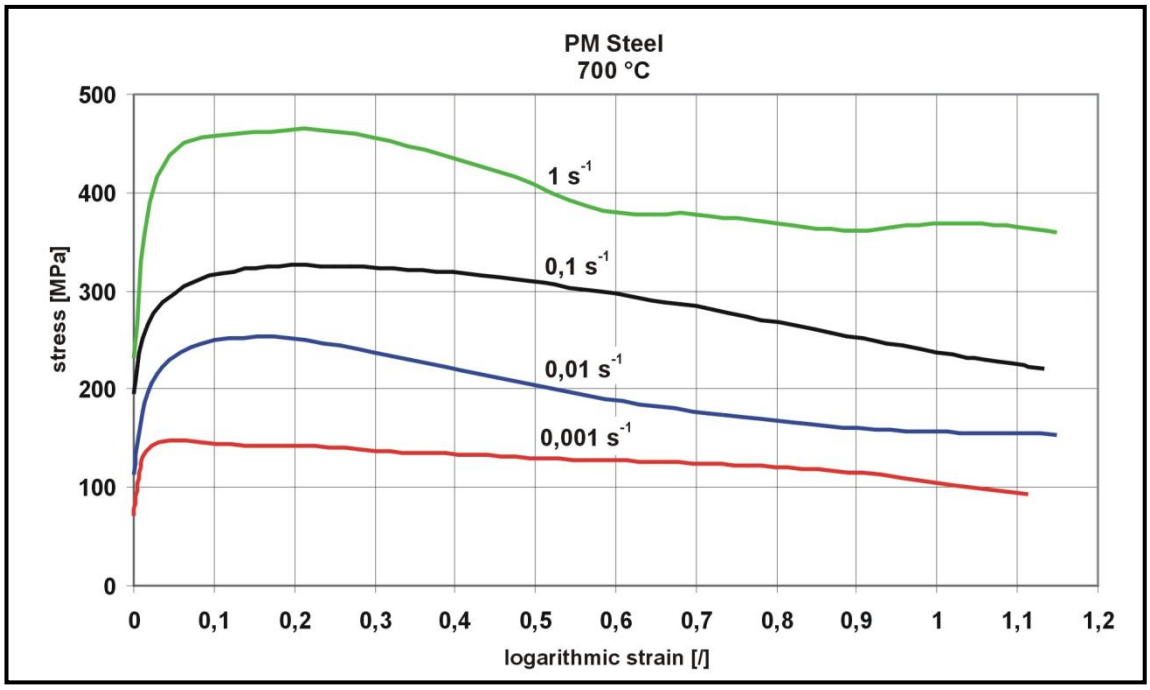

Figure 4.23: Compressive stress-natural strain relationships for Fe-1.4C-0.6Si-0.85Mo PM steel at 700oC at strain rates in the range of 0.001 to 1 sec^{-1}.

Table 4. 14 Warm forging of spheroidised specimens carried out at TUBA Freiburg, Germany. Yield strengths were estimated from the diametral disc compression tests.

No.	sintered Density (g/cm^3)	forged Density (g/cm^3)	Strain Rate (S^{-1})	Hardness $VH_{10}(\pm 10)$	Height. Red. %
S1	~7.2	7.78	1	270	71.9
S2	~7.2	7.78	0.1	280	71.16
S3	~7.2	7.79	0.01	295	71.43
S4	~7.2	7.79	0.001	310	73.26

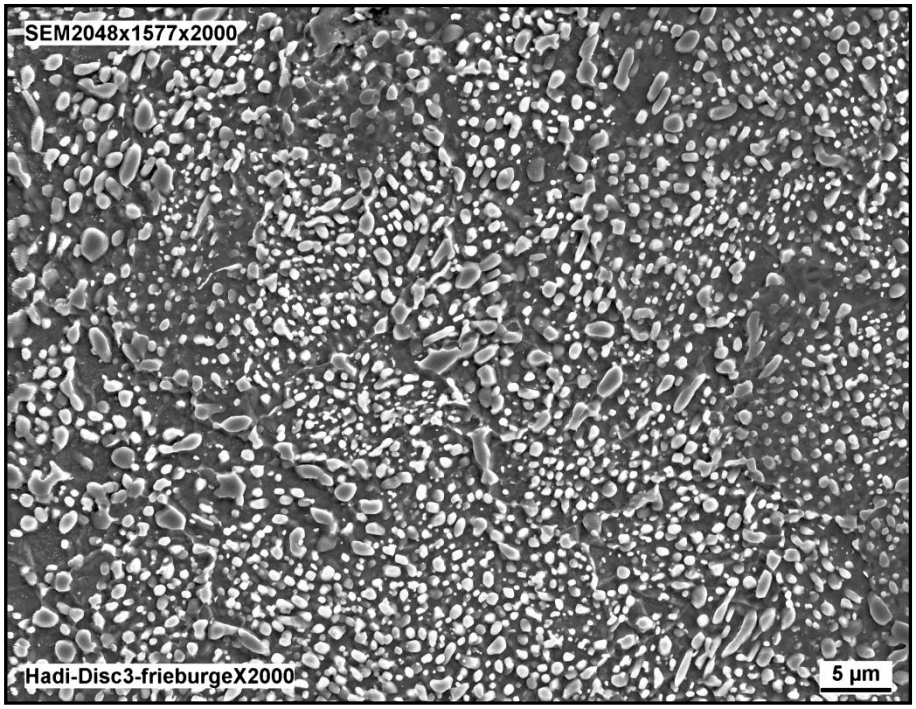

Figure 4.24: Scanning electron micrograph of a spheroidised specimen heated to 700^0C and forged at a strain rate of $0.01sec^{-1}$.

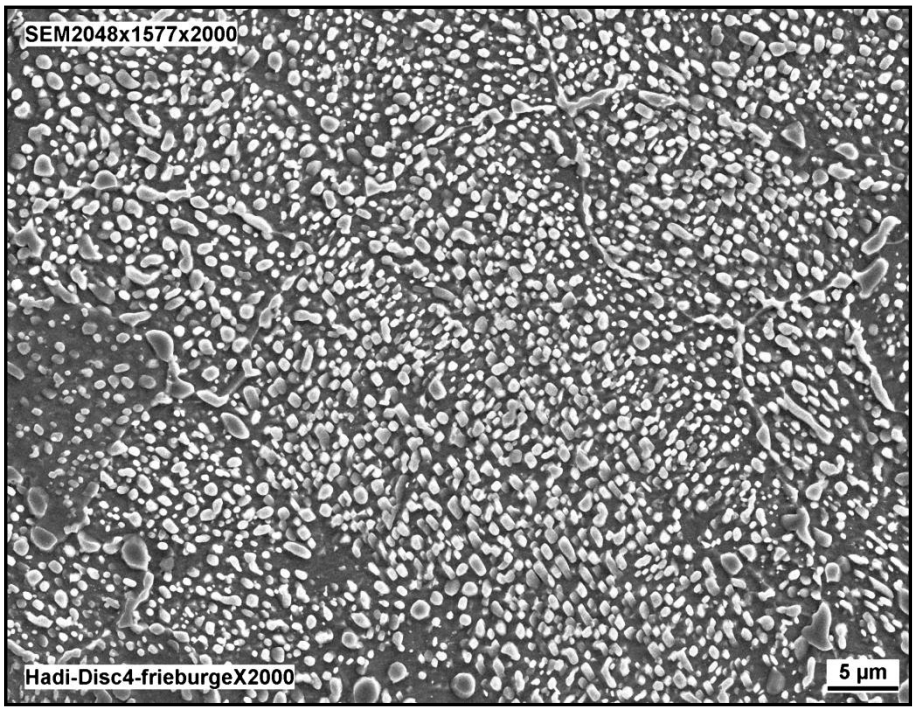

Figure 4.25: Scanning electron micrograph of a spheroidised specimen heated to 700^{0}C and forged at a strain rate of 0.001sec^{-1}.

Testing discs in diametrical compression is known as: the diametral compression, Brazilian disc or the indirect tensile test. The test induces variable biaxial stresses: compressive, σ_3, and tensile, σ_1, in the transverse direction of the applied compressive load. It is used as a mechanical testing technique to determine the (brittle) tensile fracture strength (under transverse compression) of (linearly) elastic materials such as concrete, ceramics, composites, pharmaceutical tablets. The relevant failure region is the disc centre where a splitting crack originates [104]. The principal stresses have been computed by Hertz [105] and at the disc centre $\sigma_1 = 2P/\pi Dt$ and $\sigma_3 = -6P/\pi Dt$, where P is the applied compressive load, D the diameter and t the specimen thickness. Photoelasticity experiments of Frocht [106] show clearly the complex stress distribution and accord with the Hertz analysis. Because of the ease of testing and the simple specimen geometry, this test has been applied to materials, which exhibit limited

macroscopic plasticity before fracture and Proccopio et al. [107] have performed finite element calculations for the elastic and perfectly plastic situations in order to incorporate the effects of limited ductility.

In experiments with work-hardening materials it was observed that plastic zones spread from the platens and meet at the disc centre as seen in the Figure 4.26. This critical event, suggested in discussion with Prof. Andrew Wronski, was chosen to try to evaluate the yield stress. Neglecting plasticity, the principal stresses predict the yield stress to equal $KP/\pi Dt$, where the factor K equals 8 and 7.2, according to Tresca and Huber-von Mises yielding criteria. The incorporation of plasticity into the finite element model, however, leads to substantial deviation between the analytical elastic expressions and the numerical elastoplastic solution. The maximum principal stress is reported to be still in the transverse direction, but that the location of this stress shifts away from the centre and that at (only) 2% diametrical strain, its magnitude is approximately 2.5–3 times the level predicted by the elastic solution. Furthermore, the volume over which all of the maximum transverse stress is acting showed a significant reduction in comparison with the purely elastic simulations.

Figure 4.26: Photograph of diametrically compressed disc of warm forged Fe-1.4C-0.65Si-0.85Mo when the plastic zones emanating from the platen contact regions meet at the disc centre.

Accordingly it is completely unrealistic to use the elastic solution for our steel and it was decided to evaluate K experimentally: by conducting experiments on mild steel discs of determined tensile yield stress. The tests were carried out in a specially constructed jig on an Instron machine at a compression rate of 0.5mm-sec^{-1}.

Tensile strength of this mild steel was found to be ~225MPa. Thus, by applying equation ($K = \frac{\sigma\pi Dt}{P}$), to one of the diametrally tested discs, the K factor was found and is presented below in Table 4.15. This Table also shows that by using this calculated K and the dimensions and loads for the disc samples S1 and S2 that the diametral yield strength appears to be self-consistent for the experiments.

$$K = \frac{\sigma\pi Dt}{P} \rightarrow K = \frac{225*3.14*11.24*2.49}{10780} \rightarrow K=1.83$$

The K factor was found to be 1.83. Using this figure calculations were made for two further tests, Table 4.15, indicating excellent reproducibility.

Table 4. 15 K factor calculations for yield strength of mild steel discs of directly determined yield strength of 225 MPa.

No	t(mm)	D(mm)	Load (N)	K	σy (MPa)
MS1	2.48	11.24	10590	1.83	221
MS2	3.00	11.31	13120	1.83	225

The same value of K was used to compute the yield strengths of forged spheroidised samples, Table 4.16.

Table 4. 16: The forged disc test results.

No.	D(mm)	t(mm)	K	Load (N)	Strain Rate (S^{-1})	σy (MPa)
FS3	12.8	2.155	1.83	35223	0.01	744
FS4	13.46	2.145	1.83	38100	0.001	769
FS=Forged spheroidised sample						

The yield stresses after warm forging at strains 10^{-3}, and 10^{-2} sec^{-1} evaluate to 769, and 744 MPa, respectively. The respective mean grain sizes were ~ 6 and ~7 μm, respectively. The yield strength increased substantially through warm forging of the spheroidised material and its dependence on grain size is consistent with the Hall-Petch effect. Ultra high carbon steels, can be made very strong and ductile at room temperature, providing that the microstructure consists of very fine ferrite grains i.e. 0.5-2μm and ultra fine spheroidised carbide [15]. Syn et al [67] have proposed, following an intensive study of the effect of the cementite-particle spacing and ferrite grain size on the strength of high carbon steels (0.5-1.8wt.%)C, that the yield strength can be predicted by microstructural observation.

Chapter Five

5 Discussion

Thermocalc predicted the necessary compositions and sintering temperatures to produce sufficient liquid phase for densification of these ultra-high carbon steels. Accordingly, processing was performed but, despite some densification, the microstructure contained large pores and consisted of pearlite plus thick, brittle cementite networks. When comparing specimens sintered in vacuum with those using the normal nitrogen/hydrogen gas-sintering atmosphere it became obvious that the porosity must be a consequence of gas formation.

Therefore, HSC chemistry software was used to model the possible gas reactions, e.g. $C + H_2O \rightarrow CO_2 + H_2$, water-gas shift reaction, $C + 2FeO \rightarrow 2Fe + CO_2$ found to be favourable from ~500ºC, and $C + CO_2 \rightarrow 2CO$ Boudouard reaction complete by ~927ºC.

These findings led to belief that water must be adsorbed onto the surface of the powders, particularly graphite with its large specific surface. Therefore, powders were dried in a vacuum oven, mixed and sintered. The results were much improved but still showed some significant porosity and again thick, cementite networks.

Concurrently, two solutions were attempted to address the above noted problems; 1) addition of Si in the form of fine SiC powder. Si is a known ferrite stabiliser and metallurgical literature shows that it helps to produce thinner cementite networks, an advantage as it makes solution of these easier in subsequent thermal treatments. An

added benefit of Si is that Thermocalc shows that the solidus line in the phase diagram is depressed; hence more densifying liquid phase is produced for a given sintering temperature. 2) The heating profile was modified to force early interconnected porosity for escape of generated gas and prevent build up of potentially damaging gas pressure. Literature tells us that faster heating rate equates to lower CO/CO_2 evolution and then by increasing the first hold temperature above the eutectoid point graphite can be made to diffuse, thus creating the interconnected porosity at the powder particles' surfaces, which is necessary for gas escape. The homogenisation holding temperature was also increased to 1100ºC to ensure that carbon and silicon were well dispersed before rising to the final sintering temperature.

After drying the graphite in a vacuum oven for overnight, by heating to ~120ºC, the graphite distribution and dusting problems were solved efficiently by introducing 0.5 cm^3 of liquid paraffin per 100g of powder to be mixed. This necessitated a modified mixing procedure where the base powder (e.g. Astaloy 85Mo or Astaloy CrL) and silicon carbide powders (plus Fe-Mn-C master alloy when required) were Turbula mixed with lubricant namely for 20 minutes, then the graphite powder was added and further mixing took place for 20 minutes to 'glue' the graphite to the base powder. However, liquid paraffin is relatively viscous and often additional amount has to be added, to ensure coverage of the mixture base powder, in order to achieve the optimum homogenous mixture. Too much coverage can lead to the graphite being redistributed into high concentration pools during pressing, which can lead to localized melting, porosity and severe distortion of sintered compacts. To help decrease the graphite agglomeration problem polypropylene glycol diluted with 50% of methanol was used instead of liquid paraffin, i.e. to guarantee that all the additive powders were 'glued' to

the base powder. The powder mixture was heated to 80ºC in a vacuum oven for at least three hours, to boil off the methanol, leaving the powder with optimum coverage thus eliminating the segregation and dusting of graphite. Additionally, higher green densities were achieved in the range of 6.75-6.94g/cm^3 and ensuring that best sintering densification would be attained.

Comparing the green compacts sintered both in vacuum and the N_2/H_2 gas atmosphere, it is evident that, with the initial sintering cycle profile, vacuum clearly provided higher densities for almost all the alloy compositions. The principal reason is higher reduction of moisture and surface oxides and better removal of the vaporized lubricants by the vacuum furnace, which also produces higher decarburisation than the gas atmosphere. Remembering that self diffusion of Fe in Fe is approximately 100 times greater in the alpha phase than in gamma phase and that time is also a strong variable, the heating profile was changed to minimise time spent in the alpha temperature range to reduce solid-state densification. Also the temperature to ensure efficient carbon and silicon diffusion was increased to 1100ºC from 900ºC with a hold of 2 hours before finally raising to the sintering temperature at 5ºC min^{-1} with sintering hold of 30-60 minutes. This combination finally proved successful in increasing sintered density and removing the large gas pores in the structure. Figures 5.1-5.3 show three different SEM microstructures for the same composition of Fe-0.85Mo+1.4C+0.6Si, sintered in $90N_2/10H_2$ gas atmosphere and different heating profile conditions. Specimens were heated to 600ºC, 750ºC and 900ºC, respectively, and then held for 15min at temperature all with the same heating rate of 10ºC-min^{-1}, followed by furnace cooling. From Figure 5.1, it easy to see graphite and silicon blocking porosity at 600ºC and preventing gases from escaping. Figure 5.2 shows that the graphite has just started to

react but not completely, whereas the silicon has not begun to react yet even in the austenitic region at temperature of ~750°C, thus the network of grain boundaries were still semi blocked. Figure 5.3 shows that the graphite and silicon were already starting to diffuse into austenite at 900°C, as the temperature increases further more diffusion takes place, which leads to more uniform contact melting, faster neck growth between particles and higher amount of liquid phase formation, before furnace cooling. When the sintering cycle was modified to minimise the amount of alpha phase sintering and to release gases from pores by speeding the heating rate to 20 °C/min, reducing the time of the 900°C hold to 15 mins, but increasing the temperature of the diffusional/homogenisation hold to 1100°C, a network of grain boundary pores formed, allowing penetration of a liquid phase as it formed at the sintering temperature, thus producing higher densification, recorded in Table 3.4.

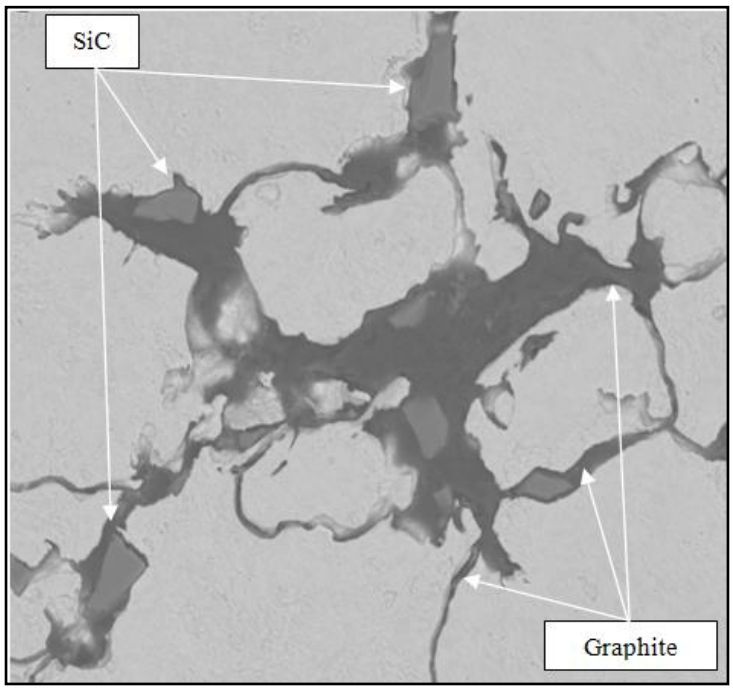

Figure 5.1: Scanning electron micrograph of microstructure of Fe-0.85Mo+1.4C+0.6Si, heated to 600°C for 15min with heating rate 10°C-min-1, and followed by furnace cooling.

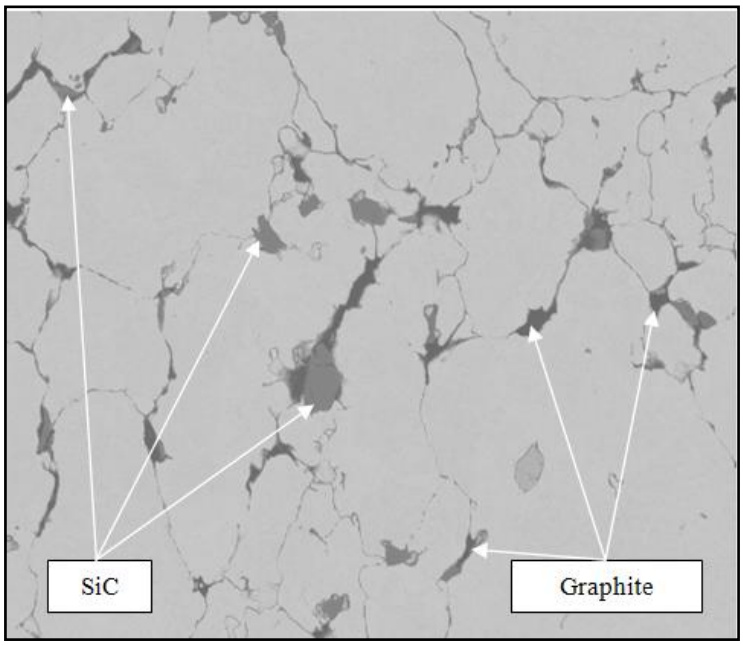

Figure 5.2: Scanning electron micrograph of microstructure of Fe-0.85Mo+1.4C+0.6Si, heated to 750^{0}C for 15min with heating rate 10^{0}C-min-1, and followed by furnace cooling.

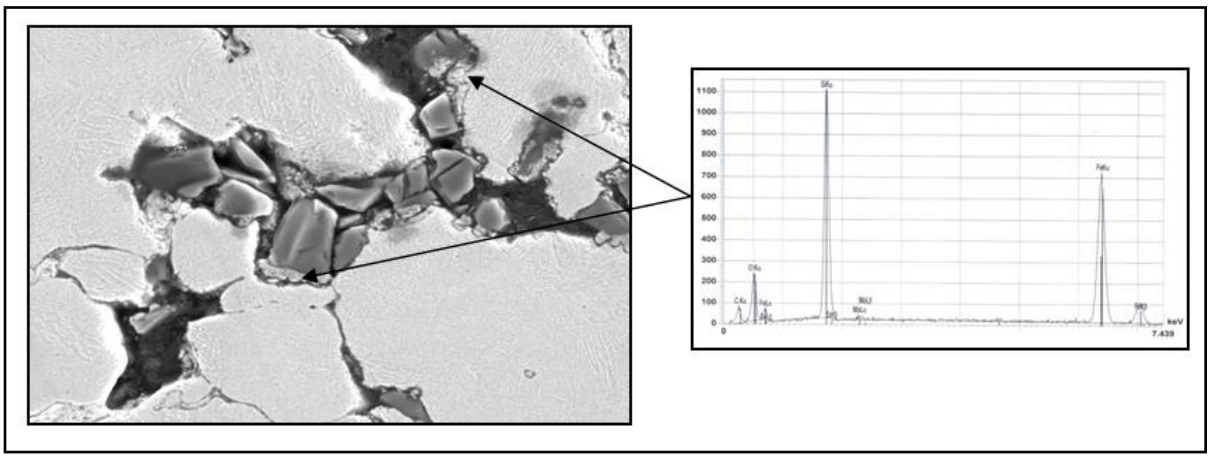

Figure 5.3: Scanning electron micrograph of microstructure of Fe-0.85Mo+1.4C+0.6Si, heated to 900^{0}C for 15min, with heating rate 10^{0}C-min-1, and followed by furnace cooling. Pearlite is now in evidence as graphite diffusion has taken place.

Increasing the silicon content enhanced the diffusion process between the two elements and, due to contact melting between iron and silicon, liquid phase sintering was activated, thereby increasing the sintered density [35]. These results are in accord with ThermoCalc modelling, i.e., as silicon, carbon, sintering temperature and time increased, liquid phase amount increased, Table 3.4, and so did the sintered density, higher than values reported for comparable compositions, ~7.40 g/cc [34, 93] for vacuum sintering (a batch process). Processing involving additions of liquid paraffin or polypropylene glycol in the mixing stage, an industrially possible process, results in green densities comparable with dry mixture and die wall lubrication, which is industrially improbable. Modifying the heating profile, again industrially attainable, overcomes the problems of large gas porosity and results in uniform high density sintered specimens.

The best gas atmosphere appears to be $90N_2/10H_2$, probably slightly better than sintering in pure nitrogen. The $90N_2/10H_2$ route allows early reduction of the oxidised iron surfaces, which is necessary for graphite to be taken into solution as austenite forms [50]. When graphite is taken into solution, paths appear between powder particles to allow escape of CO/CO_2, thus preventing build up of potentially damaging gas pressure. The nitrogen route however is purely carbothermic and thus uses up some graphite for cleaning surfaces and, in so doing, lowers the carbon available for formation of the liquid phase [108-110]. The $95N_2/5H_2$ atmosphere does not appear to provide sufficient H_2 to maintain sufficiently low atmosphere dewpoint. It should be recalled that dewpoint is defined as H_2/H_2O ratio, the higher the ratio the better the dewpoint. Now if we have excess of H_2 then, even if H_2O is formed as oxides reduce and oxygen in the furnace is reduced, the dewpoint will be good. If we have only a

marginal amount of hydrogen, in our case not more than 5%, then in some regions the dewpoint will be poor and inhibit oxide removal and thus prevent the formation of clean surfaces and strong sinter necks. Graphite solution will be delayed and possibly block escape of gas formed during processing. If liquid begins to form before surfaces are adequately cleaned, then porosity could close, but may trap gas still being formed as surfaces are cleaned. Observation of fracture surfaces confirmed the formation of isolated large pores, although the overall density was only impaired by ~0.1 g/cc.

Now, depending on the amount of liquid phase controlled by a combination of carbon and silicon contents and sintering temperature, large improvement in sintered density was obtained with gas sintering now better than that of vacuum sintering. A typical sintered microstructure was shown in Figure 4.11.

Manganese was added in the form of a gas-atomised master alloy (Fe-35Mn-4.4C) in an attempt to reduce either the sintering temperature necessary to produce sufficient liquid phase, thus promoting densification, or the amount of graphite. However, results obtained from these Mn containing compositions did not show a significant increase in sintered densities even with formation of a high amount of liquid phase (>20%) for both sintering furnaces either in vacuum or reducing atmosphere ($90N_2/10H_2$), as can be seen in Table 4.3. This was due to the manganese particles beginning to volatilise and to generate a cloud of manganese vapour (volatilisation begins at a temperature of ~700°C) [50]. This vapour will spread and fill the pores thereby covering the particles' surfaces. From the results, it can be seen that combination of Si and Mn is best avoided due to formation of stable complex spinel type of oxides. This spinel oxide formation is due to the reduction of oxides by Si as SiC reacts, diffuses and forms a liquid during the heating part of the sintering cycle starting at ~1175ºC, i.e. the point at which Gibbs free

energy, ΔG(KJ) becomes negative, see appendix A. SiO_2 and/or complex $MnSiO_3$ is in evidence in specimens containing Mn. Moreover, calculations were obtained from HSC chemistry software, showing that the carbothermic reduction of the complex oxide ($MnSiO_3$) should not occur until ~1320°C, see appendix A.

Astaloy CrL powder has been used in this work in order to increase the mechanical properties, while this powder contains elements that strengthen the α-iron phase, such as Cr and Mo. During scanning electron microscope examination of Astaloy CrL powder particles' cross sections, small inclusions of silicate type slag plus a thin layer of oxide covering the particles' surfaces were both observed, obviously formed during the powder manufacturing process. These surface oxides and slag helped to prevent proper wetting of the particles' surfaces by the liquid phase, thus reducing the metallic bonding and neck growth. Because the oxides contaminated the pore surfaces and prevented adequate wetting, then huge pores were left behind, therefore densification was low compared with Astaloy 85Mo, as seen in Figure 5.4.

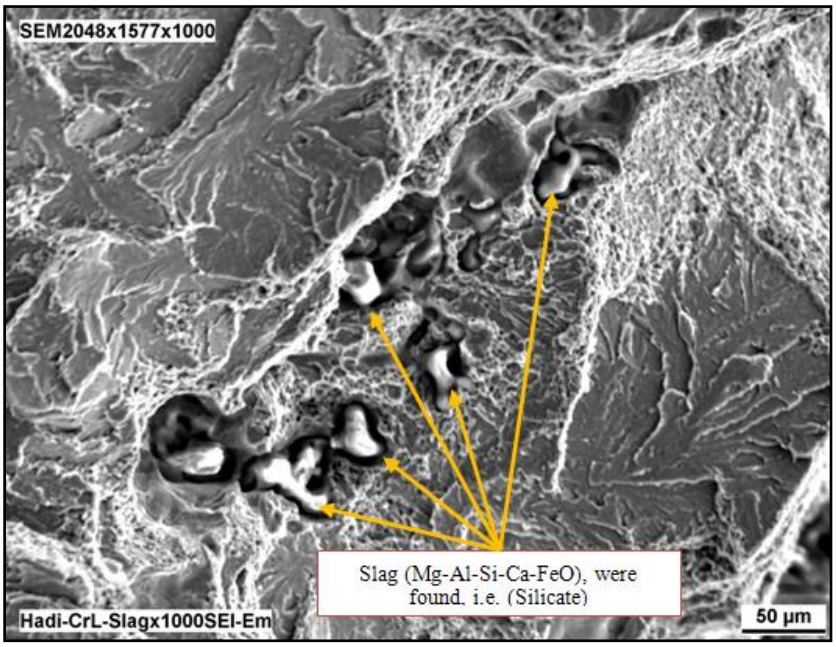

Figure 5.4: Scanning electron micrograph shows number of slag and huge pores after sintering for Astaloy CrL powder.

Considering the theoretical calculations performed and examining the obtained microstructures it can be seen that the semi-closed container method must be producing an oxygen partial pressure as low as ~$1E^{-21}$ atm. The recent work of Cias & Mitchell, 2004, [50] presented successful sintering of Mn alloy steels at 1140°C in semi-closed containers, which demands this low partial pressure of oxygen to prevent oxide of manganese from forming. However, the very low partial pressure required to dissociate SiO_2 shows that once this oxide forms there is little chance of reducing it using conventional sintering even using the semi-closed container system.

Predominance diagrams (Tpp Diagrams) are another thermodynamic method to determine the partial pressures of O_2, CO and CO_2 necessary to achieve the metal-oxide reduction at a chosen equilibrium temperature. Predominance diagrams of MnO and SiO_2 are in good agreement with the calculations stated previously in chapter three. Figures 5.5-5.6 show the oxygen partial pressure required to dissociate the metal oxide bond at different equilibrium temperatures. The partial pressure ratio of CO/CO_2 necessary for oxide dissociation at different equilibrium temperatures is shown in Figures 5.7-5.8, for metal oxides MnO and SiO_2 respectively. It can be seen that lower partial pressure of CO is necessary for oxide dissociation as temperature is lowered [50].

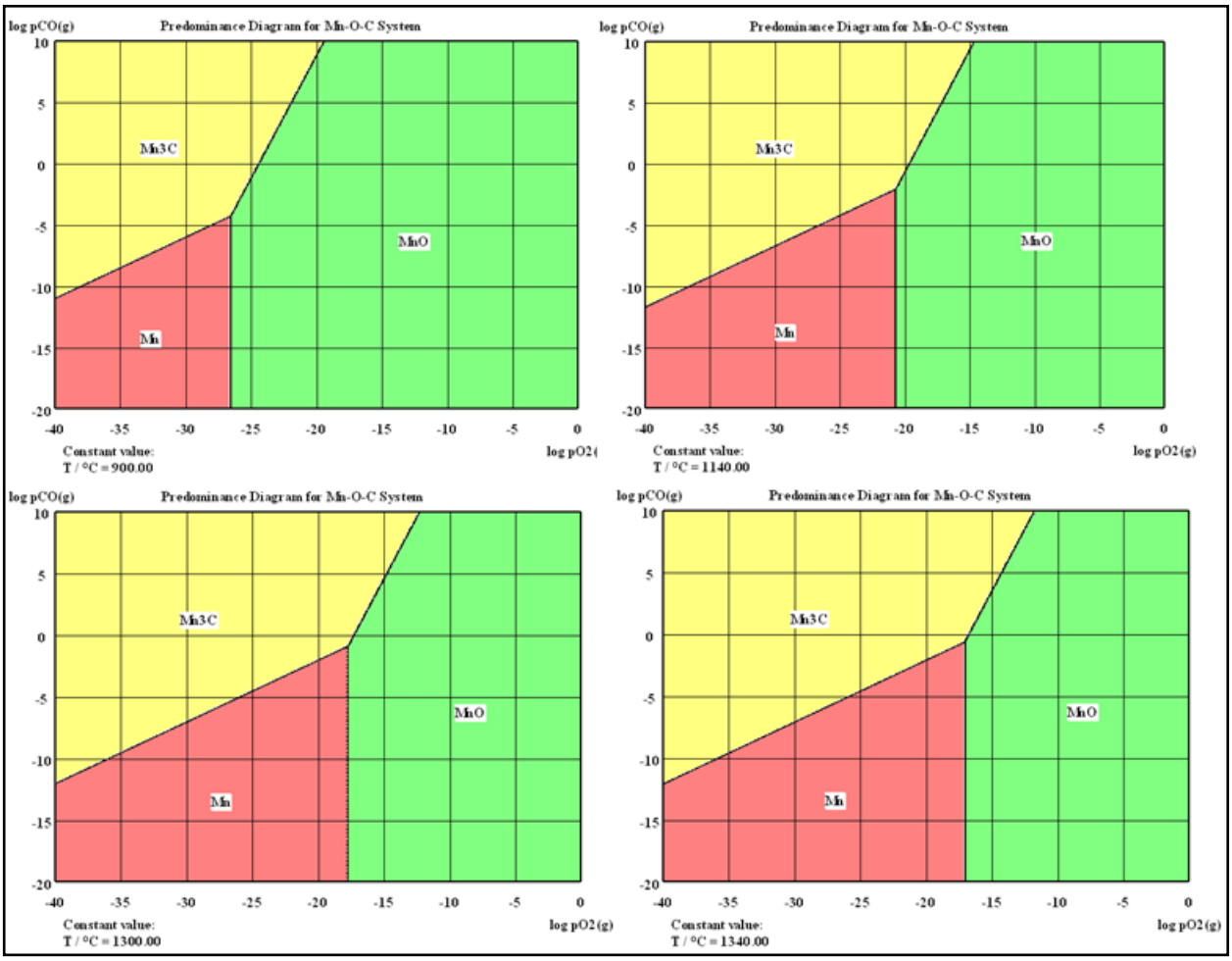

Figure 5.5: Predominance diagrams of MnO, shows the oxygen partial pressure required to dissociate the metal oxide bond at different equilibrium temperatures; upper left) ~ 900^{0}C and oxygen partial pressure 1.0E^{-26} atm, upper right) 1140^{0}C and oxygen partial pressure 1.0E^{-21} atm, bottom left) 1300^{0}C and oxygen partial pressure 1.0E^{-18} atm, bottom right) 1350^{0}C and oxygen partial pressure 1.0E^{-17} atm.

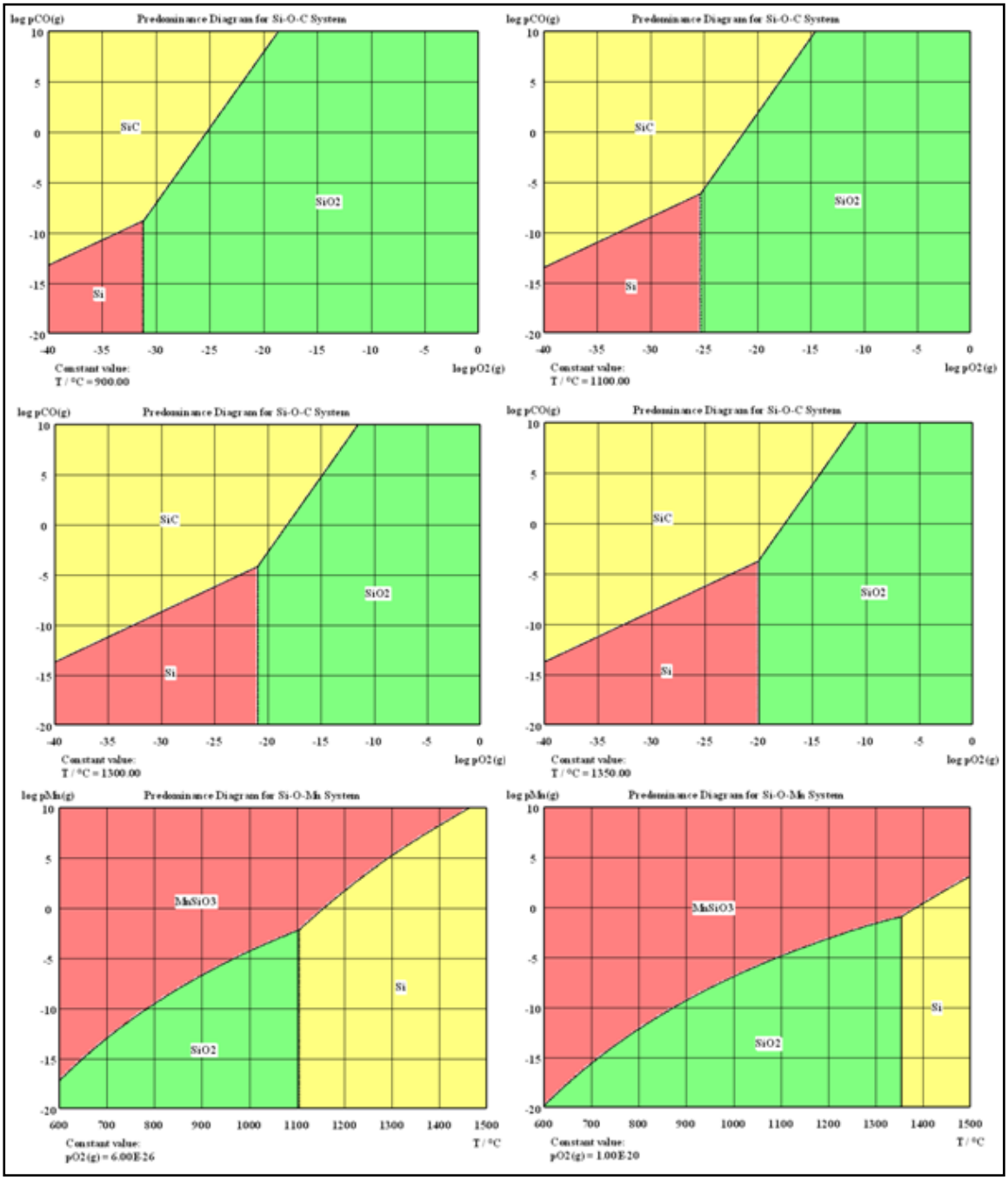

Figure 5.6: Predominance diagrams of SiO_2, shows the oxygen partial pressure required to dissociate the metal oxide bond at different equilibrium temperatures; upper left) ~ 900°C and oxygen partial pressure $1.0E^{-31}$ atm, upper right) 1100°C and oxygen partial pressure $1.0E^{-25}$ atm, mid left) 1300°C and oxygen partial pressure $1.0E^{-21}$ atm, mid right) 1350°C and oxygen partial pressure $1.0E^{-20}$ atm. Also shows '$MnSiO_3$' slag which is quite stable in the presence of Mn vapour even at high temperature, bottom left) 1100°C and oxygen partial pressure $6.0E^{-26}$ atm and bottom right) 1350°C and oxygen partial pressure $1.0E^{-20}$ atm.

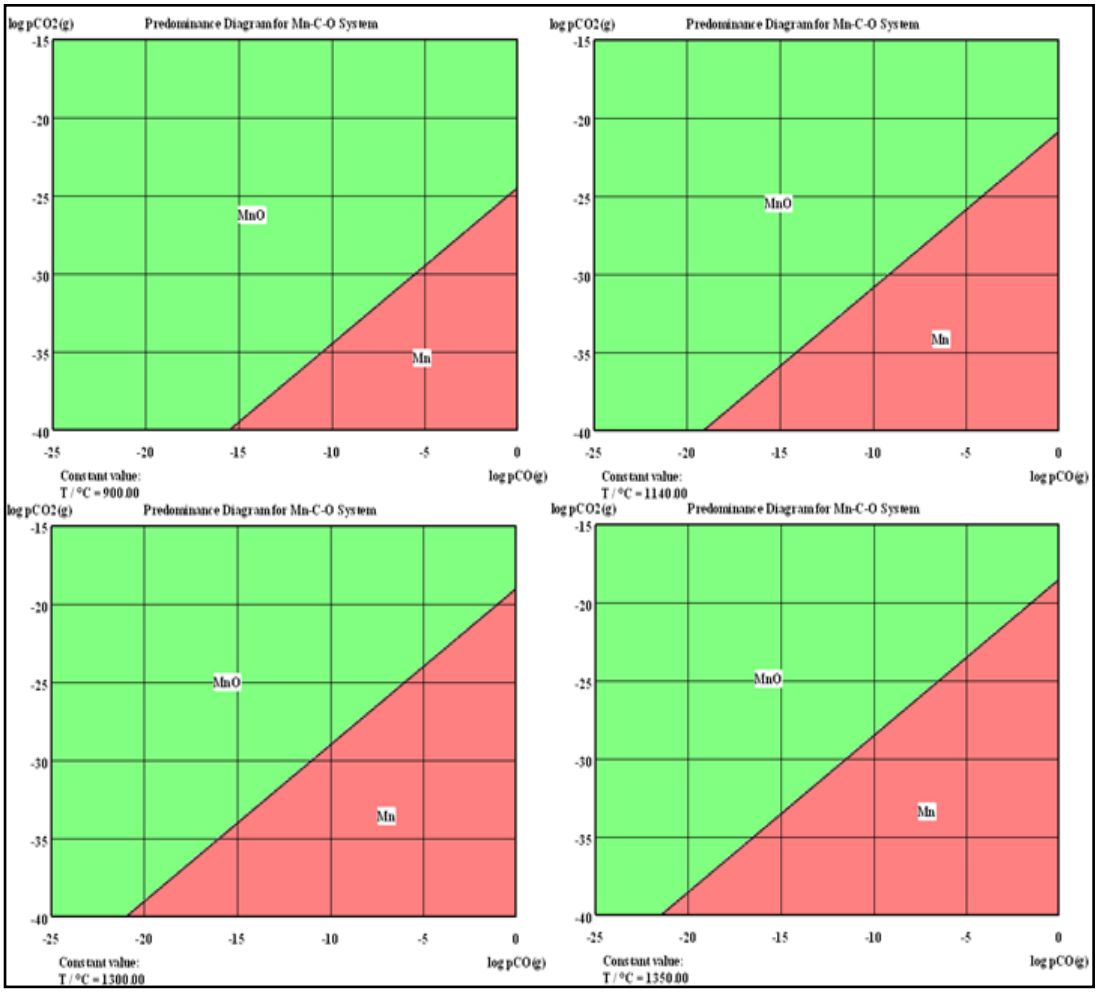

Figure 5.7: Predominance diagrams of MnO, at different equilibrium temperature shows the partial pressure of CO/CO_2, upper left) ~900^{0}C, upper right) 1140^{0}C, bottom left) 1300^{0}C and bottom right) 1350^{0}C.

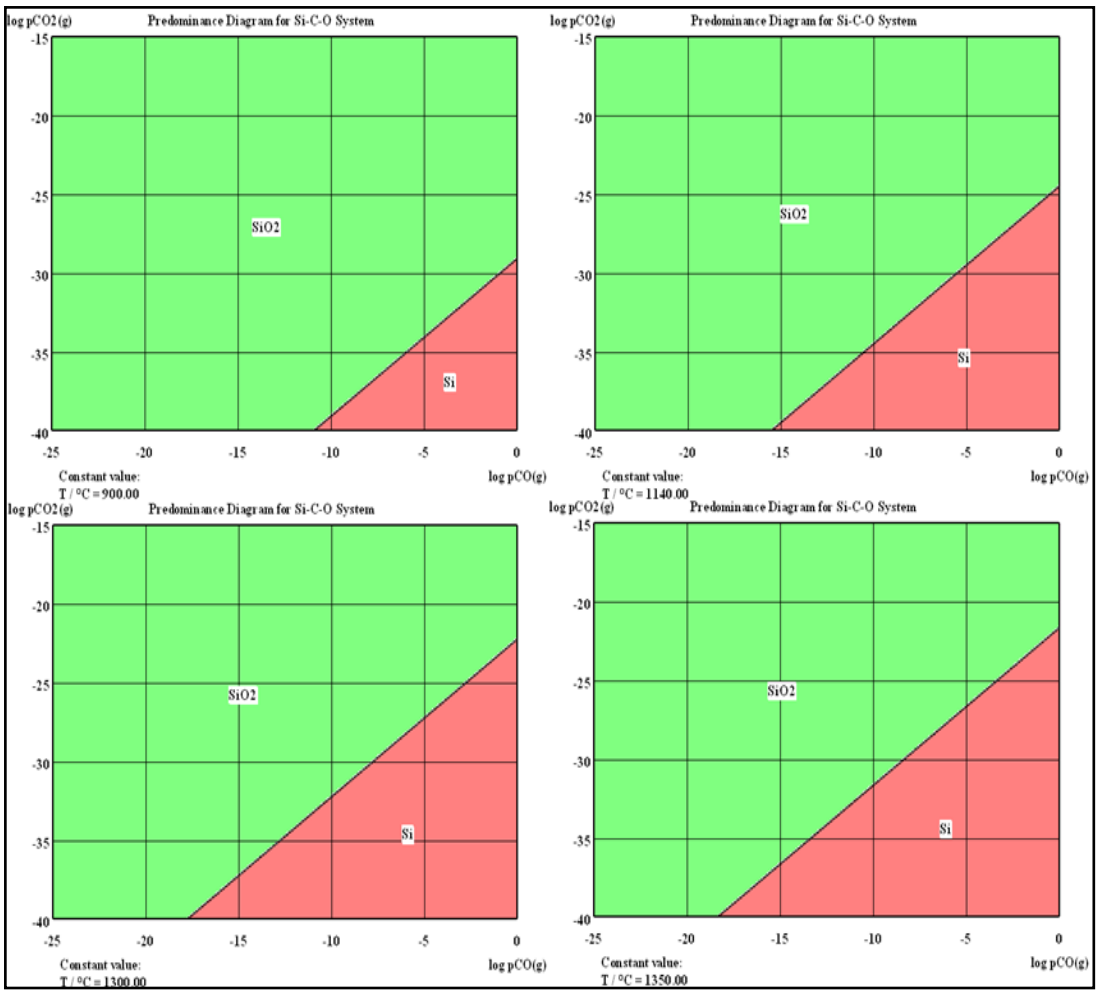

Figure 5.8: Predominance diagrams of SiO_2, at different equilibrium temperature shows the partial pressure of CO/CO_2, upper left) ~900^{0}C, upper right) 1140^{0}C, bottom left) 1300^{0}C and bottom right) 1350^{0}C.

Heat Treatment

Following the sintering success and the ability to tailor density by Thermocalc prediction of liquid phase volume percentage versus composition and temperature it was decided to experiment with a combination of heat treatments that would produce tough microstructure with the possibility of re-sizing, despite the very high carbon contents.

The heat treatment had to be modified as conventional oil quenching resulted in microcracking of the martensite, owing to thermo-mechanical shocks induced by

crystallographic volume change as martensite is formed during the fast cooling process. An isothermal quench (auto-tempering) was conducted into a fan assisted oven running at Ms-(10-15ºC) for ~20-40 minutes, in order to improve the microstructure and avoid microcracking. Calculations were attempted using e.g. Andrew's formula to predict Martensite start temperature (M_s). These calculations were obviously in error, as they suggested that M_s would be less than room temperature and from experience this was incorrect.

Predictive software using Bayesian networks [103] was also employed to predict Martensite start and Martensite 10% of completion temperatures, these results were in accord with the experimental ones. The Martensite start temperatures for various compositions are summarized in Table 4.5 and Figure 4.15 shows the data graphically. The fan assisted oven quench temperature depends on the alloy composition, as presented in Table 4.5. It is well known that martensite forms when the quenching rate is fast enough to prevent the carbon from diffusing, leading to formation of body centred tetragonal (BCT) crystal structure and a large volume change will occur. Therefore, the concept of this iso-thermal quench and hold procedure is to give enough time for carbon to diffuse, i.e. for auto-tempering take place, when the 10% of martensite transforms to tempered martensite, which in this case is composed of stable ferrite plus very fine eta-carbide. Thereby, partial loss of tetragonality of martensite occurs resulting in decrease in internal stress and an increase in toughness. When followed by cooling to room temperature to transform the rest of the available ~90% martensite to BCT structure the accompanying volume increase will not produce sufficient internal stress to create micro cracking, i.e. the generated internal stress is less than the critical internal stress to cause cracking of the martensite laths. This procedure

ensured crack-free microstructures of martensitic structure, which were then spheroidised by reheating at ~750ºC for 3 hours to produce microstructures and hardnesses comparable favourably with similarly heat-treated wrought materials [91]. It is interesting to add that microstructures of UHCS are comparable to those of Damascus steels, as reported by Sherby and Wadsworth [111] in an article entitled "Ancient blacksmiths, the Iron Age, Damascus steels, and modern metallurgy".

Mechanical properties

The three most important parameters influencing the mechanical properties of the sintered specimens were carbon content, sintering temperature and the cooling rate [73]. Carbon content plays the most important role in increasing the mechanical properties but in contrast reduces the elongation as a result of brittleness caused by presence of a network of grain boundary carbides (cementite). These cementite networks are very strong but brittle and as-sintered specimens failed at stresses of 590-720 MPa.

Hardness values, for as-sintered and heat-treated specimens, were carried out on a Vickers machine with a 10kg load (HV_{10}) and 20g ($HV_{0.02}$) load for apparent and microhardness respectively, as presented in Tables 4.6-4.9. It is clearly shown that both apparent and microhardness values increased as the silicon and manganese contents increased, because silicon is known as an effective strengthening element, while the manganese is found to be very effective in shifting the C-curves (pearlite transformation curves) to the right and allows martensite to form even at lower cooling rates, thereby increasing hardness. Carbon has less effect on hardenability, since it shifts the pearlite transformation just slightly to the right, however when the carbon increases so does the hardness due to increased amount and type of martensite [73]. Also hardness values

obtained from gas sintering are slightly higher than those obtained from vacuum sintering, this is as expected, because some amount of carbon was lost during vacuum sintering due to the Boudouard reaction.

Yield strength, UTS, % elongation, and TRS, values were investigated and measured for both as-sintered and heat treated specimens for each base powder i.e. Astaloy 85Mo and Astaloy CrL, with different additive elements such as Si, C, and Mn as well as different lubricants, at different sintering time (e.g. 30-60min), temperature (e.g. 1285, 1295 and 1300°C) and sintering atmosphere (vacuum or N_2/H_2 reducing atmosphere).

The results showed that the spheroidised specimen of Astaloy 85Mo and 1.35-1.4wt%C with an addition of 0.4-0.6wt-%Si, added as SiC, sintered at 1300ºC, improved the yield strength to ~400-410MPa, the UTS to ~900-945MPa, and the TRS to ~1644-1650 MPa, with plastic strain 16-18%. This was expected owing to, more liquid phase forming which leads to solid-solution strengthening and higher densification, these results are not as high as some literature values [13, 15, 16] for UHCSs, but the combination of strength and ductility, illustrated in Figure 4.18(b), allows further (thermo) mechanical working. However as silicon content increases so the % elongation decreases, mainly due to the ferrite strengthening effect of Si, while the cementite network precipitates. One other advantage of adding Si is that it reduces the thickness of the cementite networks formed at grain boundaries in the slow cooled as-sintered microstructure and makes solution of these networks easier to achieve in subsequent thermal treatments. Spheroidised samples of Astaloy 85Mo containing Mn showed slightly higher mechanical strength (not as much as expected) and hardness, e.g. UTS ~980MPa, Yield strength ~525MPa and TRS ~1960 MPa, with 10% plastic strain, while the hardness

was about 260HV_{10}. As stated above, Astaloy CrL powder has been used in this work in order to increase the mechanical properties, while this powder contains elements that strengthen the α-iron phase. But the mechanical properties were not high as expected, due to powder contamination which leads to low densification and therefore lower mechanical properties.

Warm Forging

Additionally and importantly the laboratory processing sequence is easily adapted to industrial processing. Warm forging compression tests at 700ºC [112] at strain rates varying from 10^{-3} - 1 sec^{-1} resulted in (nominal) strains in excess of 70%. With a sufficiently fine grain size, in the appropriate temperature range, super-plastic forming [94] should become possible with further improvement in strength and significant energy saving.

PM spheroidised steel, with yield and fracture strengths above 400 and 900 MPa, respectively, and plastic strains of ~16% has already a very useful combination of mechanical properties. These can be further enhanced, to yield strengths above 740 MPa, by warm forging at ~ 700°C. This technique has the added advantage of accurate dimensional control. Depending on strain rate, compressive peak stresses of only 150-470 MPa were required. Superplasticity, however, was not observed in this set of experiments. Further work, including with as-sintered materials, is planned. The proposed new method of evaluating yield strength of discs was shown to be acceptable by carrying out experiments on mild steel. The methodology was extended to specimens for which the yield strength could not be directly determined. Further validation, especially regarding the general applicability of the calibration factor, is required.

The yield strength increase through warm forging results from a drastically reduced (mean) grain size, *d*, from ~ 30 to 6-7 μm, formation of sub-grains, and probably an increase in the friction stress, $\sigma_{0,}$, consistent with the Hall-Petch relation:

$$\sigma_y = \sigma_0 + k_y d^{-1/2}$$

where σ_y is yield strength and k_y the Hall-Petch strengthening coefficient. Syn et al [8], for spheroidised steels, went on to express σ_0 in terms of the inter carbide spacing, which is reduced somewhat by the warm forging.

Chapter Six

6 Conclusions

In the present work, extensive experimental tests have been performed to enable the laboratory based production of ultra-high carbon powder metallurgy steels, which are high density, have excellent spheroidised microstructure and mechanical properties that combine strength and ductility. Several problems have been faced throughout this work such as, mixing, compacting, sintering conditions and heat treatment; these can be concluded as follows:

6.1 Compaction Characteristics

1. Mixing of the prealloyed powder such as Astaloy 85Mo and Astaloy CrL with additives such as graphite, silicon, and manganese for 20 minutes each resulted in good homogenous blending when liquid lubricant was added to 'glue' these additives to the base powder. This technique prevented segregation and gave reasonable green densities in the range 6.80-7.03 g/cm^3 depending on the compaction pressure.
2. The optimum compaction pressure, promoting highest densification and optimum microstructure, was found to be 600 MPa.
3. Liquid lubricant shows better densification than using either PTFE die wall spray or acrawax lubricant.
4. When liquid paraffin was substituted by polypropylene glycol diluted with 50% methanol higher sintered densities were obtained. The polypropylene glycol

burnt off leaving a network of grain boundary pores allowing escape of generated gases and the penetration of liquid phase thus enabling higher densification.

6.2 Sintering Characteristics and Microstructures Achieved

1. It became clear that the sintered density and microstructure were directly related to the alloy composition and sintering conditions such as sintering temperature, time and reducing atmosphere.
2. Predicted data obtained from ThermoCalc software was very much in accord with experimental results.
3. Drying graphite at 120°C overnight in order to reduce the moisture significantly improved the microstructure.
4. Modifying the heating profile cycle, i.e. the fourth heating profile used, produced the best results.
5. Alloy Fe-0.85Mo+0.6Si+1.4C, compacted at 600 MPa, sintered under $90N_2/10H_2$ gas at 1300°C for 60 min, gave highest sintered density ~ 7.75 g/cm^3.
6. As the silicon content increased so did the sintered density and microstructure with only very tiny pores observed. At the same time mechanical properties improved in line with density and microstructure.
7. Manganese has less effect on the sintered density, owing to manganese vapour generated during sintering process, but is very effective for increasing the hardenability of the steel.
8. Astaloy CrL, produced low sintered densities and non-uniform microstructure, resulting from as-received powder impurities, and that the data obtained from

this powder are not consistent and depend very much on the gas atmosphere employed. Furthermore, specimens were distorted by forming relatively massive 'blow-holes' especially when sintered under pure nitrogen atmosphere. These 'blow-holes' were created by gas pressure generated as chromium oxides were reduced carbothermically.

6.3 Heat treatment response and hardness values

1. Fully martensitic structures dominated all the heat treated specimens produced via both oil quenching and forced air cooling combined with upper and lower bainite and some retained austenite.
2. Micro-cracks were visible optically across the martensite laths in most of the microstructures of conventional oil quenched and air cooling heat treated specimens.
3. An isothermal quench (auto-tempering) was conducted into a fan assisted oven running at Ms-(10-15ºC) for ~20-40 minutes in order to improve the microstructure, minimise internal stress and therefore, crack-free microstructures of martensitic structure were obtained.
4. The crack-free microstructures were spheroidised by reheating at ~740-760ºC for 3 hours to give a ferrite plus fine sub-micron carbide microstructure.

6.4 Mechanical Properties

1. High mechanical properties, i.e. Yield strengths ~410 MPa, fracture strengths ~950 MPa and strains ~16% were obtained from alloy composition of Fe-0.85Mo+0.6Si+1.4C processed with polypropylene glycol diluted with 50%

methanol. This combination of properties is very unusual for ultra-high carbon steels, which normally exhibit brittle behaviour.

2. It should be emphasised that the combination of Si and Mn is best avoided due to formation of stable complex spinel type oxides, which tend to inhibit densification thus leading to lower mechanical properties.
3. Fracture microstructures showed higher ductility for base powder of Astaloy Fe-85Mo, than those made from Astaloy CrL.
4. Specimens made from Astaloy CrL powder showed lower mechanical properties than expected, due to the as-received powder contamination.
5. Generally, mechanical properties are not as high as some other results reported for UHCSs, but the combination of strength and ductility allows further (thermo) mechanical working.

6.5 Warm Forging Operation

Warm forging of spheroidised PM Fe-1.4C-0.6Si-0.85Mo at 700°C reduced the ferrite grain size from ~30 to 6-7 μm, with sub-grains and a fine dispersion of sub-micron carbides. As a result of warm forging the yield stress increased from ~ 400 to above 700 MPa. A method commonly used to determine the tensile strength of brittle materials, diametral compression of discs, has been adapted to the evaluation of the yield stress of a ductile material. These preliminary experiments indicate that warm forging promises improvement of both properties and dimensional control for knowledge transfer to an industrial situation, e.g. for high-density engine PM connecting rods.

6.6 Future Work

To consider better use of warm forging by:

1) Minimising energy usage by lowering sintering temperature thus less densification and finer prior austenite grain size, therefore possible use of post-sintering warm forging where process densification will occur at the same time as the breaking up of cementite networks and spheroidisation of carbides.
2) Investigate temperature/strain rate response by employing a heated tensile testing jig to determine optimum conditions necessary for super-plastic forming.
3) Further validation, especially regarding the general applicability of the calibration factor, is required.

References:

1. A. Lawley and T. F. Murphy, Metallurgy of powder materials, Material Characterization, 2003, 51: pp. 315-327.
2. R. M. German, Powder metallurgy of iron and steel. 1998, New York: Wiley.
3. Z. Zhang, K. Frisk, A. Salwen, and R. Sandstrom, Mechanical properties of Fe-Mo-Mn-Si-C sintered steels, Powder Metallurgy, 2004, 47(3): pp. 239-246.
4. M. R. Pickus, Improving properties of P/M steels through liquid phase sintering, International journal of powder metallurgy, Powder technology; (United States), 1984, 20(4): pp. 311-323.
5. R. M. German, Liquid phase sintering. 1985, New York: Plenum Press.
6. R. M. German, Sintering theory and practice. 1996, New York: Wiley.
7. M. M. Oliveira, J. Mascarenhas, and A. S. Wronski, Supersolidus sintering and mechanical properties of water atomised Fe-2.3C-4.0Cr-7.0Mo-10.5Co-6.5V-6.5W high speed steel, Powder Metallurgy, 1993, 36(4): pp. 281-287.
8. C. S. Wright, M. Youseffi, A. S. Wronski, I. Ansara, M. Durand-Charre, J. Mascarenhas, M. M. Oliveira, F. Lemoisson, and Y. Bienvenu, Supersolidus liquid phase sintering of high speed steels, Part 3: Computer aided design of sinterable alloys, Powder Metallurgy, 1999, 42(2): pp. 131-146.
9. S. C. Mitchell, M. Selecká, and M. Stoytchev, NATO Science for Peace Project 972395, Final Report, 2003.
10. A. Šalak, M. Selecká, and R. Bureš, Sintering atmospheres for ferrous components, In: Höganäs Chair Seminar, TU Vienna, Höganäs AB, Höganäs, 1999.

11. A. Salak and V. Riecansky, Ferrous powder metallurgy, 1995, Cambridge: Cambridge International Science.

12. H.-j. Li, B.-q. Wang, X.-y. Song, S.-z. Guo, and N.-j. Gu, New spheroidizing technique of ultra-high carbon steel with aluminum addition, Journal of Iron and Steel Research, International, 2006, 13(3): pp. 9-13.

13. O. D. Sherby, C. M. Young, B. Walser, and E. M. Cady, Superplastic ultrahigh carbon steel, 1976: US Patent No: 3,951,697, (April 20, 1976).

14. O. D. Sherby, Ultrahigh carbon steels, Damascus steels and ancient blacksmiths, ISIJ International, 1999, 39(7): pp. 637-648.

15. O. D. Sherby, M. Carsi, W. J. Kim, R. D. Lesuer, O. A. Ruano, C. K. Syn, M. Taleff E, and J. Wadsworth, Mechanical propertry-microstruture relations in iron-carbon alloys from 1.9 to 5.2% carbon, Materials Sience Forum, 2003 426-432 pp. 11-18.

16. E. M. Taleff, C. K. Syn, D. R. Lesuer, and O. D. Sherby, Pearlite in ultrahigh carbon steels: heat treatments and mechanical properties, Metallurgical and Materials Transactions A: Physical Metallurgy and Materials Science, 1996, 27 A(1): pp. 111-118.

17. J. R. Lyman and M. Orono, High carbon steel microcracking control during hardening, 1985: US-Patent No: 4523965 (June 18, 1985).

18. R. A. Grange, W. Township, and W. P. Land County, Method of Hardening hyperutectoid steel, in US Patent No: 3,337,376, (Aug. 22, 1967). 1967.

19. R. A. Grange, Method for the case carburizing of steel, 1975: United States Patent No: 3891474, (June 24, 1975).

20. R. M. German, Powder metallurgy science, 2nd ed., 1994, Princeton, N.J.: Metal Powder Industries Federation.

21. F. Thümmler and R. Oberacker, An introduction to powder metallurgy, Book, 1993, London: Institute of Materials.

22. EPMA, Introduction to Powder Metallurgy: the Process and Its Products, 1989.

23. G. Dowson, Powder metallurgy: the process and its products, 1990, Bristol: Hilger.

24. S. J. Hirschhorn, Introduction to powder metallurgy, 1969, New York, American Powder Metallurgy Institute.

25. I. Jenkins and J. V. Wood, Powder metallurgy : an overview, Institute of Metals series on powder metallurgy, 1991, London: Institute of Metals.

26. M. Selecka, A. alak, and H. Danninger, The effect of boron liquid phase sintering on properties of Ni-, Mo- and Cr-alloyed structural steels, Journal of Materials Processing Technology, 2003, 143-144(1): pp. 910-915.

27. B. H. Xiao, Z. Bin Yuan, S. Yu Ping, H. Bo, C. Gang, and A. H. Ke, Improving the performance of carbon composites by liquid phase activated sintering of MCMBs doped with Ti/Ni or Fe/Ni, 2005, 43: pp. 79-85.

28. S. B. Li, H. X. Zhai, Y. Zhou, and Z. L. Zhang, Synthesis of Ti3SiC2 powders by mechanically activated sintering of elemental powders of Ti, Si and C, Materials Science and Engineering: A, 2005, 407(1-2): pp. 315-321.

29. B. W. Chua, L. Lu, M. O. Lai, and G. H. L. Wong, Investigation of complex additives on the microstructure and properties of low-temperature sintered PZT using the Taguchi method, Journal of Alloys and Compounds, 2005, 386(1-2): pp. 303-310.

30. J. Kazior, M. Nykiel, T. Pieczonka, T. M. Puscas, and A. Molinari, Activated sintering of P/M duplex stainless steel powders, Journal of Materials Processing Technology, 2004, 157-158(SPEC. ISS.): pp. 712-717.

31. A. Upadhyaya, D. Sarathy, and G. Wagner, Advances in sintering of hard metals, Materials and Design, 2001, 22(6): pp. 499-506.

32. R. M. German and Z. A. Munir, Systematic Trends in Chemically Activated Sintering of Tungsten, Juornal of High Temperature science, 1976, Vol. 8: pp. 267-280.

33. W. D. Kingery, H. K. Bowen, and D. R. Uhlmann, Introduction to ceramics, 2nd ed. Wiley series on the science and technology of materials, 1976, New York; London (etc.)): Wiley-Interscience.

34. R. Shivanth, P. Jones, and L. Stackpole, Making metal powder articles by sintering spheroidising and warm forming, in Canadain Patent, 2252745 1997: Canada.

35. R. M. German and B. H. Rabin, Enhanced sintering through second phase additions, Powder Metallurgy, 1985, 28(1): pp. 7-12.

36. W. Khraisat and L. Nyborg, Liquid phase sintering of ferrous powder by carbon and phosphorus control, Powder Metallurgy, 2003, 46(3): pp. 265-270.

37. J. Liu and R. M. German, Densification and shape distortion in liquid-phase sintering, Metallurgical and Materials Transactions A: Physical Metallurgy and Materials Science, 1999, 30(12): pp. 3211-3217.

38. A. Lal, R. G. Iacocca, and R. M. German, Densification during the supersolidus liquid-phase sintering of nickel-based prealloyed powder mixtures,

Metallurgical and Materials Transactions A: Physical Metallurgy and Materials Science, 1999, 30(8): pp. 2201-2208.

39. R. M. German, Supersolidus liquid-phase sintering of prealloyed powders, Metallurgical and Materials Transactions A: Physical Metallurgy and Materials Science, 1997, 28 A(7): pp. 1553-1567.
40. C. S. Wright and B. Ogel, Supersolidus sintering of high speed steels Part 1: Sintering of molybdenum based alloys, Powder Metallurgy, 1993, 36(3): pp. 213-219.
41. K. S. Narasimhan, Sintering of powder mixtures and the growth of ferrous powder metallurgy, Materials Chemistry and Physics, 2001, 67(1-3): pp. 56-65.
42. W. D. Callister, Materials science and engineering: an introduction, 7th ed. 2003, New York ; Chichester: Wiley.
43. H. Danninger, S. Kremel, G. Leitner, K. Jaenicke-Roessler, and Y. Yu, Degassing during sintering of CrMo steels prepared from prealloyed powder, 2002, 13(291-301): pp. 291-301.
44. A. Cias, and S. C. Mitchell, Carbothermic reduction of oxides during nitrogen sintering of manganese and chromium steels, Powder Metallurgy Progress, 2004, Vol. 4, No. 3: pp. 132-142.
45. HSC Chemistry software, version 5.11, FIN - 28101 PORI, FINLAND.
46. R. Mariappan, S. Kumaran, and T. S. Rao, Effect of sintering atmosphere on structure and properties of austeno-ferritic stainless steels, Materials Science and Engineering: A, 2009, 517(1-2): pp. 328-333.

47. S. C. Mitchell, M. Youseffi, A. A. S. Abosbaia, and J. Ernest, Processing and heat treatment of high carbon liquid phase sintered steels, Powder Metallurgy Progress 2008, 8,No. 8: pp. 91-100.

48. M. Jaliliziyaeian, C. Gierl, H. Danninger, and E. Dudrová, Fracture Surfaces Studied on PM Steels Prepared From Prealloyed Steel Powders and Sintered in Different Atmospheres Powder Metallurgy Progress, 2008, Vol. 8, No 2: pp. 128-134.

49. S. Kremel, H. Danninger, H. Altena, and Y. Yu., Low-pressure carburizing of sintered alloy steels with varying porosity, Powder Metallurgy Progress, 2004, 4(3): pp. 119-130.

50. S. C. Mitchell, A. Cias, Carbothermic reduction of oxides during nitrogen sintering of manganese and chromium steels, Powder Metallurgy Progress, 2004, 4, No. 3: pp. 132-142.

51. P. Ortiz and F. Castro, Thermodynamic and experimental study of role of sintering atmospheres and graphite additions on oxide reduction in Astaloy CrM powder compacts, Powder Metallurgy, 2004, 47(3): pp. 291-298.

52. A. L. Ortiz, A. Munoz-Bernabé, O. Borrero-Loópez, A. Dominguez-Rodriguez, F. Guiberteau, and N. P. Padture, Effect of sintering atmosphere on the mechanical properties of liquid-phase-sintered SiC, Journal of the European Ceramic Society, 2004, 24(10-11): pp. 3245-3249.

53. J. Abenojar, F. Velasco, A. Bautista, M. Campos, J. A. Bas, and J. M. Torralba, Atmosphere influence in sintering process of stainless steels matrix composites reinforced with hard particles, Composites Science and Technology, 2003, 63(1): pp. 69-79.

54. M. Youseffi, C. S. Wright, and F. M. Jeyacheya, Effect of carbon content, sintering temperature, density, and cooling rate upon properties of prealloyed Fe-1.5Mo powder, Powder Metallurgy, 2000, 43(3): pp. 270-274.

55. S. C. Mitchell, The development of powder metallurgy manganese containing low-alloy steels, PhD Thesis, in School of engineering design and technology. 2000, University of Bradford: Bradford.

56. T. G. Pieczonka, M. Stoytchev, S.C. Mitchell, D. Teodosiev, S. Gyurov, The use of a solid hydrocarbon as a graphite substitute for Astaloy CrM sintered steel, Powder Metallurgy Progress, 2004, 4: pp. 211-244.

57. A. K. Sinha, Physical metallurgy handbook, 2003, New York ; London: McGraw-Hill.

58. K. E. Thelning, Steel and its heat treatment, 2nd ed., 1984, London: Butterworths.

59. R. B. Wilson, Metallurgy and heat treatment of tool steels, 1975, London [etc.]: McGraw-Hill.

60. S. Kalpakjian and S. R. Schmid, Manufacturing engineering and technology, 4th ed., 2001, London: Prentice Hall.

61. S. Y. Hong and H. K. D. H. Bhadeshia, Austenite Grain Size and the Martensite-Start Temperature, Scripta Materialia, 2009, 60: pp. 493-498.

62. C. Capdevila, F. G. Caballero, D. E. Garcia and C. Andres, Determination of Ms temperature in steels: A Bayesian Neural Network Model, ISIJ International, 2002, Vol. 42(No.8): pp. 894-902.

63. R. W. K. Honeycombe and H. K. D. H. Bhadeshia., Steels: Microstructure and Properties, third ed., 2006: Elsevier ltd.

64. B. L. Bramfitt and A. O. Benscoter, Metallographer's guide: practices and procedures for irons and steels, 2002, Materials Park, OH: ASM International.

65. S. A. Sajjadi and S. M. Zebarjad, Isothermal transformation of austenite to bainite in high carbon steels, Journal of Materials Processing Technology, 2007, 189(1-3): pp. 107-113.

66. M. Philip and W. Bolton, Technology of engineering materials, 2002, Oxford: Butterworth-Heinemann.

67. C. K. Syn, D. R. Lesuer, and O. D. Sherby, Influence of microstructure on tensile properties of spheroidised ultrahigh carbon (1.8 Pct C) steel, Metallurgical and Materials Transactions A: Physical Metallurgy and Materials Science, 1994, 25A: pp. 1481-1493.

68. B. L. Bramfitt and A. O. Benscoter, Metallographer's guide: practices and procedures for irons and steels, 2002, Materials Park, Ohio: ASM.

69. M. Atkins, Atlas of continuous cooling transformation diagrams for engineering steel, British Steel Corporation, 1978.

70. D. R. Askeland, F. Haddleton, P. Green, and H. Robertson, The science and engineering of materials, 3rd. S.I., 1998, Cheltenham: Stanley Thornes.

71. E. Bayraktar, F. A. Khalid, and C. Levaillant, Deformation and Fracture Behaviour of High Manganese Austenitic Steel, Materials Processing Technology, 2004, 147: pp. 145-154.

72. A. Tahara. and T. Shinohara, Influence of the alloy element on corrosion morphology of the low alloy steels exposed to the atmospheric environments, Corrosion Science, 2005, 47: pp. 2589-2598.

73. M. Youseffi, C.S. Wright, and F.M. Jeyacheya, Effect of silicon addition and process conditions upon a phase sintering, Sinter Hardening, and Mechanical Properties of Fe Mo Powder, Powder Metallurgy, 2002, 45, No.1: pp. 53-62.

74. M. Youseffi and K. Y. Chong, Enhanced sintering and mechanical properties of 316L stainless steel with silicon additions as sintering aid, Powder Metallurgy, 2003, 46(1): pp. 30-38.

75. S. Kalpakjian and S. R. Schmid, Manufacturing engineering and technology, 4th ed. 2001, London: Prentice Hall.

76. X. J. Gu, S. J. Poon, and G. J. Shiflet, Effects of carbon content on the mechanical properties of amorphous steel alloys, Scripta Materialia, 2007, 57(4): pp. 289-292.

77. P. R. Wilson and Z. Chen, The effect of manganese and chromium on surface oxidation products formed during batch annealing of low carbon steel strip, Corrosion Science, 2007, 49(3): pp. 1305-1320.

78. L. Guangmin, W. Jiansheng, F. Junfei, S. Haisheng, L. Yijian, and Z. Jingguo, Deformation behavior of an ultrahigh carbon steel (UHCS-3.0Si) at elevated temperature, Materials Science and Engineering A, 2004, 379 pp. 302-307.

79. N. Antón, J. L. Delgado, F. Velasco, and J. M. Torralba, Influence of alloying element additions on tribological behaviour of sintered steels with high content in manganese-nickel, Journal of Materials Processing Technology, 2003, 143-144: pp. 475-480.

80. A. Cias, S. C. Mitchell, A. Watts, and A. S. Wronski, Microstructure and mechanical properties of sintered (2–4)Mn–(0·6–0·8)C steels, Powder Metallurgy, 1999, Vol. 42 No. 3 (0032–5899): pp. 227-233.

81. M. Youseffi, C. S. Wright, A. S. Wronski, and A. Cias, Sintering, micerostructure, and mechanical properties of PM manganese- molybdenum steels, Powder Metallurgy, 2000, Vol. 43, No: 4(0032-5899): pp. PP. 353-358.

82. P. E. Zovas, R. M. German, K. S. Hwang, and C. J. Li, Activated and liquid-phase sintering - progress and problems, Journal of Metals 1983, 35(1): pp. 28-33.

83. M. M. A. Bepari and K. M. Shorowordi, Effects of molybdenum and nickel additions on the structure and properties of carburized and hardened low carbon steels, Journal of Materials Processing Technology, 2004, 155-156(1-3): pp. 1972-1979.

84. M. E. Garber, E. V. Rozhkova, and I. I. Tsypin, Effect of carbon, chromium, silicon, and molybdenum on the hardenability and wear resistance of white cast irons, 1969(5): pp. 11-14.

85. M. Azadbeh and N. P. Ahmadi, Effect of alloying contents and processing factors on the microstructure and homogenization of Si alloyed Cr-Mo sintered steels, Current Applied Physics, 2009, 9(4): pp. 777-782.

86. H. R. Song, E. G. Kang, and W. J. Nam, Effect of alloying elements on work hardening behavior in cold drawn hyper-eutectoid steel wires, Materials Science and Engineering A, 2007, 448-451: pp. 1147-1150.

87. T. Tarui, T. Takahashi, S. Ohashi, and R. Uemori, Effect of silicon on the age softening of high carbon steel wire, I & SM, 1994, 21(9): pp. 25-30.

88. H. Chen, Y. Y. Li, Y. B. Liu, and X. J. Cao, Influence of chromium on microstructure and sintering properties of FeNiMoCu system prealloyed

powders, Journal of Materials Processing Technology, 2007, 182(1-3): pp. 462-468.

89. O. D. Sherby, B. Walser, C. M. Young, and E. M. Cady, Superplastic ultra-high carbon steels, Scripta Metallurgica, 1975, 9(5): pp. 569-573.

90. L. Yongning, Z. Jiewu, and X. Yan, Microstructure and mechanical properties of a 1.4%C ultra high carbon steel, Key Engineering Materials, 2005, 297-300 II: pp. 1178-1182.

91. E. M. Taleff, B. L. Bramfitt, C. K. Syn, D. R. Lesuer, J. Wadsworth, and O. D. Sherby, Processing, structure, and properties of a rolled, ultrahigh-carbon steel plate exhibiting a damask pattern, Materials Characterization, 2001, 46(1): pp. 11-18.

92. O. D. Sherby, T. G. Nieh, and J. Wadsworth, Overview on superplasticity research on small-grained materials, Materials Science Forum, 1994, 170-172: pp. 13-22.

93. R. Shivanath, P. Jones, and D. T. Duc Thieu, Hi-density sintered alloy and spheroidization method for pre-alloyed powders, in US patent, 5641922. 1997.

94. S. Szczepanik and J. Sińczak, Determination of the conditions for heavy deformations of sintered steel containing 1.4%C, Metallurgy and Foundry Engineering, 1994, 20 (4): pp. 441-448.

95. S. Szczepanik and J. Sińczak, Forming of sintered high -carbon steel under superplasticity conditions, Materiały Konferencyjne V Konferencja Naukowo-Techniczna Problemy narzędziowe w obróbce plastycznej, Bydgoszcz Pieczyska, 1993, pp. 141-150

96. S. Kalathur, K. S. Narasimhan, and C. Nikhilesh, Metal-based powder compositions containing silicon carbide as an alloying powder, 2002, Hoeganaes Corporation: US-Patent.

97. H. G. Rutz and F. G. Hanejko, High density processing of high performance ferrous materials by new P/M process, Industrial Heating, 1994, 61(12): pp. 39-43.

98. M. Hrubovčáková and E. Dudrová, Thermodynamic and experimental study of role of temperature and graphite additions on oxide reduction during sintering astaloyCrL, Acta Metallurgica Slovaca, 2009, 15, No. 4: pp. 248-254.

99. D. Chasoglou, E. Hryha, and L. Nyborg, Effect of sintering atmosphere on the transformation of surface oxides during the sintering of chromium alloyed steel, Powder Metallurgy Progress, 2009, 9, No 3: pp. 141-155.

100. Standard test methods for metal powder and powder metallurgy products, 1991, Metal Powder Industries Federation.

101. Standard test methods for transverse rupture strength for sintered mtal powder specimens, ASTM Standard B 528-76.

102. A. Simchi, Effects of lubrication procedure on the consolidation, sintering and microstructural features of powder compacts, Materials and Design, 2003, 24(8): pp. 585-594.

103. C. Capdevila, F. G. Caballero, D. E. Garcia, and C. Andres, determination of ms temperature in steels: A Bayesian Neural Network Model, ISIJ International, 2002, Vol. 42(No.8): pp. 894-902.

104. P. Jonsen, H. A. Haggblad, and K. Sommer, Tensile strength and fracture energy of pressed metal powder by diametral compression test, Powder Technology, 2007, 176(2-3): pp. 148-155.

105. H. Hertz and G. Werke, Collected works, 1895, Leipzing.

106. M. M. Frocht, Photoelasticity, 1941, New York, London C: Wiley; Chapman & Hall.

107. A. T. Procopio, A. Zavaliangos, and J. C. Cunningham, Analysis of the diametrical compression test and the applicability to plastically deforming materials, Journal of Materials Science, 2003, 38(17): pp. 3629-3639.

108. S. Kremel, H. Danninger, and Y. Yu, Effect of sintering conditions on particle contacts and mechanical properties of PM steels prepared from 3%Cr prealloyed powder, Powder Metall. Progress, 2002, 2(4): pp. 211 - 221.

109. H. Danninger, C. Gierl, S. Kremel, G. Leitner, K. Jaenicke-Rößler, and Y. Yu, Degassing and deoxidation processes during sintering of unalloyed and alloyed PM steels, Powder Metall. Progress, 2002, 2(3): pp. 125 - 140.

110. G. F. Bocchini, R. Cesari, M. R. Pinasco, and E. Stagno, Sintering of carbon steels : Controlled atmospheres, equipment, practical results, in International Latin-American conference on powder technology, No: 1, 1997, Advanced powder technology: São Paulo , BRESIL. pp. 224-248.

111. O. D. Sherby and J. Wadsworth, Ancient blacksmiths, the Iron Age, Damascus steels, and modern metallurgy, Journal of Materials Processing Technology, 2001, 117(3): pp. 347-353.

112. S. Szczepanik and S. C. Mitchell, unpublished results, 2009.

113. F. Kick, Das Gestz Des proportionalen Widerstandes und Anwendung, Felix (1885).

114. E. Meyer: Investigations of hardness testing and hardness. Phys., Z. 9, 66 (1908).

Appendix A: 'Metal oxide reduction reactions'

HSC Chemistry was used to calculate the metal oxide reduction temperature as seen in the following reactions.

Reaction of SiC with the MnO.

HSC chemistry results are tabulated below.

$SiC + 3MnO = SiO_2 + 3Mn + CO(g)$

T °C	deltaH kcal	deltaS cal/K	deltaG kcal	K	Log(K)
1000	51.71	35.522	6.486	7.70E-02	-1.113
1020	51.721	35.53	5.775	1.06E-01	-0.976
1040	51.732	35.539	5.064	1.44E-01	-0.843
1060	51.742	35.547	4.354	1.93E-01	-0.714
1080	51.753	35.554	3.642	2.58E-01	-0.588
1100	53.318	36.704	2.918	3.43E-01	-0.464
1120	53.386	36.753	2.183	4.55E-01	-0.343
1140	54.803	37.757	1.446	5.98E-01	-0.224
1160	54.897	37.823	0.69	7.85E-01	-0.105
1180	**54.992**	**37.889**	**-0.067**	**1.02E+00**	**0.01**
1200	55.089	37.955	-0.825	1.33E+00	0.122
1220	55.187	38.022	-1.585	1.71E+00	0.232
1240	55.286	38.088	-2.346	2.18E+00	0.339
1260	64.641	44.246	-3.194	2.85E+00	0.455
1280	64.739	44.309	-4.08	3.75E+00	0.574
1300	64.836	44.371	-4.967	4.90E+00	0.69
1320	64.932	44.432	-5.855	6.36E+00	0.803
1340	65.027	44.491	-6.744	8.20E+00	0.914
1360	65.122	44.55	-7.634	1.05E+01	1.022
1380	65.216	44.607	-8.526	1.34E+01	1.127
1400	65.309	44.663	-9.419	1.70E+01	1.23

Reaction of SiC to reduce the MnO formed during the heating part of the sintering cycle begins at ~1175°C, i.e. the point at which delta G (kJ) becomes negative. This must be why we see SiO_2 or perhaps complex $MnSiO_3$ in our sintered specimens. Some Si will

have gone into solution in the Fe matrix as we have seen during sinter quench experiments where SiC is beginning to dissociate at ~900-1000°C.

Reduction of Complex oxide (MnSiO3).

It is also possible that a complex oxide ($MnSiO_3$) could be formed during partial reduction of MnO starting at ~1150°C.

SiC + 4MnO = MnSiO3 + 3Mn + CO(g)

T °C	deltaH kcal	deltaS cal/K	deltaG kcal	K	Log(K)
1000	44.903	31.66	4.595	1.63E-01	-0.789
1020	44.919	31.673	3.962	2.14E-01	-0.67
1040	44.936	31.686	3.328	2.79E-01	-0.554
1060	44.954	31.699	2.694	3.62E-01	-0.442
1080	44.972	31.712	2.06	4.65E-01	-0.333
1100	46.546	32.869	1.412	5.96E-01	-0.225
1120	46.622	32.924	0.754	7.62E-01	-0.118
1140	48.049	33.935	0.094	9.67E-01	-0.015
1160	**48.154**	**34.008**	**-0.586**	**1.23E+00**	**0.089**
1180	48.261	34.083	-1.267	1.55E+00	0.191
1200	48.37	34.157	-1.949	1.95E+00	0.289
1220	48.481	34.232	-2.633	2.43E+00	0.385
1240	48.594	34.308	-3.318	3.02E+00	0.479
1260	57.964	40.476	-4.091	3.83E+00	0.583
1280	58.078	40.55	-4.901	4.90E+00	0.69
1300	74.228	50.876	-5.806	6.41E+00	0.807
1320	74.421	50.997	-6.825	8.64E+00	0.936
1340	74.612	51.116	-7.846	1.16E+01	1.063
1360	74.802	51.233	-8.87	1.54E+01	1.187
1380	74.99	51.348	-9.896	2.03E+01	1.308
1400	75.177	51.46	-10.924	2.67E+01	1.427

Possibility to reduce complex MnSiO3 oxide carbothermically.

The reducing of the complex $MnSiO_3$ oxide carbothermically, should not occur until ~1320°C but in our semi-closed container (providing it is almost full to reduce amount of gas volume available) then the amount of O_2 available coupled with a low positive pressure of CO <<1atmosphere should lower the reaction temperature. This should ensure that at least some of the complex oxide is reduced back to Mn and Si for alloying with the matrix.

$MnSiO_3$ + 4C + H_2O = Si + Mn + 4CO(g) + H_2(g)

T	deltaH	deltaS	deltaG	K	Log(K)
C	kcal	cal/K	kcal		
1000	259.943	165.639	49.06	3.78E-09	-8.422
1020	259.447	165.252	45.751	1.85E-08	-7.733
1040	258.95	164.871	42.45	8.60E-08	-7.066
1060	258.452	164.494	39.156	3.81E-07	-6.42
1080	257.953	164.123	35.87	1.61E-06	-5.794
1100	257.972	164.138	32.587	6.50E-06	-5.187
1120	257.491	163.79	29.307	2.52E-05	-4.598
1140	257.46	163.765	26.035	9.40E-05	-4.027
1160	256.986	163.433	22.763	3.38E-04	-3.472
1180	256.512	163.104	19.497	1.17E-03	-2.933
1200	256.039	162.781	16.238	3.90E-03	-2.409
1220	255.564	162.461	12.986	1.26E-02	-1.901
1240	255.09	162.145	9.74	3.92E-02	-1.407
1260	257.7	163.864	6.472	1.20E-01	-0.923
1280	257.224	163.556	3.197	3.55E-01	-0.45
1300	240.71	152.997	0.023	9.93E-01	-0.003
1320	**240.154**	**152.646**	**-3.034**	**2.61E+00**	**0.416**
1340	239.598	152.299	-6.083	6.67E+00	0.824
1360	239.042	151.957	-9.126	1.67E+01	1.221
1380	238.488	151.619	-12.161	4.05E+01	1.608
1400	237.933	151.286	-15.19	9.65E+01	1.984

Appendix B: ‘Publications’

Powder Metallurgy Progress, Vol.8 (2008), No 2

PROCESSING AND HEAT TREATMENT OF HIGH CARBON LIQUID PHASE SINTERED STEELS

Stephen C Mitchell[1], Mansour Youseffi[1], Alhadi A S Abosbaia[1], Jonah Ernest[2]

Abstract
This work attempts to offer solutions to some of the problems of processing high carbon, high-density steels. Thermocalc modelling was used to predict the amount of densifying liquid phase for a range of alloys versus sintering temperature, in the range 1285 to 1300°C and 1.2 to 1.4wt.% C. The water gas reaction forms CO gas in the early part of sintering and can lead to large porosity, which lowers mechanical properties. With the use of careful powder drying, low dew point atmospheres and optimisation of heating profiles, densities in excess of 7.4 g/cc can readily be achieved. The brittle microstructure, containing carbide networks, is transformed by intelligent heat treatment to a tougher one of ferrite plus sub-micron spheroidised carbides. This gives the potential for production of components, which are both tough and suitable for sizing to improve dimensional tolerance.

Keywords: PM processing, high-carbon steels, heat treatment, brittle carbides, spheroidisation, ductility, CO generation.

INTRODUCTION

Previously Mitchell et al [1, 2] attempted high-carbon sintering utilising thermally degraded PVC as the major carbon donor bonded to the iron base powder. The use of thermally degraded PVC was in response to problems of banding of the microstructure, which occurred due to segregation of graphite during handling [3]. Degradation of PVC is environmentally damaging due to hydrochloric acid forming as chlorine is driven from the PVC and which acts to catalytically convert the structure to a conjugated polymer containing double bonds. Therefore the subject was subsequently revisited using only graphite as the carbon source, but now bound to the surfaces of the base powder by judicious use of liquid paraffin during the mixing process. It is the purpose of this communication to show that a careful combination of Thermocalc modelling, powder mixing, processing and heat treatments can help minimise the potential problems of high carbon sintering and create a microstructure suitable for the production of components with good dimensional tolerance and which are subjected to high cyclical loadings.

EXPERIMENTAL PROCEDURES

Höganäs Astaloy 85Mo HP was used as the base iron powder. Carbon was introduced as fine graphite (of 99.5% purity) varying from 1.2 to 1.45wt%. 0.2 – 0.6 wt% silicon was added as fine <9μm silicon carbide powder and manganese as fine <20μm Fe-Mn-C in the form of a gas atomised master alloy. Starting compositions chosen can be seen in Table 1. Turbula powder mixing was performed initially without a binder and then as follows: the base powder and silicon carbide (plus Fe-Mn-C master alloy when required) were mixed for 20 minutes and then 0.5 cc of liquid paraffin/100 g of powder mix was carefully added and mixing resumed for 20 minutes in order to coat base powder and additive metal powders with paraffin. The mixing was then stopped, graphite powder added and mixing re-started in order to 'glue' the graphite to the base powder particles.

Stephen C Mitchell, Mansour Youseffi, Alhadi S. Abosbaia, Engineering Materials Research Group, School of Engineering, Design & Technology, University of Bradford, Bradford, United Kingdom
Jonah Ernest, Botswanan Bureau of Standards, Botswana

Die compaction at 600 MPa of 15.3 mm x 15.3 mm x 5 mm size specimens was performed and followed by sintering in nearly full semi-closed steel containers with a labyrinth seal, illustrated in Fig.1. Pure (99.9%) alumina paper was placed between the bottom of the container and the samples to ensure no diffusion of carbon between sample and container. The container had no additional oxygen getter material. The container was pushed into the mullite tube furnace. The furnace atmospheres were either 10% hydrogen – 90% nitrogen with a gas flow of ~500 cm^3 min^{-1} and an inlet dew point no worse than -60°C or vacuum. At least 6 compacts were simultaneously sintered; heating rates were 10°C min^{-1} to 600ºC with a hold of 15 minutes for removal of liquid paraffin and adsorbed water and hydroxides, then 10ºC min^{-1} to 900ºC with a hold of 2 hours, to allow distribution of the carbon and silicon, followed by heating to the sintering temperature at 5ºC min^{-1} with sintering time of 30 minutes at sintering temperatures varying from 1285 to 1295°C. After sintering, the specimens were allowed to cool slowly to room temperature.
Heat treatments were performed using a container with flowing argon atmosphere placed into a pre-heated muffle furnace to dissolve carbide networks, followed by quenching to produce a martensite plus retained austenite structure. The samples were then placed immediately into a refrigerator in an attempt to transform some of the retained austenite to martensite. This quenching procedure was later modified to an iso-thermal treatment and is detailed in the following text. A spheroidising treatment followed using a container with flowing argon gas inserted into a muffle furnace and heated to AC1 plus 20ºC temperature for a particular alloy then held for 2 hours, followed by slow cooling to room temperature.

Metallographic specimens were prepared by mounting in Bakelite, polishing, etching in Nital (2 vol.% HNO_3 in ethanol) and examined either using a Reichert MeF3 optical microscope or a JEOL 6400 scanning electron microscope equipped with a Kevex Sigma-3 microanalysis system.

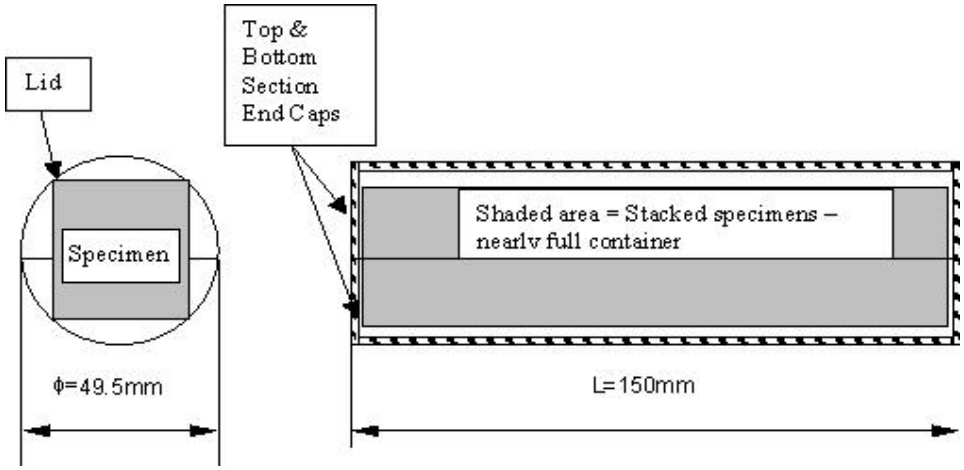

Fig. 1: Schematic of semi-closed sintering container

To minimise the number of necessary sintering experiments, Thermocalc, TCW3, thermo-chemistry software was used to generate phase equilibrium diagrams with the especial aim to predict the amount of liquid phase that would be present for a given alloy at a particular sintering temperature. The assumption was made from experience that ~15 to 20% volume of liquid would be necessary for efficient liquid phase sintering and densification. The effect of varying the amounts of carbon, silicon and manganese was modelled and typical results are presented in Table 1 below.

Table 1: Thermocalc Liquid Phase Volume % versus temperature and composition.

Base-Powder	Carbon wt. %	Silicon wt. %	Manganese wt. %	Temperature (ºC)	Liquid Phase %
Astaloy 85Mo	1.3	0.3	0.0	1285	2.19
	1.3	0.3	0.0	1295	5.81
	1.3	0.4	0.0	1285	8.57
	1.3	0.4	0.0	1295	12.3
	1.3	0.5	0.0	1285	10.81
	1.3	0.5	0.0	1295	13.37
	1.3	0.6	0.0	1285	10.8
	1.3	0.6	0.0	1295	15.27
	1.4	0.3	0.0	1285	13.44
	1.4	0.3	0.0	1295	16.67
	1.4	0.4	0.0	1285	14.7
	1.4	0.4	0.0	1295	18.1
	1.4	0.5	0.0	1285	16.40
	1.4	0.5	0.0	1295	19.9
	1.4	0.6	0.0	1285	18.1
	1.4	0.6	0.0	1295	20.8
	1.27	0.6	1.5	1300	18.8
	1.3	0.65	1.00	1300	20.00

EXPERIMENTAL RESULTS

Microstructural observations of Figures 2a and 2b led to the belief that the additional porosity and its size must be linked to gas evolution during the heating cycle. The obvious gas production route was that of the water gas reaction (see below for details). It was decided therefore to dry the graphite by heating to 120ºC overnight in a vacuum oven and then reproducing the same composition mixes but with reduced water content. The results can be seen below in Figures 3 and 4: Figure 3 shows gas sintered microstructure before graphite drying and Figure 4 after graphite drying. Even after drying the best density obtained at 1295ºC in gas atmosphere was ~7.4 g/cm^3 compared with 7.55 g/cm^3 sintered in vacuum. This is clearly illustrated in Figure 5.

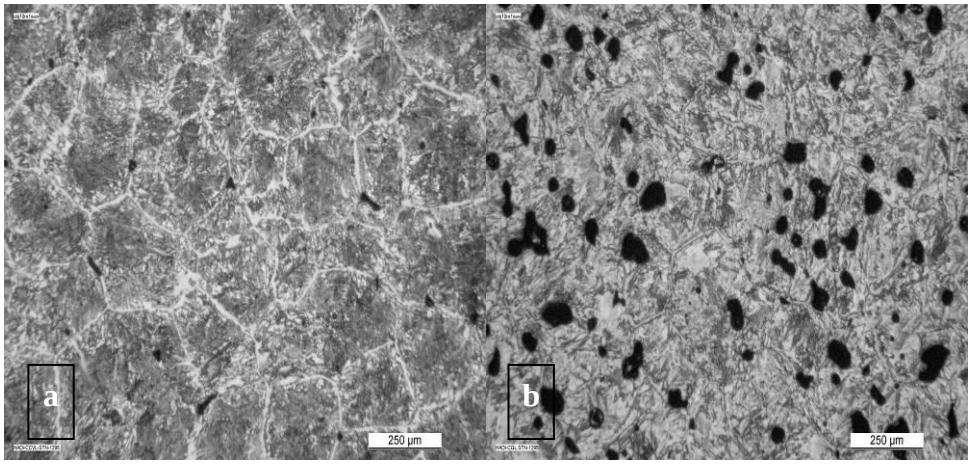

Figure 2: Microstructural variation for the same composition (Fe-0.85%Mo+0.6%Si+1.4%C+0.5cc LP) in different sintering furnaces a) vacuum furnace (left) and b) gas atmosphere ($90N_2/10H_2$) furnace (right).

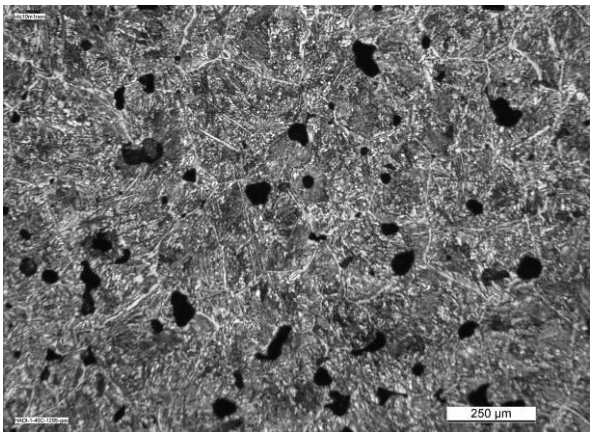

Figure 3: Large pores of alloy composition Fe-0.85%Mo+0.6%Si+1.4%C+0.5 cc LP:

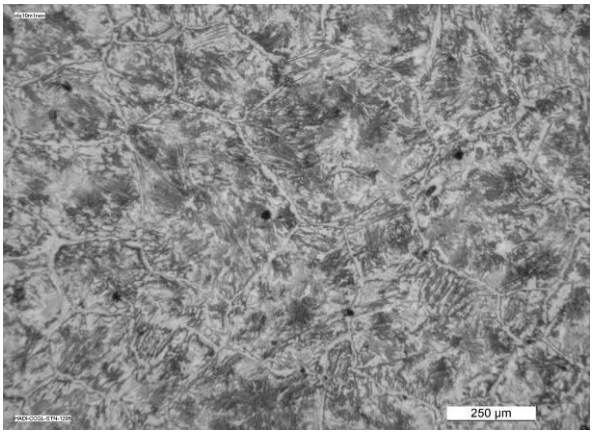

Figure 4: Few pores of alloy composition Fe-0.85%Mo+0.6%Si+1.4%C+0.5cc

Again, on comparing vacuum and gas sintered microstructures, it was obvious that some gas 'bubbles' were still preventing maximum densification during sintering. It was therefore decided to adjust the conventional sintering heating profile to minimise the amount of alpha sintering due to the Fe in Fe self diffusion by speeding up the heating rate and also increasing the temperature for the first hold to above the alpha-gamma transition temperature. The profile was changed as follows: heat 10ºC min^{-1} to 900ºC with a hold of 15 minutes for removal of liquid paraffin and adsorbed water and hydroxides, then 10ºC min^{-1} to 1100ºC with a hold of 2 hours to allow distribution of the carbon and silicon, followed by heating to the sintering temperature at 5ºC min^{-1} with sintering time of 30 minutes.

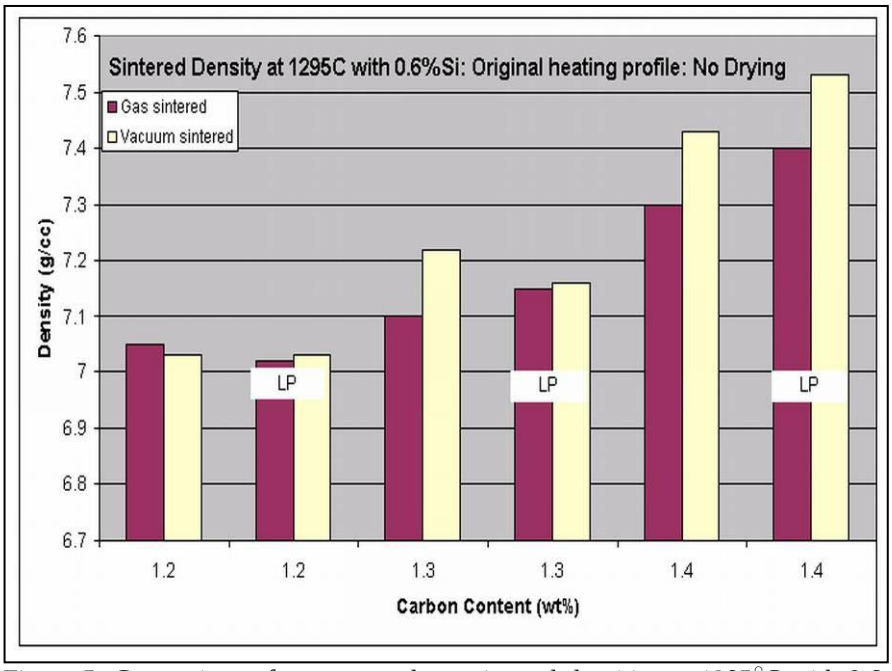

Figure 5: Comparison of vacuum and gas sintered densities at 1295°C with 0.6wt% Si addition versus temperature (LP=liquid paraffin): original heating profile.

The results showed significant improvements in sintered densities, which can be seen below in Table 3 and a graphical representation in Figure 6.

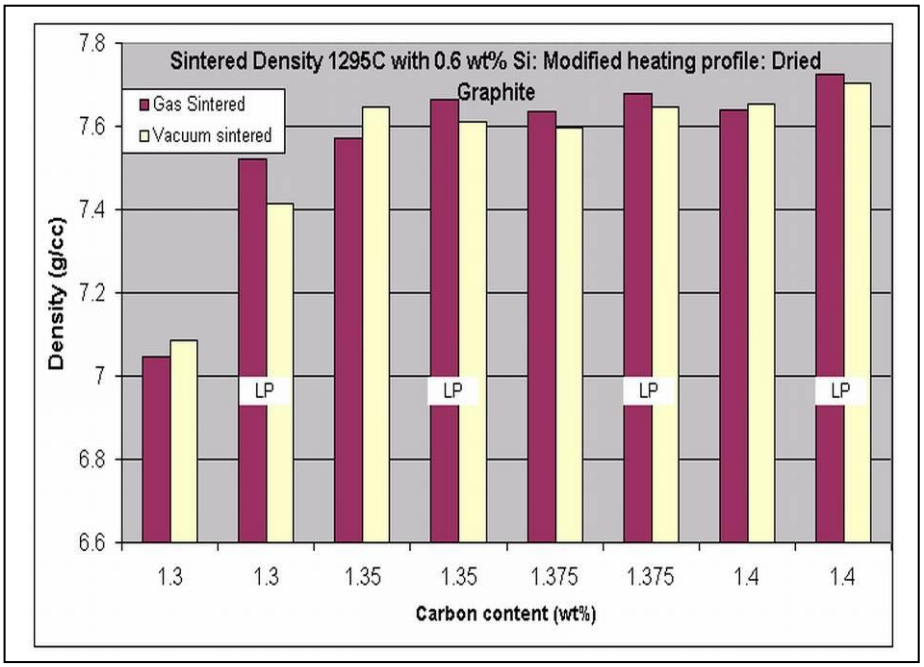

Figure 6**:** Comparison of vacuum and gas sintered densities at 1295°C with 0.6wt% Si addition versus temperature (LP=liquid paraffin): Dried graphite plus modified heating profile.

Table 3: Density results for gas and vacuum sintering after modification of the heating profile and drying of graphite powder.

Gas Furnace Results 1295ºC: Fe-0.85%Mo-0.6%Si: LP=liquid paraffin: Heating Profile 2			
Composition (Wt%)	Sample No.	Green Density (g/cc)	Sintered Density (g/cc)
1.4C + LP	1.1	6.84	7.70
1.4C + LP	1.2	6.78	7.75
1.4C	2.1	6.74	7.65
1.4C	2.2	6.87	7.63
1.375C + LP	7.1	6.84	7.67
1.375C + LP	7.2	6.87	7.69
1.375C	8.1	6.92	7.64
1.375C	8.2	6.89	7.63
1.35C + LP	5.1	6.86	7.64
1.35C + LP	5.2	6.81	7.63
1.35C	6.1	6.83	7.70
1.35C	6.2	6.88	7.61
1.3C + LP	3.1	6.76	7.54
1.3C + LP	3.2	6.87	7.50
1.3C	4.1	6.84	7.05
1.3C	4.2	6.79	7.04
Vacuum Furnace Results 1295ºC: Fe-0.85%Mo-0.6%Si: LP=liquid paraffin: Heating Profile 2			
Composition Wt%	Sample No.	Green Density (g/cc)	Sintered Density (g/cc)
1.4C + LP	1.3	6.86	7.69
1.4C + LP	1.4	6.75	7.72
1.4C	2.3	6.88	7.66
1.4C	2.4	6.80	7.65
1.375C + LP	7.3	6.93	7.65
1.375C + LP	7.4	6.93	7.64
1.375C	8.3	6.89	7.59
1.375C	8.4	6.89	7.60
1.35C + LP	5.3	6.90	7.62
1.35C + LP	5.4	6.90	7.60
1.35C	6.3	6.88	7.63
1.35C	6.4	6.90	7.66
1.3C + LP	3.3	6.88	7.39
1.3C + LP	3.4	6.92	7.44
1.3C	4.3	6.81	7.10
1.3C	4.4	6.94	7.07

Metallographic and Microstructural Observations

The sintered microstructures consisted of fine pearlite plus cementite networks at the grain boundaries. A typical example is presented in Fig. 7 containing 1.4wt%C and 0.6wt%Si sintered at 1295ºC. The microstructures of both gas and vacuum sintered samples were very similar when processed using dried graphite and the modified heating profile. It is obvious from the microstructure that the material would be brittle due to the grain boundary cementite network and it was necessary to design heat treatments to confer some ductility to the compacts.

Severe quenching into oil from 970°C invariably led to micro-cracking across the martensite laths (see Fig. 8) and a modified iso-thermal quench/autotemper route was chosen (see details in Discussion) and the crack-free microstructure is presented in Figure 9.

The successfully hardened alloy was spheroidised at 750°C for 2 hours to give a ferrite plus fine carbide microstructure, is presented in Figure 10.

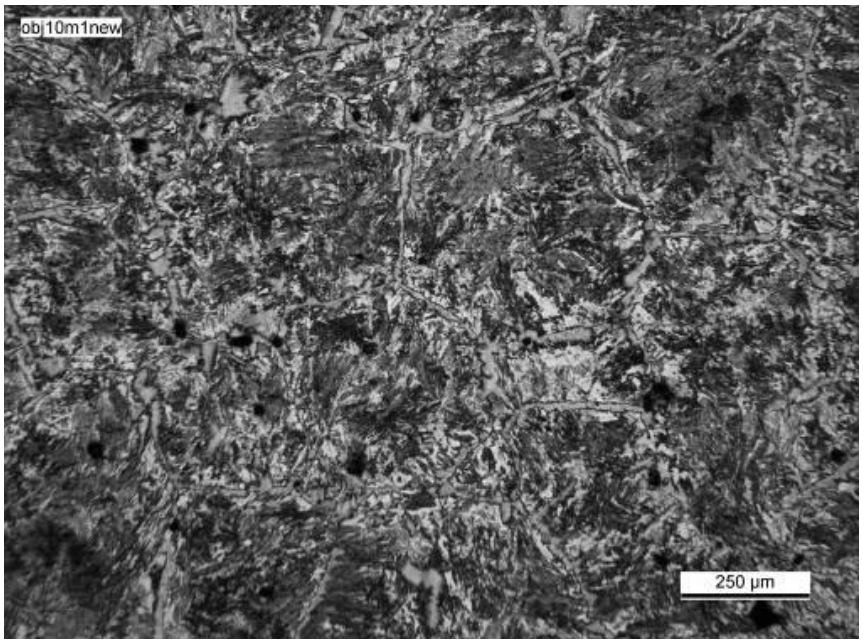

Figure 7: Typical as-sintered microstructure showing fine pearlite matrix with cementite networks at prior austenite grain boundaries.

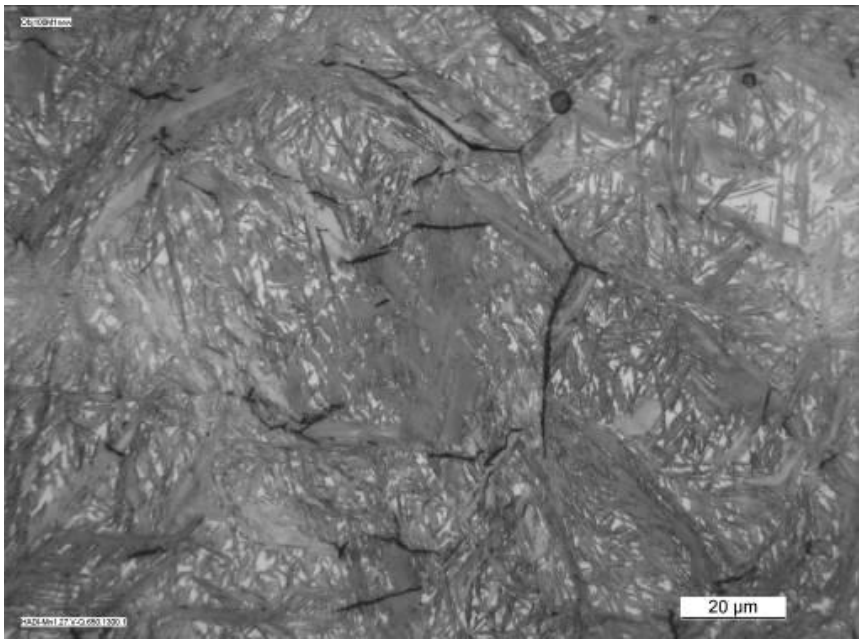

Figure 8: Microcracking resulting from large volume change of martensite during severe quench.

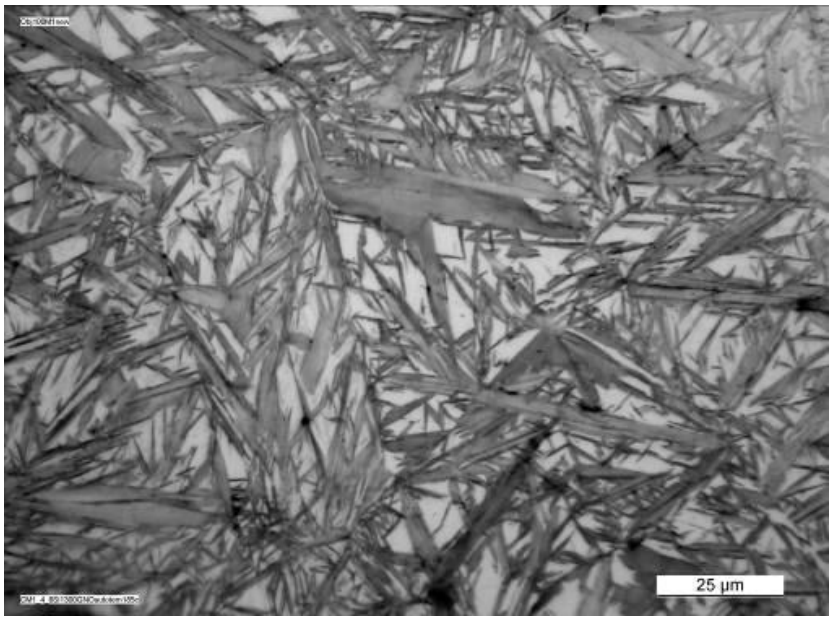

Figure 9: Martensitic microstructure free from cracks following a quench from 970°C into fan assisted oven at 180°C and isothermal hold for 2 hours, followed by removal from oven and cooling to room temperature.

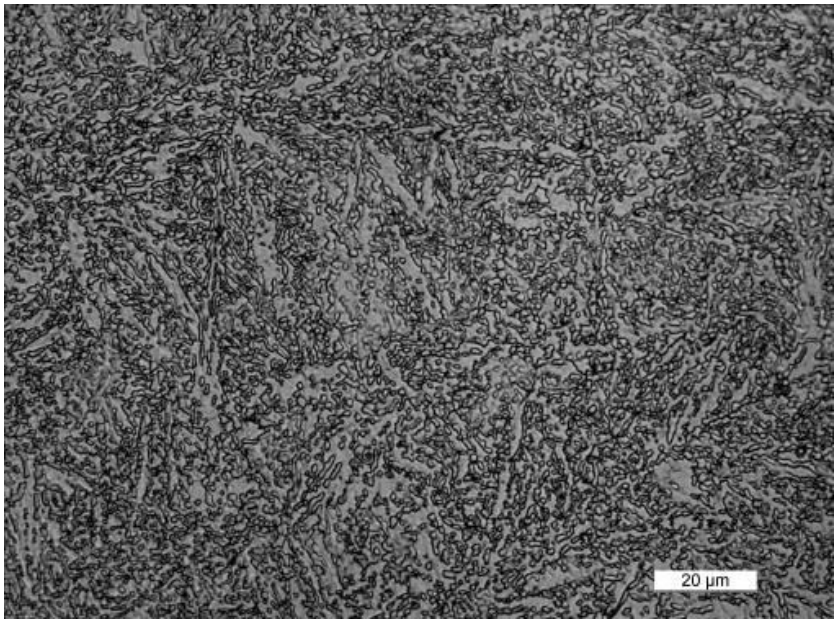

Figure 10: Microstructure following spheroidising treatment at 750°C for 3 hours: Shows ferrite matrix plus fine well dispersed spheroidal carbides.

DISCUSSION

The work presented here has the ultimate aim to increase dynamic mechanical properties by improvements in density and optimisation of microstructure by careful selection of processes, i.e. mixing, binding, alloying, heating profile and intelligent heat treatment. The modulus of ferrous materials is highly dependent on the density as can be seen in Figure 11 below.

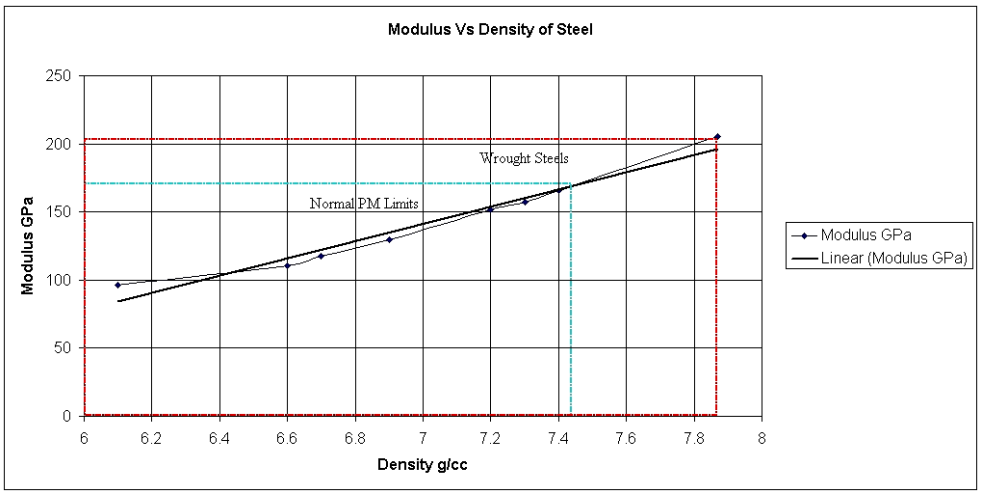

Figure 11: Dependence of Young's modulus on sintered density, also showing normal PM limits and the targeted limit for wrought materials [5].

Many challenging problems had to be solved during this work aimed at the production of a carbide plus ferrite structure soft enough to allow limited re-sizing for dimensional control, namely: inhomogenous distribution of graphite during mixing and handling, excessive gas formation creating gas 'bubbles' during sintering, micro-cracking of the structure during quenching due to volume change induced by transformation to martensite.

The graphite distribution problem was solved efficiently by introducing 0.5 cm^3 of liquid paraffin per 100g of powder to be mixed. This necessitated a modified mixing procedure where the Astaloy 85Mo and silicon carbide powders were Turbula mixed with liquid paraffin for 10 minutes, then the graphite powder was added and further mixing took place for 15 minutes to 'glue' the graphite to the Astaloy 85Mo. After this procedure was put into place, no further problems of graphite separation were noted.

The problem of gas formation and the large sintered porosity presented more of a challenge to solve. It was noted that, on comparing the initial trial samples from gas and vacuum furnace sintering, porosity was less for vacuum. This was obviously because more gas could be pulled from the internal part of the vacuum sintering compact during the early part of heating while porosity was still interconnected. Also the evolving gas must be formed either from reduction of oxides or from adsorbed water vapour. CO_2/CO gas production is dictated by kinetics as follows:

$C + H_2O \rightarrow CO + H_2$ (Water gas reaction: From ~500ºC)
$C + 2FeO \rightarrow 2Fe + CO_2$ (From ~500ºC)
$CO_2 + C \rightarrow 2CO$ (Boudouard reaction: From ~500ºC complete ~930ºC)

Therefore removal of the adsorbed water vapour was attempted by drying the graphite at 120ºC in a vacuum oven overnight before mixing. This proved successful in reducing the porosity but did not completely remove it, especially in the gas sintering process. It was discovered that there was another reason for retention of gas porosity. Remembering that self diffusion of Fe in Fe is approximately 100 times greater in the alpha phase than in gamma phase and that time is also a strong variable, the heating profile was changed to minimise time spent in the alpha temperature range to reduce solid-state densification. Also the temperature to ensure efficient carbon and silicon diffusion was increased to

1100ºC from 900ºC with a hold of 2 hours before finally raising to the sintering temperature at 5ºC min^{-1} with sintering hold of 30 minutes. This combination finally proved successful in increasing sintered density and removing the large gas pores in the structure.

Now, depending on the amount of liquid phase controlled by a combination of carbon and silicon contents and sintering temperature, large improvement in sintered density was obtained with gas sintering now closely resembling that of vacuum sintering. A typical sintered microstructure was shown above in Figure 7.

Following this success and the ability to tailor density by Thermocalc prediction of liquid phase volume percentage versus composition and temperature it was decided to experiment with a combination of heat treatments that would produce tough microstructure with the possibility of re-sizing, despite the very high carbon contents. Lessons for prospective heat treatments can be learned from the area of high carbon wire drawing and also from experiments conducted by the Stackpole Company over the last decade. It was decided to use a simple quenching heat treatment to produce initially a martensite plus retained austenite structure. This was performed by heating in a small container, through which argon was flowing, placed into a muffle furnace pre-heated to 950ºC and held for 30 minutes after reaching temperature to ensure that all carbides were taken into solution. The samples were quickly quenched into oil, then sectioned and microstructures examined carefully. This showed problems of microcracking, where large volume change and hence build up of internal stress had occurred. The experiments were repeated using air cooling to room temperature but again microcracks appeared due to the high hardenability of the material. This again prompted some serious thought to provide a solution to the problem and after consulting heat treatment text books and looking at TTT and CCT diagrams, it was decided to attempt an isothermal quench into a fan assisted oven running at 180ºC. This temperature was decided on after performing calculations for martensite start temperature (Ms) using Andrew's formula [4]. For the Fe- 0.85Mo-0.6Si-1.4C material the Ms temperature was found to be 210ºC and the Ms-10% temperature ~180ºC. To improve the chances of success this iso-thermal quench was allowed to run for 2 hours in the hope that auto-tempering of the martensite laths would reduce internal stresses before the compacts were removed from the furnace and allowed to transform further on cooling to room temperature. The samples were sectioned and examined and showed no micro-cracking and still showed hardness of ~650-700HV_{10}.

These successfully hardened specimens were then given a standard spheroidising treatment to try to produce a ferrite plus sub-micron carbide structure suitable for structural components such as automotive or compressor connecting rods and also soft enough to allow a modest amount of re-sizing for dimensional control purposes. A typical spheroidised microstructure is shown in Figure 10 having a hardness of ~160-180HV_{10}.

CONCLUSIONS

The work reported here looks extremely promising with gas sintering now producing marginally higher density than the more expensive vacuum sintering route. Mechanical and re-sizing tests are planned for the near future to ensure that the microstructural evidence obtained is adequately translated into the necessary properties for commercial exploitation.

Further work is planned and the effects of manganese additions, in the form of a master alloy powder, are also being investigated in an attempt to reduce either the amount of graphite or the sintering temperature necessary to produce sufficient liquid phase to promote densification.

ACKNOWLEDGEMENTS

The authors wish to thank The School of Engineering, Design & Technology at The University of Bradford for making facilities available for this work and are grateful to Hoganas UK for supplying the Astaloy 85Mo base powder. Also thanks are expressed to Ms. Linda Maude for her technical assistance.

References:

1. Mitchell Stephen C., Georgiev Jordan and Stoytchev Marin, "Mechanical properties of Mn-Cr-Mo steels nitrogen sintered from hydrocarbon-coated powders"**,** Proc. of PM2004 Congress, Vol. 3, pp 313-318, Vienna, 17- 21st October, 2004. ISBN 1899072 15 2

2: T. PIECZONKA, J. GEORGIEV, M. STOYTCHEV, S.C. MITCHELL, T. TEODOSIEV and S. GYUROV, *Proc. Euro PM2003*, EPMA, Vol. 1, pp 441-446.
3: S.C. MITCHELL, M. SELECKÁ, M. STOYTCHEV, *NATO Science for Peace project 972395 Final Report*, April 2003.
4: Steel Forming and Heat Treatment Handbook, Antonio Augusto Gorni, April 2007, www.gorni.eng.br .
5: United States Patent US5516483: Hi-density Sintered Alloy, Stackpole Ltd. (CA), 1996.

LIQUID PHASE SINTERING, HEAT TREATMENT AND PROPERTIES OF ULTRA HIGH CARBON STEELS

by

ALHADI A S ABOSBAIA, STEPHEN C MITCHELL, MANSOUR YOUSEFFI and ANDREW S WRONSKI

Abstract

ThermoCalc modelling was employed to predict liquid phase amounts for Fe-0.85Mo- (0.4-0.6)Si-(1.2-1.4)C in the temperature range 1285-1300ºC and such powder mixes were pressed and liquid phase sintered. In high-C steels carbide networks form at the prior particle boundaries, leading to brittleness, unless the steel is heat-treated. To assist the breaking up of these continuous carbide networks, 0.4-0.6% silicon, in the form of silicon carbide, was added. After solution of processing problems associated with the formation of CO gas in the early part of the sintering cycle, and hence large porosity, densities in excess of 7.75g/cc were attained. A spheroidising treatment resulted in microstructures having the potential of producing components, which are both tough and suitable for sizing - to improve dimensional tolerance. Yield strengths up to 410 MPa, fracture strengths up to 950 MPa and strains of up to 16 % were attained.

Keywords: Ultra-high carbon PM steels, phase diagram modelling, liquid phase sintering, spheroidisation.

Mr. A.A.S. Abosbaia, Dr. S.C. Mitchell, Dr. M. Youseffi and Professor Emeritus A. S. Wronski are with the Engineering Materials Group of the School of Engineering, Design and Technology, University of Bradford, West Yorkshire, BD7 1DP, UK.

Introduction

Liquid phase sintering, technically proven for e.g. high speed steels[1-3], has been shown, on the laboratory scale[4], to be applicable to structural steels. For direct sintering to full density of high speed steels, annealed high-carbon powders tend to be used. When the starting powder is low-carbon (alloyed) iron, however, one of the processing problems is the introduction of carbon. If it is added simply as graphite, segregation during handling[5] results in banding of the microstructure. Mitchell et al[5] attempted high-carbon sintering utilising PVC, which had been heated in argon atmosphere to catalytically convert the structure to a conjugated polymer containing double bonds, as the major carbon donor bonded to the iron base powder. This conversion technique, however, is environmentally damaging, as hydrochloric acid forms from the PVC and is driven off as a corrosive vapour. This communication deals with a modified method of introducing graphite, by a judicious use of liquid paraffin or polypropylene glycol, bound to the surfaces of the base powder, during the mixing process. In order to optimise the sintering cycle, ThermoCalc modelling was employed to design and predict combinations of alloy composition(s) and temperature(s) to maintain a permanent liquid phase during sintering, and thus promote densification with a low porosity microstructure.

Ultrahigh-carbon steels[6-17], UHCSs, i.e. where C is in the range of 1.0-2.1%, have tended to be neglected by industry due to their brittleness, resulting from the presence of a severe grain boundary carbide network. Traditional heat treatments used for normal steels create coarse microstructures[9]; a spheroidisation treatment, however, can produce fine spheroidised carbides in fine ferrite. PM UHCSs have been extensively studied by Sherby et al [6,8,9,11-15]. Yield strengths reaching 1.5 GPa[10] and super-plastic properties [7,11,14,15,17] of UHCSs have been reported.

EXPERIMENTAL PROCEDURES

Höganäs Astaloy Mo85HP was used as the base iron powder. Carbon was introduced as fine graphite (of 99.5% purity), varying from 1.2 to 1.45wt%, and silicon, 0.4 – 0.6 wt%, was introduced as fine <9µm silicon carbide, which reacts with the iron powder forming a Fe-Si-C liquid phase at ~1080°C (ThermoCalc). Starting compositions are recorded in Table 1. Turbula dry mixing of the base powder and graphite was carried out for 20 minutes. Using dry wall lubrication, these powders were pressed: adequate green densities were recorded, but the microstructures exhibited banding. To distribute C and Si uniformly, the heating profile included a high temperature hold below the sintering temperature. Liquid paraffin was introduced into the powder mix, increasing the base carbon level by about 0.05%, thus creating more liquid phase during sintering. Then powder mixing was performed as follows: 100 g of the base powder and silicon carbide were dry mixed for 20 minutes. Then 0.5 cc of liquid paraffin was

carefully added to the powder and mixing resumed for 20 minutes - thereby coating the metal powders with paraffin. The mixing was then stopped, graphite powder added and mixing re-started in order to 'glue' the graphite to the base powder particles. Metallographic specimens 15.3 mm x 15.3 mm x 5 mm high were die compacted, generally at 600 MPa. Green and sintered densities were measured using physical calculation for ρ: green densities were ~ 6.8 g/cc.

Sintering was carried out in nearly full semi-closed steel containers[18] pushed into a mullite tube furnace, with pure (99.9%) alumina paper placed between the bottom of the container and the samples - to ensure no diffusion of carbon between sample and container. Each container had a labyrinth seal, but no additional oxygen getter material. The furnace atmospheres were either vacuum or nitrogen plus 0-10% hydrogen, with a gas flow of ~500 cm^3 min^{-1} and an inlet dew point no worse than -60°C. Sintering temperatures were chosen in accord with ThermoCalc calculations (see Fig. 1) to ensure presence of 2-20% liquid phase (Table 1). At least 6 compacts were simultaneously sintered. Dry mixed compacts were concurrently sintered with those that had liquid paraffin added to the powder mix.

Initially heating rates were 10C min^{-1} to 600ºC with a hold of 15 minutes for the removal of liquid paraffin and adsorbed water and hydroxides, then 10ºC min^{-1} to 900ºC, with a hold of 2 hours, to allow distribution of carbon and silicon, followed by heating to the sintering temperature at 5ºC/min, with sintering time of 30-60 minutes at temperatures varying from 1285 to 1300°C. After sintering, the specimens were allowed to cool slowly to room temperature.

Microstructural observations of initially sintered specimens showed excessive porosity. It was noted that, on comparing samples from gas and vacuum sintering, that porosity was less for vacuum, because more gas could escape from the internal part of the sintering compact during the early stage of heating in vacuo, while porosity was still interconnected. As the evolving gas must be formed either from reduction of oxides or from adsorbed water vapour, via the water-gas reaction: $C + H_2O \rightarrow CO + H_2$, from ~500ºC, therefore graphite was dried by heating to 120ºC overnight in a vacuum oven.

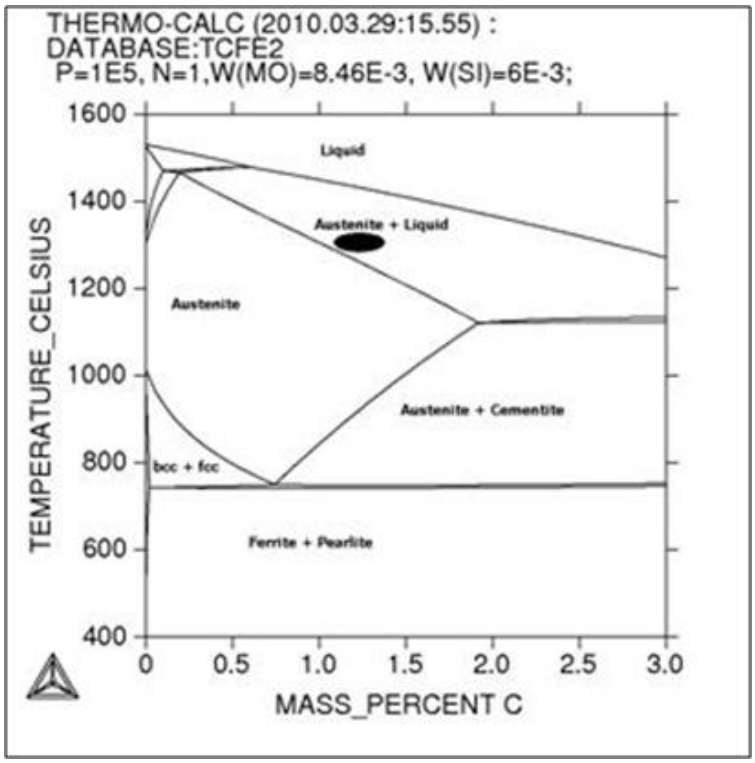

Fig. 1. ThermoCalc Phase Diagram for Fe.0.85Mo.0.6Si-C.

Table 1: Starting powder compositions and Thermocalc % volume liquid-phase calculations at selected temperatures.

Carbon wt. %	Silicon wt.%	Temperature, ºC	Liquid Phase, %
1.3	0.3	1285	2.2
		1295	5.8
	0.4	1285	8.6
		1295	12.3
	0.5	1285	10.8
		1295	13.4
	0.6	1285	10.8
		1295	15.3
1.35	0.6	1300	19.6
1.4	0.3	1285	13.4
		1295	16.7
	0.4	1285	14.7
		1295	18.1
	0.5	1285	16.4
		1295	19.9
	0.6	1285	18.1
		1295	20.8
		1300	22.6

This procedure was only partially successful; after drying the best density obtained at 1295ºC in gas atmosphere was ~7.40 g/cc and ~7.55 g/cc for vacuum. Gas escape was hindered by very low carbon diffusion rates below 600ºC, at 900ºC graphite will diffuse into the now austenitic Fe-Mo, creating linked porosity to facilitate gas escape. To reduce this type of porosity, an alternative mixing procedure was then employed in which polypropylene glycol, diluted to 50% by methanol, was substituted for the liquid paraffin. Noting that self diffusion of Fe in Fe is approximately 100 times greater in the alpha than in the gamma phase and that time is also a strong variable, the heating profile was changed to minimise time spent in the alpha temperature range.

The heating rate was increased to 20ºC/min and the 900ºC hold was reduced to 10 mins. This still ensured that graphite could begin to go into solution in the austenite and leave gaps (pores) for escape of any gases produced, simultaneously with minimisation of CO_2/CO production and any alpha phase sintering. The temperature to ensure carbon and silicon diffusion and homogenisation was increased from 900ºC to 1100ºC, with a hold of 2 hours. Finally at 5ºC/minute temperature was raised for sintering at 1285-1300 ºC for 30-60 mins, followed by slow-cooling. Large improvement in (macroscopic) sintered density was obtained, with gas sintering now closely resembling vacuum sintering and propylene glycol processed specimens possessing a homogeneous porosity distribution.

Initially a simple quenching heat treatment to produce a martensite plus retained austenite structure was performed. This involved loading the specimens into a small container, through which argon was flowing, placing it into a muffle furnace pre-heated to 950ºC and holding for 45-60 minutes after reaching this temperature - to ensure that all carbides were taken into solution. The samples were then quenched into oil, which resulted in some micro-cracking, where large volume change and hence build up of internal stress had occurred. Air cooling to room temperature did not solve the problem due to the high hardenability of the material and an isothermal quench into a preheated fan assisted oven proved necessary.

A temperature of 130ºC was decided, since the martensite start temperature, M_s, for Fe-0.85Mo-0.6Si-1.4C is 145ºC and the M_s-10% temperature 130ºC[19,20]. To promote auto-tempering of the martensite laths, this isothermal quench was for 2 hours, which also reduced internal stresses before the compacts were

removed from the oven, and allowed further transformation on cooling to room temperature. The crack-free hardened specimens were then given a standard spheroidising treatment to produce a ferrite plus sub-micron carbide structure, soft enough to allow a modest amount of resizing for dimensional control purposes.
Polished metallographic specimens were etched in 2 % Nital and examined either using a Reichert MeF3 optical microscope or a JEOL 6400 scanning electron microscope equipped with a Kevex Sigma-3 microanalysis system. Hardness tests, on as-sintered and heat-treated specimens, were carried out on a Vickers machine with a 10 kg load (HV_{10}). Tensile specimens were uniaxially pressed at 600MPa using a spring loaded floating dog-bone type die to dimensions specified by ISO 2740. They were uniaxially tested on an Instron 1195 SM219 machine at a crosshead speed of 0.5 mm/min.

RESULTS

Green densities for dry-mixed specimens were generally 6.8-7.0 g/cc, decreasing with an increase in silicon content[21], and were similar for specimens processed using liquid paraffin (Table 2). Using the initial sintering profile for these specimens, optimum sintered density, 7.55 g/cc, was obtained for Fe.0.85Mo.1.45C.0.6Si sintered in vacuum at 1300ºC for 60 min., comparable to values attained by Shivanath et al[22,23]. For gas sintering similar densities were attainable, but microstructural observations of sintered samples, Fig.2a, showed, that, in spite of relatively high overall densities, there were regions of high porosity linked to gas evolution during the heating cycle. When this problem was overcome by graphite drying and modification of the heating profile, satisfactory microstructures, e.g. Fig. 2b, and densities, up to 7.75 g/cc, presented in Table 2, were attained. It should be added that closed porosity is attained at ~ 7.4 g/cc and therefore to attain this (and improvement in anti-fatigue properties) a minimum of 1.3%C is required for sintering at 1300°C.

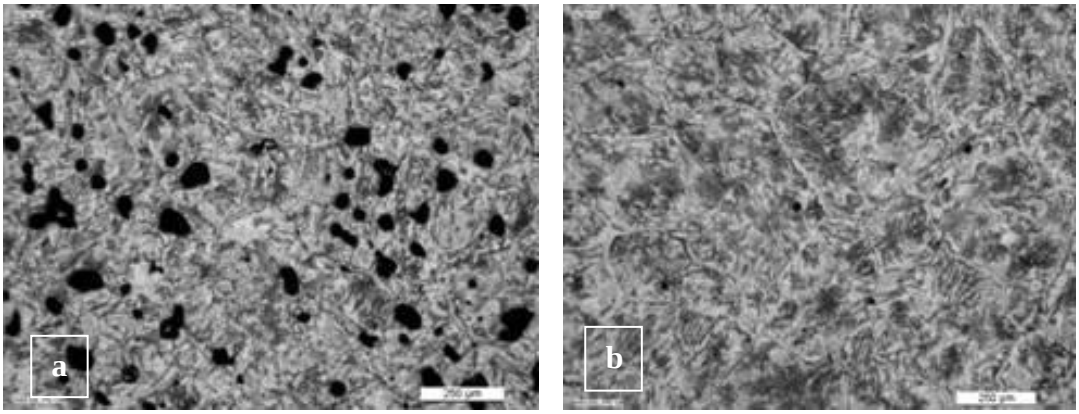

Fig. 2. Microstructural variation for liquid lubricant processed Fe 0.85%M+o.0.6%Si+1.45%C after sintering in $90N_2/10H_2$ atmosphere: (a) initial and (b) final heating profiles.

The sintered microstructures consisted of fine pearlite plus cementite networks at the grain boundaries. The materials were brittle due to the grain boundary cementite, failing at stresses of 590-680 MPa. Severe quenching into oil from 970°C invariably led to micro-cracking across the martensite laths (Fig. 3a), but, utilising a modified isothermal quench/autotemper route, a crack-free microstructure resulted, Fig. 3b. The successfully hardened alloy was spheroidised at 750°C for 3 hours to give a ferrite plus fine carbide microstructure, presented in Fig. 4.

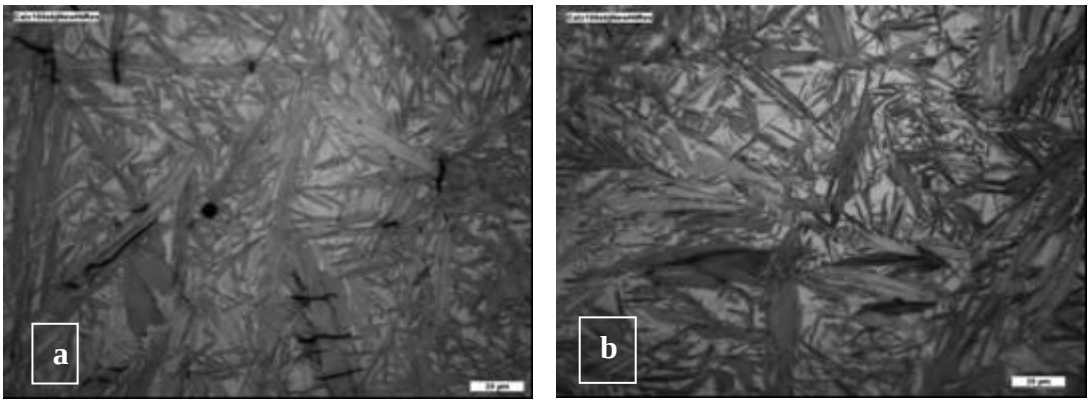

Fig. 3. (a) Microcracking in Fe0.85%Mo.0.6%Si.1.45%C resulting from severe quench-induced large volume change due to martensite formation, and (b) its absence when isothermal quench/auto-temper route was employed.

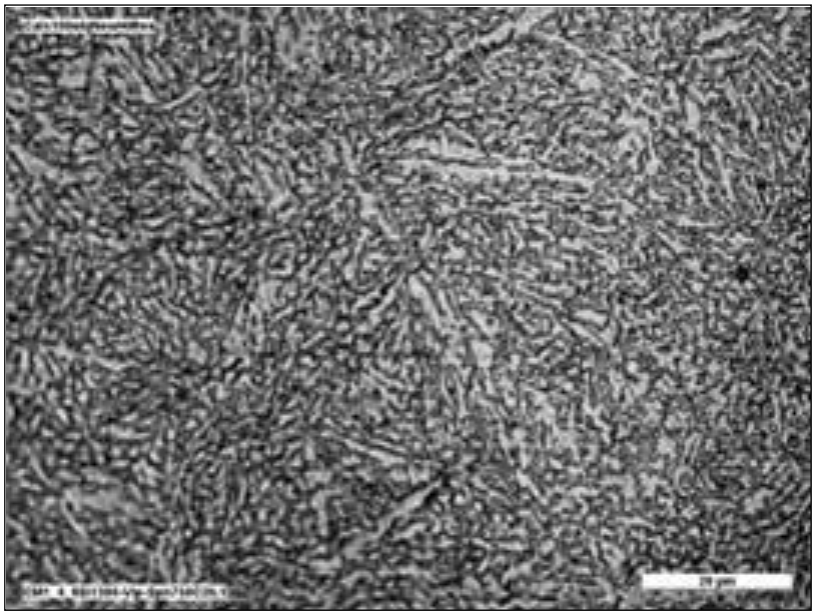

Fig. 4. Microstructure of Fe.0.85%Mo.0.6%Si.1.45%C resulting from the spheroidising treatment at 750°C for 3 hours: ferrite matrix plus fine well-dispersed spheroidal carbides.

Table 3 lists the apparent hardness values of Fe-Mo-C-Si, dry, liquid paraffin and polypropylene glycol processed specimens, (1) sintered at 1300 ºC (gas or vacuum), reheated in argon and then either (2) oil quenched or (3) quenched into a fan controlled oven followed by air cooling and refrigeration, and (4) then spheroidised. Results of tensile testing of similarly processed specimens are presented in Table 4. To be noted is macroscopic brittleness of all specimens except those spheroidised, which exhibited strains up to 16%. Fractographs of as-sintered and spheroidised tensile specimens are presented in Fig. 5; the latter showing extensive plasticity and (micro) dimple rupture.

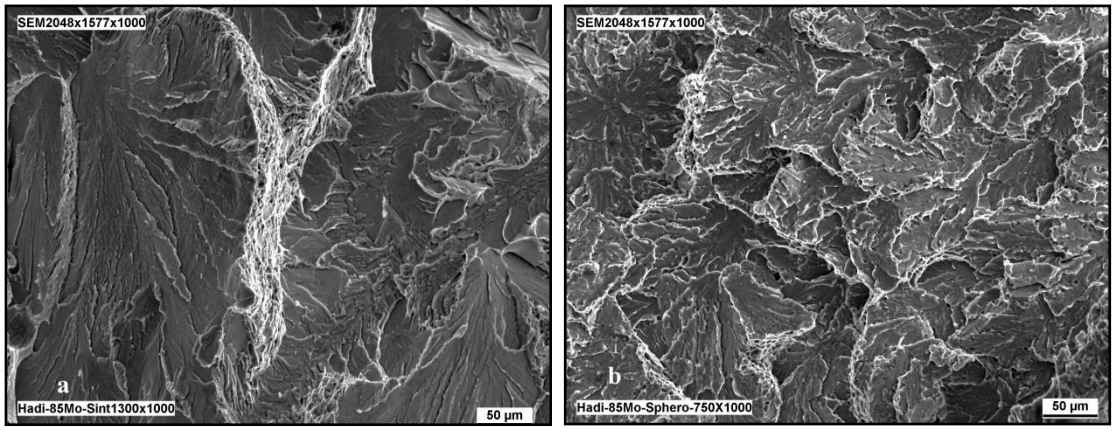

Fig. 5. Fractographs of tensile specimens of Fe.0.85Mo.0.6Si.1.4C: (a) as-sintered, macroscopically brittle: and (b) spheroidised, exhibiting 13% plastic strain. Please note in (a) cracking following cementite networks with a tiny amount of ductility in the ferrite, and in (b) extensive (micro) dimple rupture as well as cleavage and intergranular rupture.

Table 2: Densities after drying of the graphite powder and mixing with either liquid paraffin or with polypropylene glycol (diluted with 50% methanol), compacting at 600 MPa and sintering at 1300ºC for 1hour in $90N_2/10H_2$ employing the modified heating profile.

Composition	Mixing additive	Green Density, g/cc	Sintered Density, g/ cc
Fe-0.85Mo-1.25C-0.6Si	Liquid paraffin	6.95	7.25
	Polypropylene glycol	6.94	7.31
Fe-0.85Mo-1.30C-0.6Si	Liquid paraffin	6.93	7.30
	Polypropylene glycol	6.92	7.35
Fe-0.85Mo-1.35C-0.6Si	Liquid paraffin	6.87	7.54
	Polypropylene glycol	6.88	7.54
Fe-0.85Mo-1.40C-0.6Si	Liquid paraffin	6.85	7.62
	Polypropylene glycol	6.85	7.64
Fe-0.85Mo-1.425C-0.6Si	Liquid paraffin	6.83	7. 66
	Polypropylene glycol	6.84	7.69
Fe-0.85Mo-1.45C-0.6Si	Liquid paraffin	6.82	7.71
	Polypropylene glycol	6.82	7.75

Table 3: Vickers hardness, HV_{10}, for as-sintered, quenched/fan oven-air cooled and spheroidised Fe-Mo-C-Si alloys, dry processed, using A: liquid paraffin and B: polypropylene glycol diluted with methanol, B.

Composition and Processing route		Vickers hardness, HV_{10}							
		Sintered at 1300ºC		Held in argon at 970ºC for 2h				Spheroidised : 750ºC for 3h, ±10 HV_{10}	
		Vacuum ±10 HV_{10}	Gas ±10 HV_{10}	Oil Quenched, ±30 HV_{10}		Fan-Oven Cooled, ±30 HV_{10},			
				Vac	Gas	Vac	Gas	Vac	Gas
Fe.0.85Mo.1.2C.0.4Si	dry	188	196	613	620	540	546	148	151
	A(+0.05C)	205	210	621	633	560	573	157	163
Fe.0.85Mo.1.2C.0.6Si	dry	208	213	620	639	577	589	155	162
	A(+0.05C)	223	227	636	647	610	626	168	160
Fe.0.85Mo.1.3C.0.4Si	dry	215	219	634	646	614	620	161	171
	A(+0.05C)	239	242	660	669	637	651	176	168
Fe.0.85Mo.1.3C.0.6Si	dry	236	233	659	667	634	643	175	183
	A(+0.05C)	271	278	693	705	669	677	193	197
Fe.085Mo.1.35C.0.6Si	B	-	300	-	795	-	-	-	215
Fe-0.85Mo.14C.0.4Si	dry	250	256	681	688	662	669	186	194
	A(+0.05C)	291	297	767	778	679	683	214	215
Fe.0.85Mo.14C.0.6Si	dry	287	293	748	765	670	672	211	217
	A(+0.05C)	305	315	795	805	710	715	221	225
	B	-	325	-	-	-	810	-	230

Table 4: Mechanical Properties of liquid paraffin and, B: polypropylene glycol processed 1.40 and 1.45C steels sintered at 1300ºC in atmospheres of 0-10%H_2/ N_2.

Sintering atmosphere :$90N_2/10H_2$			
As-Sintered			
Composition	Yield strength, MPa	Fracture Strength MPa	Plastic Strain, %
Fe.0.85Mo.1.35C.0.6Si (B)	-	600	-
Fe.0.85Mo.1.40C.0.6Si	-	590	-
Fe.0.85Mo.1.40C.0.6Si (B)	-	630	-
Fe.0.85Mo.1.45C.0.6Si	-	610	-
Quenched			
Fe.0.85Mo.1.35C.0.6Si (B)	-	680	-
Fe.0.85Mo.1.40C.0.6Si	-	530	-
Fe.0.85Mo.1.40C.0.6Si (B)	-	700	-
Fe.0.85Mo.1.45C.0.6Si	-	592	-
Spheroidised			
Fe.0.85Mo.1.35C.0.6Si (B)	400	951	16
Fe.0.85Mo.1.40C.0.6Si	400	906	14
Fe.0.85Mo.1.40C.0.6Si (B)	410	945	15
Fe.0.85Mo.1.45C.0.6Si	410	907	12
Sintering atmosphere :$95N_2/5H_2$			
As-Sintered			
Fe.0.85Mo.1.40C.0.6Si	-	610	-
Fe.0.85Mo.1.45C.0.6Si	-	600	-
Quenched			
Fe.0.85Mo.1.40C.0.6Si	-	615	-
Fe.0.85Mo.1.45C.0.6Si	-	490	-
Spheroidised			
Fe.0.85Mo.1.40C.0.6Si	350	748	10
Fe.0.85Mo.1.45C.0.6Si	370	857	12
Sintering atmosphere : N_2			
As-Sintered			
Fe.0.85Mo.1.40C.0.6Si	-	680	-
Fe.0.85Mo.1.45C.0.6Si	-	669	-
Quenched			
Fe.0.85Mo.1.40C.0.6Si	-	690	-
Fe.0.85Mo.1.45C.0.6Si	-	586	-
Spheroidised			
Fe.0.85Mo.1.40C.0.6Si	380	893	13
Fe.0.85Mo.1.45C.0.6Si	395	880	10

DISCUSSION

Comparing the green compacts sintered both in vacuum and the $90N_2/10H_2$ atmosphere, it is evident that, with the initial sintering cycle profile, vacuum clearly provided higher densities for almost all the alloy compositions. The principal reason is higher reduction of moisture and surface oxides and better removal of the vaporized lubricants by the vacuum furnace, which also produces higher decarburisation than the gas atmosphere. When the sintering cycle was modified to minimise the amount of alpha phase sintering and to release gases from pores by speeding the heating rate to 20 ºC/min, reducing the time of the 900ºC to 10 mins, but increasing the temperature of the diffusional/homogenisation hold to 1100ºC, a network of grain boundary pores formed, allowing penetration of a liquid phase as it formed at the sintering temperature, thus producing higher densification, recorded in Table 2. Increasing the silicon content enhanced the diffusion process between the two elements and, due to contact melting between iron and silicon, liquid phase sintering was activated, thereby increasing the sintered density[24]. For the initial sintering cycle, Table 2, the increasing density with increasing carbon content and sintering temperature is due to the formation of a higher amount of a liquid phase. A good example is the alloy Fe.0.85Mo.0.6Si.1.45C sintered at 1285, 1295 and 1300ºC for 30 min with predicted liquid phase of 18.1, 20.8 and 23.0%, which attained densities of ~ 7.26, ~ 7.54 and ~ 7.55 g/cc, respectively.

These results are in accord with ThermoCalc modelling, i.e., as silicon, carbon, sintering temperature and time increased, liquid phase amount increased, Table 1, and so did the sintered density, higher than values reported for comparable compositions, ~7.40 g/cc[22,23] for vacuum sintering (a batch process). Processing involving additions of liquid paraffin or polypropylene glycol in the mixing stage, an industrially possible process, results in green densities comparable with dry mixing and die lubrication, which is industrially improbable. Modifying the heating profile, again industrially attainable, overcomes the problems of large gas porosity and results in uniform high density sintered specimens/components. The best gas atmosphere appears to be $90N_2/10H_2$, probably slightly better than sintering in pure nitrogen. The $90N_2/10H_2$ route allows early reduction of the oxidised iron surfaces, which is necessary for graphite to be taken into solution as austenite forms[4,18]. When graphite is taken into solution, paths appear between powder particles to allow escape of CO/CO_2, thus preventing build up of potentially damaging gas pressure. The nitrogen route however is purely carbothermic and thus uses up some graphite for cleaning surfaces and, in so doing, lowers the carbon available for formation of the liquid phase [26-28]. The $95N_2/5H_2$ atmosphere does not appear to provide sufficient H_2 to maintain sufficiently low atmosphere dewpoint. It should be recalled that dewpoint is defined as H_2/H_2O ratio, the higher the ratio the better the dewpoint. Now if we have excess of H_2 then, even if H_2O is formed as oxides reduce and oxygen in the furnace is reduced, the dewpoint will be good. If we have only a marginal amount of hydrogen, in our case not more than 5%, then in some regions the dewpoint will be poor and inhibit oxide removal and thus the formation of clean surfaces and strong sinter necks. Graphite solution will be delayed and possibly block escape of gas formed during processing. If liquid begins to form before surfaces are adequately cleaned, then porosity could close, but may trap gas still being formed as surfaces are cleaned. Observation of fracture surfaces confirmed the formation of isolated large pores, although the overall density was only impaired by ~0.1 g/cc.

The heat treatment had to be modified as conventional quenching resulted in microcracking of the martensite. An isothermal quench into a fan assisted oven running at M_s-(10-15ºC) was followed by cooling to room temperature - to transform the rest of the available austenite to martensite. This procedure ensured crack-free microstructures, which were spheroidised by reheating at 750ºC for 3 hours to produce microstructures and hardnesses comparable favourably with similarly heat-treated wrought materials[13]. It is interesting to add that microstructures of UHCS are comparable to those of Damascus steels, as reported by Sherby and Wadsworth[25] in an article entitled "Ancient blacksmiths, the Iron Age, Damascus steels, and modern metallurgy".

The strengths of our spheroidised samples: yield of 350-410 MPa and fractures at 750-950 MPa with strains of 10-16 %, Table 4, are not as high as some literature values [6, 9-11] for UHCSs, but the combination of strength and ductility, illustrated in Fig. 5(a), allows further (thermo) mechanical working. Additionally and importantly the laboratory processing sequence is easily adapted to industrial processing. With a sufficiently fine grain size, in the appropriate temperature range, super-plastic forming[17] should become possible. Compression tests at 700ºC [29] at strain rates of 10^{-3} - 1 sec^{-1} resulted in (nominal) strains in excess of 200%. Further experiments are planned.

CONCLUSIONS

Combination of practical work with computer programming software (ThermoCalc) allowed proper design of alloy composition and PM processing steps, terminating by liquid phase sintering, for a series of

high density ultra high carbon steels. This involved choosing the proper lubricant (best proved to be 50% polypropylene glycol/50% methanol), drying the graphite, optimising the mixing procedure and modifications to the heating stage of the sintering cycle. Similarly, the conventional spheroidisation heat treatment procedure had to be modified, especially to avoid microcracking. The best mechanical properties, including plastic strains of 12-16%, were obtained with an atmosphere of $90N_2/10H_2$, slightly better than sintering in pure nitrogen. With a sufficiently fine grain size, in the appropriate temperature range, super-plastic forming should become possible.
Detailed work is planned on the effects of manganese additions, in the form of a master alloy powder, particularly in an attempt to reduce either the amount of graphite or the sintering temperature necessary to produce sufficient liquid phase to ensure reproducible considerable densification.

ACKNOWLEDGEMENTS

The authors wish to thank The School of Engineering, Design and Technology at The University of Bradford for making facilities available for this work and are grateful to Höganäs UK for supplying the Astaloy 85Mo base powder. We are particularly grateful to Ms. Linda Maude for her technical assistance.

REFERENCES

[1]. C. S. Wright, M. Youseffi, A. S. Wronski, I. Ansara, M. Durand-Charre, J. Mascarenhas, M. M. Oliveira and Y. Bienvenu, Powder Met., 1999, 42, 131-146.
[2]. M. M. Oliveira, J. Mascarenhas, and A. S. Wronski, Powder Met., 1993, 36, 281-287.
[3]. R. M. German, 'Sintering Theory and Practice', John Wiley and Son, 1996.
[4]. S. C. Mitchell, M. Youseffi, A. A. S. Abosbaia, and J. Ernest, Powder Met. Progress, 2008, 8, 91-100.
[5]. S.C. Mitchell, M. Selecká and M. Stoytchev, NATO Science for Peace Project 972395, Final Report, 2003.
[6]. O. D. Sherby, B. Walser, C. M. Young, and E. M. Cady, Scripta Met., 1975, 9, 569-573.
[7]. H. Li, B. Wang, X. Song, S.Guo and N. Gu , JISR, Int., 2006, 13, 9-13.
[8]. O. D. Sherby, ISIJ Int. 1999, 39, 637-648.
[9]. O. D. Sherby, M. Carsi, W. J. Kim, R. D. Lesuer, O. A. Ruano, C. K. Syn,
[10]. E. M. Taleff and J. Wadsworth, Materials Science Forum, 2003, 426-432, 11-18.
[11]. W. Lin, Y. Fan, Z. Zhang, J. Zhu and Y. Liu, Key Eng. Materials, 2006, 324-325, 907-910.
[12]. E. M. Taleff, C. K. Syn, D. R. Lesuer and O. D. Sherby, Met. Mat. Trans. A,
1996, 27A, 111-118.
[13]. D. R. Lesuer, C. K. Syn, J. D. Whittenberger, and O. D. Sherby, Met. Mat. Trans. A, 1996, 30A, 1559-1568.
[14]. E. M. Taleff , B. L. Bramfitt, C K. Syn, D. R. Lesuer, J. Wadsworth and O. D. Sherby, Materials Characterization, 2001, 46, 11-18.
[15]. H. Sunana, J. Wadsworth, J. Lin and O.D. Sherby, Mater. Sci. Eng. 1979, **38**, 35-40.
[16]. C. K. Syn, D. R. Lesuer, and O. D. Sherby, Met. Mat. Trans. A, 1994, 25, 1481-1493.
[17]. A. Fernandez-Vicente, M. Carsı, F. Penalba, E. Taleff, and O.A. Ruano, Mat. Sci. Eng. A, 2002, 335, 175-185.
[18]. S. Szczepanik and J. Sinczak, Metallurgy and Foundry Engineering, 1994, 20, 441-448.
[19]. S. C. Mitchell, and A. Cias, Powder Met. Progress, 2004, 4, 132-142.
[20]. HSC Chemistry version 5.11, Outokumpu Research Oy, P.O. Box 60, FIN - 28101 Pori, Finland.
[21]. C. Capdevila, F. G. Caballero and C. Garciïa DE Andrés, ISIJ International, 2002, 42, 894-902.
[22]. M. Youseffi, C. S. Wright, and F. M. Jeyacheya, Powder Met., 2002, 45, 53-62.
[23]. R. Shivanath, P. and Jones, 'Canadian Patent, No. 2252745, 1997.
[24]. R. Shivanath, P. Jones, D. and T. D. Thieu, Canadian Patent, No. 2182389, 1995.
[25]. R. M. German, and B. H. Rabin, Powder Met., 1985, 28, 7-12.
[26]. O. D. Sherby and J. Wadsworth, J. Materials Processing Technology, 2001, 117, 347-353.
[27]. H. Danninger, C. Gierl, S. Kremel, G. Leitner, K. Jaenicke-Roessler and Y. Yu., Powder Met., 2002, 2, 125-140.
[28]. S. Kremel, H. Danninger, and Y. Yu, Powder Met., 2002, 2, 211-221.
[29]. G. F. Bocchini, R. Cesari, M. R. Oinasco, and E. Stagno, Materials Science Forum, 1999, 299-300, 224-248.
[30]. S. Szczepanik and S.C. Mitchell, 2009, unpublished results.

WARM FORGING OF SPHEROIDISED ULTRAHIGH CARBON STEEL

Stefan Szczepanik,
Faculty of Metallurgy and Material Science, AGH - University of Science and Technology, Krakow, Poland

Stephen C. Mitchell, Alhadi A. S. Abosbaia, Andrew S. Wronski
Engineering Materials Group, School of Engineering, Design and Technology, University of Bradford, W. Yorks, United Kingdom

Abstract

Liquid phase sintered and spheroidised Fe-1.4C-0.65Si-0.85Mo specimens were warm forged to discs at 750 and 700°C. The latter experiments were conducted at strain rates of 10^{-3}, 10^{-2}, 10^{-1} and 1 s^{-1} to ~ 1.15 natural strain. Ferrite grain size of the spheroidised PM steel, ~30 μm, diminished as a result of the forging to 6-7 μm, with a fine distribution of sub-micron carbides. The discs were tested in diametral compression and a procedure is presented for the determination, in this testing geometry, of the (compressive) yield strength, These values, above 740 MPa, compare favourably with 350-410 MPa , determined directly in tension, for the as-spheroidised material.

Keywords: ultrahigh carbon ductile steels, spheroidisation, warm forging

INTRODUCTION

Liquid phase sintering, heat treatment, microstructure and mechanical properties of Powder Metallurgy, PM, spheroidised ultrahigh carbon, UHC, steels are being reported in a concurrent publication [1]. These materials have yield and tensile strengths above 400 and 900 MPa, respectively and plastic strains of ~ 15%. The aim was to examine in detail the resultant microstructures, especially in the contexts of increased (room temperature) strength and the possibility of superplastic elevated temperature forming [2].

EXPERIMENTAL PROCEDURES

Dried [1] Höganäs Astaloy Mo85HP was used as the base iron-molybdenum powder, 0.6% silicon was introduced as fine <9μm silicon carbide, and 1.35% carbon as fine graphite (of 99.5% purity), which reacts with the Fe-Mo powder, forming a transient Fe-Si-C liquid phase at ~ 1080°C, speeding up diffusion of Si into the base powder [1], Turbula dry mixing of the base powder and SiC was carried out for 20 minutes. Liquid paraffin was introduced into the powder mix, thereby coating the metal powders with paraffin in order to bind the graphite to the base powder particles. This addition increased the base carbon level by about 0.05%, thus creating more liquid phase during sintering. Graphite was eventually added and mixing resumed for 20 minutes. Rings of outside and inside diameter 30 and 10 mm, respectively, and height 26.5 mm were pressed at 550 MPa to give green densities of ~ 6.8 g/cc.

Sintering of Fe-1.4C-0.6Si-0.85Mo at 1300C was carried out for 1 hr in nearly full semi-closed steel containers [1,3] pushed into a mullite tube furnace in nitrogen plus 0-10% hydrogen, with a gas flow of ~500 cm^3 min^{-1} and an inlet dew point no worse than -60°C. The rings were cooled slowly from the sintering temperature, austenitised at 950°C for 1 hour, then quenched into a warm fan assisted oven at ~130°C, followed by air cooling and refrigeration, then spheroidised at 750°C for 3 hours [1], slow cooled to room temperature, to give densities of ~7.2 g/cc and grain sizes of ~ 30 μm.

Two types of forging experiments were subsequently carried out. In one, the rings were heated to the working temperature in argon for 30 minutes and forged on a screw press between flat plates heated to 200°C. Examined were specimens after 1 strike at 700°C and after a similar strike, heating to 750°C, and a subsequent strike. The second set of experiments was carried out on discs of 8 mm diameter and 12 mm in height (cut from the rings) on a Gleeble HDV-40 machine at TUBA, Freiberg. The specimens were heated in argon to 700°C and then forged at strain rates of 10^{-3}, 10^{-2}, 10^{-1} and 1 s^{-1} to (recorded) ~ 1.15 natural (logarithmic) strain, Fig 1. The resultant discs had diameters of ~ 13 mm and were 3.15 mm thick.

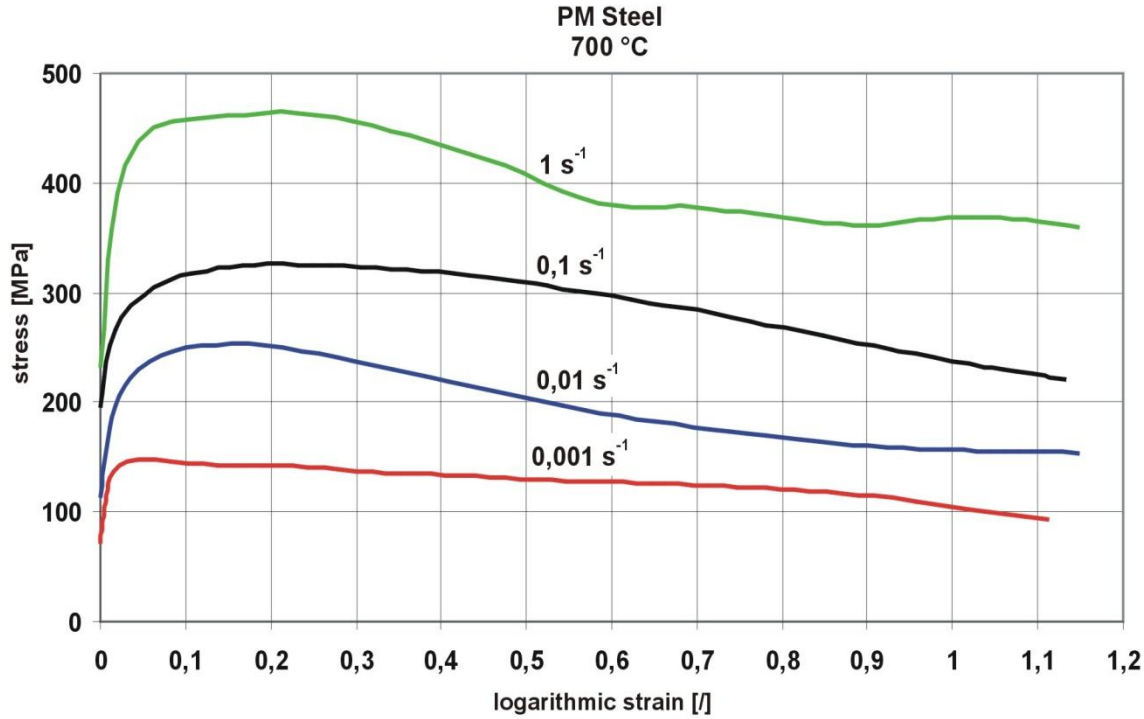

Fig. 1: Compressive stress – natural strain relationships for Fe-1.4C-0.65Si-0.85Mo PM steel at 700°C at strain rates in the range of 10^{-3} - 1 s^{-1}.

These forged discs had unsuitable geometry for conventional mechanical testing. Accordingly it was decided to employ diametral compression to the discs: adapt the procedure of determination of brittle fracture strength [4,5] to the meeting of plastic zones at the disc centre [5]. The tests were carried out in a specially constructed jig on an Instron machine at a compression rate of 5.10^{-1} s^{-1}.

RESULTS
Density and Microstructure.

The as-spheroidised microstructures, density of ~ 7.2 g/cm^3, consisted of ferrite plus, generally, fine carbides, e.g. Fig.2. Occasionally the original cementite network has not "balled" up completely and showed a cementite necklace in places. The one forging strike at 700°C did not weld up the pores completely but already evident were more and smaller carbides, Fig.3. The second, at 750°C, strike started to break up ferrite grain size and gave an even better carbide distribution, Fig.4. Gleeble 700°C forging resulted in densities approaching 7.8 g/cm^3 and microstructures with no pores, sub-grains and a uniform fine distribution of sub 1-2 micron-sized carbides, Figs. 5 and 6. These specimens were tested in diametral compression.

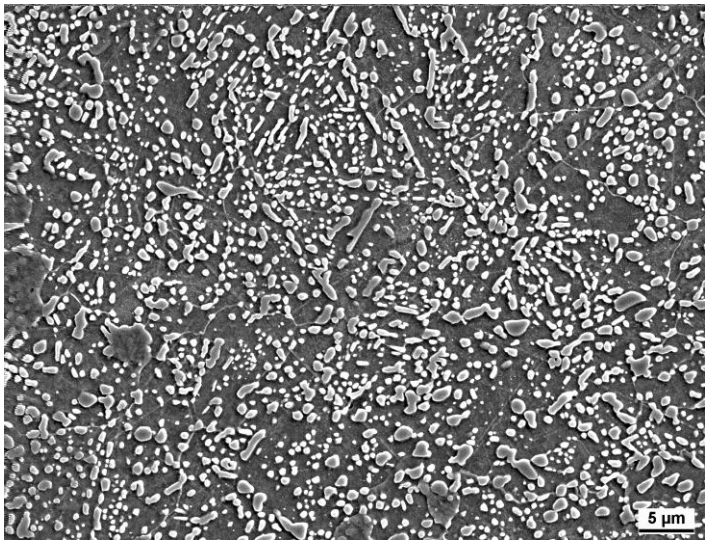

Fig. 2: Microstructure of as-spheroidised Fe-1.4C-0.6Si-0.85Mo.

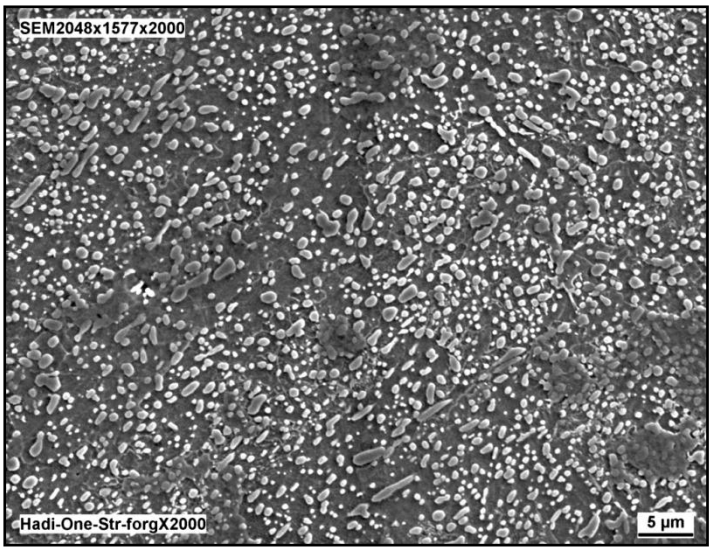

Fig. 3: Microstructure of as-spheroidised Fe-1.4C-0.6Si-0.85Mo forged on a screw press at 700°C. Note the fineness of the carbides, occasionally in "necklaces".

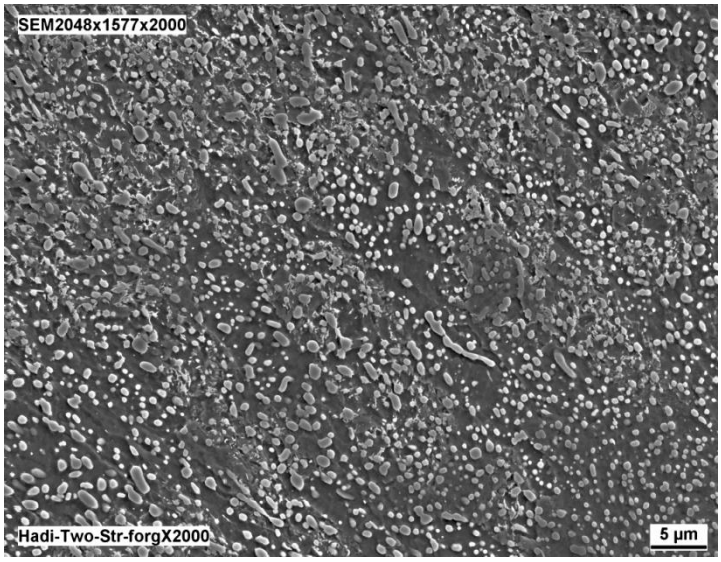

Fig. 4: Microstructure of as-spheroidised Fe-1.4C-0.6Si-0.85Mo forged on a screw press at 700°C, reheated and given a second strike at 750°C. Note the improved carbide distribution.

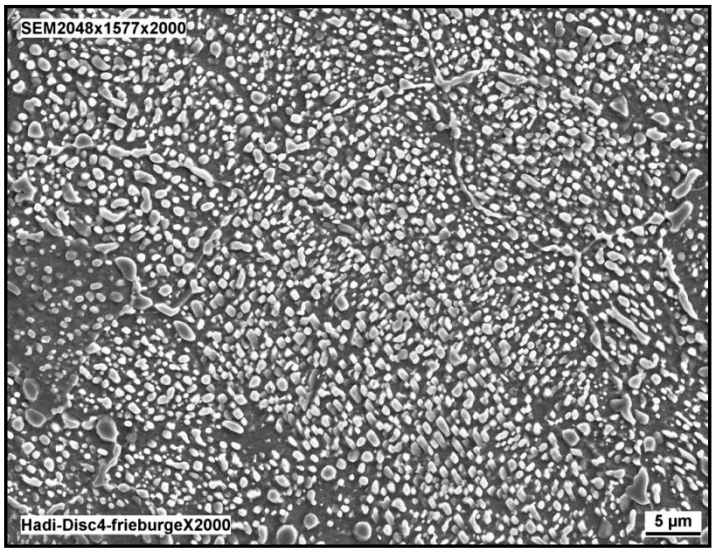

Fig.5: Uniform microstructure of ferrite grains and fine sub-micron spheroidised carbides after forging Fe-1.4C-0.6Si-0.85Mo at 700°C at a strain rate of 10^{-3} s^{-1}.

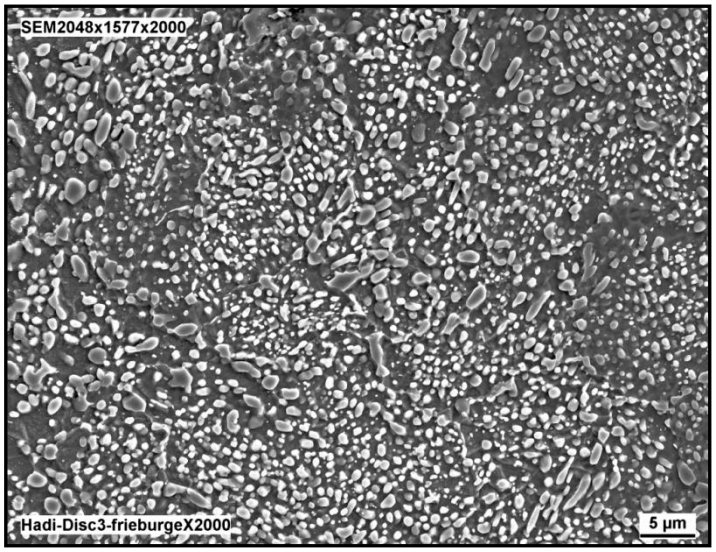

Fig.6: Uniform microstructure of ferrite grains and fine sub-micron carbides after forging Fe-1.4C-0.6Si-0.85Mo at 700°C at a strain rate of 10^{-2} s^{-1}.

Yield Strength

The as-spheroidised specimens had yield and tensile strengths above 400 and 900 MPa, respectively and plastic strains of ~ 16%, determined in conventional tensile tests. To estimate the as-forged yield strength, the diametral disc compression test was adapted [4,5]. This test is known also as Brazilian disc test and the indirect tensile test. Axial loading induces variable biaxial stresses: compressive, σ_3, and tensile, σ_1, in the transverse direction of the applied compressive load. It is used as a mechanical testing technique to determine the (brittle) tensile fracture strength (under transverse compression) of (linearly) elastic materials such as concrete, ceramics, composites, pharmaceutical tablets, PM compacts. The relevant failure region is the disc centre where a splitting crack originates [4,5]. The principal stresses have been computed by Hertz [6] and at the disc centre $\sigma_1 = 2P/\pi Dt$ and $\sigma_3 = -6P/\pi Dt$, where P is the applied compressive load, D the diameter and t the specimen thickness. Photoelasticity experiments of Frocht [7] show clearly the complex stress distribution and accord with the Hertz analysis. Because of the ease of testing and the simple specimen geometry, this test has been applied to materials which exhibit limited macroscopic plasticity before fracture and Proccopio et al. [5] have performed finite element calculations for the elastic and perfectly plastic situations in order to incorporate the effects of limited ductility.

In our experiments with work-hardening materials it was observed that plastic zones spread from the platens and meet at the disc centre (Fig. 7). This PM disc, 2.15 mm thick, had initial and final heights of 13.5 .and 9.2 mm, respectively. The critical event of plastic zones meeting was chosen to try to evaluate the yield stress. Neglecting plasticity, the principal stresses predict the yield stress to equal $KP/\pi Dt$, where the factor K equals 8 and 7.2, respectively, according to Tresca and Huber- criteria. The incorporation of plasticity into the finite element model, however, leads to ***substantial*** deviation between the analytical elastic expressions and the numerical elastoplastic solution. The maximum principal stress is reported to be still in the transverse direction, but that the location of this stress shifts away from the centre and that at (only) 2% diametrical strain, its magnitude is approximately 2.5–3 times the level predicted by the elastic solution. Furthermore, the volume over which all of the maximum transverse stress is acting showed a significant reduction in comparison with the purely elastic simulations. Thus it is completely unrealistic to use the elastic solution for our steel and it was decided to evaluate K experimentally: by conducting experiments on mild steel discs of determined tensile yield stress of 225 MPa. 3 experiments with discs evaluated K as 1.82, 1.84 and 1.82, respectively. Accordingly K=1.83 is now used with confidence to evaluate the yield stress of forged discs of the materials under investigation. Assuming uniaxial yield stress to equal 1.83 $P/\pi Dt$, the yield stresses after warm forging at 10^{-3}, and 10^{-2} sec^{-1} evaluate to 769 and 744 MPa, respectively. Sub-grains formed and grain sizes were in the range 6-7 µm. The yield strength thus increased substantially, from ~ 410 MPa, through warm forging of the spheroidised material.

Fig 7. Photograph of diametrically compressed disc of Fe-1.4C-0.6Si-0.85Mo when the plastic zones emanating from the platen contact regions meet at the disc centre. The height of the disc, warm forged at 700°C at a strain rate of 10^{-3} s^{-1}, reduced from 13.5 to 9.2 mm.

DISCUSSION

PM spheroidised steel, with yield and fracture strengths above 400 and 900 MPa and plastic strains of ~ 16% has already a very useful combination of mechanical properties. These can be further enhanced, to yield strengths above 740 MPa, by warm forging at ~ 700°C. This technique has the added advantage of accurate dimensional control. Depending on strain rate, compressive peak stresses of only 150-470 MPa were required. Superplasticity, however, was not observed in this set of experiments. Further work, including with as-sintered materials, is planned.

The proposed new method of evaluating yield strength of discs was shown to be acceptable by carrying out experiments on mild steel. The methodology was extended to specimens for which the yield strength could not be directly determined. Further validation, especially regarding the general applicability of the calibration factor, is required.

The yield strength increase through warm forging results from a drastically reduced (mean) grain size, *d*, from ~ 30 to 6-7 μm, formation of sub-grains, and probably an increase in the friction stress, σ_0, consistent with the Hall-Petch relation:

$$\sigma_y = \sigma_0 + k_y d^{-1/2}$$

where σ_y is yield strength and k_y the Hall-Petch strengthening coefficient. Syn et al [8], for spheroidised steels, went on to express σ_0 in terms of the inter carbide spacing, which is reduced somewhat by the warm forging.

CONCLUSIONS

Forging of spheroidised PM Fe-1.4C-0.65Si-0.85Mo at 700°C reduced the ferrite grain size from ~30 to 6-7 μm, with fine dispersion of submicron carbides. As a result of warm forging the yield stress increased from ~ 400 to above 700 MPa. A method commonly used to determine the tensile strength of brittle materials, diametral compression of discs, has been adapted to the evaluation of the yield stress of a ductile material. These preliminary experiments indicate that warm forging promises improvement of both properties and dimensional control for knowledge transfer to an industrial situation, e.g. for high-density engine PM connecting rods.

ACKNOWLEDGEMENTS

The work described forms part of the cooperative programme between the University of Bradford and AGH University of Science and Technology, Kraków. The authors gratefully acknowledge to one of us (SS) provision for instrumented forging on a Gleeble HDV-40 machine by Prof. R. Kawalla of the Metalforming Institut, TU BA Freiberg, Germany.

REFERENCES

[1], Abosbaia, A.A.S., Mitchell S.C., Youseffi, M., Wronski A.S., Powder Met., *submitted to*.
[2]. Szczepanik, S., Sinczak,J., Metallurgy and Foundry Engineering, vol.20,1994, p.441.
[3]. Cias, A., Mitchell, S.C., Pilch, K., Cias, H., Sulowski, M., Wronski, A.S.: Powder Metall., vol. 46, 2003, p. 165.
[4]. Jonsén, P., Häggblad., H.-Å., Sommer, K., Powder Technology, Vol. 176, 2007, p. 148.
[5]. Procopio, A.T., Zavaliangos, A, Cunningham, J.C., J. Materials Science Vol.38, 2003, p. 3629.
[6]. Hertz, H., GesammelteWerke (CollectedWorks), Leipzig, 1895.
[7]. Frocht .M.M., Photoelasticity, vol. 2, John Wiley & Sons Inc, New York, 1948.
[8], Syn, C.K., Lesuer, D.R., Sherby, O.D., Met. Trans.A, Vol. 25A, 1994, p. 1481